

POWER-SCAVENGING MEMS ROBOTS

THESIS

Daniel J. Denninghoff, Second Lieutenant, USAF

AFIT/GE/ENG/06-17

DEPARTMENT OF THE AIR FORCE
AIR UNIVERSITY

AIR FORCE INSTITUTE OF TECHNOLOGY

Wright-Patterson Air Force Base, Ohio

APPROVED FOR PUBLIC RELEASE; DISTRIBUTION UNLIMITED

The views expressed in this thesis are those of the author and do not reflect the official policy or position of the United States Air Force, Department of Defense, or the United States Government.

AFIT/GE/ENG/06-17

POWER-SCAVENGING MEMS ROBOTS

THESIS

Presented to the Faculty

Department of Electrical and Computer Engineering

Graduate School of Engineering and Management

Air Force Institute of Technology

Air University

Air Education and Training Command

In Partial Fulfillment of the Requirements for the

Degree of Master of Science in Electrical Engineering

Daniel J. Denninghoff, BSEE

Second Lieutenant, USAF

March 2006

APPROVED FOR PUBLIC RELEASE; DISTRIBUTION UNLIMITED

AFIT/GE/ENG/06-17

POWER-SCAVENGING MEMS ROBOTS

Daniel J. Denninghoff, BSEE
Second Lieutenant, USAF

Approved:

LaVern A. Starman, PhD, Maj, USAF (Chairman)	6 MAR 06 Date
James A. Fellows, PhD, Lt Col, USAF (Member)	6 MAR 06 Date
Guna S. Seetharaman, PhD (Member)	6 MAR 06 Date

Abstract

This thesis includes the design, modeling, and testing of novel, power-scavenging, biologically inspired MEMS microrobots. Over one hundred 500-µm and 990-µm microrobots with two, four, and eight wings were designed, fabricated, characterized. These microrobots constitute the smallest documented attempt at powered flight. Each microrobot wing is comprised of downward-deflecting, laser-powered thermal actuators made of gold and polysilicon; the microrobots were fabricated in PolyMUMPs® (Polysilicon Multi-User MEMS Processes). Characterization results of the microrobots illustrate how wing-tip deflection can be maximized by optimizing the gold-to-polysilicon ratio as well as the dimensions of the actuator-wings. From these results, an optimum actuator-wing configuration was identified. It also was determined that the actuator-wing configuration with maximum deflection and surface area yet minimum mass had the greatest lift-to-weight ratio. Powered testing results showed that the microrobots successfully scavenged power from a remote 660-nm laser. These microrobots also demonstrated rapid downward flapping, but none achieved flight. The results show that the microrobots were too heavy and lacked sufficient wing surface area. It was determined that a successfully flying microrobot can be achieved by adding a robust, light-weight material to the optimum actuator-wing configuration—similar to insect wings. The ultimate objective of the flying microrobot project is an autonomous, fully maneuverable flying microrobot that is capable of sensing and acting upon a target. Such a microrobot would be capable of precise lethality, accurate battle-damage assessment, and successful penetration of otherwise inaccessible targets.

Acknowledgments

We don't accomplish anything in this world alone ... and whatever happens is the result of the whole tapestry of one's life and all the weavings of individual threads from one to another that creates something.

~Sandra Day O'Connor

Before delving into a study of microrobots, I am excited to recognize some very important people. My sweet wife deserves my thanks for the lonely hours she's spent waiting for me to come home from the lab; for those sleepless late nights I spent finishing assignments; for the many weekends we didn't make it to Yellow Springs or the movies. I want to thank her also for all the yummy PB&J sandwiches and breakfast burritos; for warm welcomes home; for listening to career options A, B, C, D, E,…. More than that, I'd like to thank her for her unfailing encouragement and constant love.

My mom and dad are deserving of my gratitude for their loving support. Like most good parents, they do more than is expected and receive little in return. I am truly grateful for their continued nurture and support.

Special thanks to my current advisor, Maj LaVern Starman, for his constant encouragement; to my first advisor, Capt Paul Kladitis, for his clear guidance. They have taught me much about MEMS, research, and life. I owe much to these fine advisors. Thanks, also, to my committee members for their time and guidance on this project.

Chris Perry and Carrie Fowler from AFRL/MNAV are to be thanked for their encouragement and financial support. Thanks also to Bill Trop and Rick Patton for patiently enduring one more new student who needs their help in the clean room. Thanks to Scott Apt for masterfully milling my samples with the focused ion beam machine.

I am especially grateful for my classmates, Steve, Mike, Jeff, Frank, Enrique, John, and Glen. It has been a pleasure solving so many seemingly impossible homework

problems as well as researching our particular topics together. I'd like to particularly thank Steve Mink for his loyal friendship; he is someone you look forward to seeing each day in the lab. He is also generously helpful. Steve willingly drove me home through a late-night blizzard and drove me home after a late-night flight; he has been thoughtful in sharing his lunch and bringing me breakfast after staying up all night in the lab; he has given me much needed encouragement and advice after listening to stories and problems. It's been a privilege to work with Steve Mink.

My friends, family, and associates have helped me throughout this challenging program. Thanks, to all.

Daniel J. Denninghoff

Table of Contents

Page

Abstract iv

Acknowledgments v

List of Figures xii

List of Tables xxv

Foreword xxvii

I. Introduction to Microrobots 1

1.1 An Argument for Microrobot Development 2
1.2 Microelectromechanical Systems (MEMS) as an Enabling Technology 3
1.3 Relevant Microrobotics Terminology 4
1.3.1 Robot 4
1.3.2 Autonomous 5
1.3.3 Microrobot 5
1.3.4 Untethered 6
1.3.5 Power-Scavenging Capability 7
1.3.6 Controlled Behavior 7
1.4 Problem Overview: Limitations in MEMS 7
1.5 Intent of Research 8
1.5.1 Proposed Solution and Research Objectives 8
1.5.2 End Goal of the Flying Microrobot Project 9
1.5.3 Design Requirements 10
1.6 Organization of Thesis 10
1.7 References 11

II. Critical Review of Miniature Robots 14

2.1 Chapter Introduction 14
2.1.1 Historical Perspective 14
2.1.2 Potential Microrobot Applications 15
2.2 Redefining "Microrobots" 18
2.3 Land-Based Miniature Robots 19
2.3.1 The Smallest Autonomous Mobile Land-Based Robot 20
2.3.2 Critical Survey of Tethered MEMS Land-Based Robots and Conveyors 21
2.3.3 Critical Survey of Untethered MEMS Land-Based Robots 36
2.3.4 Summary of MEMS Land-Based Robots 43
2.4 Airborne Miniature Robots 44
2.4.1 The Smallest Autonomous Powered Airborne Vehicle 44
2.4.2 Critical Survey of Miniature Airborne Vehicles 45

Page

2.4.2.1 Flapping (Ornithoptic) Miniature Airborne Vehicles..... 46
2.4.2.2 Fixed-Wing Miniature Airborne Vehicles..... 49
2.4.2.3 Rotary Miniature Airborne Vehicles..... 49
2.4.3 Summary of Miniature Airborne Vehicles 50
2.5 Chapter Summary 51
2.6 References..... 52

III. Theory 63

3.1 Chapter Introduction 63
3.2 Heat Transfer 63
3.2.1 Conduction..... 63
3.2.2 Convection 65
3.2.3 Radiation..... 66
3.3 Thermal Expansion 66
3.3.1 Elongation and Contraction 66
3.3.2 Vertical Deflection in Bimorph Structures 67
3.4 Optical Absorption..... 69
3.4.1 Photon Energy and Bandgap Relationship..... 69
3.4.2 Optical Absorption Coefficient 71
3.4.3 Photon Absorption 72
3.4.4 Heat and Power Generation 74
3.5 Total Optical Power Efficiency 75
3.6 Chapter Summary 77
3.7 References..... 78

IV. Modeling and Simulations..... 80

4.1 Chapter Introduction 80
4.2 MEMS Material Properties..... 80
4.2.1 PolyMUMPs® Silicon, Polysilicon, Silicon Dioxide, and Gold Properties..... 81
4.2.2 Stress in PolyMUMPs® Polysilicon and Gold Layers 82
4.3 Analytical Prediction of Initial Deflection in Cantilever Beams 83
4.3.1 Derivation of Initial Deflection Equations 85
4.3.2 Calculating Initial Deflection 91
4.4 CoventorWare® Finite Element Simulations of Cantilever Beams 94
4.4.1 Mesh Efficiency Study using Cantilever Beams..... 95
4.4.2 Calibrating CoventorWare® using Cantilever Beams 96
4.4.3 Comparison of Cantilever Beam Deflection Values 98
4.5 CoventorWare® Finite Element Simulations of Microrobot Wings 100
4.5.1 Microrobot Wing Model 1: The Separated Wing 101
4.5.2 Microrobot Wing Model 2: The Connected Wing..... 102
4.5.3 Microrobot Wing Model 3: The Raised Wing..... 103
4.5.4 Summary of Microrobot Wing Deflection Values..... 104

Page

4.6 Downward Deflection in Cantilevers 105
4.6.1 Temperature-Deflection Relationship in Cantilevers 105
4.6.2 Power-Deflection Relationship in Cantilevers 107
4.6.3 Non-Uniform Temperature Distribution 109
4.7 Downward Deflection in Microrobot Wings 112
4.8 Modeling to Predict Performance 113
4.9 Chapter Summary 117
4.10 References 118

V. Designs and Fabrication 120

5.1 Chapter Introduction 120
5.2 Design Inspiration 120
5.2.1 Sponsor Requirements 120
5.2.2 Inspiration from Insects 121
5.2.3 Inspiration from Theory and Modeling 122
5.2.4 The Dominant Design Elements 124
5.3 PolyMUMPs® Fabrication Process 129
5.4 Microrobot Design Concept 130
5.5 Microrobot Design Details 133
5.6 Summary 142
5.7 References 143

VI. Experiments and Procedures 145

6.1 Chapter Introduction 145
6.2 660-nm Laser Diode Operation 145
6.3 Laser Diode Characterization 146
6.3.1 Current-Power Relationship 146
6.3.2 Spot Size Characterization 149
6.3.2.1 Gaussian Beam Propagation Model 149
6.3.2.2 Laser Diode Propagation at Threshold and Maximum Current 152
6.4 Laser Setup Optimization 156
6.5 PolyMUMPs® Sacrificial Oxide Release 162
6.6 Microrobot Characterization 168
6.6.1 Initial Deflection Measurements 168
6.6.2 Microrobot Imaging 171
6.7 Microrobot Performance 173
6.7.1 Challenges in Testing Laser-Powered Deflection 173
6.7.2 Solutions to Testing Challenges 173
6.8 Summary 178
6.9 References 179

Page

VII. Results and Analyses 180

7.1 Chapter Introduction 180
7.2 Cantilever Initial Deflection 180
7.3 Trends in Microrobot Initial Deflection 183
7.4 Powered Deflection in Microrobot Test Wings 190
7.5 Optimized Microrobot Design Results 193
7.6 Laser-Powered Deflection 197
7.7 Towards a Flying Microrobot 197
7.7 Summary 198
7.8 References 199

VIII. Conclusions and Recommendations 200

8.1 Chapter Introduction 200
8.2 Thesis in a Nutshell 200
8.3 Novel Contributions of this Thesis 202
8.4 Recommendations 203
8.4.1 Recommendations for Flying Microrobots in PolyMUMPs® 204
8.4.2 Recommendations for Flying Microrobots in other Processes 206
8.4.3 Words of Wisdom 207
8.5 Summary 207

Appendix A: L-edit Mask Layouts for PolyMUMPs® Fabrication 208

A.1 MUMPs® Run 66 Masks 210
A.2 MUMPs® Run 67 Masks 212
A.3 MUMPs® Run 68 Masks 215
A.4 MUMPs® Run 69 Masks 224

Appendix B: MatLab® Code 237

B.1 Light Penetration Depth 237
B.2 Residual Stress Deflection in Cantilevers 238
B.3 Temperature-Deflection Relationship in Cantilevers 239
B.4 Power-Deflection Relationship in Cantilevers 240
B.5 Temperature Distribution in a Conduction-Convection System 241
B.6 Normalized Gaussian Beam Intensity 242
B.7 Pixelscope Data Plotter 242
B.8 Scaling in Insects 243

Appendix C: Laser Safe Operating Procedures 244

Appendix D: Laser Equipment Operation Instructions 247

D.1 TEC 2000 Thermoelectric Temperature Controller Procedures 247

Page

D.2 LDC 500 Laser Diode Controller Procedures 247
D.3 S20MM Silicon Power Meter Operation Procedures 248

Appendix E: Microrobot Complete Initial Deflection Data 249

E.1 Deflection in MUMPs® 66 Microrobots 250
E.2 Deflection in MUMPs® 67 Microrobots 252
E.3 Deflection in MUMPs® 68 Microrobots 257
E.4 Deflection in MUMPs® 69 Microrobots 263

Appendix F: Challenges in Measuring Power-Deflection in Microwings 267

Vita 270

List of Figures

Page

Figure 2.1: Photograph of the Sandia robot, which is the smallest reported autonomous mobile land-based robot at 4096 mm^3 in volume and 28 g in mass [46]. 20

Figure 2.2: Photograph of a 4.8-mm nickel car driven by an electromagnetic step motor positioned on a 5-cent coin. The car is a $1/1000^{th}$ scaled version of a full-size automobile and clocked a maximum speed of 100 mm/sec [49]. 21

Figure 2.3: Photograph of a 4.8-mm nickel car positioned among grains of rice. The attached 18-μm copper wires transmit power from a 100-Hz AC source to the electromagnetic stepper motor [48]. 23

Figure 2.4: SEM micrograph of one motion pixel of a microconveyer; it is comprised of four 430-μm-long polyimide cilia actuator legs in a common-center configuration [50]. 24

Figure 2.5: Diagram of programmable polyimide leg for a microconveyor pixel, which is comprised of both thermal and electrostatic actuators to provide 3 DOF [50]. 24

Figure 2.6: SEM micrographs of a 10 x 10-mm^2 robot with six-leg insect gate. (a) Image of an erected leg, comprised of an out-of-plane polysilicon thermal actuator with both two and three DOF. (b) Robot with belly and 96 legs in the air [51], [52]. 25

Figure 2.7: Diagram of piezoelectric slip-stick locomotion method developed in 1998 and later used in several centimeter-scale robots [26]. 26

Figure 2.8: SEM micrographs of a ciliary microconveyor array after complete fabrication [54]. 27

Figure 2.9: Diagram of the polyimide-bimorph thermal ciliary microactuator for a microconveyor [53]. 28

Figure 2.10: Diagram of a microconveyer system in which the two sets of legs are powered by phase-shifted square waves [63]. 29

Figure 2.11: Diagram of the microconveyer from Figure 2.10 in which two sets of legs are powered by separate square waves [63]. 30

Page

Figure 2.12: Conceptual diagram illustrating forward motion of a robot based on the two-phase microconveyer scheme as illustrated in Figure 2.10 [56]. 30

Figure 2.13: Diagram illustrating the actuation principle for the leg movements based on a four-V-groove joint. Each leg is retracted when cooled and uncurled when heated due to greater thermal expansion of the polyimide near the heater than away from the heater [56]. 31

Figure 2.14: Expanding polyimide actuation principle illustrated by diagrams of (a) cool and (b) heated actuators [62]. 31

Figure 2.15: Photograph of 15-mm-long robot carrying a 2500-mg weight (30 times its own weight), which is a record for miniature robots [56]. 32

Figure 2.16: Photograph of a 30 x 10 x 1-mm^3 ciliary-based robot capable of 3-DOF movement [64]. 33

Figure 2.17: Micrograph of the SDA robot—"Scratchuator"—positioning a 2 x 2 x 0.5-mm^3 die across an insulated silicon wafer [25]. 34

Figure 2.18: Diagram of the stepping process of a scratch drive array electrostatic actuator [25]. 34

Figure 2.19: Diagram of the complete 6 x 3.5 x 0.5-mm^3 thermally actuated robot based on a six-legged insect locomotion scheme [65]. 35

Figure 2.20: Diagram of the stepping process from (a) to (d). A 120-μm step size from individual legs was demonstrated [65]. 35

Figure 2.21: SEM micrograph of a robot containing surface-micromachined hinges for joints [70]. 36

Figure 2.22: SEM micrograph of one of four gap-closing actuator (GCA) sections in an inchworm electrostatic motor [70]. 37

Figure 2.23: Photograph of the first solar-powered robot which uses electrostatic gap-closing actuators with a gear and clutch combination to move its legs [74]. 38

Figure 2.24: Diagram of the three-chip assembly process of the first autonomous solar-powered robot [73]. 39

Page

Figure 2.25: SEM micrograph of the silicon legs, hinges, and one section of a GCA [73]. 40

Figure 2.26: Images of the 760 x 710-μm^2 laser-powered microrobot [20]. 41

Figure 2.27: SEM micrograph of the first untethered walking microrobot [78]. 42

Figure 2.28: Diagram of the capacitive-coupled power delivery system required for untethered scratch drive actuators [78]. 42

Figure 2.29: The Black Widow is the smallest reported autonomous powered aircraft with a 15-cm wing span and 60-g take-off weight [79]. 45

Figure 2.30: 1.5-mm-long flying robot concept (a) in a diagram showing the polysilicon wings, the aluminum contact plates, and the silicon chip; (b) a photograph of the fabricated structure [86], [89]. 46

Figure 2.31: Photograph of the 25-mm Mechanical Flying Insect (MFI) thorax in its current state, including a carbon-fiber frame, two polyimide wings, and four piezoelectric actuators [95]. 48

Figure 2.32: Diagram of future features of the MFI, including sensors, ocelli (eyes), a processor, a battery, and an antenna [95]. 48

Figure 2.33: Photographs of 8 x 5 x 8-mm^3 rotary flying device (a) before takeoff and (b) during flight [114]. 50

Figure 3.1: Diagram of a gold-polysilicon cantilever illustrating the principle of heat conduction (top). 65

Figure 3.2: Conceptual diagram of the upward deflection caused by cooling a gold-polysilicon cantilever. 68

Figure 3.3: Conceptual diagram of downward deflection caused by laser heating in a gold-polysilicon cantilever. 68

Figure 3.4: Band diagram illustrating photon absorption for (a) $h\nu = E_g$ and (b) $h\nu > E_g$. Unless defects exist in the material, a photon with (c) $h\nu < E_g$ is not absorbed [13]. 70

Figure 3.5: Optical absorption coefficient for Ge, GaAs, and Si. The value in the parenthesis is the cutoff wavelength [13]. 71

Page

Figure 3.6: Experimentally determined optical absorption coefficients for doped polysilicon compared to single-crystalline silicon [15]. 72

Figure 3.7: Graph showing the percentage of light energy absorbed per layer thickness in phosphorus-doped polysilicon. 73

Figure 3.8: Graph showing the efficiency of converting absorbed energy into heat in silicon (E_g = 1.12 eV) for wavelengths from 0.2 to 1.2 μm. 74

Figure 3.9: Graph of polysilicon reflectivity as a function of incidence angle for five different laser wavelengths [16]. 75

Figure 4.1: SEM image of a PolyMUMPs® 49-μm gold-polysilicon cantilever beam. The beam is measured from the anchor to the tip of the beam since that is the only portion that is free to deflect. 83

Figure 4.2: Free-body diagrams of a gold-poly2 cantilever. 84

Figure 4.3: Manhattan brick mesh of MUMPs® 66 cantilevers. The finite element sizes are 10 x 0.75 x 50 μm^3, which yield accurate results with minimal simulation time expended. 95

Figure 4.4: Zygo® IFM vertical deflection measurements of MUMPs® 66 cantilevers. The beams with lengths from 49 to 249 μm were measured; the longest beam exhibits the most deflection. 96

Figure 4.5: MemMech simulation results of cantilevers with calibrated stress values. 98

Figure 4.6: Graphed results from Table 4.8, illustrating the comparison among analytical, experimental, and simulated cantilever initial deflection results. 99

Figure 4.7: L-edit mask layout of a microrobot wing chosen for simulation. 100

Figure 4.8: 3-D image of a 210-μm separated wing model with the extruded brick mesh. 101

Figure 4.9: MemMech simulation results of a 210-μm separated wing showing a 7.4-μm tip deflection on all flexure widths. 101

Figure 4.10: 3-D image of the 210-μm connected wing model with a tetrahedral mesh; the maximum element dimensions are 30 x 30 μm^2. 102

Page

Figure 4.11: MemMech simulation results of a 210-μm connected wing showing a 7.4-μm tip deflection at all points around the rim. 102

Figure 4.12: 3-D image of the 210-μm raised wing model that includes a poly1 spacer under the three center flexures. 103

Figure 4.13: 3-D image of the raised wing model with a tetrahedral mesh; the maximum element dimensions are 30 x 30 μm^2. 103

Figure 4.14: MemMech simulation results of the 210-μm raised wing model with the poly1 spacer. 104

Figure 4.15: Diagrams of gold-poly2 cantilevers in a simple modeling case with constant heat throughout the device and no convection losses. 106

Figure 4.16: MatLab® plot of downward deflection as a function of temperature in several gold-poly2 cantilevers. 107

Figure 4.17: MatLab® plot of downward deflection as a function of absorbed power in several gold-poly2 cantilevers. 108

Figure 4.18: Diagram of a gold-poly2 device with non-uniform temperature distribution. 109

Figure 4.19: Graph of the temperature distribution for a 249-μm-long and an infinitely long gold-poly2 cantilever with 400-K end-tip and 300-K ambient temperatures. 111

Figure 4.20: Coventor® image of the connected wing model in the steady-state incremental temperature analysis. 112

Figure 4.21: Thermal simulation of the connected wing model with an applied incremental steady-state temperature; a 0.6-m/s airflow is applied to account for forced convection losses during wing movement. 113

Figure 4.22: Reported residual stress values in PolyMUMPs® poly2 layer. The histogram shows a normal distribution with a mean of 8.68 MPa and standard deviation σ of 3.14 MPa. 114

Figure 4.23: Reported residual stress values in PolyMUMPs® gold layer. 115

Figure 4.24: Reported residual stress values in PolyMUMPs® poly2 layer from runs 37–69. 116

Page

Figure 5.1: Illustration of the trend in insect wing flapping frequency versus mass. Smaller insects tend to flap faster than larger insects (adapted from [2]). 121

Figure 5.2: Diagram illustrating the downward deflection in a microrobot wing. 125

Figure 5.3: Diagram of the available layers in PolyMUMPs® 129

Figure 5.4: Diagram of an eight-wing 500-μm gold-polysilicon microrobot design concept. 131

Figure 5.5: Diagram of a four-wing 500-μm gold-polysilicon microrobot design concept.....132

Figure 5.6: SEM micrograph of an eight-wing 500-μm gold-polysilicon microrobot fabricated in MUMPs®. 133

Figure 5.7: SEM micrograph of a four-wing 500-μm gold-polysilicon microrobot fabricated in MUMPs®. 134

Figure 5.8: SEM micrograph of a 2 x 2-mm^2 microrobot chip containing 9 500-μm robots and matching electrically powered test wings. 135

Figure 5.9: SEM micrograph of a two-wing 990-μm microrobot surrounded by 500-μm microrobots. 135

Figure 5.10: SEM micrographs of (left) a poly2 substrate anchor with breakable tethers and (right) a microrobot with the anchors on one side. 136

Figure 5.11: Zygo® data image of a microrobot anchored on one side. 136

Figure 5.12: Photograph of microrobots that were destroyed in the drying chamber. 137

Figure 5.13: SEM micrographs of microrobots with tethers on opposite sides of the device.....137

Figure 5.14: Zygo® data image of a microrobot with tethers on both sides. 137

Figure 5.15: SEM micrographs of (left) a microrobot center with just poly2, and (right) poly1-poly2 center connected through a via oxide etch.....138

Page

Figure 5.16: SEM micrographs of (left) the poor gold adhesion that results from making the gold-poly2 flexures too narrow; (right) the merging poly2 flexures that results from making the flexure spacing too close. 139

Figure 5.17: SEM micrographs of (left) the unattached poly1 spacer under the center of the wing and (right) that poly0 spacer. 140

Figure 5.18: SEM micrograph of electrically powered test wings for several microrobot wing configurations. 141

Figure 5.19: Close-up SEM micrograph of an electrically powered test wing corresponding to a 500-μm microrobot. 141

Figure 5.20: Close-up SEM micrograph of an electrically powered test wing corresponding to a 990-μm microrobot. 142

Figure 6.1: Photographs of laser operating equipment. 146

Figure 6.2: Photograph of equipment used to measure laser power. 147

Figure 6.3: Graph of the measured current-power relationship for the 660-nm laser diode for various operating temperatures. 148

Figure 6.4: Diagram of a Gaussian beam propagating along the *z*-axis. 150

Figure 6.5: MatLab® model of a normalized Gaussian beam intensity at increasing distances from the laser source: (a) beam waist $z = 0$; (b) Raleigh range $z = z_0$; (c) $z = 2z_0$. 151

Figure 6.6: Diagram of the experiment used to measure the laser beam spot size. 152

Figure 6.7: Measured data plots of the laser beam spot size at a 50-mA driving current for various distances from the laser: (a) at 1 in (2.54 cm); (b) at the beam waist 6.5 in (16.51 cm); (c) and at 11 in (27.94 cm). 153

Figure 6.8: Measured data plots of the laser beam spot size at a 109-mA driving current for various distances from the laser: (a) at 1 in (2.54 cm); (b) at the beam waist 6.5 in (16.51 cm); (c) and at 11 in (27.94 cm). 154

Figure 6.9: Measured data plots of the laser beam spot size at a fixed 2.54-cm distance between the CCD and the laser for increasing power values: (a) 51-, (b) 55-, (c) and 109-mA driving currents. 155

Page

Figure 6.10: Diagram of an improved optical setup with just a mirror and a lens. 158

Figure 6.11: Graph of measured laser power after each element in the 1300-mm optical setup (1300 mm represents the distance from laser to robot).....158

Figure 6.12: Diagram of an optimized optical setup with the same components as those in Figure 6.10. 159

Figure 6.13: Graph of measured laser power in the optimized 650-mm optical setup.....159

Figure 6.14: Photographs of the optimized 650-mm laser test setup: (a) the entire laser setup including a microscope and two cameras; (b) 25.4-mm-diameter mounted mirror; (c) 12.7-mm-diameter mounted lens (f = 12.7 mm); (d) laser diode and mount. 160

Figure 6.15: Photograph of the top view of the optimized 650-mm optical setup. 161

Figure 6.16: Photographs of: (a) the robot chip on the stage with the lens removed and the microscope light off; (b) the lens replaced with the camera light on.....161

Figure 6.17: Photograph of a gel box with six columns of unreleased chips (left) and a magnified image of one chip (right). 163

Figure 6.18: Photographs of the three chemicals used in the release procedure—methanol, acetone, and hydrofluoric acid (HF)—on a weighing scale (left) and the separate storage unit for the highly corrosive HF (right) 164

Figure 6.19: Photograph of the beakers and labels of the seven-step release process: (1) first acetone bath, (2) second acetone bath, (3) first methanol bath (4) first de-ionzed water rinse (5) HF release, (6) second de-ionized water rinse, and (7) final methanol bath.....165

Figure 6.20: Photograph of the first step in the release process—a 10-minute acetone bath.....165

Figure 6.21: Zygo® IFM image of a partially released microrobot. The center of the microrobot is unintentionally attached to the substrate by incompletely etched oxide.....166

Figure 6.22: Diagram of the side view of: (left) a microrobot chip before performing an HF release; (right) an incompletely etched chip showing an attached oxide post.....166

Page

Figure 6.23: Zygo® IFM image of a completely released microrobot. Gently agitating the HF beaker replenishes fresh HF in the oxide regions, achieving a complete release. 166

Figure 6.24: Zygo® image of a completely released microrobot that was dried on a hotplate at 110 °C. 167

Figure 6.25: Photographs of (a) the entire supercritical CO_2 dryer unit, and (b) the required pre-run chamber cleaning....168

Figure 6.26: Photograph of the Zygo® interferometric microscope workstation used to precisely measure microrobot vertical deflection. 169

Figure 6.27: Zygo® IFM images of (a) complete vertical deflection data in a microrobot, and (b) incomplete data. 170

Figure 6.28: Zygo® IFM image of an electrically powered test wing with no power applied. 171

Figure 6.29: Photographs of (a) video capture equipment and (b) the Micromanipulator® probe station used for inspecting, applying power to, and probing MEMS samples. 172

Figure 6.30: Photograph of the scanning electron microscope (SEM) used for high-resolution imaging. A scanned microrobot is featured. 172

Figure 6.31: SEM image of a hinged flip-up ruler used to measure the downward vertical deflection of laser-powered microrobots. 174

Figure 6.32: A close-up SEM image of the poly2 staple hinge for the flip-up ruler used to measure downward deflection in laser-powered robots. 174

Figure 6.33: SEM images of a flip-up ruler in its: (a) unlocked and (b) locked positions....175

Figure 6.34: SEM images of a microrobot launch pad formed by back-side etching a MUMPs® chip. The launch pad was patterned and etched using a focused ion beam (FIB) machine [5]. 176

Figure 6.35: SEM image of a microrobot launch pad formed by etching a pit into the substrate and by stacking every PolyMUMPs® layer to form a post. 176

Figure 6.36: SEM image of rulers, launch pads, and microrobots. 177

Page

Figure 6.37: Zygo® image showing the 10-μm post height fabricated by etching 4 μm into the substrate and by stacking every PolyMUMPs® layer into a 6-μm post. 177

Figure 7.1: Zygo® image of gold-poly2 cantilever deflection measurements. 180

Figure 7.2: Graphed data of gold-poly2 cantilever deflection measurements from MUMPs® runs 66, 68, and 69.....181

Figure 7.3: Zygo® data showing a microrobot surface map and deflection profile. 183

Figure 7.4: Photograph of nine 500-μm microrobots fabricated in MUMPs® 67.....184

Figure 7.5: Photographs of (left) the M68rob1 chip, and (right) the M68rob2 chip. 185

Figure 7.6: SEM images of the two different microrobot wing configurations from Figure 7.5. 185

Figure 7.7: L-edit® design schematics of (left) the M68rob1 chip, and (right) the M68rob2 chip. 186

Figure 7.8: Wing-tip deflection measurements of microrobots in the M68rob1 and M68rob2 chips. Except for positions 1 and 2, the deflection in M68rob1 is greater. 187

Figure 7.9: L-edit® schematic of three 210-μm electrically testable wings from 500-μm microrobots fabricated in MUMPs® 69. 190

Figure 7.10: Zygo® images of a 210-μm electrically powered test wing at (a) 0.0 V and (b) 2.0 V. 191

Figure 7.11: Powered deflection in three 210-μm electrically powered test wings at increasing input power levels. 191

Figure 7.12: SEM image of a 420-μm electrically testable wing from a 990-μm microrobot fabricated in MUMPs® 69. 192

Figure 7.13: Powered deflection of a 420-μm electrically testable wing from a 990-μm microrobot compared with the 210-μm wing from Figure 7.9. The 420-μm has a greater deflection-power ratio. 192

Page

Figure 7.14: Photographs of the 500-μm microrobots with the highest combined deflection-mass and area-mass ratios: (a) is M68rob1pos6; (b) is M68pos2pos6; and (c) is M69rob1pos8. 193

Figure 8.1: L-edit® mask layout of a 990-μm microrobot frame with actuators based on the most successful 500-μm robot fabricated in this thesis. 205

Figure A.1: L-edit® color scheme for identifying the mask layers available for photolithographic patterning in PolyMUMPs®. 209

Figure A.2: L-edit® color mixing scheme of all the possible overlapping mask layers, starting from Poly0/Poly1/Poly2/Gold row and moving in the direction of the arrows. 209

Figure A.3: MUMPs® 66 Denninghoff Chip1 Robots 210

Figure A.4: MUMPs® 66 Denninghoff Chip2 Test Structures 211

Figure A.5: MUMPs® 67 Denninghoff Chip1 Robots1 212

Figure A.6: MUMPs® 67 Denninghoff Chip2 Robots2 213

Figure A.7: MUMPs® 67 Denninghoff Chip3 Test Structures 214

Figure A.8: MUMPs® 68 Denninghoff Chip1 Robots1 T 215

Figure A.9: MUMPs® 68 Denninghoff Chip2 Robots1 R 216

Figure A.10: MUMPs® 68 Denninghoff Chip3 Robots2 T 217

Figure A.11: MUMPs® 68 Denninghoff Chip4 Robots2 R 218

Figure A.12: MUMPs® 68 Denninghoff Chip5 Robots3 T 219

Figure A.13: MUMPs® 68 Denninghoff Chip6 Robots3 R 220

Figure A.14: MUMPs® 68 Denninghoff Chip7 Insects T 221

Figure A.15: MUMPs® 68 Denninghoff Chip8 Insects R 222

Figure A.16: MUMPs® 68 Denninghoff Chip9 Test Structures 223

Figure A.17: MUMPs® 69 Denninghoff Chip1 Robots1 224

Page

Figure A.18: MUMPs® 69 Denninghoff Chip2 InsectsT 225

Figure A.19: MUMPs® 69 Denninghoff Chip3 InsectsR 226

Figure A.20: MUMPs® 69 Denninghoff Chip4 Large Bugs 227

Figure A.21: MUMPs® 69 Denninghoff Chip5 Large Bugs2 228

Figure A.22: MUMPs® 69 Denninghoff Chip6 Launch Pad1 229

Figure A.23: MUMPs® 69 Denninghoff Chip7 Launch Pad2 230

Figure A.24: MUMPs® 69 Denninghoff Chip8 Launch Pad3 231

Figure A.25: MUMPs® 69 Denninghoff Chip9 66-67 Wings 232

Figure A.26: MUMPs® 69 Denninghoff Chip10 68 Wings.....233

Figure A.27: MUMPs® 69 Denninghoff Chip11 69 Wings.....234

Figure A.28: MUMPs® 69 Denninghoff Chip12 Large Wings 235

Figure A.29: MUMPs® 69 Denninghoff Chip13 Test Structures.....236

Figure E.1: Zygo® data showing a microrobot surface map and deflection profile.....249

Figure E.2: (left) L-edit® design schematic and (right) photograph of MUMPs® 66 microrobots. The positions are numbered from 1–9 for reference.....250

Figure E.3: Wing-tip deflection measurements of MUMPs® 66 microrobots. 250

Figure E.4: (left) L-edit® design schematic and (right) photograph of MUMPs® 67 version 1 microrobots. 253

Figure E.5: Wing-tip deflection measurements of MUMPs® 67 version 1 microrobots. 253

Figure E.6: (left) L-edit® design schematic and (right) photograph of MUMPs® 67 version 2 microrobots. 255

Figure E.7: Wing-tip deflection measurements of MUMPs® 67 version 2 microrobots. 255

Page

Figure E.8: (left) L-edit® design schematic and (right) photograph of MUMPs® 68 version 1 microrobots. 257

Figure E.9: Wing-tip deflection measurements of MUMPs® 68 version 1 microrobots. 257

Figure E.10: (left) L-edit® design schematic and (right) photograph of MUMPs® 68 version 2 microrobots. 259

Figure E.11: Wing-tip deflection measurements of MUMPs® 68 version 2 microrobots. 259

Figure E.12: (left) L-edit® design schematic and (right) photograph of MUMPs® 68 version 3 microrobots. 261

Figure E.13: Wing-tip deflection measurements of MUMPs® 68 version 3 microrobots. 261

Figure E.14: (left) L-edit® design schematic and (right) photograph of MUMPs® 69 version 1 microrobots. 263

Figure E.15: Wing-tip deflection measurements of MUMPs® 69 version 1 microrobots. 263

Figure E.16: (left) L-edit® design schematic and (right) photograph of four 990-μm two-wing microrobots from MUMPs® 69 265

List of Tables

Page

Table 2.1. Description of MEMS components, observation methods, and technologies compared with those of other fields [41]. 19

Table 2.2. Summary and Comparison of Land-Based MEMS Robots and Conveyors. 43

Table 3.1. Thermal conductivity values of gold, silicon, and silicon dioxide [1], [3], [4]. 65

Table 3.2. Thermal expansion coefficients of gold film and polysilicon [1]. 67

Table 3.3. Summary of the total power efficiency in the photon absorption process for phosphorus-doped polysilicon. 76

Table 4.1. Material properties of single-crystalline silicon, poly-crystalline silicon, deposited silicon dioxide, and gold (adapted from [2]). 81

Table 4.2. Reported material properties for MUMPs® poly2 layer [14]. 82

Table 4.3. Reported material properties for MUMPs® gold layer [14]. 82

Table 4.4. Parameters and values used in calculations for gold and poly2. 91

Table 4.5. Analytical calculations of deflection for various gold-poly2 beams. 94

Table 4.6. Actual experimental deflection measurements of four samples of MUMPs® 66 cantilevers {all units in μm}. 97

Table 4.7. Comparison between preliminary MUMPs® 66 values and calibrated stress values used in Coventor® 97

Table 4.8. Analytical, experimental, and simulated cantilever deflection results. 98

Table 4.9. Comparison of cantilever and robot wing deflections 105

Table 5.1. Summary of the design elements and requirements for a flying microrobot. 124

Table 5.2. Overview of the 27 microrobot and test-structure chips of this thesis. 134

Table 6.1. Laser diode and hardware required for continuous and pulsed operation. 145

Page

Table 6.2. Procedures for characterizing the diode power-current relationship.....148

Table 6.3. PolyMUMPs® sacrificial oxide release procedures (adapted from [1]).....163

Table 6.4. Abbreviated operating instructions for the Zygo® IFM. 169

Table 7.1. MUMPs® 66 cantilever deflection measurement values {units in μm}.....181

Table 7.2. MUMPs® 68 cantilever deflection measurement values {units in μm}.....182

Table 7.3. MUMPs® 69 cantilever deflection measurement values {units in μm}.....182

Table 7.4. Reported residual stress data for MUMPs® poly2 and gold layers [1]. 182

Table 7.5. Measured deflection compared with calculated mass and surface area in M68rob1 microrobots.....188

Table 7.6. Measured deflection compared with calculated mass and surface area in M68rob2 microrobots.....188

Table 7.7. Microrobot design element advantages and disadvantages.....189

Table 7.8. The 500-μm microrobots with the best combined deflection-mass and area-mass ratios. 194

Table 7.9. Calculations of thrust and weight from the microrobots in Figure 7.14. 195

Table E.1. Rankings of MUMPs® 66 microrobots in terms of deflection, mass, and area.....251

Table E.2. Rankings of MUMPs® 67 version 1 microrobots.....254

Table E.3. Rankings of MUMPs® 67 version 2 microrobots.....256

Table E.4. Rankings of MUMPs® 68 version 1 microrobots.....258

Table E.5. Rankings of MUMPs® 68 version 2 microrobots.....260

Table E.6. Rankings of MUMPs® 68 version 3 microrobots.....262

Table E.7. Rankings of MUMPs® 69 version 1 microrobots.....264

Table E.8. Deflection, mass, and surface area values for 990-μm microrobots from MUMPs® 69. 265

Foreword

Almost every researcher hopes, at least subconsciously, that his labors will result in a grand solution to some pressing issue in science—a great breakthrough for which he will be famous. Or he imagines that the applicability of his research stretches from the largest galaxy to the smallest nanotube. Such was my dream throughout this thesis work. I have been humbled by the inescapable truth of most research projects: the result is nothing more than one small piece added to the puzzle. But to me, that piece looks more like a precious gem than a jagged piece of cardboard. And so, my words will reflect my biased opinion. I hope you will forgive me for this. What I consider my very best work is contained in the following pages. I welcome and expect feedback and suggestions for improvement in both the prose and the research.

Daniel J. Denninghoff
March 2006

POWER-SCAVENGING MEMS ROBOTS

I. Introduction to Microrobots

Throughout the millennia, mankind has gazed at the numberless stars in the nighttime sky and wondered what else is out there. This simple curiosity has stimulated the development of marvelous inventions such as space exploratory vehicles, powerful earth-based and earth-orbiting telescopes, and complex imaging systems. While the imagery from these remarkable devices is truly spectacular, it is a mere glimpse of the gigantic galactic frontier—so much is still unexplored. Mankind's fascination with the colossal is also evident in the extraordinary engineering of skyscrapers, sports stadiums, ocean liners, and immense highway and bridge systems.

The opposite end of the size spectrum—the micro and nanoscopic—is similarly attractive. Equally marvelous inventions such as scanning electron microscopes (SEMs), transmission electron microscopes (TEMs), and atomic force microscopes (AFMs) provide analogously probing images of the infinitesimal micro and nano world. Congruent with this curiosity, researchers have created gears smaller than ants [1], functional cars smaller than rice [2], and human figurines composed of a few molecules [3]. Practical, commercial devices such as miniature accelerometers are now sufficiently reliable for automobile airbags [4], and millions of movable micromirrors now form a digital light-processing system that outperforms other display devices [5], [6]. Indeed, the microsystem field is limited only by the inventor's creativity.

Although the technological capability to construct virtually any imaginable device is available, a successful product is still elusive in many projects. Such is the case in developing successful autonomous microrobots. While significant advances have been made in other fields associated with semiconductor technology—integrated circuitry, communication systems, computer systems, and a plethora of other devices—a mobile, autonomous, power-scavenging micro-sized (less than 1 x 1 x 1-mm^3) robot has yet to be developed.

1.1 An Argument for Microrobot Development

The fact has been stated—micrometer-sized robots do not yet exist—but developing a system for the sake of its mere existence is rarely a satisfactory motive, especially in the Air Force. The Air Force is interested in microrobot development because of a few modern warfare issues: enemies are dispersing in urban environments, caves, and mountains; collateral damage must be minimized; targets are more hardened and deeply buried than before; and limited bomb damage information is available to warfighters following an attack. The mandate is that munitions must adapt to overcome these issues. Specifically, they must be smarter and smaller. Smarter munitions would be capable of situational awareness and could provide an accurate assessment of the situation. Equipped with a degree of supervised autonomy, these munitions could perform routine functions without a remote human pilot; the munitions would necessarily be controlled, however, to prevent unintended detonation or surveillance [7]. The demand for smarter and smaller munitions is a call for miniature robots, even microrobots.

In a day of automation, the importance of developing such robots cannot be over-emphasized. Comparable in size to a fine grain of sand [8], a microrobot is unobtrusive,

economical, and would yield precise micro-scale performance. It could completely evade detection, thus proving useful in clandestine military operations. At such a small scale, millions of disposable sensing microrobots could also collect accurate, real-time environmental data. Not only could microrobots improve the performance of existing systems, they could perform tasks that are currently non-existent. Precise medicine delivery would improve the quality of life in patients every day; this is such a function microrobots would be well suited to perform.

There are many advantages to miniaturizing robots and, in general, mechanical systems. Besides decreasing volume and weight, miniaturization technologies can increase system reliability and performance while reducing energy consumption [9]. Due to scaling factors, as devices become smaller their performance is enhanced, yielding higher throughput, greater accuracy, lower cost per device, and less chip space used [10]. Thus, microsystems are advantageous in handling small objects, where speed, accuracy, and gentleness are required. As micromachining technologies improve, mass production will reduce the cost per device [11].

1.2 Microelectromechanical Systems (MEMS) as an Enabling Technology

Microelectromechanical systems (MEMS) make up the relatively new field of science that combines miniature electrical components and moving mechanical structures—in essence, sensors and actuators. Despite having emerged only as recently as the early 1980's, MEMS have already been accepted and applied in industry, government, and academia [12], [13]. The success and reliability of MEMS components are due in part to the mature lithographic microfabrication technologies developed from the integrated circuitry field, upon which MEMS fabrication is also based. The precision

and reliability available in micrometer-sized devices are superior to that of their macro-size counterparts [9]. Already a plethora of reliable sensors and actuators have been implemented in commercial applications, from automotive airbag units to ink jet nozzles and high-bandwidth frequency synthesizers [14].

The ultimate triumph of the MEMS field is to fabricate intelligent devices capable of sensing, planning, making decisions, and reliably performing certain functions [15]. An intelligent, moving microrobot is one example of such a pursuit. Forming a complete microsystem, such as a microrobot, requires the integration of micro-sized sensors and actuators with on-chip processing circuitry [16]. The efficacy of MEMS-based sensors and actuators for an autonomous microrobot is asserted in this thesis. This research presents the development of a novel mobile, autonomous, power-scavenging microrobot (with dimensions less than 1 x 1 x 1 mm^3).

1.3 Relevant Microrobotics Terminology

Because the development of microsystems has only recently begun, many of the terms in this field are unclear and are often used incorrectly. It is imperative to elucidate this terminology so that the research in this field is accurately described. Moreover, the novelty contained in this very thesis depends upon the unambiguous definition of these terms. The following sections comprise explanations of microrobotics terminology pertinent to this research.

1.3.1 Robot

Robots have been employed in many fields throughout the years, yet they still lack a clear, unambiguous, universally accepted definition. Generally speaking, a robot is "an automatic apparatus or device that performs functions ordinarily ascribed to human

beings" [17]. Narrowing the focus to the electrical engineering field, a robot is defined as "a mechanical device with an incorporated computer that is able to perform programmed tasks [which] may or may not be autonomous" [18]. Because robot characteristics and components vary depending on the application, *robotics* has been loosely applied to any "feedback-controlled mechanical system" [19]. For the purpose of this research, a combination of these terms is appropriate: a robot is a mechanical device that performs a task and may be controlled either remotely or autonomously. Furthermore, it may have either an onboard or a remote power supply.

1.3.2 Autonomous

A robot that senses and operates independently of remote-controlled inputs is best described by the term *autonomous*—i.e., independent, free from external control, or self-directing [20]. Therefore, an autonomous robot operates independently of an external operator's commands or controls, and a non-autonomous robot requires external commands (usually remote-controlled) to function. A robot is autonomous when it performs its programmed function with nothing but power to activate it. It is important to note that robots could vary in degree of their autonomy, from non-autonomous to fully autonomous.

1.3.3 Microrobot

Since the birth of micromachining, a clear research objective has been the development of a completely autonomous mobile microrobot [21]. A microrobot is defined by its size and functionality. A microrobot must be on the order of a few cubic micrometers (μm^3), and the largest dimension must be less than 1 mm. If the largest dimension of any component exceeds the micrometer range, then the device is a "minirobot"; in the nanometer range, a "nanorobot."

Size is not the only discriminator. A microrobot must possess some functional capability, such as manipulation or locomotion. A micro-sized piece of dust, for example, is not a microrobot because it possesses no functionality. On the other hand, many non-mobile robotic devices capable of micrometer positioning have emerged and bear the hot microrobot label. These should more accurately be called "microconveyors," "micromanipulators," "micromachines," etc. These devices are usually centimeter-sized (or larger) with micro-sized grippers and possess micrometer positioning capabilities [22]. Since the size of their largest dimension exceeds the micrometer range, they cannot be considered microrobots. In this thesis, only functional micro-sized devices are considered microrobots, and all other stationary devices bear some other name that accurately describes their function.

To restate, a microrobot is a micro-sized device (with no dimension exceeding the micrometer range) that performs a given function. It may be mobile or non-mobile, as long as it possesses some functionality in place of mobility. It may or may not be autonomous, though autonomous is the end goal [23]. Its power supply may be onboard the microrobot or remote. Any additional sensory or actuating features certainly make the microrobot more useful, but these features are strictly descriptive, instead of definitive, in nature. As microrobots are developed by both institutes and industry, they will possess a plethora of useful features. This thesis focuses on the fundamental microrobot design issues, such as power-scavenging abilities and controlled movement.

1.3.4 Untethered

Untethered means not connected by wires. While not definitive of a microrobot, an untethered feature is certainly desirable for injection into the body or deployment into a remote environment.

1.3.5 Power-Scavenging Capability

A robot that collects energy from its surrounding environment to power its system is considered power-scavenging. For example, a robot that converts solar power into electrical power to drive its circuitry and actuate its legs is power-scavenging. In other words, power-scavenging implies that the robot is free from power-supplying wires and does not have a battery.

1.3.6 Controlled Behavior

Controlled movement is necessary in any mobile device. Behavior implies that the robot moves in a predictable, repeatable fashion. Anything less would be impractical, though not entirely useless; it could be a building block. Motion in a straight line, motion towards an object, motion away from an object, hovering above a surface, etc. are all examples of controlled behavior.

1.4 Problem Overview: Limitations in MEMS

Having identified the motivation for and the definitions of microrobotics, the reasons autonomous microrobots have not been realized are identified here. The fundamental problems in miniaturizing robots are based on power and movement: most MEMS actuators require more power—current or voltage—than is available from miniature power sources; and most MEMS robots are intended to walk, but few effective locomotion techniques exist for walking. These two issues are described in detail here.

The two most simple and effective actuation methods used in MEMS systems are thermal and capacitive actuation; the reason is both can be fabricated with standard micromachining techniques and materials. Compared to capacitive actuators, thermal actuators provide larger displacement and larger forces on a load. The dynamics of thermal actuators—expansion and contraction—are caused by Joule heating from current

flowing through the actuator. The response time of thermal actuators, therefore, is limited by the thermal exchange, which is relatively slow. Another disadvantage is the large current required to power even micro-sized thermal actuator devices [16].

Capacitive, or electrostatic, actuators operate at much higher frequencies than thermal actuators. The operating force in capacitive actuators is the electrostatic attraction between two parallel plates, which is controlled by the relatively rapid charging and discharging of the plates. The electrostatic attraction, however, is relatively weak within its working range; this corresponds to a weak acting force. Electrostatic actuators usually require large voltages, though the power drain—resulting only from the capacitive leakage current—is minimal. Another disadvantage is the parallel plate surface area is usually large, which opposes the miniaturization trend [24].

To summarize the problem, thermal actuators typically require large currents while electrostatic actuators require large voltages. Large, powerful deflection is available from thermal actuators, while faster response and minimal power drain are characteristics of capacitive actuators. But even if a sufficiently small, wireless power supply were available, the second part of the problem—lack of effective MEMS locomotion techniques—has not been solved. This issue is evident in a very successful miniature robot that will be discussed in the next chapter: solar panels harness energy and processing circuitry autonomously controls its motors, but it cannot walk [25].

1.5 Intent of Research

1.5.1 Proposed Solution and Research Objectives

The solution to these limitations must lie in an elegant design—simple, reliable, and efficient. First, the robot must be comprised of low-power actuators or it must

scavenge energy from the environment, similar to the solar-powered robot mentioned above. Second, the robot must generate sufficient force, grip, and speed to move. Walking has been attempted most often, which is evident in the large number of walking miniature robots discussed in the next chapter. However, walking is difficult. As is evident in the next chapter, prior to the Mechanical Flying Insect project (MFI) [26], flying in the millimeter scale had rarely been attempted, though some success has been realized in larger scales [27], [28]. Flying, with its flexibility and agility, is a promising locomotion technique and would especially be useful in Air Force applications.

A flying microrobot that scavenges power from the environment is a lofty goal for an entire team of researchers, but every noteworthy project must have some beginning. This individual thesis marks the beginning of the flying microrobot project [29]. The following list contains the objectives of this research:

1. Design a novel integrated micro-sized actuator-wing that flaps downwards
2. Characterize and optimize the micro actuator-wing
3. Combine the actuator-wings to form a wireless microrobot (smaller than 1 mm x 1 mm x 1 mm^3)
4. Demonstrate wireless actuation by scavenging power from a light source
5. Demonstrate controlled microrobot hovering
6. Demonstrate microrobot flight towards a light source

1.5.2 End Goal of the Flying Microrobot Project

In order to become a practical device, the robot must eventually be autonomous and equipped with appropriate sensors and actuators [21]. These would be obtainable with considerable follow-on research and are not within the scope of this thesis. The

locomotion progress of the flying microrobot project begins with flapping and ends with maneuvering: flap → flap fast → hover → take off → ascend → descend → maneuver. Once these are achieved, more sophisticated capabilities must be added: autonomous control → autonomous motion → sensing and transmitting data → automatic target recognition → performing a given function at the target.

1.5.3 Design Requirements

This research is based on the design requirements as recommended by the sponsor. Initially, the sponsor desired an untethered 500 x 500-μm^2 robot capable of repeatable and reliable behavior-based motion [30]. This movement could be walking, flying, floating, etc. Later, the sponsor indicated that the dimensions could be larger than 500 x 500 μm^2, that flying was the preferred choice of locomotion, and that repeatable behavior was still a requirement [7]. As will be illustrated in the design chapter, most of the robot designs were based on the original 500 x 500-μm^2 size requirement, but a few 999-μm-diameter robots were also designed.

1.6 Organization of Thesis

Chapter 1 introduces the microrobot research, argues why it is important, identifies major MEMS-related problems, and proposes a solution. Chapter 2 includes the background of microrobots and identifies the merits and limitations of many miniature robots. Chapter 3 covers the theory important to a flying, power-scavenging MEMS robot. The modeling of the robot wings and the predicted performance are covered in Chapter 4. The design details and fabrication characteristics are described in Chapter 5. The experiments are described in Chapter 6, and the results are in Chapter 7. The conclusions for this project and suggestions for further research are in Chapter 8.

1.7 References

[1] M. J. Madou, *Fundamentals of Microfabrication: The Science of Miniaturization* (2nd Edition), Boca Raton, FL: CRC Press, 2002, p. 50.

[2] T.-R. Hsu, *MEMS and Microsystems: Design and Manufacture*, Boston: McGraw-Hill, 2002, pp. 19, 21.

[3] P. Zeppenfeld, C. P. Lutz, and D. M. Eigler, "Manipulating Atoms and Molecules with a Scanning Tunneling Microscope," *Ultramicroscopy*, vol. 42, pp. 128–133, 1992.

[4] "ADXL204 - High Precision 1.7g Dual Axis Accelerometer Specified for 3.3V Supply," Product data sheet from the Analog Devices website, n. pag. http://www.analog.com/UploadedFiles/Data_Sheets/531154838ADXL204_0.pdf. 1 Dec. 2005.

[5] L. J. Hornbeck and W. E. Nelson, "Bistable Deformable Mirror Device," *OSA Technical Digest Series, vol. 8, Spatial Light Modulators and Applications,* p. 107, 1988.

[6] L. J. Hornbeck, "Digital Light Processing™: A New MEMS-Based Display Technology," White paper from the Texas Instruments DLP Website, n. pag. http://www.dlp.com/dlp_technology/images/dynamic/white_papers/117_Digital_Light_Processing_MEMS_display_technology.pdf. 1 Dec. 2005.

[7] C. Perry. Team Lead, Microplatform Development for Advanced Munitions Team, Flight Vehicles Integration Branch, Munitions Directorate, Air Force Research Laboratory (AFRL/MNAV), Eglin AFB, FL. Personal Correspondence. 13 Jun. 2005.

[8] G. Elert, "Diameter of a Grain of Sand," Excerpt from The Physics Factbook, n. pag. http://hypertextbook.com/facts/2000/IlanaPrice.shtml. 4 Apr. 2005.

[9] G. T. A. Kovacs, *Micromachined Transducers Sourcebook*, Boston: McGraw-Hill, 1998, p. 1.

[10] W. S. N. Trimmer, "Microrobots and Micromechanical Systems," *Sensors and Actuators*, vol. 19, no. 3, pp. 267–287, September 1989.

[11] S. Fatikow and U. Rembold, *Microsystem Technology and Microrobotics*, Berlin: Springer, 1997, pp. 24–25.

[12] G. T. A. Kovacs, *Micromachined Transducers Sourcebook*, Boston: McGraw-Hill, 1998, Preface, p. i.

[13] K. E. Peterson, "Prologue," *Micromachined Transducers Sourcebook*, Boston: McGraw-Hill, 1998, p. iii.

[14] K. E. Petersen, "Silicon as a Mechanical Material," *Proceedings of the IEEE*, vol. 70, no. 5, pp. 420–457, May 1982.

[15] S. Fatikow and U. Rembold, *Microsystem Technology and Microrobotics*, Berlin: Springer, 1997, p. 1.

[16] S. Baglio, S. Castorina, L. Fortuna, and N. Savalli, "Modeling and Design of Novel Photo-Thermo-Mechanical Microactuators," *Sensors and Actuators A: Physical*, vol. 101, pp. 185–193, 2002.

[17] P. B. Gove, Ed., "Robot," *Webster's Third New International Dictionary of the English Language: Unabridged*, Springfield, MA: G. & C. Merriam Company, 1971.

[18] S. M. Kaplan, Ed., "Robot," *Electrical and Electronics Engineering Dictionary*, Hobonken, NJ: John Wiley & Sons, 2004.

[19] S. P. Parker, Ed., "Robotics," *Concise Encyclopedia of Science and Technology* (4th Edition), New York: McGraw-Hill, 1998.

[20] P. B. Gove, Ed., "Autonomous," *Webster's Third New International Dictionary of the English Language: Unabridged*, Springfield, MA: G. & C. Merriam Company, 1971.

[21] T. Ebefors and G. Stemme, "Microrobotics," in *The MEMS Handbook*, Ed. M. Gad-El-Hak. Boca Raton, FL: CRC Press, 2002.

[22] P. Dario, R. Valleggi, M. C. Carrozza, M. C. Montesi, and M. Cocco, "Microactuators for Microrobots: A Critical Survey," *Journal of Micromechanics and Microengineering*, vol. 2, no. 3, pp. 141–157, September 1992.

[23] S. Fatikow and U. Rembold, *Microsystem Technology and Microrobotics*, Berlin: Springer, 1997, p. 304.

[24] P. E. Kladitis, Class Notes and Discussion, EENG 636, Microelectromechanical Systems, Graduate School of Engineering and Management, Air Force Institute of Technology, Wright-Patterson AFB, OH, Winter Quarter 2005.

[25] S. Hollar, A. Flynn, C. Bellew, and K. S. J. Pister, "Solar Powered 10 mg Silicon Robot," *Proceedings of the 16th Annual IEEE International Conference on Micro Electro Mechanical Systems—MEMS `03*, pp. 706–711, Kyoto, Japan, 19–23 Jan. 2003.

[26] R. Fearing, "Micromechanical Flying Insect (MFI) Project," Excerpt from the University of California at Berkeley online webpage. n. pag. http://robotics.eecs.berkeley.edu/~ronf/MFI/mfi.html. 11 Feb. 2005.

[27] D. Kemp, "Micro-Unmanned Aerial Vehicles—Micro Wave," *Jane's Defence Weekly Online*, n. pag. www.janes.com, 23 Feb. 2005.

[28] J. M. Grasmeyer and M. T. Keennon, "Development of the Black Widow Micro Air Vehicle," Report from Aerovironment Inc., www.aerovironment.com, copyright by *American Institute of Aeronautics and Astronautics*, 2001.

[29] D. J. Denninghoff, L. A. Starman, C. E. Perry, and P. E. Kladitis, "Autonomous Power-Scavenging MEMS Robots," *48th International IEEE Midwest Symposium on Circuits and Systems—MWSCAS 2005*, pp. 367–370, Cincinnati, OH, 7–10 Aug. 2005.

[30] F. R. Szabo, *Demonstrating Optothermal Actuators for an Autonomous MEMS Microrobot*, MS thesis, AFIT/GE/ENG/04-23. School of Engineering and Management, Air Force Institute of Technology (AU), Wright-Patterson AFB OH, March 2004 (AD-A426469).

II. Critical Review of Miniature Robots

2.1 Chapter Introduction

This chapter tells the story of how miniature robots have been developed throughout the years. Two main categories of robots are examined: land-based (rolling, walking, crawling, etc.), and airborne (flapping, fixed-wing, and rotary) types. The notable developments as well as the limitations of each robot are identified. After summarizing the features of current miniature robots, this chapter concludes by proposing a novel flying microrobot. The realization of this goal would be an unprecedented breakthrough in microsystem development.

In order to illustrate the significance of microrobot development, some important historical events are highlighted. The role of microrobots is identified, illustrating their tremendous potential just waiting to be realized. This first section concludes by discussing how microrobots could be employed in military, industrial, medical, and domestic applications.

2.1.1 Historical Perspective

Even before the official birth of the microrobotics field in 1987—when the Institute of Electrical and Electronics Engineers (IEEE) held the first Micro-Robots and Teleoperators Workshop—scientists had contemplated the possibilities of making micro-sized devices. In 1959, the great scientist and Nobel Prize recipient Richard Feynman challenged the world to develop microsystems, from computers to information storage to biologically inspired robots [1]. More than twenty years later, a comprehensive review of the scientific community's response to the micromechanical development challenge was given. This classic paper identified the many advantages of using silicon as a

micromechanical material to develop a range of inexpensive, batch-fabricated, high-performance sensors and actuators [2]. Revisiting the microsystem topic in 1983, Feynman proposed microfabrication processing ideas, such as sacrificial layers, electrostatic actuation; he also predicted that stiction—the tendency of devices to stick together due to surface tension—would be an issue at the micro scale. Feynman suggested using electromagnetic induction for powering and controlling mobile microrobots, which he foresaw performing industrial and surgical tasks [3].

Feynman inspired countless scientists, many seeking guidance and inspiration from nature to develop micro-sized and even nano-sized devices [4]–[10]. In the 8th annual 2005 Nano Science and Technology Institute (NSTI) Nanotechnology Conference and Trade Show, for example, there were 170 exhibiting companies and 2500 companies participating in some form—quite a response to Feynman's challenge [11]. The presence of MEMS device production in automotive applications alone is astounding. In 2000, for example, 47.5 million passenger vehicles equipped with MEMS were produced worldwide. This demand fuels a $1.3-billion MEMS/microsystem automobile sensor market and is expected to grow at 16.9% per year [12]. The future is promising in the medical field as well, which expects over $1 billion in MEMS medical product sales for 2006 [13]. The future of microrobotics looks bright as major corporations contribute to its funding.

2.1.2 Potential Microrobot Applications

The best role of microrobots is in applications that require performing simple, repetitive tasks; handling and manipulating of small objects; accessing small, tight areas; assembling and testing clean microstructures or microelectronics; and performing tasks that are at (or beyond) the limits of human manipulation, patience, or safety [4], [14].

The purpose of microrobotics in the military is to better and more safely perform the dangerous tasks now attempted by human combatants [15]. The Air Force Research Laboratory is sponsoring projects that use MEMS devices in combat. Inspired by insects that encroach inside even well sealed houses, researchers propose making miniature robots that encroach inside hardened or deeply buried targets [16]. In modern warfare, some important enemy targets—caves, bunkers, mountainous retreats, etc.—that are inaccessible to or protected against conventional munitions are potentially vulnerable to micro-sized detonators. Working collectively, microrobots could deposit trace amounts of explosives to destroy these inaccessible targets. Furthermore, instead of pilots flying expensive stealth aircraft into hostile enemy territory, swarms of flying microrobots could operate virtually undetected and perform the same mission without putting the pilot's life or the multi-million-dollar aircraft at risk—the element of surprise would be ensured without the high cost of stealth. Flying microrobots could also perform the same reconnaissance or battle damage assessment missions that unmanned aerial vehicles perform in combat today at a lower cost [17] and with a negligible radar footprint [18].

Besides combative operations, microrobots could perform police reconnaissance and surveillance missions—totally undetected [19]. They would be the smallest spies in the world, gathering information about the alleged criminal when he thinks no one is looking. Equipped with appropriate sensors, microrobots could search dangerous areas contaminated with chemical or biological agents, or they could inspect aircraft engines without requiring disassembly.

Microrobots are well suited to replace unwanted human interaction in industrial applications, such as: inspecting pipes in chemical factories and nuclear power plants

[20]; performing tests and surface characterization of microelectronic chips; and inspecting or operating in complex machinery much too impractical or expensive to disassemble. Besides doing the dirty (or clean) work, microrobots could perform tedious or mundane positioning tasks. Capable of submicron positioning accuracy, microrobots are ideal for performing microassembly [21]–[26], metrology [27]–[33], micro-optics [34], and cell positioning [35]–[37]. Additionally, due to their small size and weight, microrobots could reduce space vehicle payloads by replacing bulkier equipment [14], [38]–[40].

The medical field is perhaps the most significant area in which microrobots could contribute. Traditionally, access to organs in living organisms is available only by making incisions with a scalpel, but the actual repair task does not require such a large opening [14]. Now, the scalpel is being replaced with steerable catheters and endoscopes in a revolutionary process, called "minimal-invasive surgery" [41]. This warmly accepted surgical procedure reduces pain and scars, thus reducing cost and recovery time; it could even provide the surgeons with real-time feedback as BioMEMS sensors are added to the surgical tools [13]. Minimal-invasive surgery could be further improved with microrobots that are equipped with appropriate microtools [35]. Useful to both surgeons and biotechnologists [42], microrobots could manipulate individual cells in neurosurgery and ophthalmology where access to the target location is difficult and where damage to the surrounding blood vessels could be fatal. Controlled remotely, microrobots could enter into blood vessels or arteries and perform a variety of measurements and manipulations, such as removing plaque, gripping, cutting, applying tourniquets, making incisions, suctioning and rinsing, et cetera [35].

Microrobots could be used in medical diagnostic and therapy applications [43], such as an implantable drug delivery system, which, when triggered by a signal, deposits medicinal chemicals at the precise location needed [41]. By depositing medicine in localized regions of the body, microrobots could prevent cancer patients from becoming "poisoned" due to the inherent non-selective nature of chemotherapy [20].

The governments in the U.S., Europe, and Japan have begun funding for microrobot and microsystem development, but these applications will be realized more as private corporations join the research effort [44]. It is entirely possible to equip a home-security and monitoring system with microrobots, which could continually probe for harmful vapors or intruders. Microrobots could be employed in countless other commercial and domestic applications as the funding and demand increase.

2.2 Redefining "Microrobots"

Since the birth of the microrobotics field in 1987, scientists pursued developing the first truly autonomous microrobot. Despite these researchers' best efforts, none have succeeded. Their excellent research, however, has led to several noteworthy millimeter-scale robots, each with certain successful characteristics as well as performance-inhibiting limitations. Despite being millimeters or even centimeters in size, these robots were misnamed "microrobots," which is entirely inaccurate. It is true that individual components of these robots are micrometer-sized, but the size of the smallest appendage does not determine the robot size classification. After all, even human beings are composed of nanometer-sized prokaryotic cells [45], but we are not considered "nanohumans." The discriminating factor is the largest dimension of the object. In order to be accurately classified as a microrobot, the largest robot dimension must be within the

micrometer range: 1 μm ≤ x < 1000 μm (where x is the size of the largest robot component). Table 2.1 illustrates the sizes and characteristics of MEMS devices compared to milli- and nano-sized devices [41].

Table 2.1. Description of MEMS components, observation methods, and technologies compared with those of other fields [41].

Devices	Size of Largest Component	Components	Observation Methods	Fabrication Technology
Milli-machines	1 ≤ x < 10 mm	Miniaturized parts	Visible	Precision manufacturing
Micro-machines	1 ≤ x < 1000 μm	Microparts	Optical microscope	Silicon/LIGA micromachining
Nano-machines	1 ≤ x < 1000 nm	Molecular parts	Scanning electron/probe microscope	Protein engineering

To state the matter boldly, a millimeter- or centimeter-sized robot with micrometer-sized appendages cannot be classified as a microrobot because its largest dimension is not less than 1000 μm (1 mm). It should be classified more appropriately as a "millirobot," a "miniature robot," or something else besides "microrobot." It is correct to assert that no true autonomous microrobots exist today. Nonetheless, as the millimeter-sized robot development is particularly interesting and informative, this chapter investigates that very research.

2.3 Land-Based Miniature Robots

The majority of all miniature robots are designed to operate on land. That which began as upside-down centimeter-sized conveyor systems have progressed into walking millimeter-sized robots capable of supporting loads many times their weight. As an autonomous micro-sized robot has yet to be developed, the following is a literature survey of only the published walking *miniature* robots and conveyor systems. In addition,

microassembly systems are briefly mentioned. Since the goal of this research is to develop a fully autonomous mobile microrobot, this section begins with the smallest known fully autonomous mobile land-based robot as a reference point. The robots examined afterwards are smaller than or about the same size as this reference-point robot.

2.3.1 The Smallest Autonomous Mobile Land-Based Robot

The smallest reported autonomous mobile land-based robot was developed in 2001 by a team at Sandia National Laboratories and is depicted in Figure 2.1. It is 4096 mm^3, or 16 x 16 x 16 mm^3 (L x W x H), in size and weighs 28 g; it is powered by three watch batteries; it moves on track wheels; and it consists of an 8-kilobyte read-only memory (ROM) processor, a temperature sensor, and two motors that drive the wheels. Its average speed is 20 in/min or 8.5 mm/sec and has successfully maneuvered through a field of dimes [46]. Unpackaged electronic components make the control system small, and laser-cured thin polymer layers make the frame light yet sturdy. As is true with battery-powered miniature devices, ultimately the power supply limits the size and operating time of the robot.

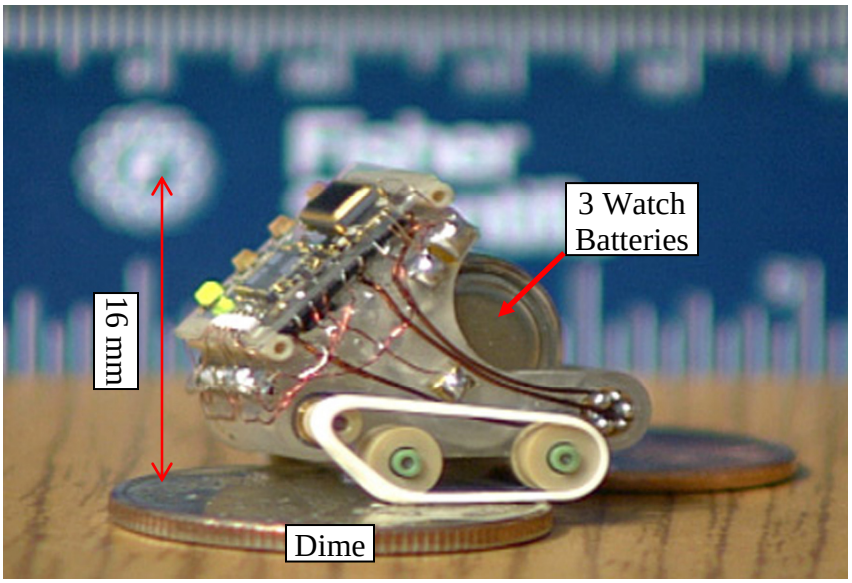


Figure 2.1: Photograph of the Sandia robot, which is the smallest reported autonomous mobile land-based robot at 4096 mm^3 in volume and 28 g in mass [46].

2.3.2 Critical Survey of Tethered MEMS Land-Based Robots and Conveyors

Many researchers have strived to develop an even smaller robot than that described in the previous section. The following robots and conveyors were fabricated with the relatively new microelectromechanical systems (MEMS) technology since smaller robot dimensions require a suitable fabrication technology commensurate with the size. The merits and shortcomings of the most successful tethered MEMS-based walking robots or promising MEMS robotic technologies are examined chronologically. It is important to note that all the miniature robots or conveyors in this section are powered through tethered bond wires; untethered robots are described in section 2.3.3.

In 1995, the smallest microfabricated cars were demonstrated—a larger one [47] with dimensions of 7 x 2.8 x 3.0 mm^3 and a smaller one [48] with dimensions of 4.8 x 1.8 x 1.8 mm^3. The smaller car is a $1/1000^{th}$ scaled version of a full-size automobile and is illustrated on a 5-cent piece in Figure 2.2.

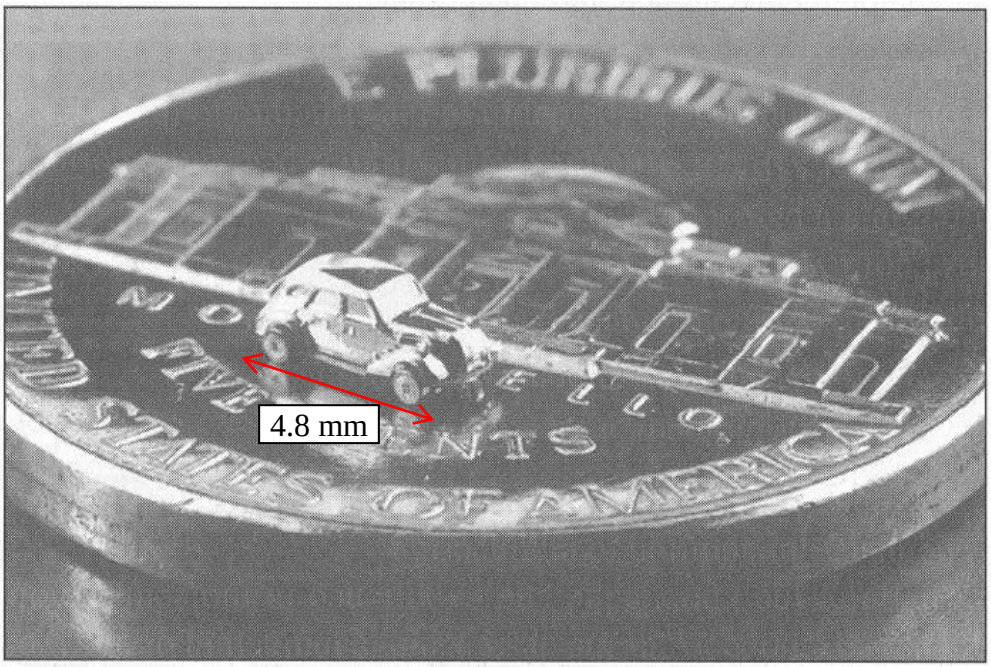


Figure 2.2: Photograph of a 4.8-mm nickel car driven by an electromagnetic step motor positioned on a 5-cent coin. The car is a $1/1000^{th}$ scaled version of a full-size automobile and clocked a maximum speed of 100 mm/sec [49].

The car consists of a 0.7-mm-diameter electromagnetic stepper motor, a structural frame or chassis, axles, tires, wheels, bumpers, a spare tire, a license plate, and a shell body. The motor rotor core is made of a 4-pole barium ferrite magnet surrounded by contact probes. The structural frame, axels, and tires were fabricated from brass using numerical control (NC) machining. The license plate and wheels were fabricated by photolithographically patterning aluminum film on a glass substrate. The bumper was fabricated from stainless steel using micro-electro-discharge machining. The shell body was fabricated in a 7-step process: (1) solid aluminum was NC machined into a 3-D model; (2) the model was placed into silicone to produce a solid cast; (3) a solid bismuth-tin (Bi-Sn) alloy was poured into the cast and allowed to harden; (4) a 30-μm-thick nickel film was then plated over the alloy; (5) the nickel layer on the bottom of the car was cut off with an electro-discharge machine; (6) the solid Bi-Sn alloy was dissolved in silicone oil; (7) and the shell body was plated with gold for protection. The separate parts were assembled with micromanipulators and the shell body was fastened as a covering.

Powered by a 100-Hz AC source through 18-μm copper wires, the motor drove the car at a maximum speed of 100 mm/sec. If this car were scaled by 1000 to its full size, this same speed would equate to 100 m/sec, or 223 mph. Illustrated in Figure 2.3 is the car positioned among rice grains, and the attached copper wire is visible. This is the smallest and fastest wheel-driven mechanism in the world, yet still not a microrobot as each of its dimensions exceeds 1 mm. The car is non-autonomous in that it has no self-directing functions. Its tethered power wires, due to the lack of an onboard power supply, would limit its application to remote locations.

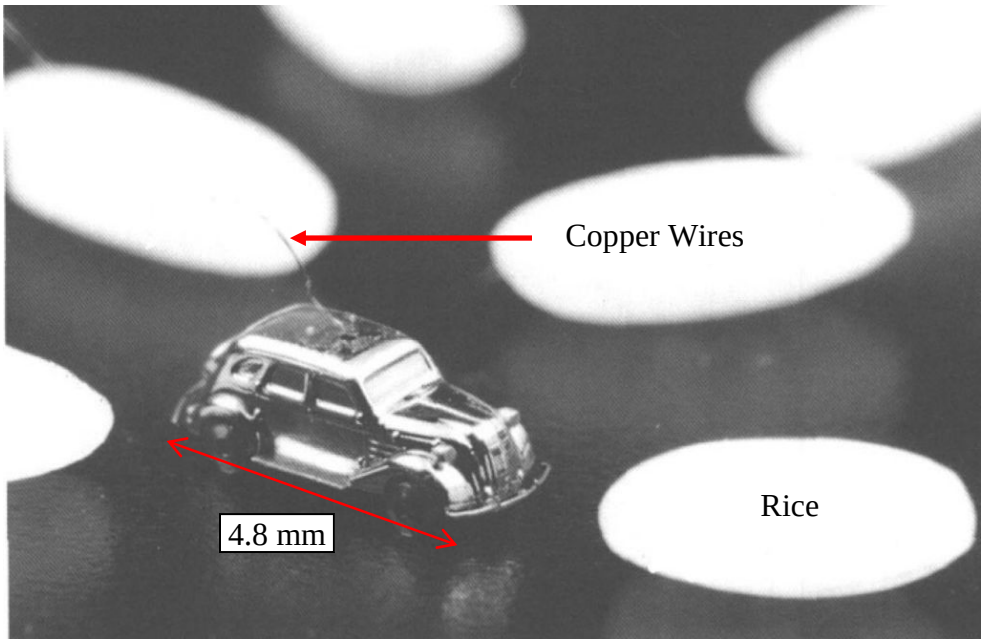


Figure 2.3: Photograph of a 4.8-mm nickel car positioned among grains of rice. The attached 18-μm copper wires transmit power from a 100-Hz AC source to the electromagnetic stepper motor [48].

The year 1997 saw significant MEMS-based robot development from independent groups. Oriented upside down, the die works as a conveyor with its cilia-type actuator legs in the air. Figure 2.4 illustrates one motion pixel of a programmable 8 x 8 array of MEMS bimorph polyimide actuators. As illustrated in Figure 2.5, each actuating paradigm combines both thermobimorph and electrostatic actuation to provide three degrees of freedom. The total size is a regular die size—10 x 10 mm^2—and each die contains 64 sets of four actuators, which are 430 μm in length and bend up 120 μm. Each actuator is composed of a TiW heating resistor; two types of polyimide with both high and low coefficients of thermal expansion (CTE); an encapsulating stiffening layer; and an electrostatic plate. Vias for wet etching are also present. To convey a 20-mg die, the conveyor required 6.7 W of power, which is disproportionate to the conveyor size [50]. Strictly speaking, the device is not a robot since it is not mobile. If it were mobile, the attached power wires would significantly limit its performance.

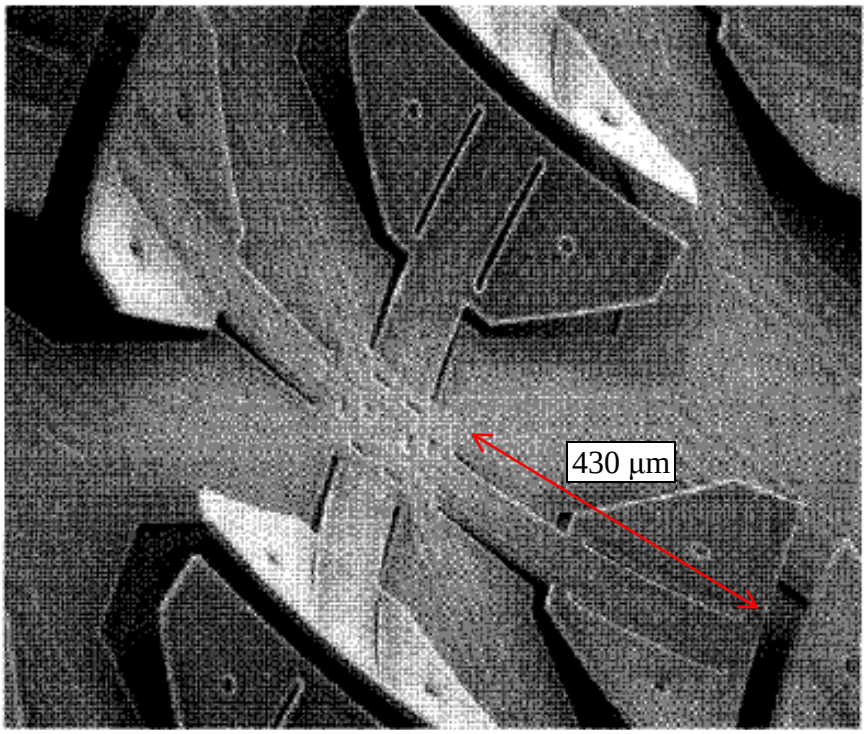


Figure 2.4: SEM micrograph of one motion pixel of a microconveyer; it is comprised of four 430-µm-long polyimide cilia actuator legs in a common-center configuration [50].

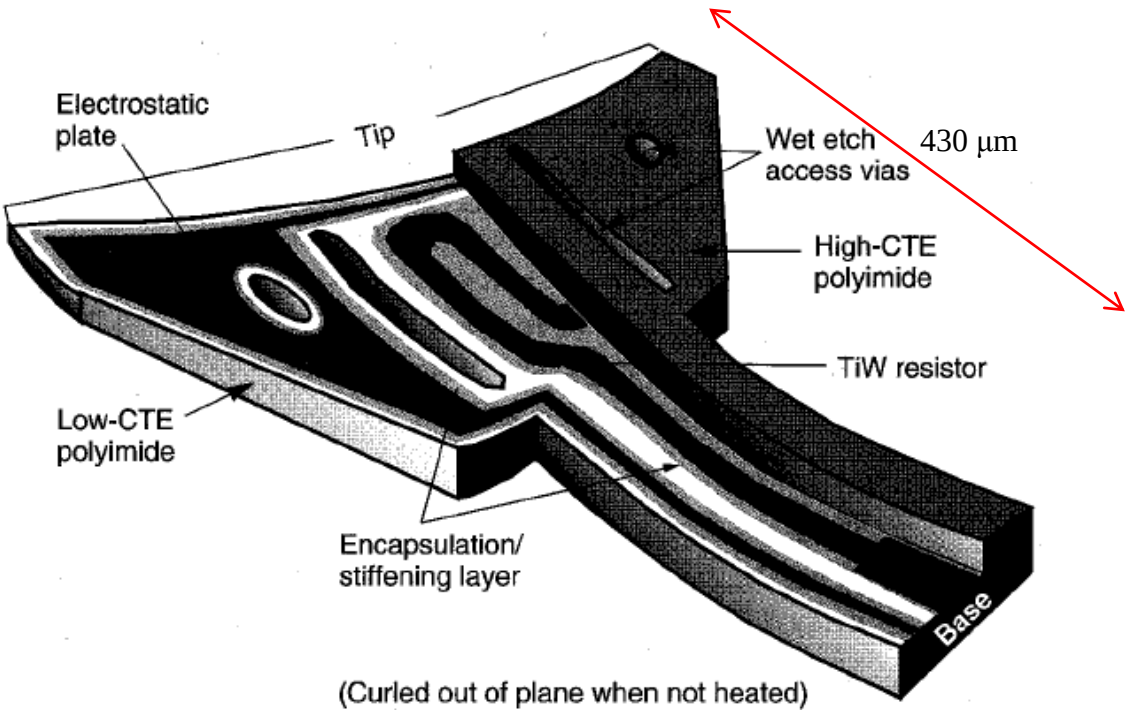


Figure 2.5: Diagram of programmable polyimide leg for a microconveyor pixel, which is comprised of both thermal and electrostatic actuators to provide 3 DOF. The leg is composed of a TiW heating resistor, high- and low-CTE polyimide, an encapsulating stiffening layer, an electrostatic plate, and wet etch access vias [50].

Also in 1997, a miniature robot design based on a six-leg insect walking gate was demonstrated. Originally intended to walk with its belly down, this 10 x 10-mm^2 robot contained 96 erected polysilicon legs, each composed of single hot-arm electrothermal actuators capable of both two- and three-DOF movement (see Figure 2.6).

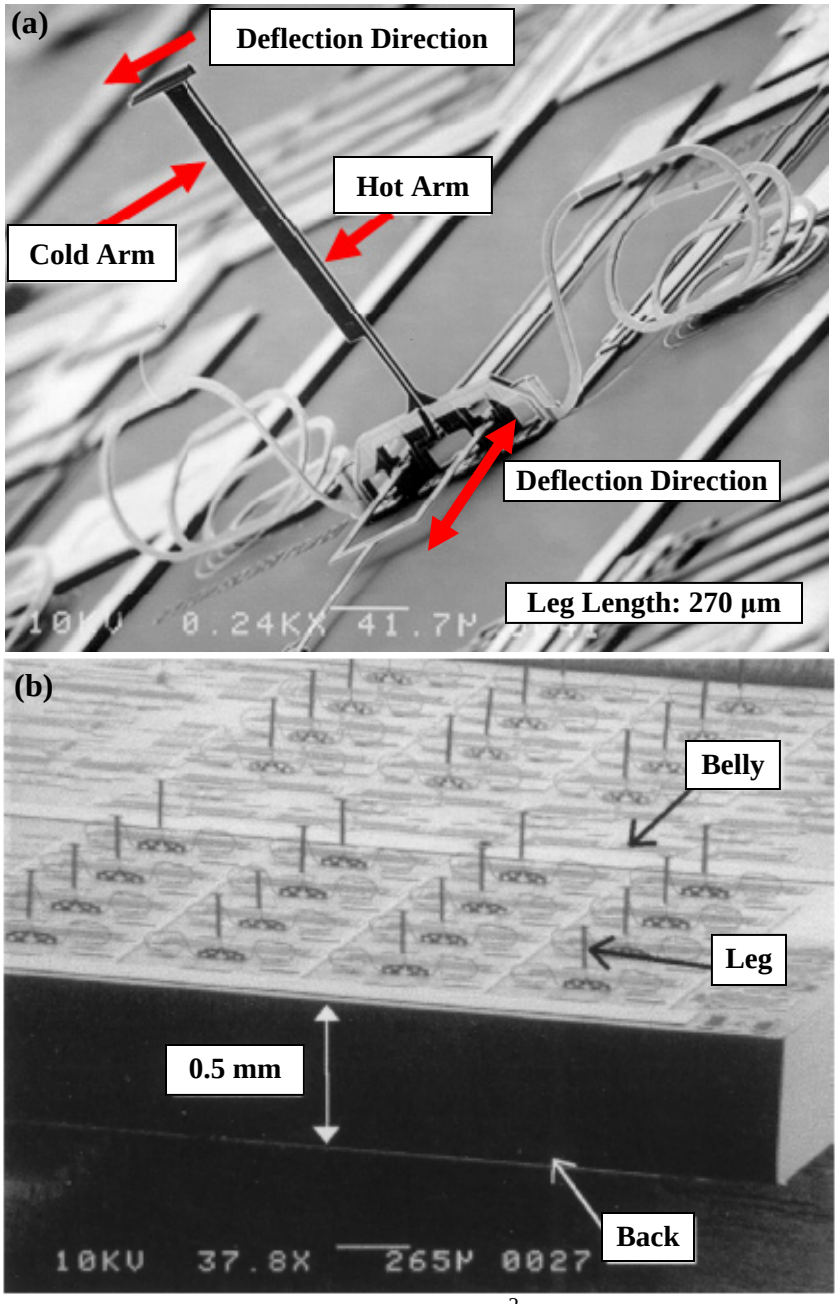


Figure 2.6: SEM micrographs of a 10 x 10-mm^2 robot with six-leg insect gate. (a) Image of an erected leg, comprised of an out-of-plane polysilicon thermal actuator with both two and three DOF. (b) Robot with belly and 96 legs in the air [51], [52].

Lying on its back with feet in the air, the robot conveyed objects at 453 μm/sec across its body, including a 68-mg load. Some ingenious inventions are evident in this research, such as flexible spring-like wires that allow the legs to actuate normal to the chip surface. However, the 2.87-W power consumption is enormous for an on-board power supply [51], [52].

In 1998, a piezoelectric slip-stick locomotion method was developed for a miniature robot platform [26]. Movement in each of the 13-mm-long piezoceramic legs is controlled by an applied varying electric field, which causes the ceramic to expand and contract. Each leg bends backward very slowly; it then takes a quick sliding step forward, followed by the platform catching up due to inertia (see Figure 2.7).

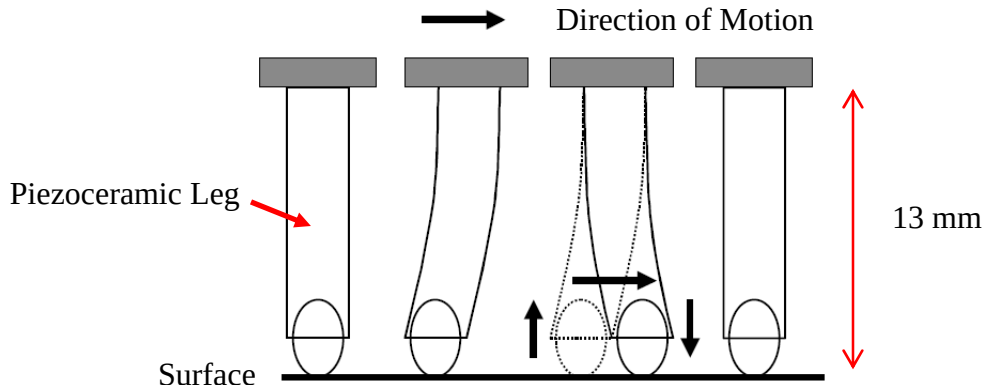


Figure 2.7: Diagram of piezoelectric slip-stick locomotion method developed in 1998 and later used in several centimeter-scale robots. The piezoceramic legs are controlled by varying an electric field. These robots are used primarily for precision measurement, manipulation, repair, and fabrication at even atomic scales [26].

In spite of the instability of the locomotion method, it was later implemented in several very capable larger robots (NanoWalker, MINIMAN, and PROHAM), which were designed to measure, manipulate, repair, and fabricate at the molecular, nanometer, and atomic scales [21]–[23], [27]–[33]. These robots range between 3 and 6 cm (about one to two inches), and clearly cannot be classified as microrobots. Their high power

consumption (the NanoWalker consumes 10 W of continuous power) also limits their performance.

The late 1990s and early 2000s saw improved microconveyor development. Compared with earlier designs illustrated in Figure 2.4 and Figure 2.5, the similarities and differences of the microconveyor depicted in Figure 2.8 and Figure 2.9 are evident. Figure 2.8 includes four SEM micrographs of the fabricated microconveyor array, illustrating the 1 x 1-mm^2 dimension of a single pixel and the 95-µm vertical and 17-µm horizontal tip deflections.

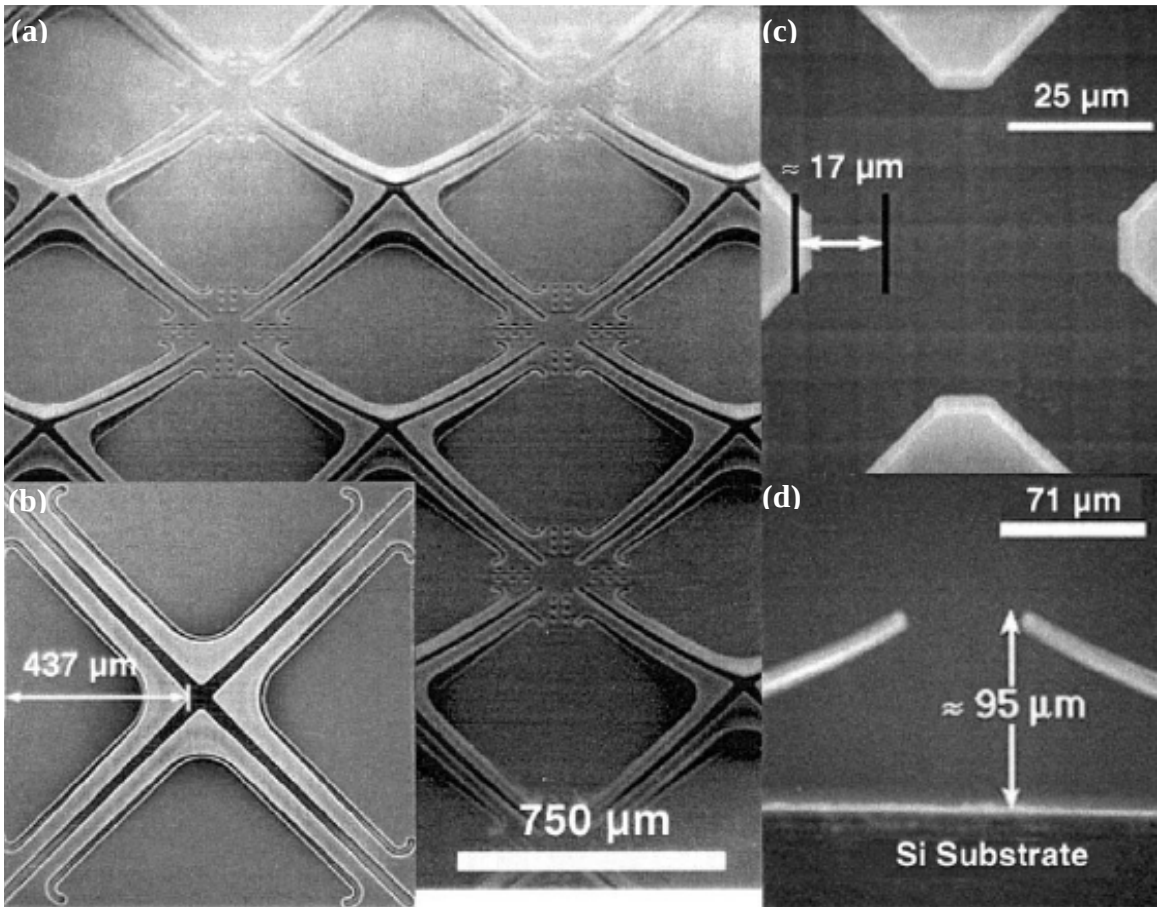


Figure 2.8: SEM micrographs of a ciliary microconveyor array after complete fabrication. (a) An array of microactuators; (b) a single 1 x 1-mm^2 motion pixel from the array; (c)-(d) images showing 17-µm horizontal and 95-µm vertical deflection [54].

Figure 2.9 illustrates the dimensions and material composition of one bimorph actuator: a TiW heating resistor, layers of high- and low-CTE polyimide, silicon nitride, and aluminum.

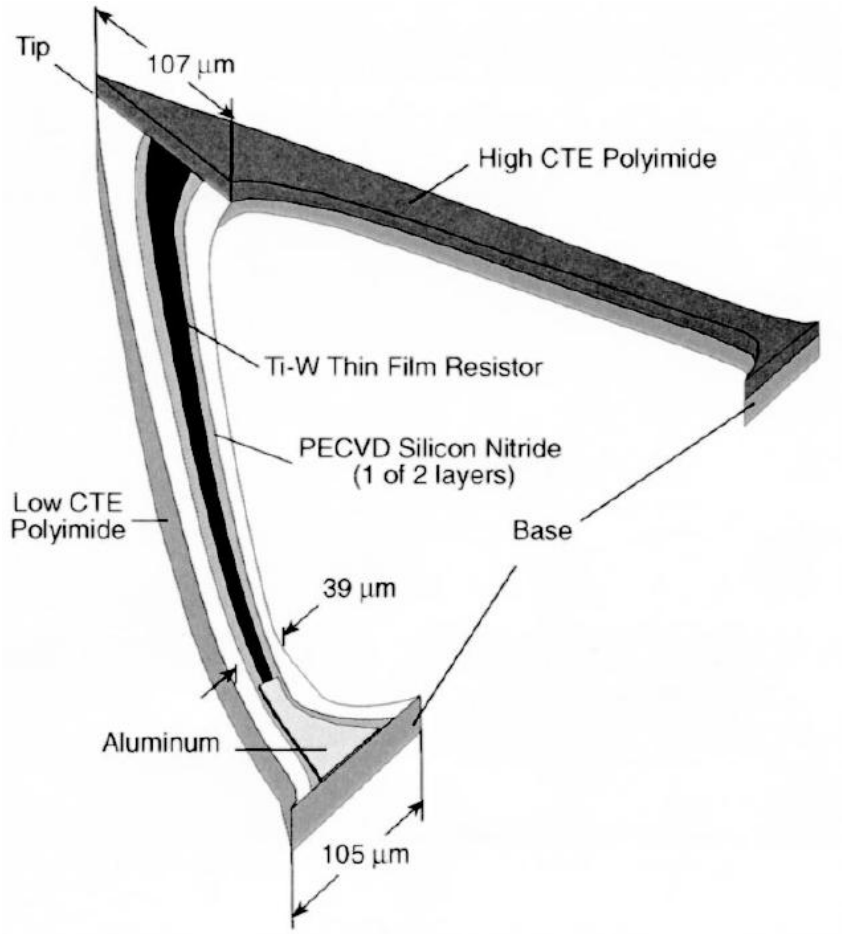


Figure 2.9: Diagram of the polyimide-bimorph thermal ciliary microactuator for a microconveyor. The actuator is shaped as an isosceles triangle and is attached to the substrate at two locations at the base. Half of the actuator in this diagram is shown with removed high-CTE polyimide and silicon nitride layers to reveal the middle layers; these include a TiW heating resistor and layers of low-CTE polyimide, silicon nitride, and aluminum [53].

The novelty of this design is the integration of a bimorph organic ciliary array with on-chip CMOS circuitry. The ciliary array is composed of an 8 x 8 array of motion pixels on a die of size 9.4 x 9.4 mm^2. Each pixel has four orthogonally oriented polyimide-based actuators, which were fabricated directly over the CMOS circuitry. The

entire circuit and actuation array consumes 5 W, to perform linear and diagonal translations as well as squeeze, centering, and rotating manipulations [53], [54].

One of the greatest developments in microrobot design transpired at the turn of the 21st century. This robot was based on a previously developed two-phase microconveyer locomotion scheme [55], in which two sets of alternating legs are controlled by separate square waves. As shown in Figure 2.10 and Figure 2.11, to convey an object horizontally in one direction, the phase shift between the two square waves is +90°; for the opposite direction, the shift is -90°; to elevate an object, there is no phase shift between the square waves [56]–[63].

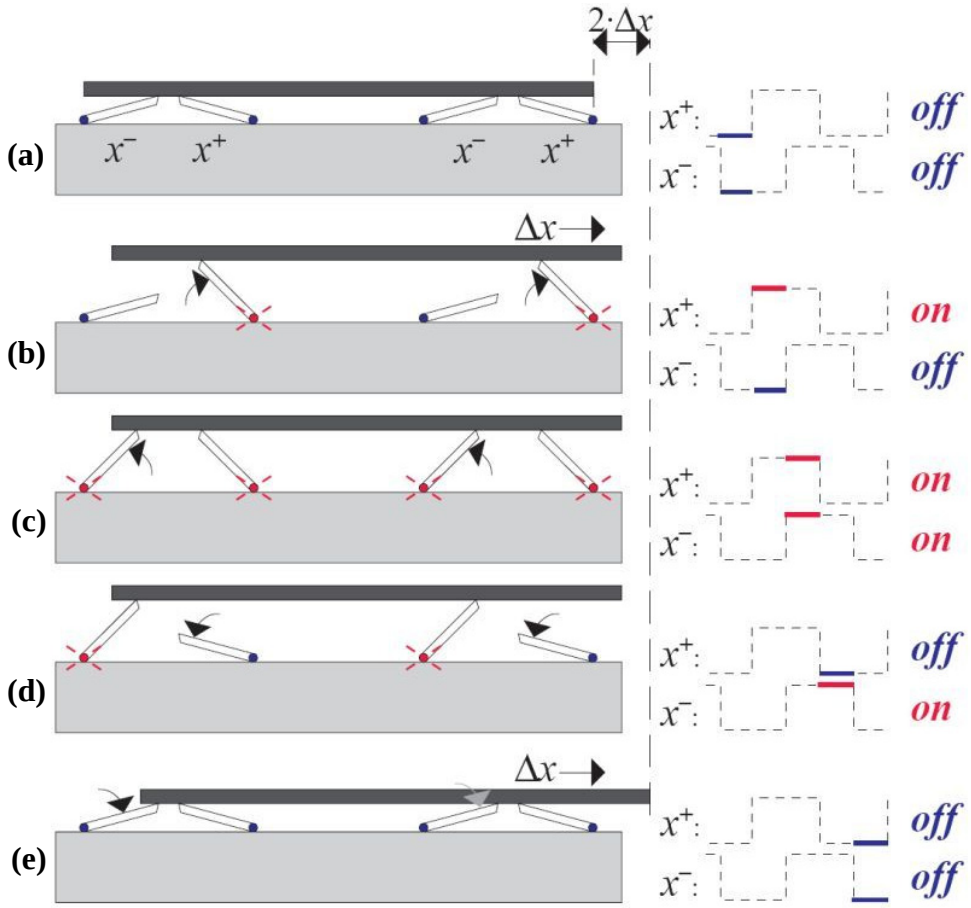


Figure 2.10: Diagram of a microconveyer system in which the two sets of legs are powered by phase-shifted square waves. At the end of one cycle—(a) through (e)—the object moves a distance 2·Δx. The legs move in the opposite direction by reversing the phase shift between the square waves [63].

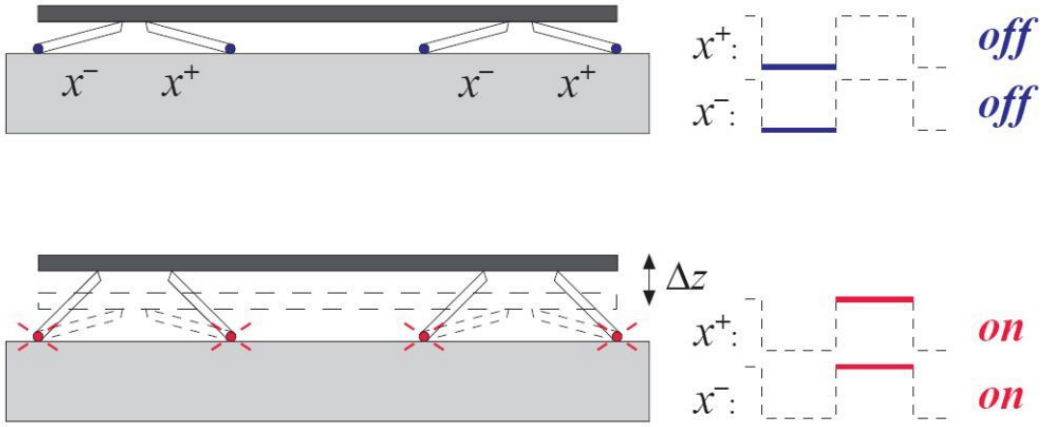


Figure 2.11: Diagram of the microconveyer from Figure 2.10 in which two sets of legs are powered by separate square waves. To move an object vertically a distance of Δz, the square waves are in phase with each other [63].

By flipping this micro-conveyer device on its other side, it became a 15 x 5 x 1.5-mm^3 walking robot with two sets of legs, as illustrated in Figure 2.12.

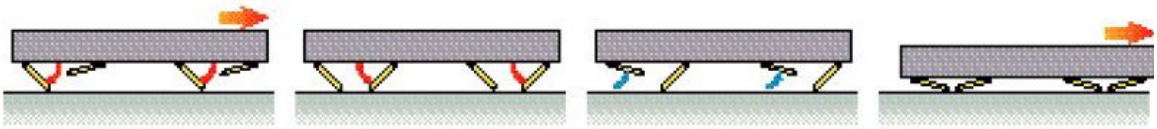


Figure 2.12: Conceptual diagram illustrating forward motion of a robot based on the two-phase microconveyer scheme as illustrated in Figure 2.10 [56].

Locomotion in the legs of the robot was achieved using electrothermal polyimide bimorph actuators. Actuation is achieved due to greater thermal expansion near the heaters than away from them, which causes the leg to uncurl. When cooled, the leg retracts. Due to the flexible nature of the polyimide, these actuators also serve as the joints of the legs. Figure 2.13 is a diagram illustrating the actuation movement as the polysilicon heaters cause the four polyimide V-groove joints to expand and contract. Figure 2.14 illustrates diagrams and corresponding SEM micrographs of each expanded and contracted leg. This robot recorded speeds of 12 mm/sec, which is the record for miniature walking robots.

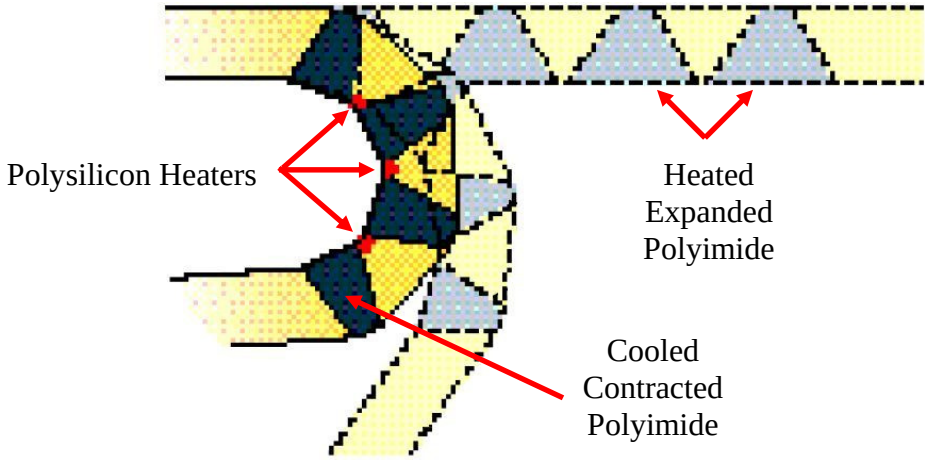


Figure 2.13: Diagram illustrating the actuation principle for the leg movements based on a four-V-groove joint. Each leg is retracted when cooled and uncurled when heated due to greater thermal expansion of the polyimide near the heater than away from the heater [56].

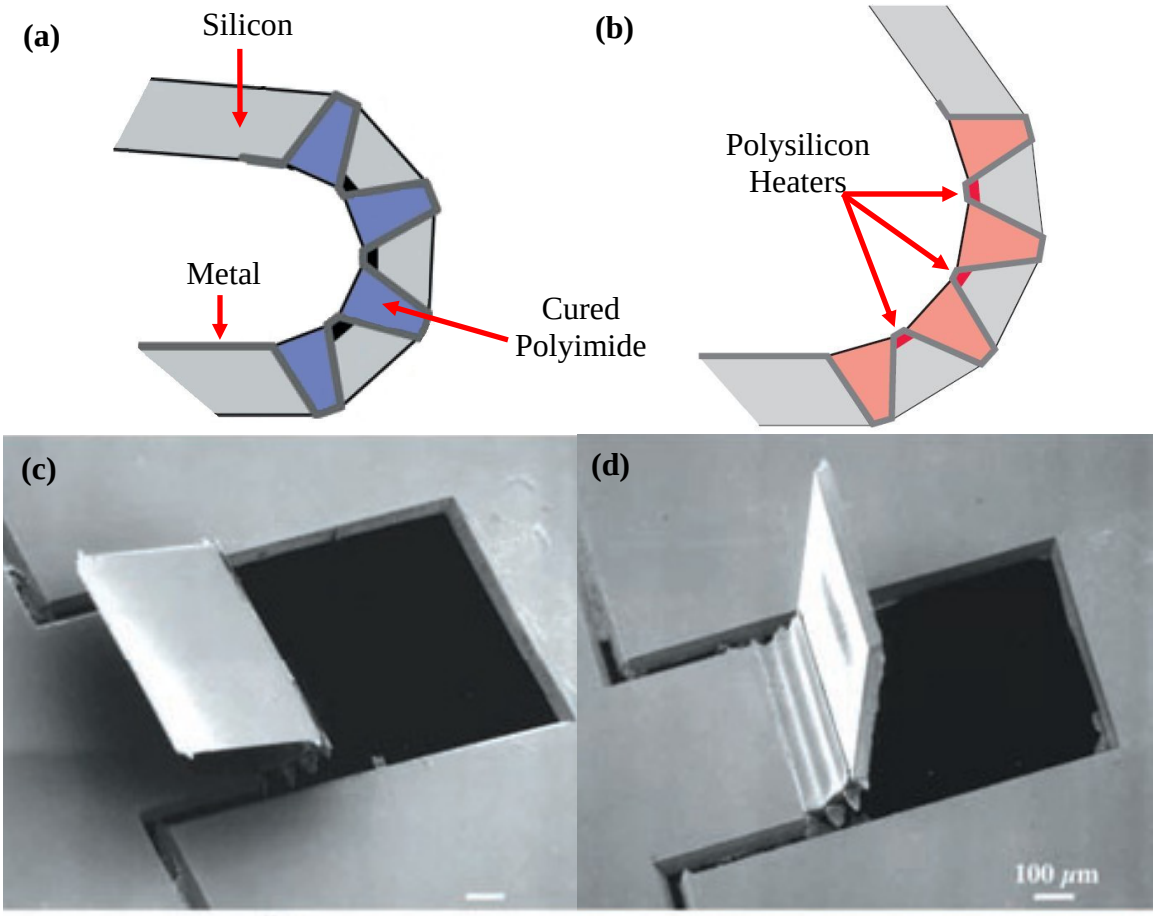


Figure 2.14: Expanding polyimide actuation principle illustrated by diagrams of (a) cool and (b) heated actuators. Images (c) and (d) are SEM micrographs of the actuators that correspond to diagrams (a) and (b) [62].

As illustrated in Figure 2.15, the robot supported a 2500-mg weight (30 times its own weight), which is another record for its size. However, the robot demanded 1.1 W of power, which was supplied through gold bond wires. The robot possesses no control circuitry to move its legs; all the commands are alternating waveform inputs. Thus, the robot lacks autonomy. Despite these limitations, this robot is arguably the most successful miniature walking robot developed to date.

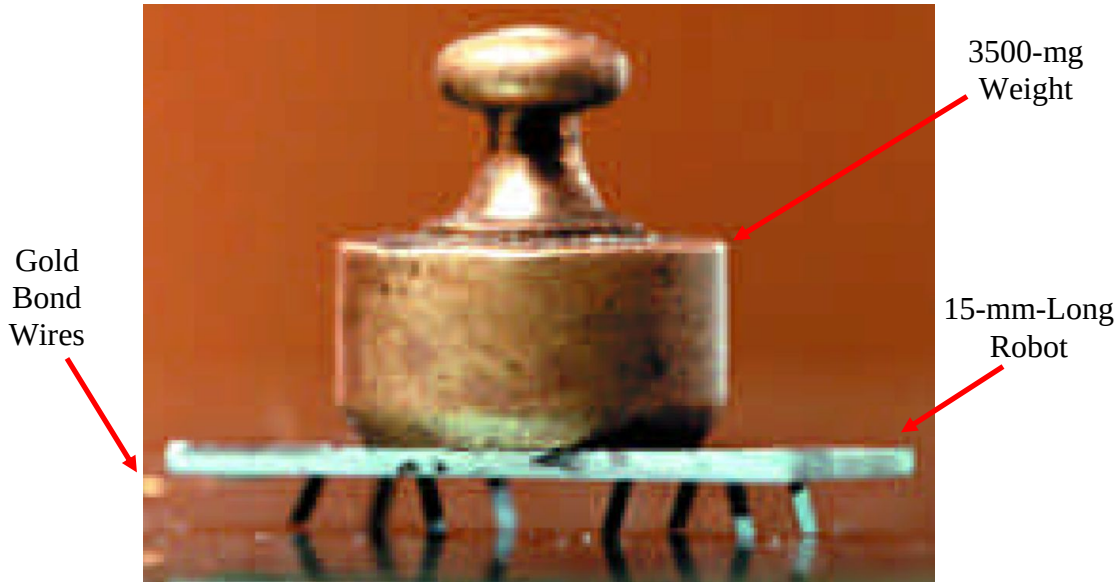


Figure 2.15: Photograph of 15-mm-long robot carrying a 2500-mg weight (30 times its own weight), which is a record for miniature robots. Note the gold bond wires supplying power on the left side of the robot. This robot set a miniature walking robot ground speed record at 12 mm/second but required 1.1 W to do so [56].

Three major miniature robots were demonstrated in 2001, the first of which was a more advanced robot based on the 8 x 8 ciliary array principle. Comprised of four orthogonally oriented electrothermal bimorph actuators, this omnidirectional mobile robot successfully demonstrated accurate three-DOF movement and clocked a 635-μm/s maximum speed. Its locomotion was limited due to the nine attached power wires, as shown in Figure 2.16. With dimensions of 30 x 10 x 1 mm^3, it is certainly not a microrobot. It has potential, however, as its size could easily be reduced [64].

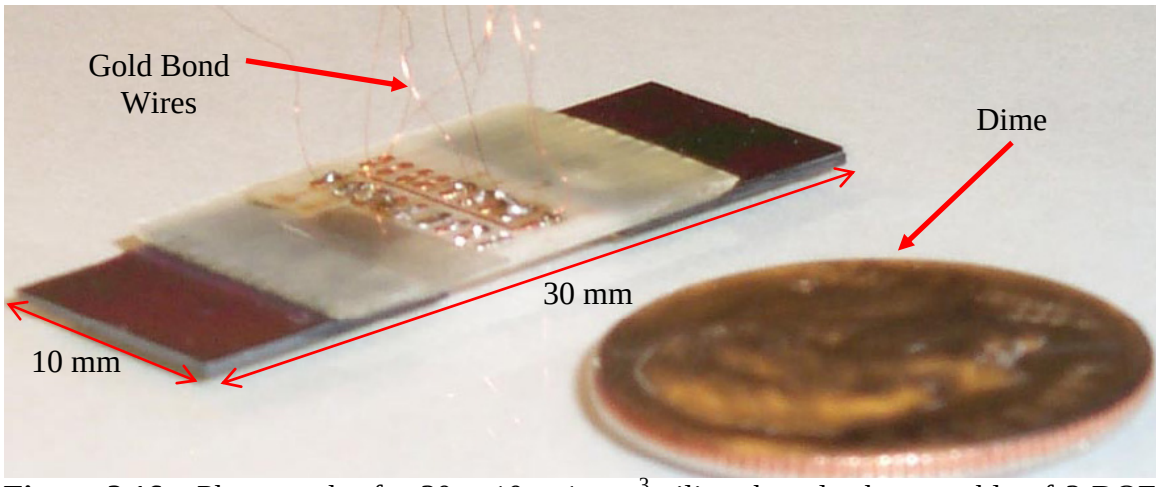


Figure 2.16: Photograph of a 30 x 10 x 1-mm^3 ciliary-based robot capable of 3-DOF movement. Two cili-filled die are bonded to the white printed circuit board. Actuated electrothermally, it clocked a 635-µm/second maximum speed and supported a 1.448-g weight. Its locomotion was limited due to the nine gold bond wires for power [64].

The second major miniature robot system developed in 2001 included a set of several relatively larger robots (20 x 20 x 18 mm^3, weighing 17.5 g) as part of a flexible microassembly system, in which the robots precisely position objects in a scanning electron microscope (SEM) vacuum chamber. Electrostatic manipulators driven by a piezoelectric lead-zirconate-titanate (PZT) bimorph actuator provide the needed precision. The piezoelectrically actuated legs move the robot at 1.2 mm/sec, and electromagnetic forces hold the robot legs in the desired position [24].

A significant new development in 2001 was the scratch drive array (SDA) robot, or "Scratchuator." Powered by a gold wire tether, the robot is capable of pushing a 2 x 2 x 0.5-mm^3 chip over 8 mm across an insulated silicon wafer. The robot in Figure 2.17 is comprised of 188 SDA arrays and is approximately 1.4 x 1.2 mm^2 in area. The robot SDA arrays are comprised of electrostatic step actuators, which produce forward motion by oscillating between the stepping and priming deflection (see Figure 2.18). As the robot SDA array 30-nm positioning accuracy makes them potential candidates for low-cost nanometer chip positioning for surface analysis and even microassembly [25].

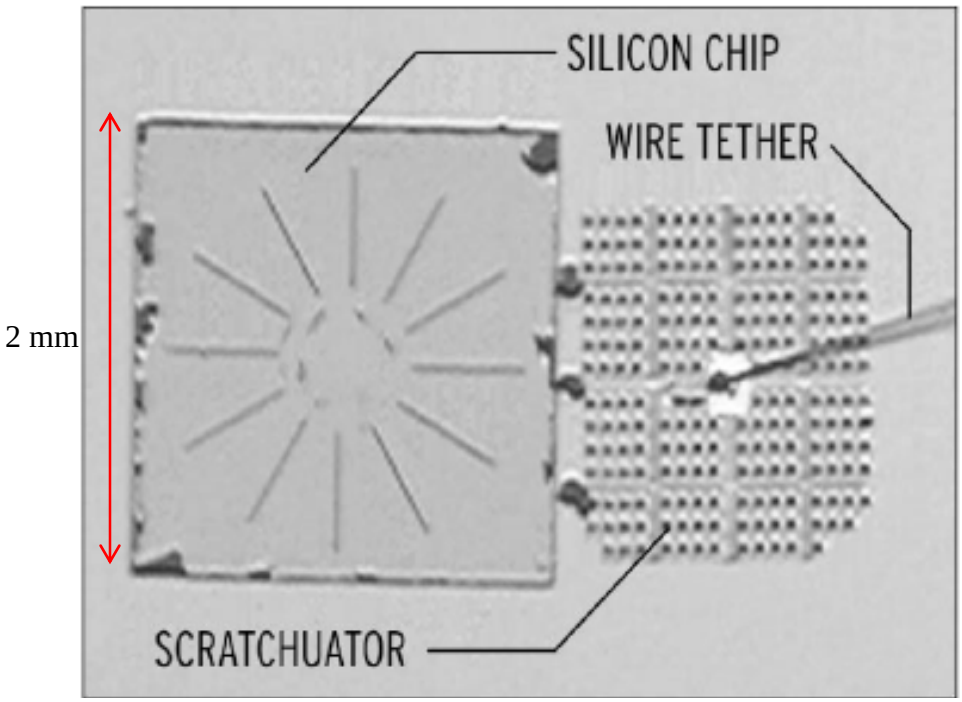


Figure 2.17: Micrograph of the SDA robot—"Scratchuator"—positioning a 2 x 2 x 0.5-mm^3 die across an insulated silicon wafer. The robot SDA arrays are powered through a gold wire tether, and it reportedly consumes less power than other SDA designs [25].

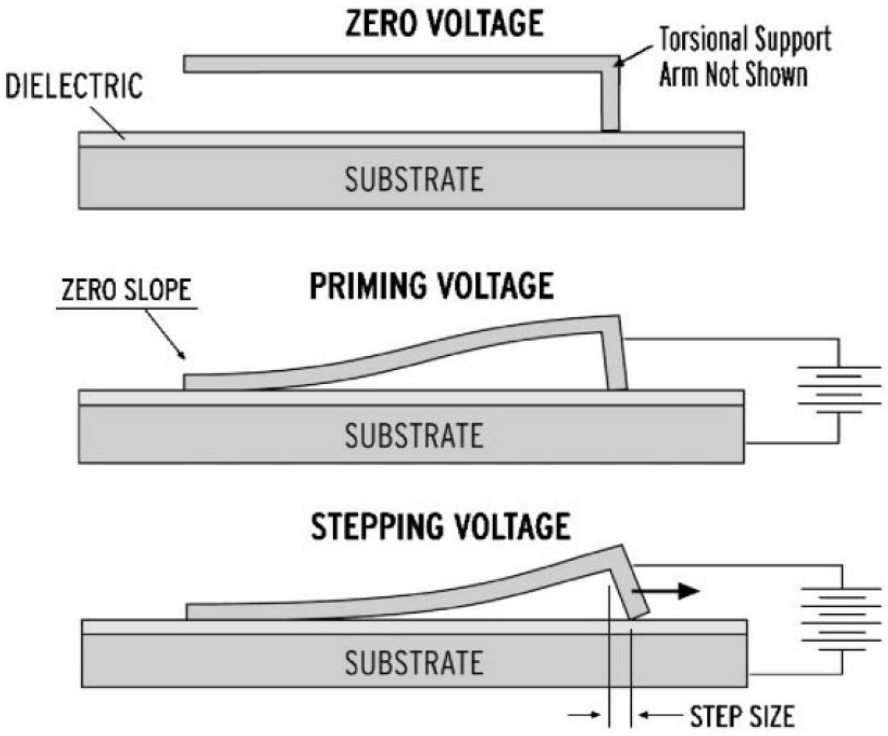


Figure 2.18: Diagram of the stepping process of a scratch drive array electrostatic actuator. This technique produces forward motion by the slipping between the alternating stepping and priming deflections. The robot stepping accuracy is 30 nm [25].

Between 2001 and 2003, another robot scheme was investigated that would use dual thermal bimorph actuators in each of its six legs to produce insect-like walking motion. Although unable to demonstrate motion in a complete robot (Figure 2.19), stepping motion for an individual leg was demonstrated. A step length of 120 µm was possible using the process illustrated in Figure 2.20. The advantage of the robot is its small size (6 x 3.5 x 0.5 mm^3) but its large power requirement (1.3 W per leg) would make it difficult to implement in a remote system [65]–[67].

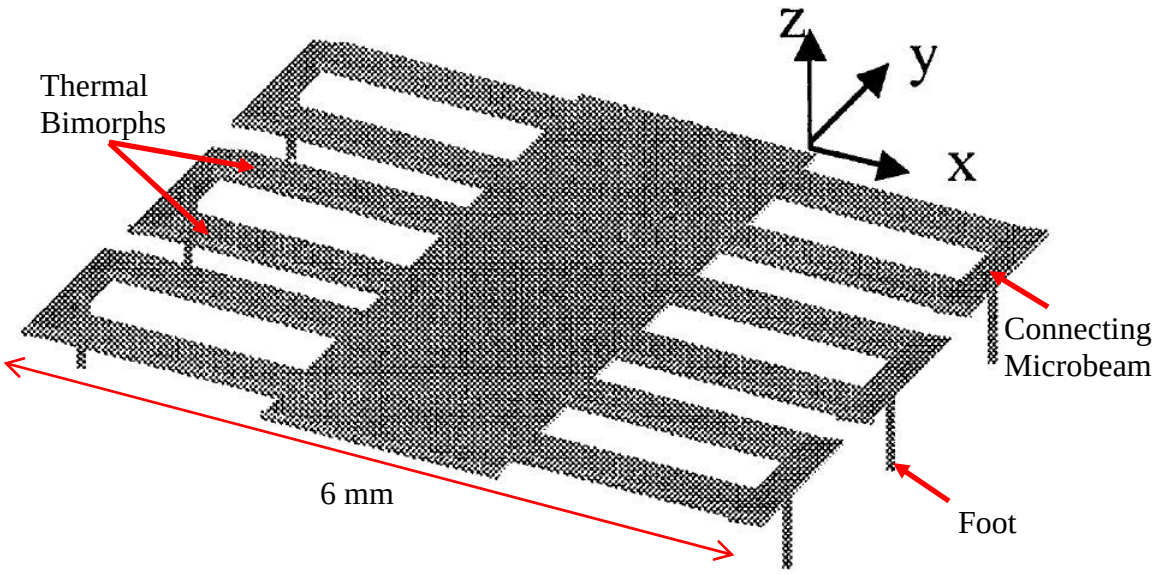


Figure 2.19: Diagram of the complete 6 x 3.5 x 0.5-mm^3 thermally actuated robot based on a six-legged insect locomotion scheme. Motion was demonstrated from only individual legs [65].

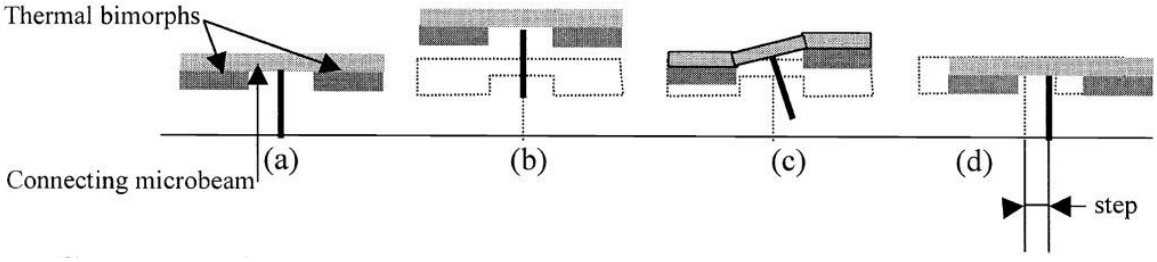


Figure 2.20: Diagram of the stepping process from (a) to (d). A 120-µm step size from individual legs was demonstrated [65].

2.3.3 Critical Survey of Untethered MEMS Land-Based Robots

Up to this point, each robot investigated in the previous section has been bound by gold bond wires that restrict its operation to a nearby power supply. In this section, each featured robot is powered wirelessly—truly a tremendous accomplishment.

For the first time in 2002–2003, significant advances were made towards an untethered, solar-powered walking robot. This work benefited from the successful elements of previously accomplished research: first, the robot appendages; next, the motors; and, finally, the power supply. The appendages were demonstrated in 1995–1996, during which time surface-micromachined hinges for joints were fabricated in robot prototypes [68]–[69]. Each leg has three DOF and is comprised of two 1.2-mm rigid polysilicon links, but the assembled robot has no motor, as illustrated in Figure 2.21.

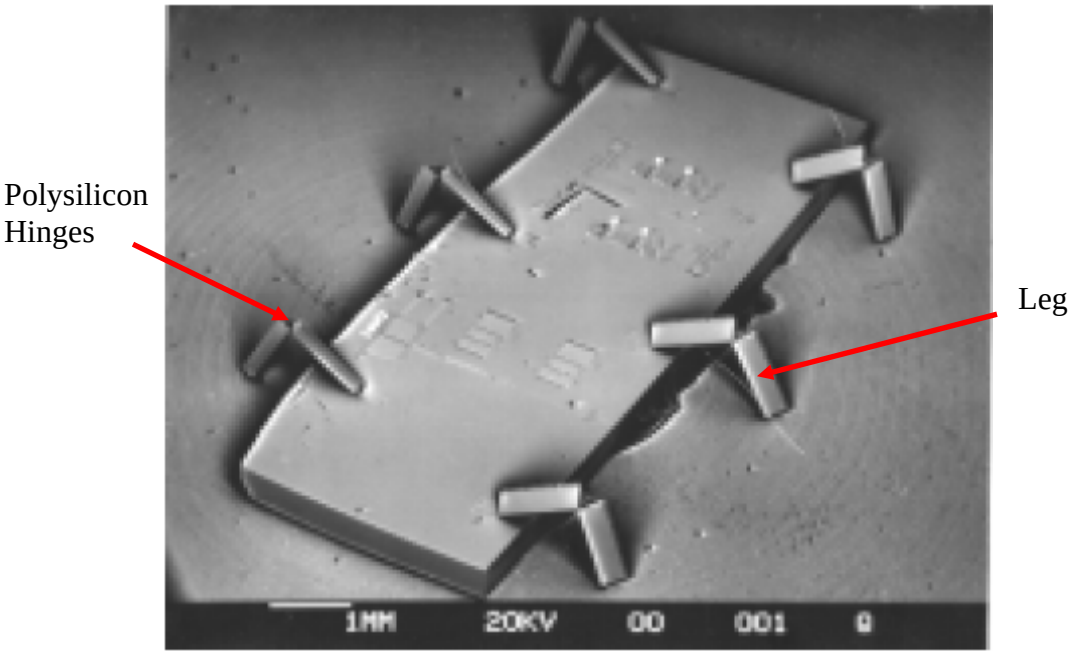


Figure 2.21: SEM micrograph of a robot containing surface-micromachined hinges for joints. Each leg has three DOF and is comprised of two 1.2-mm long rigid polysilicon links. The robot is immobile as it lacks a motor [70].

The robot motor came later in 2001–2002, during which time a high-force, low-power, large-displacement electrostatic "inchworm" step motor was designed. This

motor could be bulk fabricated with a single silicon-on-insulator (SOI) mask [70]–[72]. Each motor consists of a shuttle that is moved by two pawls, each of which is powered by a clutch-drive pair of gap-closing actuators (GCAs). Figure 2.22 illustrates one GCA section of the inchworm motor; also visible is an attached pawl, which is used to displace a movable shuttle.

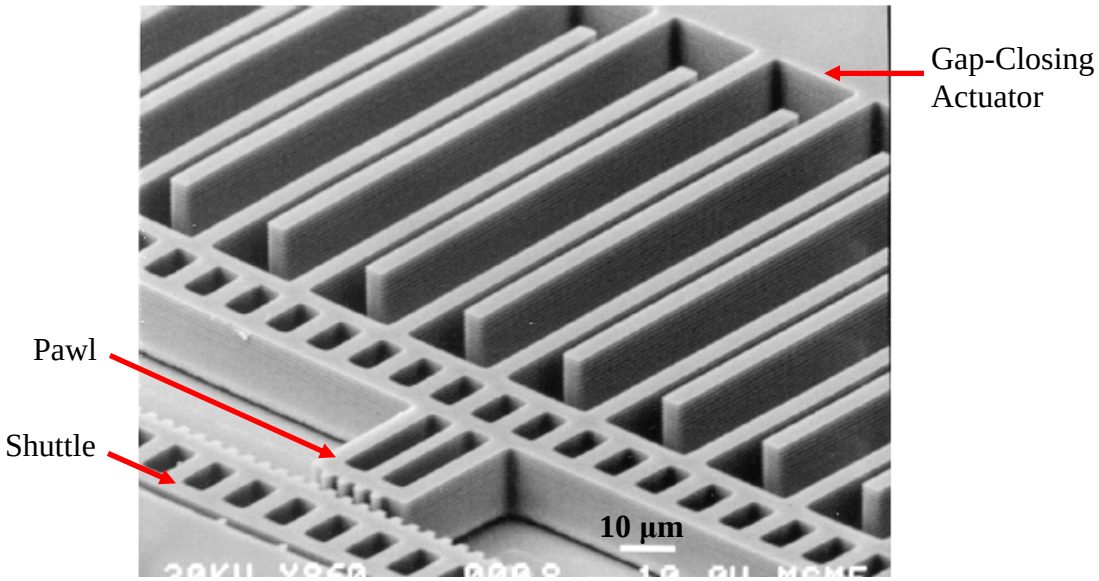


Figure 2.22: SEM micrograph of one of four gap-closing actuator (GCA) sections in an inchworm electrostatic motor. The motor connects to a movable shuttle via a gripped pawl. Four input sequences are capable of moving the shuttle 80 µm [70].

Four input signals are required to operate the four GCAs in each motor with the following sequence: (1) the clutch-1 GCA engages the first pawl teeth into the shuttle teeth; (2) the drive-1 GCA slides the shuttle; (3) the clutch-2 GCA engages the second pawl into the shuttle; (4) and the first pawl is disengaged; (5) the drive-2 GCA slides the shuttle while the first pawl is returned to its initial position; (6) the first pawl is re-engaged; (7) the second pawl is disengaged and returns to its starting position; the sequence is then repeated. One sequence of alternating clutch-drive GCA pairs yields 80 µm of displacement and 100 µN of force. Although fabricated separately from the robot structure, the motor was designed to power a robot leg.

Reported in 2003, a single SOI chip containing solar cells and high-voltage transistors was fabricated [73]. In order to create the high voltages required to power the GCAs, 90 solar cells were connected in series to produce a 50-V open-circuit voltage and 100 uW of power under solar illumination [74]. Separate sections of the solar cells could also be engineered for smaller voltages to power processing circuitry.

At this point, separate robot appendages, motors, and a power source had been successfully yet individually fabricated. The last piece of the puzzle involved integrating these elements and adding "brains" or processing circuitry, which was achieved in 2003. Shown in Figure 2.23 is a complex 8.6 x 3.1 x 0.5-mm^3 three-section robot; it consists of a solar cell/high-voltage buffer chip, a CMOS sequencer chip, and a chip with motors and legs. This robot consumes only 2.6 μW—a record for miniature robots [70], [74].

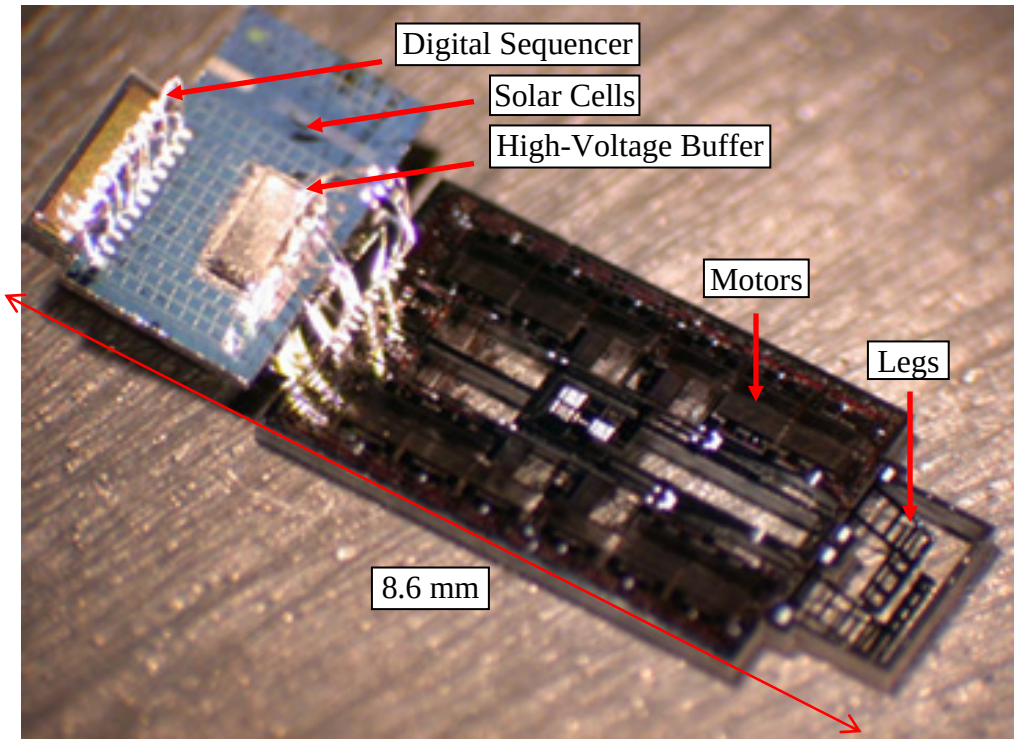


Figure 2.23: Photograph of the first solar-powered robot which uses electrostatic gap-closing actuators with a gear and clutch combination to move its legs. This robot consists of an SOI chip with solar cells and high-voltage buffers, a digital sequencing chip, and a chip with motors and legs. The robot has dimensions of 8.6 x 3.1 x 0.5 mm^3 and consumes a mere 2.6 μW of power [74].

The physical integration of each chip is straight-forward: the solar cell/high-voltage chip is wire bonded to the CMOS sequencer chip; the solar cell/high-voltage chip is wax bonded and then wire bonded to the robot chip (see Figure 2.24).

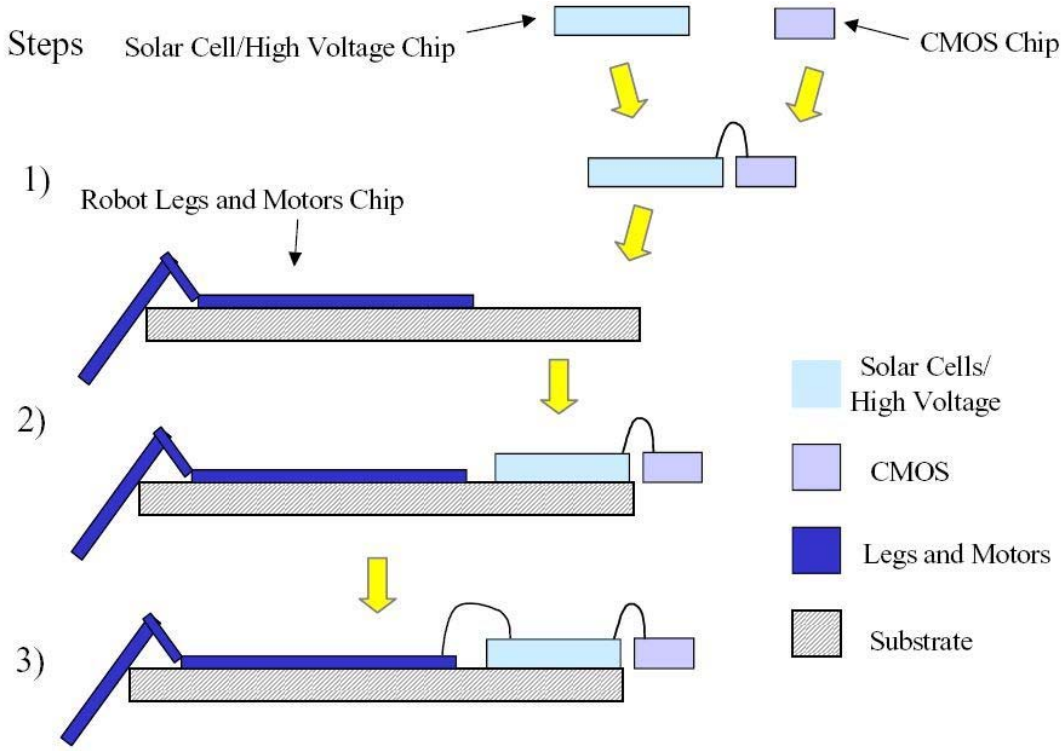


Figure 2.24: Diagram of the three-chip assembly process of the first autonomous solar-powered robot. In step 1, the solar cell/high-voltage chip is wire bonded to the CMOS sequencer chip. In step 2, the solar cell chip is bonded to the robot chip with wax. In step 3, the solar cell and robot chips are wire bonded together [73].

Once integrated into a single unit, the robot is capable of producing autonomous motion. The process is as follows: the solar cells provide a 1-V signal to power the digital sequencer logic circuit and a 3-V supply to amplify the sequencer output signal; the solar cells also provide 50 V to the high-voltage buffer, which converts the 0- to 3-V digital sequencer output signal to a 0- to 50-V signal to each GCA motor.

The four GCA motors control a single leg, while four more GCA motors control the opposite leg. The silicon legs, joints, and a section of a GCA are illustrated in Figure 2.25. Also visible are bulk-etched pits for reducing the mass of the robot. While this

robot is the first untethered, solar-powered, miniature robot with autonomous control, its legs failed to provide enough traction to move the entire robot unit.

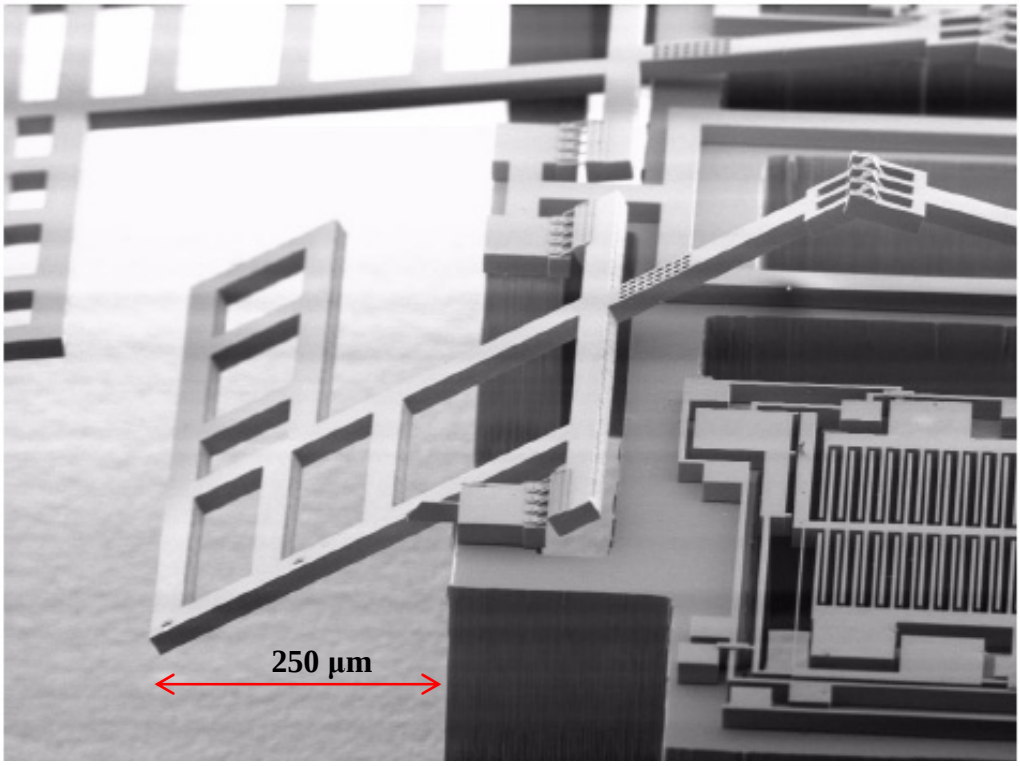


Figure 2.25: SEM micrograph of the silicon legs, hinges, and one section of a GCA. Sections of the chip were bulk-etched to reduce the mass of the robot to 10.2 mg [73].

Reported in 2004 was an untethered 760 x 710-µm^2 microrobot that received its power from a remote pulsed laser [20], [75]. The microrobot motor was comprised of two sets of polysilicon thermal actuators—horizontally deflecting and downward-deflecting—that could push a pair of legs into the ground to make the robot move. Actuation is achieved by the photo-thermal technique in which the absorbed photons from the laser cause the polysilicon actuators to heat and expand; during the off-cycle, the actuators cool and contract. Using a 60-mW pulsed laser, each actuator individually demonstrated 2 µm of deflection. Due to the high power required from each actuator, however, the two could not be demonstrated simultaneously. Otherwise, this device would have been the first walking wireless microrobot (see Figure 2.26).

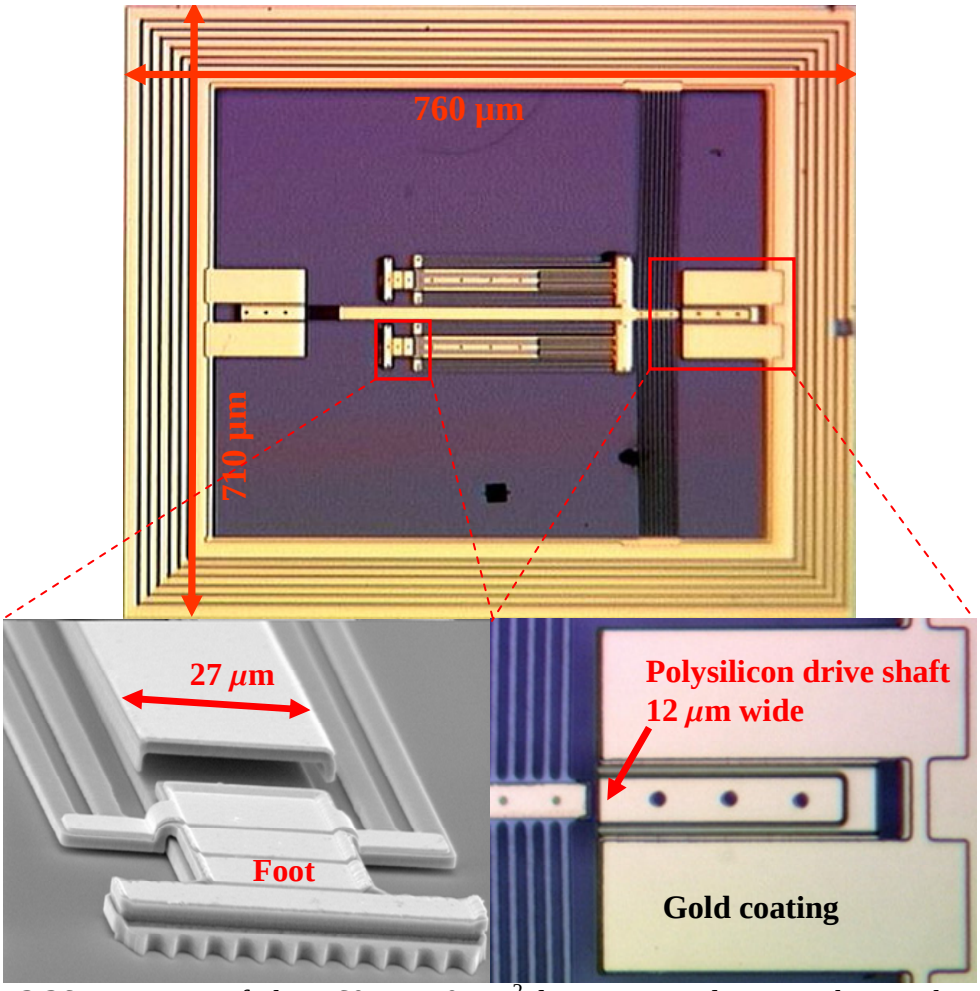


Figure 2.26: Images of the 760 x 710-µm^2 laser-powered microrobot. The foot is actuated forward and downward by two sets of thermal actuators [20].

In the fall of 2005, the first untethered walking microrobot was demonstrated [76]–[78]. With dimensions of 250 x 60 x 10 µm^3, it recorded speeds of over 200 µm/sec with an average step size of 12 nm. The device consists of a 120 x 60-µm^2 untethered scratch drive actuator that moves the microrobot forward; a 133-µm-long side-protruding cantilever arm with a 36-µm-diameter disc steers the device. The microrobot is situated on wavy insulated interdigitated polysilicon electrodes. These pads provide capacitive power to the scratch drive: the microrobot scratch drive actuator forms the top plate of a capacitor; this is insulated from oppositely charged rows of electrodes, which form the bottom plates of the capacitor (see Figure 2.27 and Figure 2.28).

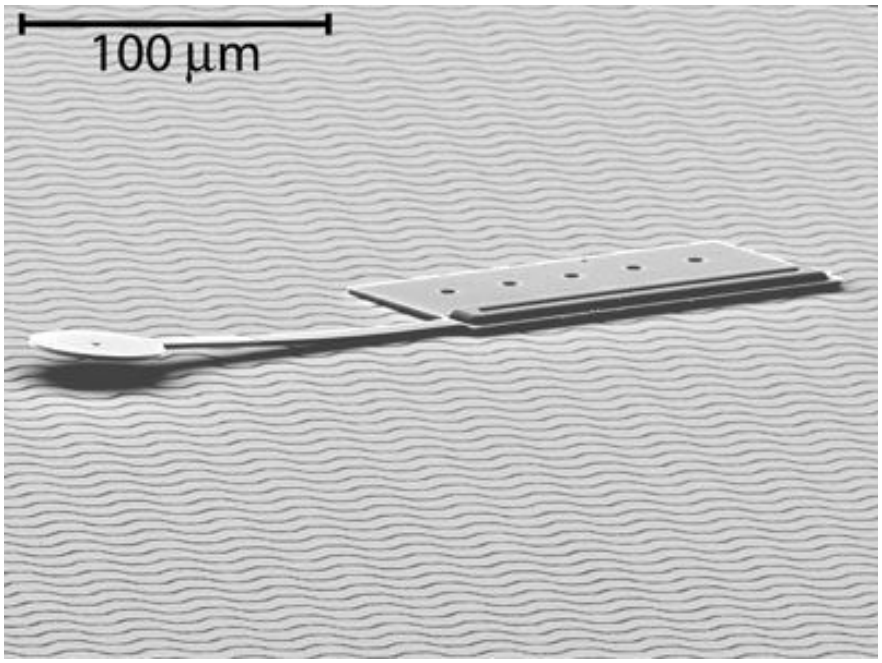


Figure 2.27: SEM micrograph of the first untethered walking microrobot. It consists of a 120 x 60-µm^2 scratch drive actuator that propels the robot forward at 200 µm/sec; the 133-µm cantilever arm provides a steering capability. The devices requires up to 140 V signals through the inter-digitated electrodes to operate [78].

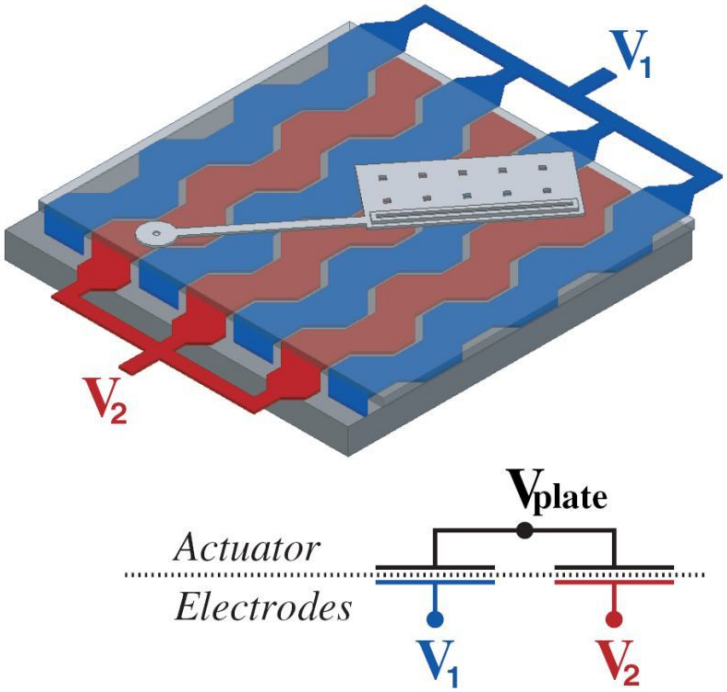


Figure 2.28: Diagram of the capacitive-coupled power delivery system required for untethered scratch drive actuators. The alternating electrodes with applied voltages V_1 and V_2 are separated from the actuators by an insulating layer. The induced voltage V_{plate} is approximately the average of V_1 and V_2 [78].

The voltage V_{plate} is induced from the voltages in the bottom electrodes V_1 and V_2. This microrobot cannot operate on anything except this special pad of electrodes. Moreover, high drive signals of 112 V for straight-line motion and 140 V for turning are required. Despite these limitations, this untethered microrobot is a tremendous success—nothing its size has ever achieved controlled motion.

2.3.4 Summary of MEMS Land-Based Robots

The information from the preceding survey of land-based MEMS robots is concisely contained in Table 2.2.

Table 2.2. Summary and Comparison of Land-Based MEMS Robots and Conveyors.

Authors	Device	Size	Actuation/ Material	Power/ Delivery	Accomplishments
Teshigahara *et al.* (1995) [47]	Minicar	4.8x1.8x1.8 mm^3	Electromagnetic Barium Ferrite	ND* Wire	100-mm/sec forward motion; **fastest rolling**
Böhringer *et al.* (1997) [50]	Conveyor	10x10x1 mm^3	Electrothermal Polyimide	6.7 W Wire	20-mg carrying capacity
Kladitis *et al.* (1999) [51]	Conveyor Robot	10x10x0.75 mm^3	Electrothermal Polysilicon	2.87 W Wire	68-mg carrying capacity; 453-μm/sec conveyance
Suh *et al.* (1999) [53]	Conveyor	9.4x9.4x1 mm^3	Electrothermal Polyimide	5 W Wire	Fabricated over CMOS circuitry; controllable conveyor manipulations
Ebefors *et al.* (1999) [59]	Walking Robot	15x5x1.5 mm^3	Electrothermal Polyimide	1.1 W Wire	2500-mg carrying capacity; 12-mm/sec forward motion; **fastest walking robot**
Mohebbi *et al.* (2001) [64]	Walking Robot	30x10x1 mm^3	Electrothermal Polyimide	ND Wire	3-DOF movement at 635 μm/sec
Aoyama *et al.* (2001) [24]	Walking Robot	20x20x18 mm^3	Piezoelectric PZT	ND Wire	1.2-mm/sec movement inside an SEM
Linderman *et al.* (2001) [25]	Walking Robot	1.5x1.5x1 mm^3	Electrostatic Polysilicon	ND Wire	Moved silicon chip; 30-nm positioning accuracy
Bonvilain *et al.* (2003) [67]	Robot	6x3.5x0.5 mm^3	Electrothermal Polysilicon	7.8 W Wire	120-μm step size for single leg
Hollar *et al.* (2003) [74]	Robot	8.6x3.1x0.5 mm^3	Electrostatic Polysilicon	2.6 μW Solar	Alternating 2-leg motion; **lowest power; autonomous robot**
Szabo *et al.* (2004) [75]	Robot	760x710x10 μm^3	Optothermal Polysilicon	60 mW Laser	2-μm leg displacement with laser
Donald *et al.* (2005) [78]	Walking Robot	250x60x10 μm^3	Electrostatic Polysilicon	ND Capactive Coupling	Forward and turning motion; 200 μm/sec; **smallest walking robot**

* ND—No data reported by the authors

The robots with the lowest power consumption use electrostatic actuation; those with the largest carrying capacity use electrothermal actuation. Among all the power delivery types—solar power, photothermal transduction, bonding wire, electrostatic capacitive coupling—only solar power is practical for applications outside the laboratory. The solar-powered robot is the only autonomously operating robot and consumes the least amount of power, but its movement is quite limited. Walking is truly a difficult paradigm. An alternate, yet quite promising, form of locomotion is flying, which is examined in the next section.

2.4 Airborne Miniature Robots

Flying miniature robots are highly useful in military surveillance operations and civilian search missions. The Defense Advanced Research Projects Agency (DARPA) is the major funding source for micro aerial vehicles (MAVs), which provided $35 million from 1998–2002 to researchers in order to develop a 15-cm-wingspan flying vehicle [79]. The term "micro" is once again misused since the MAV maximum dimension is 15 cm, according to the DARPA design requirement. Several MAV prototypes have been developed since then, and some are being used by the Army and Marines [17]. These MAVs constitute the smallest autonomous airborne vehicles, though progress is being made in even smaller insect-sized flying robots.

2.4.1 The Smallest Autonomous Powered Airborne Vehicle

Among the successfully autonomous mini-UAVs that have been developed [19], [79], the smallest reported UAV capable of autonomous powered flight is AeroVironment's Black Widow (depicted in Figure 2.29). Its notable features are: 15-cm wing span, 60-g maximum take-off weight (including 7-g payload), 30-mph speed,

30-minute endurance time, and a 2-km maximum communications range. The Black Widow provides live video feed to the pilot, who controls it remotely most of the time. It can also fly autonomously through an autopilot feature, which includes altitude hold, airspeed hold, heading hold, and yaw damping. It was designed for visual reconnaissance, situational awareness, damage assessment, surveillance, biological or chemical agent sensing, and communications relay. Besides these military missions, the Black Widow is well suited to perform search and rescue, border patrol, air sampling, police surveillance, and field research [80].

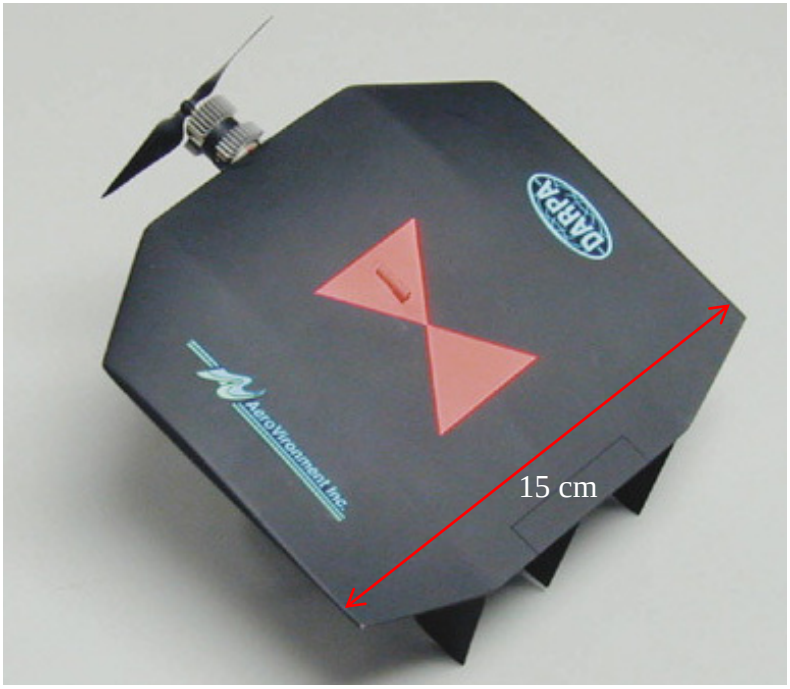


Figure 2.29: The Black Widow is the smallest reported autonomous powered aircraft with a 15-cm wing span and 60-g take-off weight. It provides live video feed and has autopilot capabilities [79].

2.4.2 Critical Survey of Miniature Airborne Vehicles

Flying miniature vehicles are generally classified as one of three types: flapping, fixed-wing, or rotary. Only a few MEMS-based miniature flying vehicles with dimensions on the order of a few millimeters are examined in any detail in this section. A thorough discussion of larger airborne vehicles would be appropriate in an aeronautical

instead of an electrical engineering thesis. Notwithstanding this, future MEMS researchers pursuing microrobotic flight could certainly benefit from at least a basic understanding of aerodynamics.

2.4.2.1 Flapping (Ornithoptic) Miniature Airborne Vehicles

Biomimetics—the science of imitating biological systems—is a hot area of robotics research, as is evident in the increasingly numerous "biologically inspired" air vehicle projects. Biomimetics has inspired researchers in the government, in academia, and in industry to develop vehicles capable of flapping, or ornithoptic, flight [81]–[84].

Some of the earliest attempts to develop ornithoptic flyers—from 1992–1995—resulted in two flying robot concepts with 1-mm-long [85] and 1.5-mm-long wing spans [86]–[91]. A polysilicon rigid-frame flapping structure with polyimide elastic joints and aluminum contact plates was mounted on a silicon chip. The 1.5-mm device demonstrated flapping motion by electrostatic actuation, as illustrated in Figure 2.30.

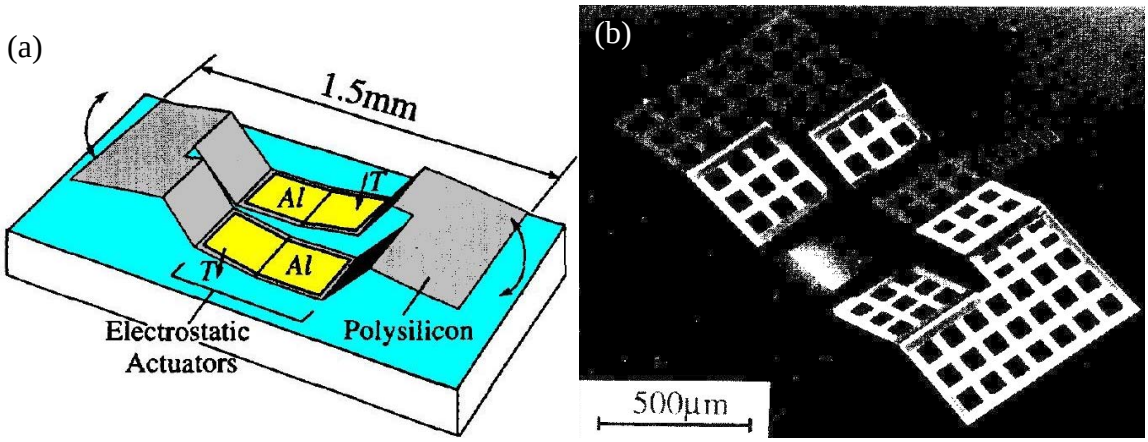


Figure 2.30: 1.5-mm-long flying robot concept (a) in a diagram showing the polysilicon wings, the aluminum contact plates, and the silicon chip; (b) a photograph of the fabricated structure. The electrostatic attraction between the wings and the chip cause downward deflection [86], [89].

As evident in Figure 2.30, the flapping mechanism is bound to the relatively heavy substrate. The electrostatic actuation strategy, in this case, requires power delivered through wires, which would severely limit the robot's flight performance.

In an effort to find a viable flight technique, researchers in 1994–1995 experimentally determined the lift and drag characteristics of a 2.39 x 1.54-mm^2 aluminum airplane structure. The main purpose of the research was to investigate the poorly understood fluid mechanics of structures with low Reynolds numbers, such as miniature airborne vehicles. Although the project initially evaluated a fixed-wing structure, it was determined that flapping is a superior approach for flying microrobots [92]–[94].

A single project that epitomizes biomimetic research is encompassed in the multidisciplinary Mechanical Flying Insect (MFI) project, which commenced in 1998 [95], [96]. The goal of this project is to create an autonomous flying robotic insect the size of a housefly—approximately a 10- to 25-mm wingtip-to-wingtip length. Much progress by biologists in identifying insect flight mechanisms has been made [97]; this has ultimately led to the development of a 26-joint, 4-actuator, 4-DOF, 2-wing carbon fiber thorax [98]–[100]. The actuators are made of a piezoelectric material that expands when a voltage source is applied. The two wings are made of a thin, transparent layer of polyimide—a photosensitive material that is stiffer and stronger than most types of photoresist. MFI prototypes have demonstrated 500 μN of lift at 160 Hz from a single wing on a test stand [95]. Current objectives are reducing weight, increasing frame strength, and improving wing motion in order to achieve hovering controlled flight of an entire robot [95], [101]–[103]. A photograph of the current carbon-fiber frame, two polyimide wings, and four piezoelectric actuators are given in Figure 2.31. Figure 2.32 illustrates the future sensory, power, processing, and communication features.

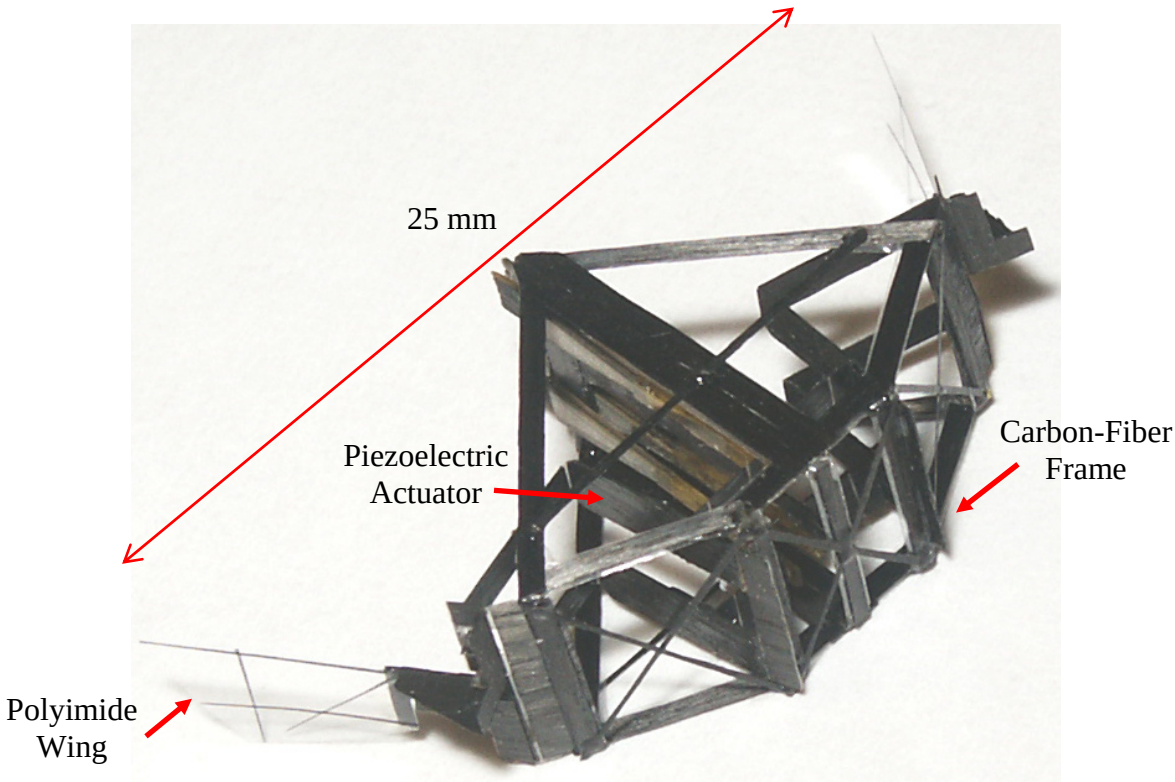


Figure 2.31: Photograph of the 25-mm Mechanical Flying Insect (MFI) thorax in its current state, including a carbon-fiber frame, two polyimide wings, and four piezoelectric actuators [95].

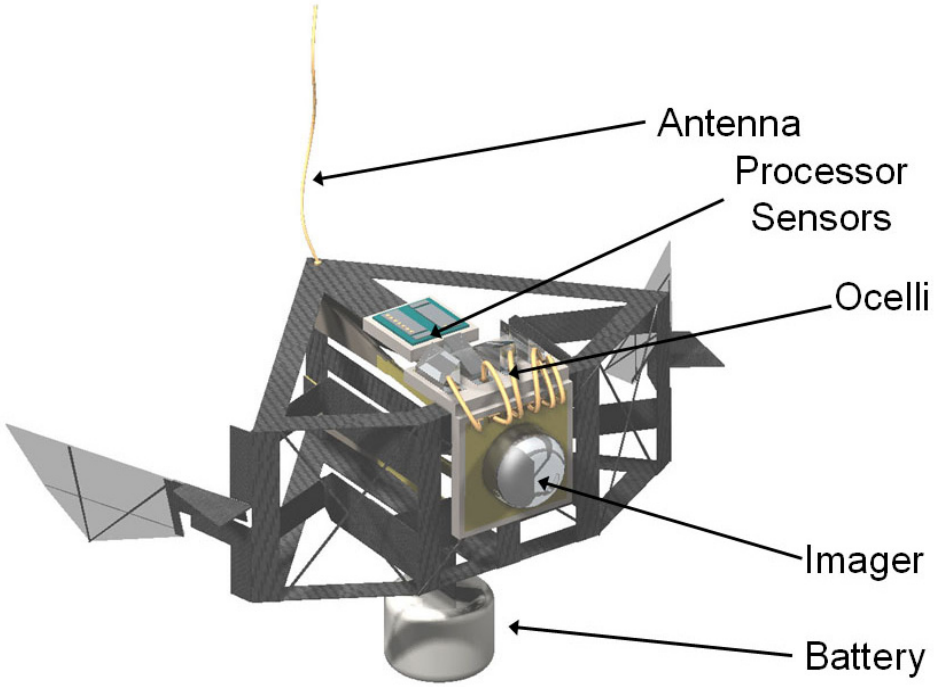


Figure 2.32: Diagram of future features of the MFI, including sensors, ocelli (eyes), a processor, a battery, and an antenna [95].

Not shown in the diagram of Figure 2.32 are solar panels, which are also proposed as the power source. These would provide a limitless supply of energy in lighted conditions. The Micromechanical Flying Insect project has the greatest potential for achieving autonomous flight in a miniature airborne vehicle. Once achieved, this would be the smallest, most successful airborne vehicle.

2.4.2.2 Fixed-Wing Miniature Airborne Vehicles

Fixed-wing miniature airborne vehicles tend to be relatively large (15-cm wingspans) and powered with attached motors. They, like the Black Widow from section 2.4.1, are part of the DARPA MAV project and are included here only for reference [19], [79], [104]–[107]. MEMS-based fixed-wing aircraft have not yet been reported.

The smallest non-MEMS fixed-wing miniature airborne vehicle was demonstrated in 2002. In this research, it was shown that a laser is capable of inducing propulsion by ablating a two-layer target. A 39 x 56 x 15-mm^3 paper airplane with an attached water-on-aluminum target achieved 1.6-m/sec flight when ablated with a 50-mJ/5-ns neodymium yttrium aluminum garnet (Nd:YAG) laser. The laser would necessarily track the airplane in order to maintain powered flight [108]. The novelty of this research is the laser-induced propulsion technique and not the simple paper aircraft.

2.4.2.3 Rotary Miniature Airborne Vehicles

The entirety of MEMS-based rotary flying vehicles is found in the work of a single research group. Their research describes how their 8 x 5 x 8-mm^3, 3.5-mg device achieved successful flight in an alternating magnetic field. The rotating blade is comprised of two 2.5-mm-long wings made of a nickel-iron alloy. As illustrated in Figure 2.33, this device achieved successful flight at 500 Hz [109]–[114].

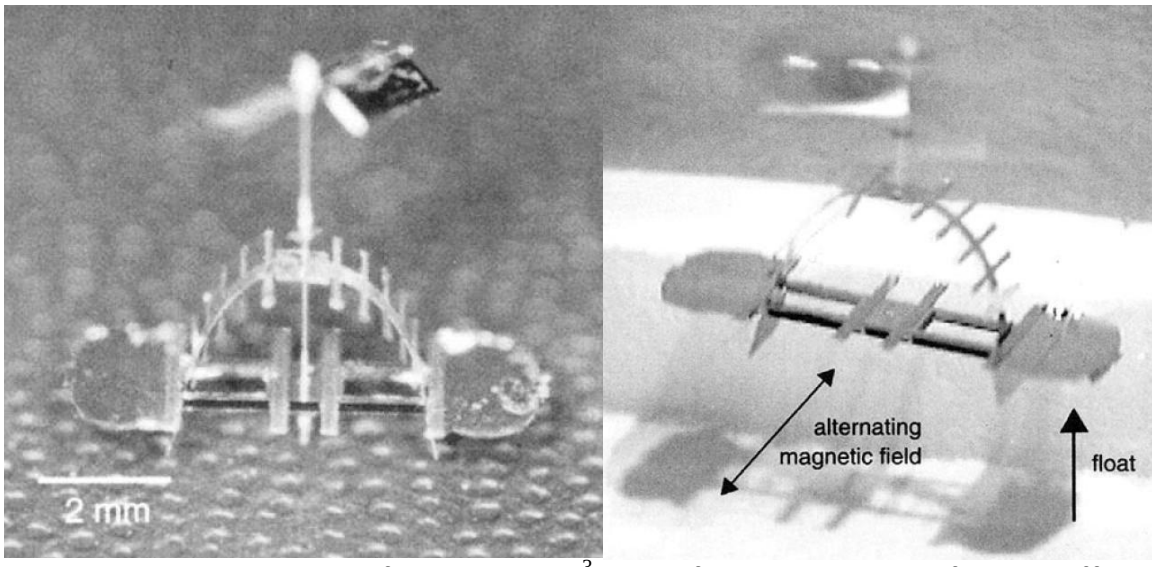


Figure 2.33: Photographs of 8 x 5 x 8-mm^3 rotary flying device (a) before takeoff and (b) during flight. The craft is powered by a 500-Hz alternating magnetic field [114].

This millimeter-scale device is the smallest known flying device; it is not autonomous, but can be considered a miniature robot. Thus, it is true to assert that no micro-sized (less than 1 mm) flying robot currently exists.

2.4.3 Summary of Miniature Airborne Vehicles

The three types of miniature robots—flapping, fixed-wing, and rotary—exhibit important achievements as well as shortcomings in the development of microrobotic flight. While the most successful autonomous flying vehicles are large (15-cm) and based on fixed-wing aircraft principles, it has been argued that the flapping, or ornithoptic, approach would be the most successful for microrobots. Ornithopters mimic biological principles, which have demonstrated autonomous miniature flight for thousands of years. The principles, however, are very complex. The Micromechanical Flying Insect is the most promising of the biomimetic robots, though much progress is yet to be realized, even in lifting off. Successful flight has been achieved devices smaller than the MFI; these 8-mm robots use the rotary principle, which is very promising.

2.5 Chapter Summary

Despite the many advances in miniature and micro-sized walking and flying robot designs, a mobile autonomous microrobot still does not exist. Most miniature walking robots have power supplies and actuation strategies that are too large for the micro-scale world. In addition, the walking process is inherently difficult. Most successful airborne vehicles are based on fixed-wing approaches, which are successful only at centimeter scales. Millimeter- and micrometer-sized devices must be based on biomimetic flapping flight; however, the wing patterns most insects routinely use are very complex. The key limitations to developing microrobotic flying vehicles are similar to those in walking robots: developing energy- and thrust-efficient actuation techniques; and developing sufficiently light, yet energy-dense power supplies.

A new strategy must be developed that eliminates complex circuitry and actuation strategies. A flying robot that scavenges power from the environment is the solution. This research will investigate ways to make the first flapping microrobot with maximum dimensions in the micrometer range. Since laser-powered thermal actuation has been successfully demonstrated, this research will borrow that technique to power thermal actuators in the robot wings. This would eliminate performance-limiting wires from the device. The microrobot will be designed to fly towards the laser source in order to demonstrate controlled behavior. A power-scavenging, light-tracking flying microrobot would truly be a tremendous breakthrough.

2.6 References

[1] R. P. Feynman, "There's Plenty of Room at the Bottom," *Journal of Microelectromechanical Systems*, vol. 1, no. 1, pp. 60–66, March 1992.

[2] K. E. Petersen, "Silicon as a Mechanical Material," *Proceedings of the IEEE*, vol. 70, no. 5, pp. 420–457, May 1982.

[3] R. P. Feynman, "Infinitesimal Machinery," *Journal of Microelectromechanical Systems*, vol. 2, no. 1, pp. 4–14, March 1993.

[4] R. S. Fearing, "Control of a Micro-Organism as a Prototype Micro-Robot," *Proceedings of the 2nd International Symposium of Micromachines and Human Sciences*, pp. 1–15, Nagoya, Japan, 8–9 Oct. 1991.

[5] A. Itoh, "Motion Control of Protozoa for Bio MEMS," *IEEE/ASME Transactions on Mechatronics*, vol. 5, no. 2, pp. 181–188, June 2000.

[6] S. Laksanacharoen, A. J. Pollack, G. M. Nelson, R. D. Quinn, and R. E. Ritzmann, "Biometrics and Simulation of Cricket for Microrobot Design," *Proceedings of the 2000 IEEE International Conference on Robotics and Automotion*, vol. 2, pp. 1088–1094, San Francisco, CA, 24–28 Apr. 2000.

[7] M. C. Birch, R. D. Quinn, G. Hahm, S. M. Phillips, B. Drennan, R. D. Beer, X. Yu, S. L. Garverick, S. Laksanacharoen, A. J. Pollack, and R. E. Ritzmann, "A Miniature Hybrid Robot Propelled by Legs," *Proceedings of the 2001 IEEE International Conference on Intelligent Robots and Systems*, pp. 845–851, Maui, HI, 29 Oct.–3 Nov. 2001.

[8] M. C. Birch, R. D. Quinn, G. Hahm, S. M. Phillips, B. T. Drennan, A. J. Fife, R. D. Beer, X. Yu, S. L. Garverick, S. Laksanacharoen, A. J. Pollack, and R. E. Ritzmann, "Cricket-Based Robots," *IEEE Robotics & Automation Magazine*, pp. 20–30, December 2002.

[9] C. D. Montemagno and H. Neves, "The Art and Science of Engineering Hybrid Living/Non-Living Mechanical Devices," *Proceedings of the 15th IEEE International Conference on Microelectromechanical Systems*, pp. 1–5, 20–24 Jan. 2002.

[10] Y. Bar-Cohen, "Biologically Inspired Intelligent Robots Using Artificial Muscles," *Proceedings of the International Conference on MEMS, NANO and Smart Systems—ICMENS `03*, pp. 2–8, 20–23 Jul. 2003.

[11] The Nano Science and Technology Institute (NSTI) Nanotech 2005 homepage. n. pag. http://www.nsti.org/Nanotech2005. 28 Nov. 2005.

[12] M. J. Madou, *Fundamentals of Microfabrication: The Science of Miniaturization* (2nd Edition), Boca Raton, FL: CRC Press, 2002, pp. 629–631.

[13] K. J. Rebello, "Applications of MEMS in Surgery," *Proceedings of the IEEE*, vol. 92, no. 1, pp. 43–55, January 2004.

[14] W. S. N. Trimmer, "Microrobots and Micromechanical Systems," *Sensors and Actuators*, vol. 19, no. 3, pp. 267–287, September 1989.

[15] J. S. Foster and L. D. Welch, "The Evolving Battlefield," *The American Institue of Physics*, vol. 53, no. 12, pp. 31–38, 2001.

[16] C. Perry. Team Lead, Microplatform Development for Advanced Munitions Team, Flight Vehicles Integration Branch, Munitions Directorate, Air Force Research Laboratory (AFRL/MNAV), Eglin AFB, FL. Personal Correspondence. 13 Jun. 2005.

[17] D. H. Lyon, "A Military Perspective on Small Unmanned Aerial Vehicles," *IEEE Instrumentation & Measurement Magazine*, pp. 27–31, September 2004.

[18] A. F. Huber, *Death by a Thousand Cuts: Micro-Air Vehicles (MAV) in the Service of Air Force Missions*, Masters Thesis, Air War College, 2001.

[19] M. Hewish, "A Bird in the Hand," *Jane's International Defense Review Online*, vol. 32, no. 11, n. pag. www.janes.com, 1 Nov. 1999.

[20] F. R. Szabo, *Demonstrating Optothermal Actuators for an Autonomous MEMS Microrobot*, MS thesis, AFIT/GE/ENG/04-23. School of Engineering and Management, Air Force Institute of Technology (AU), Wright-Patterson AFB OH, March 2004 (AD-A426469).

[21] K. Santa and S. Fatikow, "Development of a Neural Controller for Motion Control of a Piezoelectric Three-Legged Micromanipulation Robot," *Proceedings of the 1998 IEEE/RSJ International Conference on Intelligent Robots and Systems*, pp. 788–793, Victoria, B. C., Canada, October 1998.

[22] K. Santa, S. Fatikow, and G. Felso, "Control of Microassembly-Robots by Using Fuzzy-Logic and Neural Networks," *Computers in Industry*, vol. 39, pp. 219–227, 1999.

[23] H. Wörn, F. Schmoeckel, A. Buerkle, J. Samitier, M. Puig-Vidal, S. Johansson, U. Simu, J. U. Meyer, and M. Biehl, "From Decimeter- to Centimeter-Sized Mobile Microrobots—The Development of the MINIMAN System," *Proceedings of the SPIE*, vol. 4568, pp. 175–186, 2001.

[24] H. Aoyama and O. Fuchiwaki, “Flexible Micro-Processing by Multiple Micro Robots in SEM,” *Proceedings of the 2001 IEEE International Conference on Robotics & Automation*, pp. 3429–3434, Seoul, Korea, 21–26 May 2001.

[25] R. J. Linderman and V. M. Bright, “Nanometer Precision Positioning Robots Utilizing Optimized Scratch Drive Actuators,” *Sensors and Actuators A: Physical*, vol. 91, pp. 292–300, 2001.

[26] S. Fatikow, U. Rembold, and H. Wörn, “Design and Control of Flexible Microrobots for an Automated Desktop-Station,” *Proceedings of SPIE*, vol. 3202, pp. 66–77, 1998.

[27] S. Martel, P. Madden, L. Sosnowski, I. Hunter, and S. Lafontaine, “NanoWalker: a Fully Autonomous Highly Integrated Miniature Robot for Nano-Scale Measurements,” *Part of the SPIE EUROPTO Conference on Microsystems Metrology and Inspection*, vol. 3825, pp. 111–122, Munich, Germany, June 1999.

[28] S. Martel, M. Szabelski, A. Leija, P. Madden, S. Lafontaine, and I. Hunter, “Initial Results of a New Type of Locomotion for a Wireless Instrumented Robot Capable of Subatomic Movements,” *Proceedings of the 1st Joint BMES/EMBS Conference*, p. 872, Atlanta, GA, 13–16 Oct. 1999.

[29] S. Martel and I. Hunter, “Piezo-Drive Circuits for Amplitude Modulated Locomotion for Miniature Wireless Robots,” *Proceedings of SPIE*, vol. 4568, pp. 199–209, 2001.

[30] S. Martel, J. B. C Ferrando, L. C. Olaque, T. Fofonoff, and I. Hunter, “Implementing Frequency Modulated Piezo-Based Locomotion for Achieving Further Miniaturization for Wireless Robots,” *Proceedings of SPIE*, vol. 4568, pp. 210–220, 2001.

[31] S. Martel, T. Koker, S. Riebel, M. Sherwood, J. Suurkivi, and I. Hunter, “An Infrastructure Suited for Supporting a Fleet of Wireless Miniature Robots Designed for Atomic-Scale Operations,” *Proceedings of SPIE*, vol. 4568, pp. 221–230, 2001.

[32] S. Martel, L. C. Olaque, J. B. C. Ferrando, S. Riebel, R. Koker, J. Suurkivi, T. Fofonoff, M. Sherwood, R. Dyer, and I. Hunter, “General Description of the Wireless Miniature NanoWalker Robot Designed for Atomic-Scale Operations,” *Proceedings of SPIE*, vol. 4568, pp. 231–240, 2001.

[33] S. Martel, J. Embler, S. Riebel, J. Gibbons, and I. Hunter, “A Novel Heat Dissipation Approach for High-Powered Miniature Robots,” *Proceedings of SPIE*, vol. 4568, pp. 241–251, 2001.

[34] V. Djakov and S. E. Huq, "Bimorph Actuators for MOEMS," *Proceedings of SPIE*, vol. 4755, pp. 804–814, 2002.

[35] T. Ebefors and G. Stemme, "Microrobotics," in *The MEMS Handbook*. Ed. M. Gad-El-Hak. Boca Raton, FL: CRC Press, 2002, pp. 28-1–28-42.

[36] A. Kortschack, O. C. Hänßler, C. Rass, and S. Fatikow, "Driving Principles of Mobile Microrobots for Micro- and Nano-Handling," *Proceedings of the 2003 IEEE/RSJ International Conference on Intelligent Robots and Systems*, pp. 1895–1900, Las Vegas, NV, October 2003.

[37] T. Trüper, A. Kortschack, M. Jähnisch, H. Hülsen, and S. Fatikow, "Transporting Cells with Mobile Microrobots," *IEE Proceedings of Nanobiotechnology*, vol. 151, no. 4, pp. 145–150, August 2004.

[38] P. Dario, R. Valleggi, M. C. Carrozza, M. C. Montesi, and M. Cocco, "Microactuators for Microrobots: A Critical Survey," *Journal of Micromechanics and Microengineering*, vol. 2, no. 3, pp. 141–157, September 1992.

[39] S. Johansson, "Micromanipulation for Micro- and Nano-Manufacturing," *Proceedings of the INRIA/IEEE Symposium on Emerging Technologies and Factory Automation*, vol. 3, pp. 3–8, 1995.

[40] P. E. Kladitis, *Self Assembly of Microstructures*, MS thesis, AFIT/GE/ENG/97D-02, School of Engineering and Management, Air Force Institute of Technology (AU), Wright-Patterson AFB OH, December 1997 (AD-A336753).

[41] S. Fatikow and U. Rembold, *Microsystem Technology and Microrobotics*, Berlin: Springer, 1997.

[42] H. Y. Chan and W. J. Li, "A Thermally Actuated Polymer Micro Robotic Gripper for Manipulation of Biological Cells," *Proceedings of the 2003 IEEE International Conference on Robotics and Automation*, pp. 288–293, Taipei, Taiwan, 14–19 Sep. 2003.

[43] D. L. Polla, "MEMS Technology for Biomedical Applications," *Proceedings of the 6th IEEE International Conference on Solid-State and Integrated-Circuit Technology*, vol. 1, pp. 19–22, 22–25 Oct. 2001.

[44] H. Fujita, "A Decade of MEMS and its Future," *Proceedings of the 10th Annual IEEE International Workshop on Microelectromechanical Systems—MEMS `97*, pp. 1–7, 26–30 Jan. 1997.

[45] R. E. Hurlbert, "Eukaryotic vs. Prokaryotic Cells," Excerpt from Microbiology 101/102 Internet Text, n. pag. http://www.slic2.wsu.edu:82/hurlbert/micro101/pages/Chap2.html, 7 Jun. 2005.

[46] C. Burroughs, “What May be the World’s Smallest Mini-Robot Being Developed at Sandia,” 21 February 2001 Sandia News Release, n. pag. http://www.sandia.gov/ media/NewsRel/NR2001/minirobot.htm, 28 May 2005.

[47] A. Teshigahara, M. Watanabe, N. Kawahara, Y. Ohtsuka, and T. Hattori, “Performance of a 7-mm Microfabricated Car,” *Journal of Microelectromechanical Systems*, vol. 4, no. 2, pp. 76–80, June 1995.

[48] H. Suzuki, N. Ohya, N. Kawahara, M. Yokoi, S. Ohyanagi, T. Kurahashi, and T. Hattori, “Shell-Body Fabrication for Micromachines,” *Journal of Micromechanics and Microengineering*, vol. 5, no. 1, pp. 36–40, March 1995.

[49] T.-R. Hsu, *MEMS and Microsystems: Design and Manufacture*, Boston: McGraw-Hill, 2002, pp. 19, 21.

[50] K. F. Böhringer, B. R. Donald, N. C. MacDonald, G. T. A. Kovacs, and J. W. Suh, “Computational Methods for Design and Control of MEMS Micromanipulator Arrays,” *IEEE Journal of Computational Science & Engineering*, pp. 17–29, January–March 1997.

[51] P. E. Kladitis, V. M. Bright, K. F. Harsh, and Y. C. Lee, “Prototype Microrobots for Micro Positioning in a Manufacturing Process and Micro Unmanned Vehicles,” *Technical Digest of the 12th IEEE International Conference on Microelectromechanical Systems—MEMS `99*, pp. 570–575, Orlando, FL, 17–21 Jan. 1999.

[52] P. E. Kladitis and V. M. Bright, “Prototype Microrobots for Micro-Positioning and Micro-Unmanned Vehicles,” *Sensors and Actuators A: Physical*, vol. 80, pp. 132–137, 2000.

[53] J. W. Suh, R. B. Darling, K. F. Böhringer, B. R. Donald, H. Baltes, and G. T. A. Kovacs, “CMOS Integrated Ciliary Actuator Array as a General-Purpose Micromanipulation Tool for Small Objects,” *Journal of Microelectromechanical Systems*, vol. 8, no. 4, pp. 483–496, December 1999.

[54] J. W. Suh, R. B. Darling, K. F. Böhringer, B. R. Donald, H. Baltes, and G. T. A. Kovacs, “Fully Programmable MEMS Ciliary Actuator Arrays for Micromanipulation Tasks,” *Symposia Proceedings of IEEE International Conference on Robotics and Automation*, vol. 2, pp. 1101–1108, 2000.

[55] M. Ataka, A. Omodaka, N. Takeshima, and H. Fujita, “Fabrication and Operation of Polyimide Bimorph Actuators for a Ciliary Motion System,” *Journal of Microelectromechanical Systems*, vol. 2, no. 4, pp. 146–150, December 1993.

[56] E. J. Lerner, “Making Micromachines,” *American Institute of Physics—The Industrial Physicist*, pp. 18–22, August 1999.

[57] T. Ebefors, E. Kälvesten, C. Veieder, and G. Stemme, "New Robust Small Radius Joints Based on Thermal Shrinkage of Polyimide in V-Grooves," *Proceedings of the IEEE International Conference on Solid-State Sensors and Actuators—Transducers `97*, pp. 675–678, Chicago, IL, 16–19 Jun. 1997.

[58] T. Ebefors, E. Kälvesten, and G. Stemme, "Three Dimensional Silicon Triple-Hot-Wire Anemometer Based on Polyimide Joints," *Proceedings of the 11th Annual IEEE International Workshop on Micro Electro Mechanical Systems—MEMS `98*, pp. 93–98, 25–29 Jan. 1998.

[59] T. Ebefors, J. U. Mattsson, E. Kälvesten, and G. Stemme, "A Walking Silicon Micro-Robot," *Proceedings of the 10th IEEE International Conference on Solid-State Sensors and Actuators—Transducers `99*, pp. 1202–1205, Sendai, Japan, 7–10 Jun. 1999.

[60] T. Ebefors, J. U. Mattsson, E. Kälvesten, and G. Stemme, "3D micromachined devices based on Polyimide Joint Technology," *Part of the SPIE Symposium on Device and Process Technologies for MEMS and Microelectronics*, vol. 3892, pp. 118–132, Queensland, Australia, October 1999.

[61] T. Ebefors, J. U. Mattsson, E. Kälvesten, and G. Stemme, "A Robust Micro Conveyer Realized by Arrayed Polyimide Joint Actuators," *Proceedings of the 12th IEEE International Conference on Micro Electro Mechanical Systems—MEMS `99*, pp. 576–581, Orlando, FL, 17–21 Jan. 1999.

[62] T. Ebefors, J. U. Mattsson, E. Kälvesten, and G. Stemme, "A Robust Micro Conveyer Realized by Arrayed Polyimide Joint Actuators," *Journal of Micromechanics and Microengineering*, vol. 10, pp. 337–349, 2000.

[63] T. Ebefors, *Polyimide V-Groove Joints for Three-Dimensional Silicon Transducers—Exemplified through a 3-D Turbulent Gas Flow Sensor and Micro-robotic Devices*, Doctoral Dissertation, Royal Institute of Technology (KTH), Stockholm, Sweden, 2000.

[64] M. H. Mohebbi, M. L. Terry, K. F. Böhringer, G. T. A. Kovacs, and J. W. Suh, "Omnidirectional Walking Microrobot Realized by Thermal Microactuator Arrays," *Proceedings of 2001 ASME International Mechanical Engineering Congress and Exposition*, pp. 1–7, New York, NY, 11–16 Nov. 2001.

[65] A. Bonvilain, J. R. Coudevylle, P. Blind, and N. Chaillet, "Micromachined Thermal Actuated Microlegs for an Insect-Like Microrobot," *Proceedings of SPIE*, vol. 4557, pp. 403–414, 2001.

[66] A. Bonvilain and N. Chaillet, "Fabrication and Experiment of Microlegs for an Insect-Like Microrobot," *Proceedings of SPIE*, vol. 4568, pp. 163–174, 2001.

[67] A. Bonvilain and N. Chaillet, “Microfabricated Thermally Actuated Microrobot,” *Proceedings of the 2003 IEEE International Conference on Robotics & Automation*, pp. 2960–2965, Taipei, Taiwan, 14–19 Sep. 2003.

[68] R. Yeh, E. J. J. Kruglick, and K. S. J. Pister, “Microelectromechanical Components for Articulated Microrobots,” *Proceedings of the 8th International Conference on Solid-State Sensors and Actuators—Transducers `95 and Eurosensors IX*, pp. 346–349, Stockholm, Sweden, 25–29 Jun. 1995.

[69] R. Yeh, E. J. J. Kruglick, and K. S. J. Pister, “Surface-Micromachined Components for Articulated Microrobots,” *Journal of Microelectromechanical Systems*, vol. 5, no. 1, pp. 10–17, March 1996.

[70] S. Hollar, A. Flynn, S. Bergbreiter, and K. S. J. Pister, “Robot Leg Motion in a Planarized SOI/2-Poly Process,” *Proceedings of the Solid-State Sensor, Actuator and Microsystems Workshop*, Hilton Head, SC, June 2002.

[71] R. Yeh, S. Hollar, and K. S. J. Pister, “Single Mask, Large Force, and Large Displacement Electrostatic Linear Inchworm Motors,” *Journal of Microelectromechanical Systems*, vol. 11, no. 4, pp. 330–336, August 2002.

[72] R. Yeh, S. Hollar, and K. S. J. Pister, “Design of Low-Power Silicon Articulated Microrobots,” *Journal of Micromechatronics*, vol. 1, no. 3, pp. 191–203, 2002.

[73] C. L. Bellew, S. Hollar, and K. S. J. Pister, “An SOI Process for Fabrication of Solar Cells, Transistors and Electrostatic Actuators,” *Proceedings of the 12th IEEE International Conference on Solid State Sensors, Actuators and Microsystems—Transducers `03*, pp. 1075–1079, Boston, MA, 8–12 Jun. 2003.

[74] S. Hollar, A. Flynn, C. Bellew, and K. S. J. Pister, “Solar Powered 10 mg Silicon Robot,” *Proceedings of the 16th Annual IEEE International Conference on Micro Electro Mechanical Systems—MEMS `03*, pp. 706–711, Kyoto, Japan, 19–23 Jan. 2003.

[75] F. R. Szabo and P. E. Kladitis, “Design, Modeling, and Testing of Polysilicon Optothermal Actuators for Power-Scavenging Wireless Microrobots,” *Proceedings of the 2004 IEEE International Conference on MEMS, NANO, and Smart Systems—ICMENS `04*, pp. 446–452, Alberta, Canada, 25–27 Aug. 2004.

[76] B. R. Donald, C. G. Levey, C. D. McGray, D. Rus, and M. Sinclair, “Power Delivery and Locomotion of Untethered Microactuators,” *Journal of Microelectromechanical Systems*, vol. 12, no. 6, pp. 947–959, 2003.

[77] B. R. Donald, C. G. Levey, C. D. McGray, D. Rus, and M. Sinclair, "Power Delivery and Locomotion of Untethered Micro-Actuators," *Proceedings of the 16th Annual IEEE International Conference on Micro Electro Mechanical Systems—MEMS `03*, pp. 124–129, Kyoto, Japan, 19–23 Jan. 2003.

[78] B. R. Donald, C. G. Levey, C. D. McGray, I. Paprotny, and D. Rus, "An Untethered, Electrostatic, Globally Controllable MEMS Micro-Robot," *Journal of Microelectromechanical Systems*, In press, 2005.

[79] D. Kemp, "Micro-Unmanned Aerial Vehicles—Micro Wave," *Jane's Defence Weekly Online*, n. pag. www.janes.com, 23 Feb. 2005.

[80] J. M. Grasmeyer and M. T. Keennon, "Development of the Black Widow Micro Air Vehicle," Report from Aerovironment Inc., www.aerovironment.com, copyright by *American Institute of Aeronautics and Astronautics*, 2001.

[81] D. L. Raney and E. C. Slominski, "Mechanization and Control Concepts for Biologically Inspired Micro Air Vehicles," *Journal of Aircraft*, vol. 41, no. 6, pp. 1257–1265, November–December 2004.

[82] T. N. Pornsin-Sisirak, S. W. Lee, H. Nassef, J. Grasmeyer, Y. C. Tai, C. M. Ho, and M. Keenon, "MEMS Wing Technology for a Battery-Powered Ornithopter," *Proceedings of the 13th Annual IEEE International Conference on Micro Electro Mechanical Systems—MEMS 2000*, pp. 799–804, Miyazaki, Japan, January 2000.

[83] K. D. Frampton and M. Goldfarb, "Passive Aeroelastic Tailoring for Optimal Flapping Wings," *Proceedings of the Conference on Fixed, Flapping and Rotary Vehicles at Very Low Reynolds Numbers*, Department of Aerospace and Mechanical Engineering, Notre Dame University, Notre Dame, IN, pp. 26–33, June 2000.

[84] H.-Y. Chan, J. H. M. Lam, and W. J. Li, "A Biomimetic Flying Silicon Microchip: Feasibility Study," *Proceedings of the 2004 IEEE International Conference on Robotics and Biomimetics*, pp. 447–451, Shenyang, China, 22–26 Aug. 2004.

[85] Y. Kubo, I. Shimoyama, and H. Miura, "Study of Insect-Based Flying Microrobots," *Proceedings of the 1993 IEEE International Conference on Robotics and Automation*, pp. 386–391, Atlanta, GA, 2–6 May 1993.

[86] K. Suzuki, I. Shimoyama, H. Miura, and Y. Ezura, "Creation of an Insect-Based Microrobot with an External Skeleton and Elastic Joints," *Proceedings of the 1992 IEEE International Conference on Micro Electro Mechanical Systems—MEMS `92*, pp. 190–195, Travenmunde, Germany, 4–7 Feb. 1992.

[87] I. Shimoyama, H. Miura, K. Suzuki, and Y. Ezura, "3D Structure of an Insect-Based Microrobot with an External Skeleton," *Proceedings of the 1992 International Conference on Robotics and Automation*, vol. 1, pp. 693–698, Nice, France, 12–14 May 1992.

[88] I. Shimoyama, H. Miura, K. Suzuki, and Y. Ezura, "Insect-Like Microrobots with External Skeletons," *IEEE Control Systems Magazine*, vol. 13, is. 1, pp. 37–41, February 1993.

[89] K. Suzuki, I. Shimoyama, and H. Miura, "Insect-Model Based Microrobot with Elastic Hinges," *Journal of Microelectromechanical Systems*, vol. 3, no. 1, pp. 4–9, March 1994.

[90] I. Shimoyama, Y. Kubo, T. Kaneda, and H. Miura, "Simple Microflight Mechanism on Silicon Wafer," *Proceedings of the 1994 IEEE International Workshop on Micro Electro Mechanical Systems—MEMS `94*, pp. 148–152, Oiso, Japan, 25–28 Jan. 1994.

[91] H. Miura, T. Yasuda, Y. K. Fujisawa, and I. Shimoyama, "Insect-Model Based Microrobot," *Proceedings of the 8th IEEE International Conference on Solid-State Sensors and Actuators, and Eurosensors IX—Transducers `95*, pp. 392–395, Stockholm, Sweden, 25–29 Jun. 1995.

[92] G. D. Getzan, M. Shimada, I. Shimoyama, Y. Matsumoto, and H. Miura, "Aerodynamic Behavior of Microstructures," *Proceedings of the 1994 IEEE International Symposium on Emerging Technologies and Factory Automation*, pp. 54–61, Tokyo, Japan, 6–10 Nov. 1994.

[93] I. Shimoyama, Y. K. Fujisawa, G. D. Getzan, H. Miura, M. Shimada, and Y. Matsumoto, "Fluid Dynamics of a Microwing," *Proceedings of the 1995 IEEE International Conference on Micro Electro Mechanical Systems—MEMS `95*, pp. 380–382, 29 Jan.–2 Feb. 1995.

[94] G. D. Getzan, M. Shimada, I. Shimoyama, Y. Matsumoto, and H. Miura, "Aerodynamic Behavior of Microstructures," *Proceedings of the 1995 IEEE International Conference on Intelligent Robots and Systems*, vol. 2, pp. 230–235, Pittsburgh, PA, 5–9 Aug. 1995.

[95] R. Fearing, "Micromechanical Flying Insect (MFI) Project," Excerpt from the University of California at Berkeley online webpage. n. pag. http://robotics.eecs.berkeley.edu/~ronf/MFI/mfi.html. 11 Feb. 2005.

[96] "Robotic Flight Gets its Buzz," Excerpt from the University of California at Berkeley news release. n. pag. http://www.berkeley.edu/news/media/releases/2002/06/fearing/home.html. 24 Jan. 2006.

[97] M. H. Dickinson, F. Lehmann, and S. P. Sane, "Wing Rotation and the Aerodynamic Basis of Insect Flight," *Science*, vol. 284, pp. 1954–1960, June 1999.

[98] J. Yan, R. J. Wood, S. Avadhanula, M. Sitti, and R. S. Fearing, "Towards Flapping Wing Control for a Micromechanical Flying Insect," *Proceedings of the 2001 IEEE International Conference on Robotics and Automation*, pp. 3901–3908, Seoul, Korea, 21–26 May 2001.

[99] J. Yan, S. A. Avadhanula, J. Birch, M. H. Dickinson, M. Sitti, T. Su, and R.S. Fearing, "Wing Transmission for a Micromechanical Flying Insect," *Journal of Micromechatronics*, vol. 1, no. 3, pp. 221–238, 2002.

[100] R. J. Wood, S. Avadhanula, M. Menon, and R. S. Fearing, "Microrobotics Using Composite Materials: The Micromechanical Flying Insect Thorax," *Proceedings of the 2003 IEEE International Conference on Robotics and Automation*, pp. 1842–1849, Taipei, Taiwan, 14–19 Sep. 2003.

[101] L. Schenato, X. Deng, and S. S. Sastry, "Flight Control System for a Micromechanical Flying Insect: Architecture and Implementation," *Proceedings of the 2001 IEEE International Conference on Robotics and Automation*, pp. 1641-1646, Seoul, Korea, 21–26 May 2001.

[102] X. Deng, L. Schenato, and S. Sastry, "Hovering Flight Control of a Micromechanical Flying Insect," *Proceedings of the 40th IEEE International Conference on Decision and Control*, pp. 235–240, Orlando, FL, December 2001.

[103] L. Schenato, W. C. Wu, and S. S. Sastry, "Attitude Control for a Micromechanical Flying Insect via Sensor Output Feedback," *IEEE Journal of Robotics and Automation*, vol. 20, no. 1, pp. 93–106, February 2004.

[104] R. C. Michelson, "The Entomopter," *Neurotechnology for Biomimetic Robots*, Cambridge: MIT Press, 2002, pp. 481–509.

[105] R. C. Michelson and M. A. Naqvi, "Beyond Biologically-Inspired Insect Flight," *Proceedings of the von Karman Institute for Fluid Dynamics RTO/AVT Lecture Series on Low Reynolds Number Aerodynamics on Aircraft Including Applications in Emerging UAV Technology*, pp. 1–19, Brussels, Belgium, 24–28 Nov. 2003.

[106] S. Morris and M. Holden, "Design of Micro Air Vehicles and Flight Test Validation," *Proceedings of the Conference on Fixed, Flapping and Rotary Vehicles at Very Low Reynolds Numbers*, Department of Aerospace and Mechanical Engineering, Notre Dame University, Notre Dame, IN, pp. 26–33, Jun. 2000.

[107] P. G. Ifju, D. A. Jenkins, S. Ettinger, Y. Lian, and W. Shyy, "Flexible-Wing-Based Micro Air Vehicle," *AIAA Paper 2001-0127*, January 2000.

[108] K. Aoki, T. Yabe, R. Nakagawa, M. Yamguchi, and C. Baasandash, "Numerical and Experimental Studies of Laser Propulsion Toward Micro-Airplane," *Proceedings of SPIE*, vol. 4760, pp. 918-928, 2002.

[109] N. Miki and I. Shimoyama, "Flight Performance of Micro-Wings Rotating in an Alternating Magnetic Field," *Proceedings of the 12th Annual IEEE International Conference on Micro Electro Mechanical Systems—MEMS `99*, pp. 153–158, Orlando, FL, 17–21 Jan. 1999.

[110] N. Miki and I. Shimoyama, "Magnetic Rotational Micro-Wings Applicable to Microrobots," *Proceedings of the 1999 IEEE International Conference on Intelligent Robots and Systems*, vol. 2, pp. 721–726, Kyongju, Korea, 17-21 Oct. 1999.

[111] N. Miki and I. Shimoyama, "A Micro-Flight Mechanism with Rotational Wings," *Proceedings of the 13th Annual IEEE International Conference on Micro Electro Mechanical Systems—MEMS 2000*, pp. 158–163, Miyazaki, Japan, 23–27 Jan. 2000.

[112] N. Miki and I. Shimoyama, "An Attitude Control of a Micro-Flight Mechanism with Rotational Wings," *Proceedings of the 14th Annual IEEE International Conference on Micro Electro Mechanical Systems—MEMS 2001*, pp. 602–605, Interlaken, Switzerland, 21–25 Jan. 2001.

[113] N. Miki and I. Shimoyama, "Dynamics of a Microflight Mechanism with Magnetic Rotational Wings in an Alternating Magnetic Field," *Journal of Microelectromechanical Systems*, vol. 11, no. 5, pp. 584–591, October 2002.

[114] N. Miki and I. Shimoyama, "Soft-Magnetic Rotational Microwings in an Alternating Magnetic Field Applicable to Microflight Mechanisms," *Journal of Microelectromechical Systems*, vol. 12, no. 2, pp. 221–227, April 2003.

III. Theory

3.1 Chapter Introduction

The realization of modern engineering marvels increasingly requires the integration of several engineering and scientific disciplines. The microelectromechanical systems field by its very name asserts this fact, and this thesis is certainly no exception. This chapter includes the theory of heat transfer, thermal expansion, solid state physics, optics, and optical engineering in order to design power-scavenging MEMS robots.

3.2 Heat Transfer

There are three fundamental modes of heat transfer: conduction, convection, and radiation [1]. A paramount goal in microsystem design is to minimize the power required for operation. This is achieved first through an understanding of heat transfer principles.

3.2.1 Conduction

Conduction is the transfer of heat from a high- to a low-temperature region within a single body or from one body in physical contact with another. In dielectric solids, heat is transferred primarily by lattice vibrations. In electrically conductive solids, heat is transferred primarily by the motion of free electrons [2].

A temperature difference in a material causes heat to flow at a certain rate. The amount of heat transferred per unit time is called the heat-transfer rate q {in units of W} and is defined by Fourier's Law of Heat Conduction:

$$q = -kA\frac{\partial T}{\partial x}, \tag{3.1}$$

where k is the material thermal conductivity $\{W \cdot m^{-1} \cdot K^{-1}\}$, A is the cross-sectional area $\{m^2\}$, T is the material temperature at a point {K}, and x is the distance along the

structure {m}. The partial differential term $\partial T/\partial x$ assumes that temperature is both time- and direction-dependent. The negative sign in Equation 3.1 shows that heat flows in the direction of decreasing temperature, which is the negative thermal gradient.

Applying steady-state conditions (temperature is constant with respect to time) to this equation yields a simplified expression:

$$q = -kA\frac{dT}{dx}. \tag{3.2}$$

Integrating Equation 3.2 yields an expression for q with known temperatures:

$$q = -\frac{kA}{\Delta x}\Delta T = -\frac{kA}{L}\left(T_2 - T_1\right) = \frac{kA}{L}\left(T_1 - T_2\right), \tag{3.3}$$

where L is the length of a beam {m}, T_1 is the temperature at one end, and T_2 is the temperature at the opposite end. This expression is analogous to Ohm's Law, where q corresponds to current; T corresponds to potential; and L/kA, called thermal resistance, corresponds to electrical resistance.

The analogy is carried one step further to a circuit diagram for a cantilever with gold on polysilicon. As illustrated in Figure 3.1, the two resistors in parallel correspond to the parallel gold and polysilicon layers; if heat were conducted from top to bottom instead of from left to right, the resistors would be in series. R_{gold} and R_{poly} are given as:

$$R_{gold} = \frac{L}{k_{gold}A_{gold}} \tag{3.4}$$

$$R_{poly} = \frac{L}{k_{poly}A_{poly}}, \tag{3.5}$$

where k and A are, respectively, the thermal conductivities and cross-sectional areas of gold and polysilicon layers.

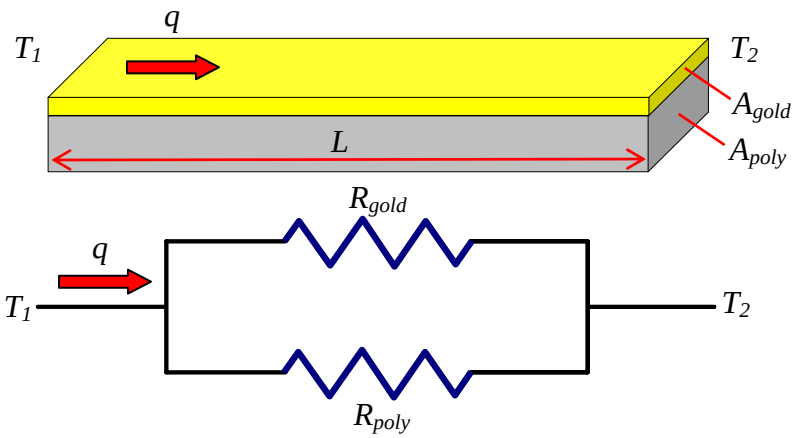


Figure 3.1: Diagram of a gold-polysilicon cantilever illustrating the principle of heat conduction (top). The bottom diagram is an analogous electrical circuit, in which q corresponds to current, T corresponds to potential, and L/kA corresponds to resistance.

For a given temperature difference in a device, heat is conducted at a high rate as the material thermal conductivity and cross-sectional area are both large. Comparing the thermal conductivity values of common microelectronic materials, gold conducts at a higher rate than does silicon, which is also true for electricity (see Table 3.1).

Table 3.1. Thermal conductivity values of gold, silicon, and silicon dioxide [1], [3], [4].

Material	Thermal Conductivity $\{W \cdot m^{-1} \cdot K^{-1}\}$	Electrical Conductivity $\{\Omega^{-1} \cdot m^{-1}\}$
Gold Film	318	48.8×10^{6}
Single-Crystalline Silicon	149	30.3×10^{-9}
Silicon Dioxide	1.4	---

3.2.2 Convection

Convection is the transfer of heat from a surface to a fluid in motion. When fluid motion is caused by a fan or blower, it is called forced convection. When fluid motion results simply from the temperature difference between itself and the surface, it is called free or natural convection [2].

Similar to conduction, a temperature difference results in a certain rate of heat convection, which is defined by Newton's Law of Cooling:

$$q_{conv} = hA\left(T_0 - T_\infty\right). \tag{3.6}$$

Here, q_{conv} is the heat loss from convection {W}, h is the experimentally determined heat-convection coefficient {$W \cdot m^{-2} \cdot K^{-1}$}, A is the surface area {m^2}, T_0 is the temperature at the surface, and T_∞ is the ambient temperature {K}.

The heat-transfer coefficient for forced convection is much higher than free convection, which is why fans are used to cool some electronic devices. Also, more heat is dissipated over a greater surface area, which explains the numerous fins in heat sinks. Convection is important in reducing the time required to cool MEMS structures.

3.2.3 Radiation

Radiation is the emission of electromagnetic energy from a body by virtue of its temperature. It is of the same nature as other electromagnetic waves—x-rays, ultraviolet rays, visible light, infrared rays, radio waves—and differs only in wavelength and source of generation [2]. Radiation is not covered in depth here since it will be neglected in the device modeling chapter.

3.3 Thermal Expansion

Most of the walking miniature robots from Chapter 2 used thermal expansion for actuation. As was noted, thermal actuation requires a disproportionately high amount of energy. Power consumption can be reduced through a better understanding of thermal expansion.

3.3.1 Elongation and Contraction

Two separate beams of the same length yet comprised of different materials will expand or contract to different lengths when heated or cooled. This difference in elongation is due to the different coefficients of thermal expansion (CTE) of the materials. An expression that illustrates this fact is simple. Given some initial length L_0 {m}, the

beam will experience some change in length ΔL {m}, so that the new length L is the sum of the two:

$$L = L_0 + \Delta L \,. \tag{3.7}$$

The change in length ΔL is a fraction of the original length L_0 and is described by the product of the CTE α {K^{-1}} and the change in temperature ΔT {K}:

$$\Delta L = L_0 \alpha \Delta T \tag{3.8}$$

$$L = L_0 + L_0 \alpha \Delta T \,. \tag{3.9}$$

An increasing temperature $\Delta T > 0$ results in $\Delta L > 0$, which means the beam expands; a decreasing temperature $\Delta T < 0$ results in $\Delta L < 0$, which means the beam contracts. The amount of expansion and contraction is determined by the material-dependent CTE. As shown in Table 3.2, gold expands and contracts more than polysilicon.

Table 3.2. Thermal expansion coefficients of gold film and polysilicon [1].

Material	Coefficient of Thermal Expansion {$10^{-6}\cdot K^{-1}$}
Gold	14.3
Polysilicon	2.33

3.3.2 Vertical Deflection in Bimorph Structures

When a single beam is composed of two different material layers, the elongation and contraction differences in the two beams result in either an upward or downward deflection [5]. In PolyMUMPs®, for example, gold film is deposited onto polysilicon at 333–383 K (60–110 °C) [6], [7]. At room temperature (300 K) the devices have cooled by 33–83 K, and the result is contraction. Due to the higher CTE of gold, the gold layer contracts more than the polysilicon layer, resulting in an upward deflection of the gold-polysilicon beam. This is illustrated in Figure 3.2.

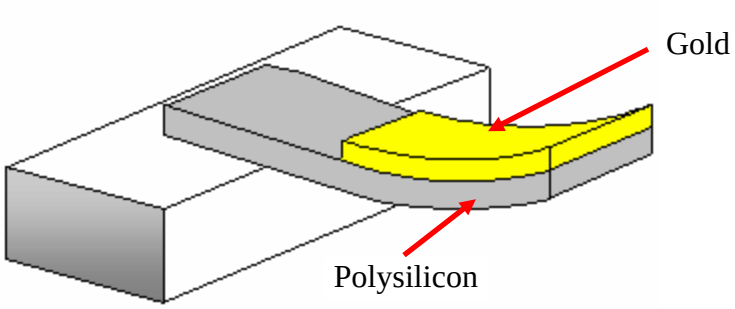


Figure 3.2: Conceptual diagram of the upward deflection caused by cooling a gold-polysilicon cantilever. The gold layer contracts more due to its higher coefficient of thermal expansion.

Though usually a negative effect when attempting to fabricate flat surfaces, deflection in gold-polysilicon structures is exploited in this research. As the gold layer expands more than the polysilicon layer, these cantilevers can be actuated downwards when heated with a focused laser (see Figure 3.3). Laser heating is a reliable optothermal actuation technique [8]–[11], which has been demonstrated in wireless microrobots [12], [13]. The optothermal actuation theory is a fundamental principle of this thesis.

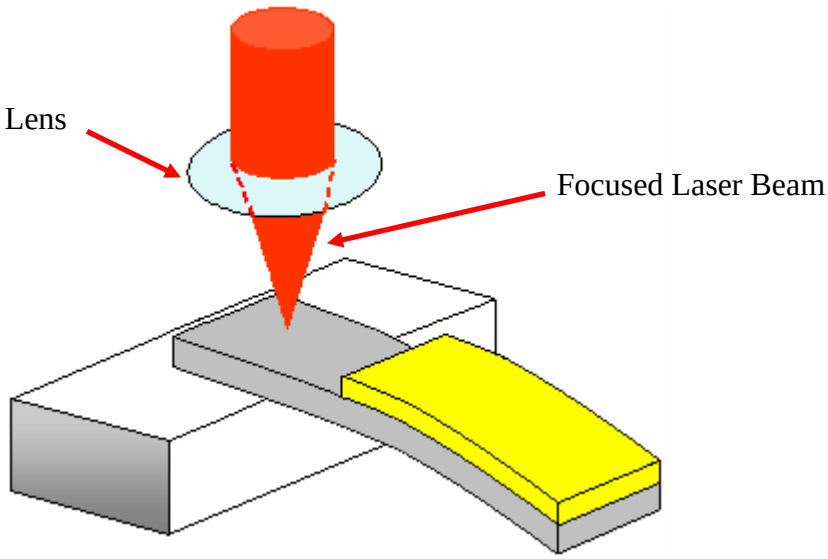


Figure 3.3: Conceptual diagram of downward deflection caused by laser heating in a gold-polysilicon cantilever. The gold expands more due to its higher coefficient of thermal expansion. This optothermal actuation technique is a fundamental operation principle of the microrobots in this thesis.

The expansion theory presented in this section illustrates how to optimize the power-deflection relationship in bi-layer devices. Maximizing deflection while minimizing power consumption can be achieved in two ways: making the devices longer, and increasing the CTE difference of the layers. The specific laser power required to actuate a device downwards is determined in Chapter 4. The next section illustrates optical absorption theory, which is necessary to maximize the energy efficiency of the device. It is also useful in designing the optical setup used to test the robots.

3.4 Optical Absorption

The manner in which light interacts with materials is called the photon-electron interaction principle. This interaction in a solid material results in one of three types of radiative transitions: absorption, spontaneous emission, and stimulated emission. Major photonic devices operate on each of these principles: solar cells and photodetectors by absorption; light-emitting diodes by spontaneous emission; and laser diodes by stimulated emission [14]. What happens to the photon energy when it is absorbed in a semiconductor depends on the photon energy $h\nu$ and the semiconductor bandgap E_g.

3.4.1 Photon Energy and Bandgap Relationship

The amount of energy each photon contains is wavelength-dependent and is given in the following expression:

$$\lambda = \frac{c}{\nu} = \frac{hc}{h\nu} \cong \frac{1.24}{h\nu}, \tag{3.10}$$

where λ is the wavelength of light {μm}, c is the speed of light in a vacuum (2.998×10^8 m/s), ν is the frequency of light {s^{-1}}, h is Planck's constant {6.626×10^{-34} J·s}, and $h\nu$ is the energy of a photon {eV}. Photon energy is inversely proportional to wavelength: the smaller the wavelength, the greater the photon energy.

The semiconductor bandgap is the threshold for photon absorption. A photon with energy that equals the bandgap ($h\nu = E_g$) is absorbed in the material. The absorbed photon energy excites an electron from the valence band E_v into the conduction band E_c. As a result, an electron-hole pair is generated. For direct bandgap semiconductors, the electron-hole pair usually recombines radiatively—by spontaneously emitting a photon. For indirect bandgap semiconductors, the electron-hole pair usually recombines non-radiatively—by dissipating energy through phonon interactions (lattice vibrations). A photon with energy greater than the bandgap ($h\nu > E_g$) is also absorbed, and the excess energy ($h\nu - E_g$) is converted into heat. A photon with energy less than the bandgap ($h\nu < E_g$) is not absorbed unless certain defects exist in the lattice; these can temporarily trap energy in the bandgap. Figure 3.4 illustrates that unless defects exist in the material, only photons with energies greater than or equal to the bandgap energy are absorbed.

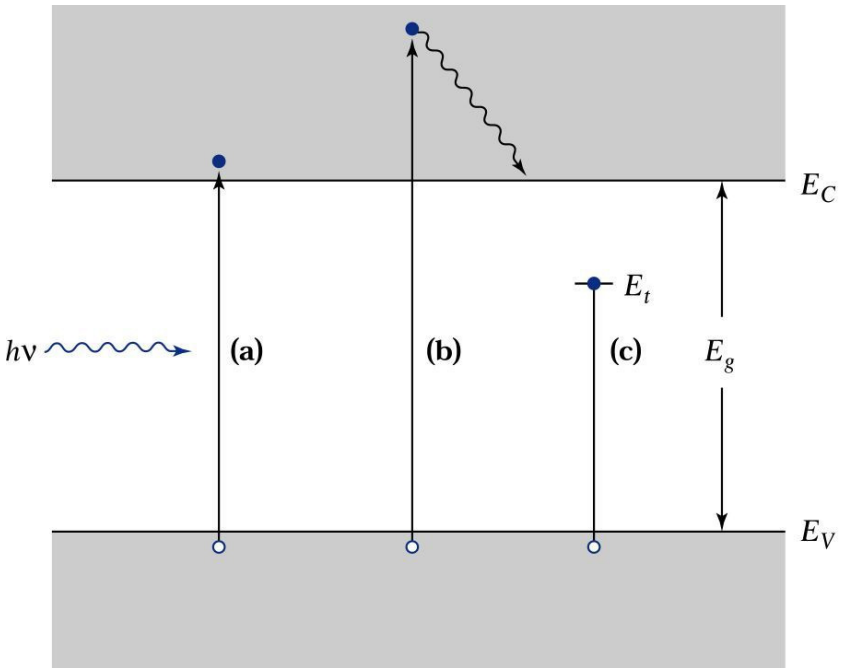


Figure 3.4: Band diagram illustrating photon absorption for (a) $h\nu = E_g$ and (b) $h\nu > E_g$. Unless defects exist in the material, a photon with (c) $h\nu < E_g$ is not absorbed [14]. For photon energy greater than the bandgap, the extra energy is converted into heat, which is desired for optothermal actuators.

3.4.2 Optical Absorption Coefficient

Another paradigm for optical absorption is the experimentally determined absorption coefficient. Figure 3.5 illustrates the absorption dependence on light wavelength. Shown in parentheses is the cutoff wavelength for each material—λ_C = 1.24/E_g—which illustrates the frequency-selective nature of the material. The general trend is an increase in absorption with an increase in photon energy $h\nu$. The red line marks the absorption in silicon for the 660-nm laser that is used in this research.

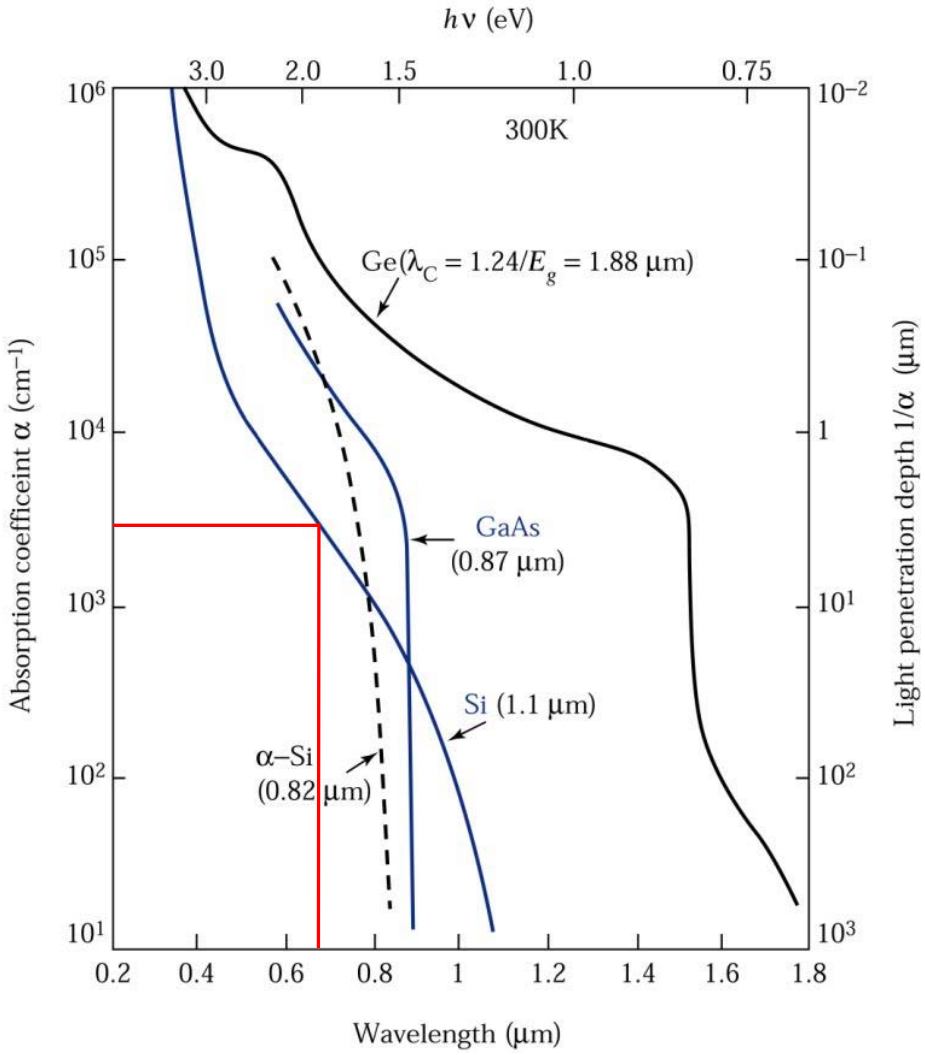


Figure 3.5: Optical absorption coefficient for Ge, GaAs, and Si. The value in the parenthesis is the cutoff wavelength [14]. The red line marks the absorption for the 660-nm laser used in this thesis.

The absorption coefficient for other materials is higher than that for silicon. However, silicon is the material of choice in many MEMS processes because of its fabrication maturity, abundance, and many superior mechanical properties [15]. As will be described later, PolyMUMPs® is a reliable, inexpensive fabrication process, in which phosphorus-doped polysilicon comprises the movable layers. Figure 3.6 shows that the absorption coefficient for polysilicon is higher than that for single-crystalline silicon [16].

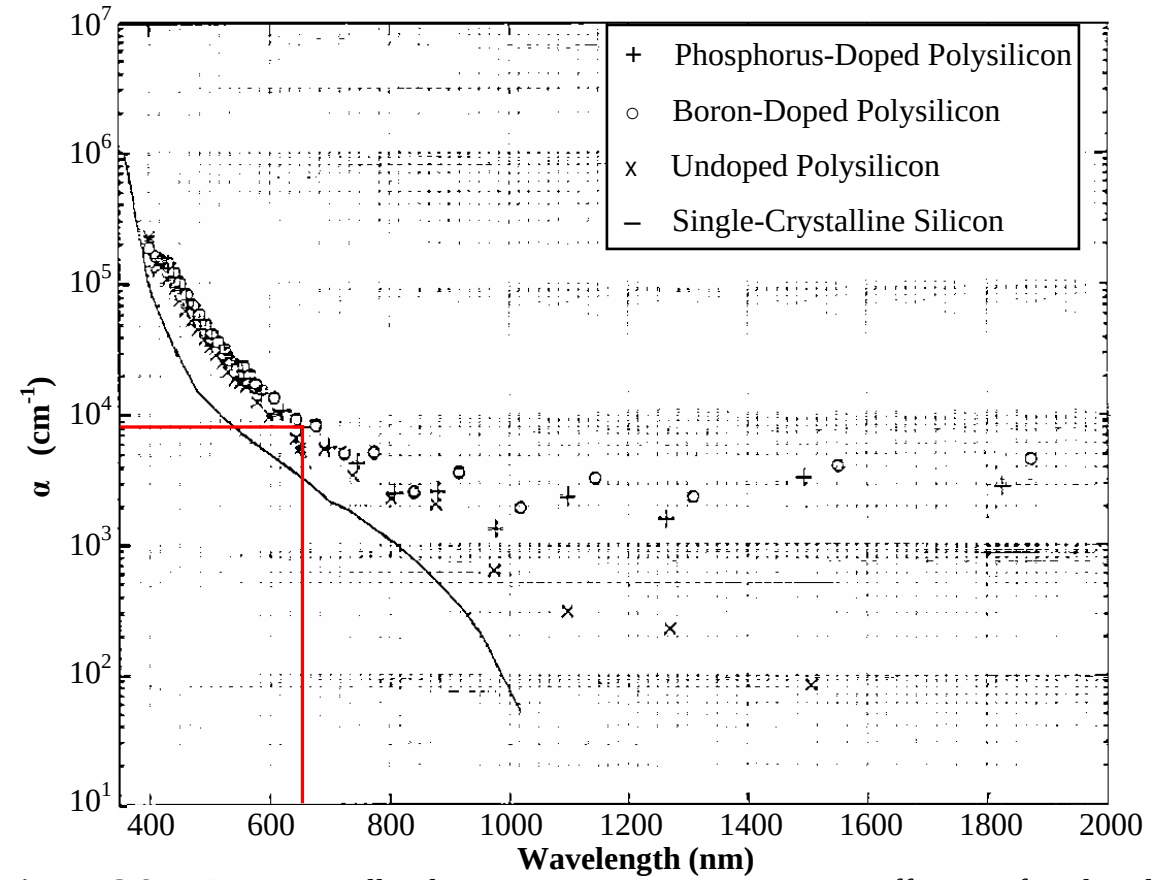


Figure 3.6: Experimentally determined optical absorption coefficients for doped polysilicon compared to single-crystalline silicon. At 660 nm, $\alpha = 8 \times 10^3$ cm^{-1} [16].

3.4.3 Photon Absorption

When a laser illuminates a semiconductor material, a portion of the light is reflected and the remaining portion is either absorbed or transmitted. The conservation of energy requires the sum to be unity: *Reflected* + *Absorbed* + *Transmitted* = 1. The absorbed and transmitted portion of the photon flux Φ_0 {photons·cm^{-2}·s^{-1}} is given by:

$$\Phi_0 = \Phi_i \left(1 - R\right), \tag{3.11}$$

where Φ_i is the incident photon flux and R is the material reflectivity {unitless}.

The absorbed photon flux $\Phi(t_0)$ {photons·cm^{-2}·s^{-1}} as a function of thickness t_0 {cm} is given by subtracting the transmitted flux from unity:

$$\Phi\left(t_0\right) = \Phi_0 \left[1 - \exp\left(-\alpha t_0\right)\right], \tag{3.12}$$

where Φ_0 is given in Equation 3.11 and α {cm^{-1}} is the material absorption coefficient. The percentage of absorbed energy in phosphorus-doped polysilicon for varying thicknesses is given in Figure 3.7. The absorbed energy is maximized by increasing the material thickness and absorption coefficient while decreasing the reflection coefficient.

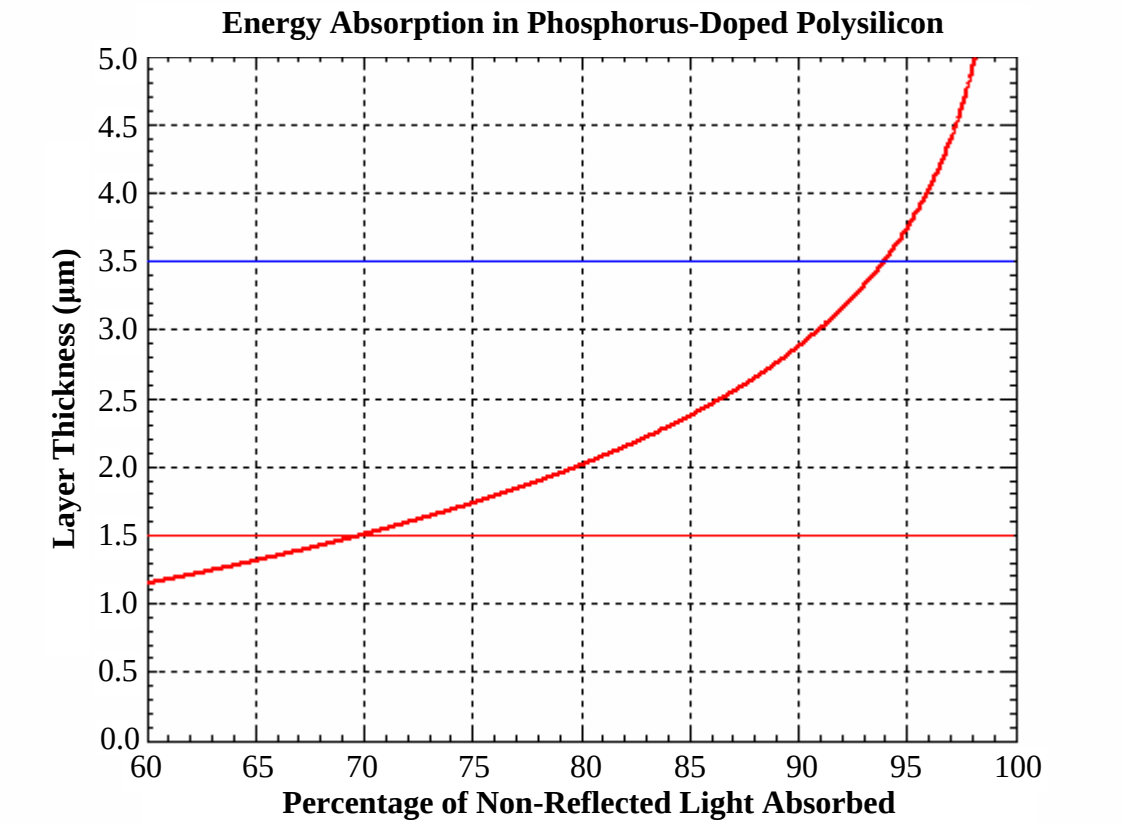


Figure 3.7: Graph showing the percentage of light energy absorbed per layer thickness in phosphorus-doped polysilicon. The lines at 1.5 µm and 3.5 µm represent, respectively, a single layer and double layers of polysilicon in PolyMUMPs®. For a 3.5-µm-thick structure, 94% of the non-reflected light is absorbed, leaving only 6% transmitted.

3.4.4 Heat and Power Generation

Of the total energy absorbed in the semiconductor, a portion equal to the bandgap generates electron-hole pairs while the photon energy in excess ($h\nu$ - E_g) generates heat:

$$\Phi_{\text{heat}} = \Phi\left(t_0\right)\frac{\left[h\nu - E_g\right]}{h\nu}, \tag{3.13}$$

where Φ_{heat} is the heat energy generated and $\Phi(t_0)$ is given in Equation 3.12. Figure 3.8 illustrates the percentage of absorbed energy that contributes to heat in a silicon device. In this graph, the absorption coefficient and the absorbed energy are held constant, though they would both increase with decreased wavelength.

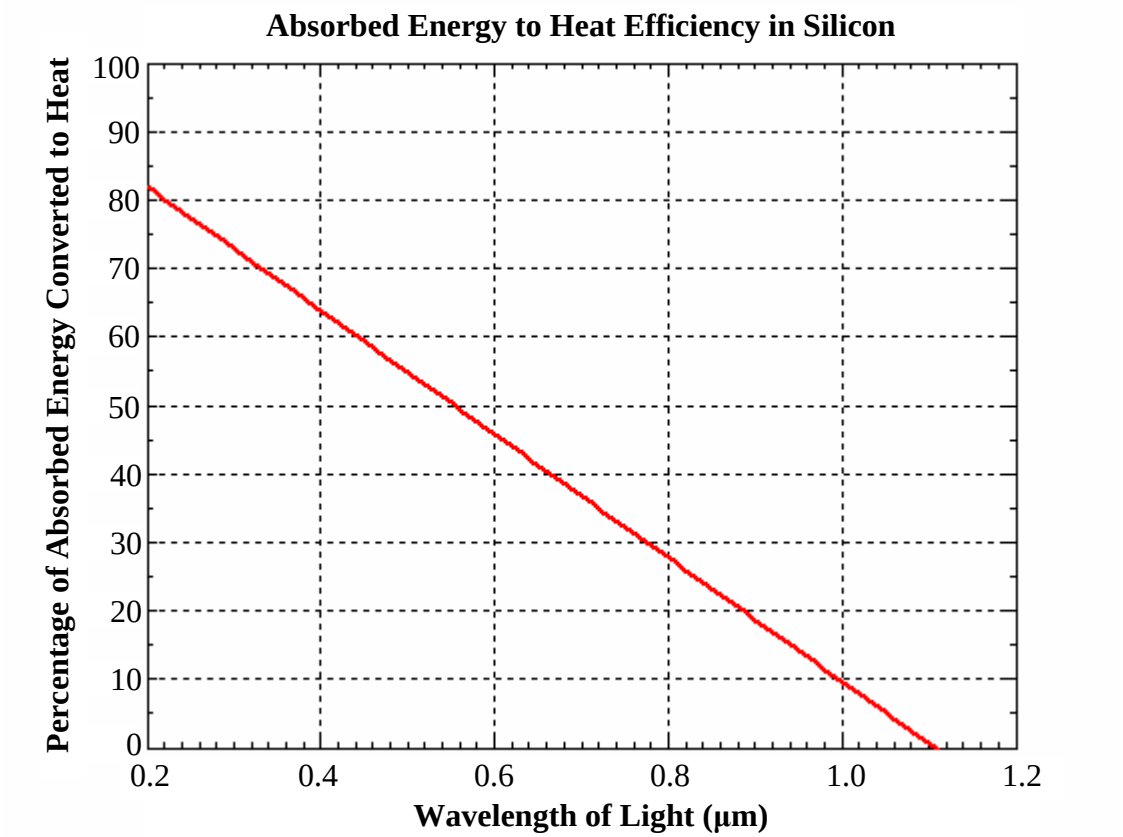


Figure 3.8: Graph showing the efficiency of converting absorbed energy into heat in silicon (E_g = 1.12 eV) for wavelengths from 0.2 to 1.2 μm. No heat is generated at the silicon cutoff wavelength (1.1 μm)—the energy which equals the bandgap of silicon. As the light energy increases, more heat is generated in the device.

Consistent with the silicon cutoff wavelength given in Figure 3.5, no heat is generated if the photon energy equals the bandgap. On the other hand, the heat energy is maximized by increasing the photon energy (decreasing the light wavelength), which is evident in Figure 3.8. In addition, this heat energy may be increased by choosing a semiconductor material with a lower bandgap.

3.5 Total Optical Power Efficiency

The preceding equations describing photon flux may be used interchangeable with optical power [14]. The final element in determing the amount of power that is converted to heat is the reflectivity of polysilicon. It has been experimentally determined that the reflectivity of polysilicon is proportional to both incidence angle and wavelength, as shown in Figure 3.9.

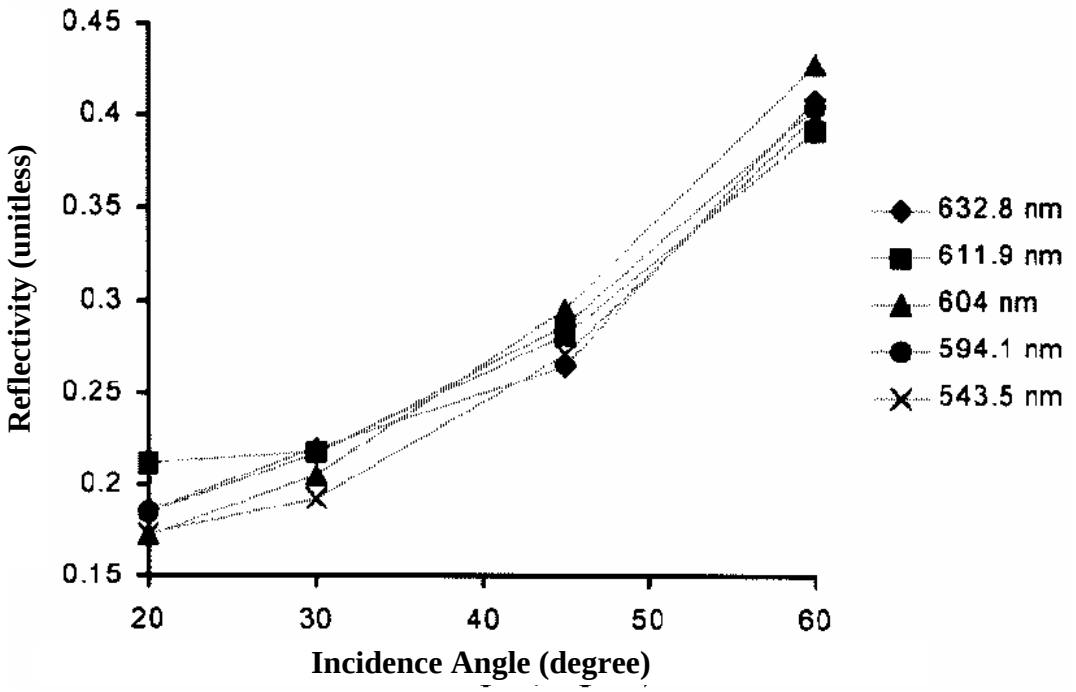


Figure 3.9: Graph of polysilicon reflectivity as a function of incidence angle for five different laser wavelengths. Reflectivity decreases proportionally with incidence angle and wavelength. Thus, a short-wavelength laser at normal incidence has the lowest reflectivity [17].

As evident from Figure 3.9, no data is available for a 660-nm laser at incidence angles smaller than 20 degrees. However, a safe estimate for R would be 0.2 because reflectivity theory shows a monotonic decrease towards 0 degrees for polysilicon [17].

The total optical efficiency can now be determined given the following parameters: R = 0.2 at 0 degrees for λ = 660 nm; t_0 = 3.5 μm; α = 8 x 10^3 cm^{-1} for polysilicon at given λ; and E_g = 1.12 eV for silicon. For a given incident laser power Φ_i, Table 3.3 shows the available power at each step in the heat-conversion process. The efficiency values from the "Remaining Available Power" column are written separately to illustrate the efficiency of each step. The total efficiency is the product of the efficiency values from each step. The MatLab® code is provided in Appendix B.1.

Table 3.3. Summary of the total power efficiency in the photon absorption process for phosphorus-doped polysilicon. R = 0.2, λ = 660 nm, t_0 = 3.5 μm, α = 8 x 10^3 cm^{-1}, and E_g = 1.12 eV for silicon.

Step in Process	Expression	Remaining Available Power	Total Efficiency
Incident Light	Φ_i	Φ_i	100%
Surface Reflection	$\Phi_0 = \Phi_i(1-R)$	(0.80) Φ_i	80.0%
Absorption	$\Phi(t_0) = \Phi_0\left[1-\exp(-\alpha t_0)\right]$	(0.939) (0.80) Φ_i	75.2%
Heat Conversion	$\Phi_{heat} = \Phi(t_0)\frac{\left[h\nu - E_g\right]}{h\nu}$	(0.404) (0.939) (0.80) Φ_i	30.4%

As shown in Table 3.3, only 30.4% of the energy from the incident light is converted to heat for a 660-nm laser in a 3.5-μm-thick layer of polysilicon. This efficiency is quite poor, especially since losses in focusing and directing the laser beam to surface are not included. On the other hand, the 20% reflection loss at the surface could actually be lower as the trend in Figure 3.9 suggests. In addition, the heat conversion

process does not account for the finite amount of heat that is generated in the non-radiative electron-hole recombination in silicon. These two factors would increase the amount of heat available for actuation.

It is obvious that the least efficient step in the absorption process is the final step, which is the actual conversion into heat: 40.4% for a 660-nm laser. A 400-nm laser would be 64% efficient at this heat-generation step. Including the improved absorption efficiency associated with a 440-nm laser ($\alpha = 2 \times 10^5$ cm^{-1}), the total efficiency for the entire process would be 51.1%, which is nearly double the total efficiency of the 660-nm laser. This would mean that a 400-nm laser at a low power could produce the same results as a 660-nm laser at a high power without even changing the robot design.

3.6 Chapter Summary

This chapter included the theory necessary to design, model, and test power-scavenging MEMS flying robots. Elements of heat transfer and thermal expansion are used in Chapter 4 to develop several thermal models of cantilevers and microrobot wings. The principles of optical absorption, reflection, and transmission are also critical in order to successfully design microrobots, which are described in Chapter 5. The experiment used to test the robots is optimized in Chapter 6 using elements of optics and optical engineering from Chapter 3. The success of this thesis, in large part, depends on the integration of all these elements.

3.7 References

[1] G. T. A. Kovacs, *Micromachined Transducers Sourcebook*, Boston: McGraw-Hill, 1998, pp. 550–559.

[2] Y. I. Cho, E. N. Ganic, J. P. Hartnett, and W. M. Rohsenow, "Basic Concepts of Heat Transfer," in *Handbook of Heat Transfer* (3rd Edition), Eds. W. M. Rohsenow, J. P. Hartnett, and Y. I. Cho. New York: McGraw-Hill, 1998.

[3] S. M. Sze, *Semiconductor Devices: Physics and Technology* (2nd Edition), New York: John Wiley and Sons, 2002, pp. 538.

[4] J. W. Gardner, V. K. Varadan, and O. O. Awadelkarim, *Microsensors MEMS and Smart Devices*, Chichester, England: John Wiley and Sons, 2001, Appendix G.

[5] D. J. Denninghoff, L. A. Starman, C. E. Perry, and P. E. Kladitis, "Autonomous Power-Scavenging MEMS Robots," *48th International IEEE Midwest Symposium on Circuits and Systems—MWSCAS 2005*, pp. 367–370, Cincinnati, OH, 7–10 Aug. 2005.

[6] D. Koester, A. Cowen, R. Mahadevan and B. Hardy, *PolyMUMPs Design Handbook: A MUMPs® Process* (Revision 10.0), MEMSCAP®. www.memscap.com/memsrus/docs/PolyMUMPs.dr.v10.pdf, 2003.

[7] K. D. Leedy. Senior Material Research Engineer, Multi-Chip Integration Branch, Aerospace Components and Subsystems Division, Sensors Directorate, Air Force Research Laboratory (AFRL/SNDI), Wright-Patterson AFB, OH. Personal Correspondence. 5 Jan. 2006.

[8] S. Baglio, S. Castorina, L. Fortuna, and N. Savalli, "Development of Autonomous, Mobile Micro-Electro-Mechanical Devices," *Proceedings of the 2002 IEEE International Symposium on Circuits and Systems—ISCAS 2002*, vol. 4, pp. 285–288, Phoenix-Scottsdale, AZ, 26–29 May 2002.

[9] S. Baglio, S. Castorina, L. Fortuna, and N. Savalli, "Technologies and Architectures for Autonomous 'MEMS' Microrobots," *Proceedings of the 2002 IEEE International Symposium on Circuits and Systems—ISCAS 2002*, vol. 2, pp. 584–587, Phoenix-Scottsdale, AZ, 26–29 May 2002.

[10] S. Baglio, S. Castorina, L. Fortuna, and N. Savalli, "Novel Microactuators Based on a Photo-Thermo-Mechanical Actuation Strategy," *Proceedings of the 1st IEEE Conference on Sensors*, vol. 1, pp. 192–197, Orlando, FL, 12–14 Jun. 2002.

[11] S. Baglio, S. Castorina, L. Fortuna, and N. Savalli, "Modeling and Design of Novel Photo-Thermo-Mechanical Microactuators," *Sensors and Actuators A: Physical*, vol. 101, pp. 185–193, 2002.

[12] F. R. Szabo and P. E. Kladitis, "Design, Modeling, and Testing of Polysilicon Optothermal Actuators for Power-Scavenging Wireless Microrobots," *Proceedings of the 2004 IEEE International Conference on MEMS, NANO, and Smart Systems—ICMENS `04*, pp. 446–452, Alberta, Canada, 25–27 Aug. 2004.

[13] F. R. Szabo, *Demonstrating Optothermal Actuators for an Autonomous MEMS Microrobot*, MS thesis, AFIT/GE/ENG/04-23. School of Engineering and Management, Air Force Institute of Technology (AU), Wright-Patterson AFB OH, March 2004 (AD-A426469).

[14] S. M. Sze, *Semiconductor Devices: Physics and Technology* (2nd Edition), New York: John Wiley and Sons, 2002, pp. 282–287.

[15] K. E. Petersen, "Silicon as a Mechanical Material," *Proceedings of the IEEE*, vol. 70, no. 5, pp. 420–457, May 1982.

[16] Y. Laghla and E. Scheid, "Optical Study of Undoped, B or P-Doped Polysilicon," *Thin Solid Films*, vol. 306, pp. 67–73, 1997.

[17] J. Zou, M. Balberg, C. Byrne, C. Liu, and D. Brady, "Optical Properties of Surface Micromachined Mirrors with Etch Holes," *Journal of Microelectromechanical Systems*, vol. 8, no. 4, p. 506–513, December 1999.

IV. Modeling and Simulations

4.1 Chapter Introduction

This chapter describes the process of modeling two aspects of novel flying MEMS robots: the initial deflection due to residual stress and downward deflection due to laser heating. The purpose of this modeling is three-fold: to accurately predict future device performance; to eliminate the "let's see if this works" approach to designing; and to optimize future designs for fabrication. The initial upward deflection of rectangular polysilicon-gold cantilevers is modeled through both analytical predictions and a finite element modeling package. The downward deflection from laser heating is also modeled. These serve as a baseline for comparison with the microrobot wings. The upward and downward deflection of a single robot wing is modeled in the CoventorWare® finite element modeling package and compared with the cantilevers.

4.2 MEMS Material Properties

An understanding of electromechanical structures can be obtained through a "building block" approach—the discipline is divided into parts, which are then assembled to form an understanding of the whole device [1]. Before modeling the deflection of MEMS beams, it is wise to begin with the first building block: relevant material properties. The values for MEMS material properties often vary from process to process, just as the acceleration of a car varies among different manufacturers. The values chosen are those commonly accepted in MEMS processes. Although MEMS is a technological field and is not defined by a single process, the scope of this section is limited to the materials used in the commercially available PolyMUMPs® fabrication process.

4.2.1 PolyMUMPs® Silicon, Polysilicon, Silicon Dioxide, and Gold Properties

PolyMUMPs® is a surface-micromachining process in which one non-releasable and two releasable layers of poly-crystalline silicon (polysilicon) are deposited and patterned on a single-crystalline silicon (SC silicon) wafer. Between the polysilicon layers are deposited sacrificial layers of phosphosilicate glass (PSG), or phosphorus-doped silicon dioxide. A gold thin-film layer may also be deposited over the top polysilicon layer. Table 4.1 (adapted from [2]) shows selected material properties of layers similar to those used in PolyMUMPs®. While most values in Table 4.1 were experimentally determined using materials from other processes, they are acceptable for modeling purposes. In addition, properties of silicon dioxide (SiO_2) are presented in the table due to the limited data on PolyMUMPs® phosphosilicate glass. Unless otherwise noted, these values are used for the calculations and modeling throughout this chapter.

Table 4.1. Material properties of single-crystalline silicon (SC silicon), poly-crystalline silicon (polysilicon), deposited silicon dioxide, and gold (adapted from [2]).

Material Property	SC Silicon	Polysilicon	Deposited SiO_2	Gold Film
Density $\{kg \cdot m^{-3}\}$	2328	2330	2200	19400
Thermal conductivity $\{W \cdot m^{-1} \cdot K^{-1}\}$	149	149	1.4	318
Thermal expansion $\{10^{-6} \cdot K^{-1}\}$	2.59	2.33	0.4	14.3
Specific heat capacity $\{J \cdot kg^{-1} \cdot K^{-1}\}$	678 [3]	678 [3]	730 [4]	129 [4]
Melting point {K}	1683 [4] (1410 °C)	---	2153 [4] (1880 °C)	1337 [4] (1064 °C)
Young's modulus {GPa}	190 (111) [5]	161 [6]	56.7 [7]	74 [8]
Poisson ratio	0.262 (111) [5]	0.23 [5]	0.20 [7]	0.44 [3]
Refractive index	3.8 (660 nm) [9]	3.65 (660 nm) [9]	1.46 [10]	---
Resistivity $\{\Omega \cdot cm\}$	1-2 [10]	7.2×10^{-3} ($n=1.36 \times 10^{20}$ cm^{-3}) [11]	---	2.2×10^{-6} [12]

4.2.2 Stress in PolyMUMPs® Polysilicon and Gold Layers

Stress exists in deposited thin-film layers due to material defects and temperature variations in the deposition process. Defects result when foreign atoms or particles are introduced into the native film and disrupt the regular molecular pattern [13]. Some foreign atoms, called dopants, are intentionally introduced into the material layer in order to alter certain layer characteristics. If this doping in uneven, it can cause residual stress in the layer, which regularly occurs in PolyMUMPs® polysilicon [6]. Stress is also introduced in the gold layer during temperature changes due to the high coefficient of thermal expansion in gold. The reported residual stress values for PolyMUMPs® poly2 and gold layers are given in Table 4.2 and Table 4.3, respectively. The data includes only the design runs used in this thesis: 66–69. The layer thickness and resistivity values are also given for later reference.

Table 4.2. Reported material properties for MUMPs® poly2 layer [14].

MUMPs® Run	66	67	68	69
Thickness {μm}	1.496	1.488	1.461	1.497
Resistivity {Ω-cm}	1.84×10^{-3}	3.25×10^{-3}	4.09×10^{-3}	3.13×10^{-3}
Residual Stress {MPa}	7.30 (C)	7.60 (C)	6.00 (C)	7.66 (C)

Table 4.3. Reported material properties for MUMPs® gold layer [14].

MUMPs® Run	66	67	68	69
Thickness {μm}	0.542	0.497	0.525	0.512
Resistivity {Ω-cm}	2.66×10^{-6}	2.88×10^{-6}	2.52×10^{-6}	2.81×10^{-6}
Residual Stress {MPa}	25.70 (T)	20.10 (T)	17.13 (T)	15.76 (T)

As shown in Table 4.2 and Table 4.3, the gold stress values are larger than those of poly2 and act in the opposite direction—gold is tensile and poly2 is compressive. Stress causes polysilicon-gold structures to bend, which is the basis for the microrobot wing designs. The amount of bending depends on layer dimensions, design shapes, and

material properties, which can be determined through simple modeling. The following section includes the derivation for predicting initial deflection in simple cantilevers. This leads to an understanding of how to optimize deflection in the microrobot wings.

4.3 Analytical Prediction of Initial Deflection in Cantilever Beams

The key to modeling is simplicity. Using this as a motivation, several gold-polysilicon cantilevers serve as a baseline, to which the robot deflections are compared. Figure 4.1: shows a captured image from a scanning electron microscope (SEM) of a series of gold-poly2 cantilevers. These cantilevers serve as the baseline for microrobot wing sections of comparable length. The free-body diagrams of a cantilever fabricated in PolyMUMPs® run 66 are illustrated in Figure 4.2; these diagrams serve as the model for the analytical predictions.

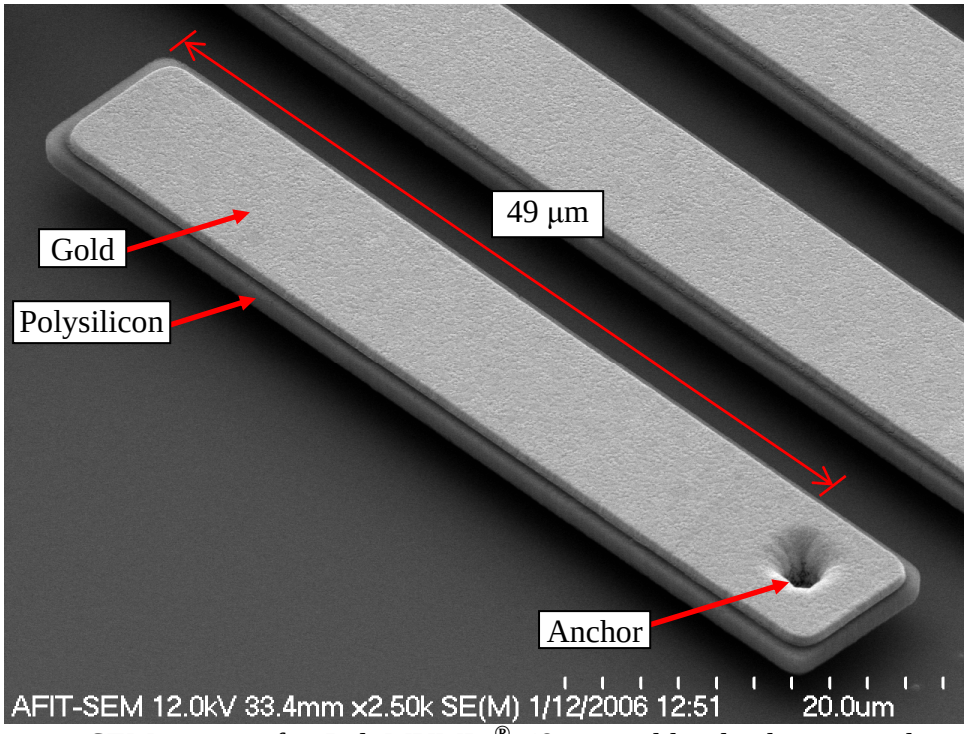


Figure 4.1: SEM image of a PolyMUMPs® 49-µm gold-polysilicon cantilever beam. The beam is measured from the anchor to the tip of the beam since that is the only portion that is free to deflect. Cantilevers of various lengths serve as the baseline for robot wing sections of comparable length.

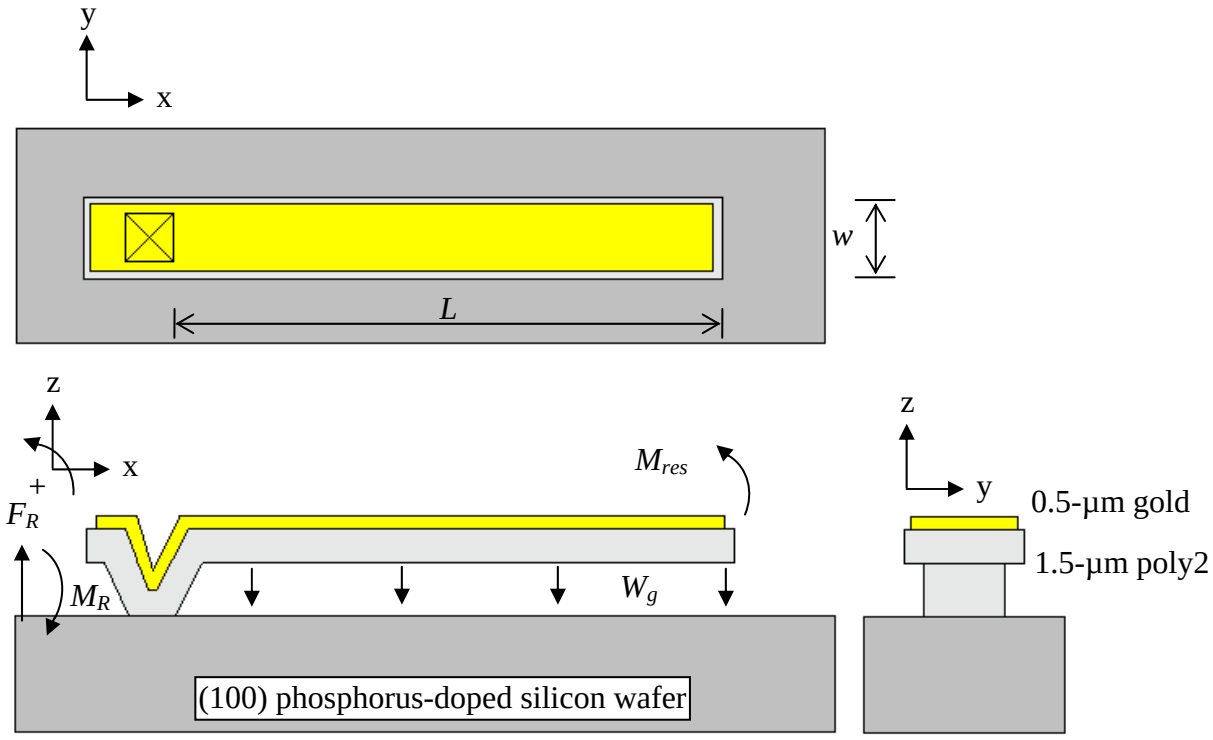


Figure 4.2: Free-body diagrams of a gold-poly2 cantilever. L represents the portion of the cantilever that is free to deflect and is measured from the anchor to the tip of the cantilever; w is the width of the beam; M_{res} is the moment due to residual stress; W_g is the weight per length due to gravity; F_R is the restoring force; and M_R is the restoring or reaction moment.

The axes in the free-body diagrams of Figure 4.2 show a positive sign convention for the forces and moments. The following assumptions are made to simplify the model:

- The only applied force is the weight of the beam due to gravity, and it will be assumed to be negligible throughout the derivations and calculations.
- The force due to residual stress can be modeled as a single moment.
- The dominant internal stress is the residual stress in gold and poly2.
- The cantilever is in equilibrium.

The first assumption—weight is negligible—is validated at the end of the derivations. It is shown that the weight of small MEMS structures, in general, may be neglected.

4.3.1 Derivation of Initial Deflection Equations

There are two sources of stress in MEMS devices that contribute to a post-fabrication vertical deflection—internal residual stress of a layer and thermal expansion differences between two layers. The deflection from each component may be described with simple equations, which are derived in this section. These equations determine the extent each source of stress exhibits on bending. An expression for the initial deflection due to residual stress may be derived starting with the equilibrium condition—the sum of forces and moments is equal to zero. This leads to an expression for the restoring force F_R {N} and the moment due to residual stress M_{res} {N·m} (illustrated in Figure 4.2):

$$\sum F = 0 \tag{4.1}$$

$$F_R = W_g L\,. \tag{4.2}$$

Thus, the restoring force is equal to the product of the weight per length due to gravity and the length of the beam. It is assumed that the restoring force is zero since the weight per length W_g {N/m} is assumed to be negligible for such thin layers. For larger structures, however, the weight is not negligible and its expression should be derived.

The weight of the beam per length W_g is equal to the product of the mass of the beam per length m {kg/m} and the acceleration due to gravity a {m/s^2}:

$$W_g = ma\,. \tag{4.3}$$

The weight of the entire beam is the product of Equation 4.3 and the length. The mass per length of each layer is equal to the product of the density of each layer D {kg/m^3}, the width w {m}, and the thickness t {m}:

$$m_{layer} = D_{layer} w_{layer} t_{layer}\,. \tag{4.4}$$

The restoring moment is derived from, again, the equilibrium condition. The three moments acting on the beam are the moment due to gravity M_g, the moment due to residual stress M_{res}, and the restoring moment M_R {all units in N·m}:

$$\sum M = 0 \tag{4.5}$$

$$M_R = M_{res} - M_g \tag{4.6}$$

$$M_R = M_{res} - \frac{W_g L^2}{2}. \tag{4.7}$$

M_g (given in [15]) goes to zero since W_g is assumed to be negligible. Thus, the restoring moment is equal to the moment due to residual stress:

$$M_R = M_{res}. \tag{4.8}$$

The expression for the moment due to residual stress M_{res} as a function of distance along the beam, x, is derived from the general equation for the stress due to bending:

$$\sigma = -\frac{Mz}{I_y}, \tag{4.9}$$

where σ, z, and I_y, are: normal stress {N/m^2 or Pa}, vertical deflection {m}, and moment of inertia about the y-axis—the axis about which the beam deflects. The moment of inertia I_y {m^4} is defined by width and thickness of the beam ($I_y = \frac{wt^3}{12}$) but will remain a variable throughout the derivation. A simple algebraic manipulation yields the moment due to residual stress:

$$M_{res} = -\frac{\sigma_{res} I_y}{z}, \tag{4.10}$$

where $M_{res} > 0$ when $\sigma < 0$ (compressive stress) and $M_{res} < 0$ when $\sigma > 0$ (tensile stress). Equation 4.10 is useful only when the residual stress and deflection are already known.

Therefore, it is a characterizing expression instead of a predicting expression. Nonetheless, it completes the expressions for the free body diagrams in Figure 4.2.

Expressions that are useful in predicting vertical deflection z and angular deflection θ may be derived from the single-layer beam-bending equations with an existing moment:

$$\frac{d^2z}{dx^2} = \frac{M_{res}}{EI_y} \quad \text{or} \quad \frac{d^2z}{dx^2} = \frac{1}{R}, \tag{4.11}$$

where R {m} is the radius of curvature of the beam, E {N/m^2 or Pa} is the Young's modulus value of the material, and I_y {m^4} is the moment of inertia about the y-axis. The duality of the beam-bending equation makes it possible to derive deflection expressions in terms of M_{res}, E, and I, or in terms of R. The former is used in the derivation. Integrating the beam-bending expression yields:

$$\int \frac{d^2z}{dx^2} = \int \frac{M_{res}}{EI_y} \tag{4.12}$$

$$\frac{dz}{dx} = \frac{M_{res}}{EI_y}x + C_1. \tag{4.13}$$

At the fixed end of the beam (x = 0), the slope of the beam is zero, which yields an expression for angular deflection:

$$\frac{dz}{dx} = 0 \text{ at } x = 0 \quad \therefore \quad C_1 = 0 \tag{4.14}$$

$$\theta = \frac{dz}{dx} = \frac{M_{res}}{EI_y}x. \tag{4.15}$$

The expression for vertical deflection as a function of position x along the beam is found by integrating the preceding expression and applying the appropriate boundary condition—zero deflection at the fixed end:

$$\int \frac{dz}{dx} = \int \frac{M_{res}}{EI_y} x \tag{4.16}$$

$$z = \frac{M_{res}}{2EI_y} x^2 + C_2 \tag{4.17}$$

$$z = 0 \text{ at } x = 0 \quad \therefore \quad C_2 = 0 \tag{4.18}$$

$$z = \frac{M_{res} x^2}{2EI_y}. \tag{4.19}$$

Substituting the length of the beam L into the expression yields the vertical deflection at the tip of the beam:

$$z = \left. \frac{M_{res} L^2}{2EI_y} \right|_{x=L} \tag{4.20}$$

The deflection expression may also be written in terms of radius of curvature:

$$z = \frac{x^2}{2R} = \left. \frac{L^2}{2R} \right|_{x=L}. \tag{4.21}$$

These expressions are in terms of the moment due to residual stress and the radius of curvature, both of which may be unknown. On the other hand, the values for residual stress are measured and reported for each MUMPs® fabrication run, which makes deflection in terms of stress more useful. An expression for residual stress may be derived from Stoney's equation:

$$\sigma_{res} = \frac{E'_{poly} t^2_{poly}}{6 t_{gold} R}, \tag{4.22}$$

where σ_{res} {N/m^2 or Pa} is the residual stress due to fabrication effects; t_{poly} and t_{gold} {m} are the thicknesses of polysilicon and gold, respectively; R {m} is the radius of curvature;

and E'_{poly} {N/m^2 or Pa} is the biaxial modulus for polysilicon, which is derived from Young's modulus (E_{poly}) and Poisson's ratio for polysilicon (υ_{poly}) {unitless}:

$$E'_{poly} = \frac{E_{poly}}{1-\upsilon_{poly}}. \tag{4.23}$$

It is necessary to interrupt the deflection derivation to note that the residual stress term σ_{res} is comprised of two components: the internal stress of polysilicon, σ_{poly}; and the thermal stress between gold and polysilicon, σ_{therm}; {all units in N/m^2 or Pa}. The internal stress of polysilicon is primarily due to the doping gradient existing in PolyMUMPs® polysilicon [6], which is reported for each MUMPs® fabrication run. The thermal stress is due to the fact that gold and polysilicon have different coefficients of thermal expansion and the gold is evaporated at a higher temperature than room temperature [16]. The derivation for the thermal stress follows from the expansion due to changing temperatures:

$$L = L_0 + L_0 \alpha_{gold} \Delta T\,, \tag{4.24}$$

where L {m} is the expanded length of a gold beam, L_0 {m} is the original length of the gold beam, α_{gold} {K^{-1}} is the coefficient of thermal expansion of gold, and the change in temperature ΔT {K} is given by:

$$\Delta T = T - T_{fab}\,, \tag{4.25}$$

where T is the room or lab temperature and T_{fab} is the fabrication temperature at which gold film was evaporated. Equation 4.24 is rewritten in terms of strain, ε_{gold} {unitless}:

$$\varepsilon_{gold} = \frac{L - L_0}{L_0} = \alpha_{gold} \Delta T\,. \tag{4.26}$$

Assuming the polysilicon beam, on which the gold film is deposited, may also expand or contract to reduce the strain in the gold, the total strain in the gold film is given by:

$$\varepsilon_{total} = \alpha_{gold}\Delta T - \alpha_{poly}\Delta T = \left(\alpha_{gold} - \alpha_{poly}\right)\Delta T \,. \tag{4.27}$$

According to Hooke's Law, stress is equal to the product of strain and the biaxial modulus for gold (similar to Equation 4.23). An expression for the stress in the film is:

$$\sigma_{gold} = E'_{gold}\varepsilon_{gold} = E'_{gold}\left(\alpha_{gold} - \alpha_{poly}\right)\Delta T \,. \tag{4.28}$$

Assuming that the thermal stress between gold and polysilicon σ_{therm} is equal to the maximum stress that occurs in the top surface of the polysilicon beam, the stress is given by simply changing the sign of Equation 4.28:

$$\sigma_{therm} = -\sigma_{gold} = E'_{gold}\left(\alpha_{poly} - \alpha_{gold}\right)\Delta T \,. \tag{4.29}$$

The total residual stress—the goal of this intermediate derivation—is given by

$$\sigma_{res} = \sigma_{poly} + \sigma_{therm} = \sigma_{poly} + E'_{gold}\left(\alpha_{poly} - \alpha_{gold}\right)\Delta T \,. \tag{4.30}$$

Equation 4.30 will not be substituted in the vertical deflection expression to keep the expression simple.

The vertical deflection derivation resumes from Equation 4.22. By first solving Stoney's equation for 1/*R* and the vertical deflection expression for 1/*R*, the following two expressions can be equated:

$$\frac{6t_{gold}\sigma_{res}}{E'_{poly}t^2_{poly}} = \frac{1}{R} \tag{4.31}$$

$$\frac{2z}{x^2} = \frac{1}{R} \,. \tag{4.32}$$

Solving for *z* yields a vertical deflection expression in terms of a known stress as a function of position *x* along the beam:

$$z = \frac{3t_{gold}\sigma_{res}}{E'_{poly}t^2_{poly}}x^2 \,. \tag{4.33}$$

The deflection z {m} at the tip of the beam of a given length L is:

$$z = \left. \frac{3 t_{gold} \sigma_{res} L^2}{E'_{poly} t^2_{poly}} \right|_{x=L}, \tag{4.34}$$

where σ_{res} is given by Equation 4.30. Taking the derivative of this expression yields the angular displacement θ {rad}:

$$\theta = \frac{dz}{dx} = \frac{6 t_{gold} \sigma_{res}}{E'_{poly} t^2_{poly}} x. \tag{4.35}$$

Equations 4.34 and 4.35 are the final deflection expressions for this derivation. They are a function of residual stress for two reasons: residual stress for each PolyMUMPs® run is reported by the foundry; and residual stress can be measured in a laboratory using test structures, such as comb resonators and fixed beams [6].

4.3.2 Calculating Initial Deflection

With these final expressions, the calculations are straight forward. The following table includes all values used in the calculations. The material properties match those of Table 4.1; the MUMPs® values are those from run 66 given in Table 4.2 and Table 4.3.

Table 4.4. Parameters and values used in calculations for gold and poly2.

Parameter	Poly2	Gold
Density {kg/m^3}	2330	19400
Thickness {μm}	1.496 [MUMPs® 66]	0.5421 [MUMPs® 66]
Width {μm}	10	8
Length {μm}	49, 99, 149, 199, 249	48, 98, 148, 198, 248
Poisson's Ratio	0.23	0.44
Young's Modulus {GPa}	161	74
Residual Stress {MPa}	-7.3 (C) [MUMPs® 66]	25.7 (T) [MUMPs® 66]
Coefficient of Thermal Expansion {K^{-1}}	2.33x10^{-6}	14.3 x10^{-6}

First, it is important to validate the assumption that the force due to gravity, or weight of the beam, may be neglected for small MEMS structures. The following calculations of a 249-μm beam illustrate this point.

$$\text{Mass}_{\text{gold}} \text{ per length} = D_{gold} w_{gold} t_{gold}$$
$$= \left(19400 \frac{\text{kg}}{\text{m}^3}\right)\left(8\text{x}10^{-6}\text{m}\right)\left(0.5421\text{x}10^{-6}\text{m}\right) \quad (4.4)$$
$$= 82.3\text{x}10^{-9} \frac{\text{kg}}{\text{m}}$$

$$\text{Weight}_{\text{gold}} \text{ per length} = ma$$
$$= \left(82.3\text{x}10^{-9} \frac{\text{kg}}{\text{m}}\right)\left(9.8 \frac{\text{m}}{\text{s}^2}\right) \quad (4.3)$$
$$= 806\text{x}10^{-9} \frac{\text{N}}{\text{m}}$$

$$\text{Mass}_{\text{poly}} \text{ per length} = D_{poly} w_{poly} t_{poly}$$
$$= \left(2330 \frac{\text{kg}}{\text{m}^3}\right)\left(10\text{x}10^{-6}\text{m}\right)\left(1.496\text{x}10^{-6}\text{m}\right) \quad (4.4)$$
$$= 34.9\text{x}10^{-9} \frac{\text{kg}}{\text{m}}$$

$$\text{Weight}_{\text{poly}} \text{ per length} = ma$$
$$= \left(34.9\text{x}10^{-9} \frac{\text{kg}}{\text{m}}\right)\left(9.8 \frac{\text{m}}{\text{s}^2}\right) \quad (4.3)$$
$$= 341.6\text{x}10^{-9} \frac{\text{N}}{\text{m}}$$

$$\text{Weight of the beam} = W_{gold} L_{gold} + W_{poly} L_{poly}$$
$$= \left(806\text{x}10^{-9} \frac{\text{N}}{\text{m}}\right)\left(248\text{x}10^{-6}\text{m}\right) + \left(342x10^{-9} \frac{\text{N}}{\text{m}}\right)\left(249\text{x}10^{-6}\text{m}\right)$$
$$= \boxed{285\text{x}10^{-12}\text{N}}$$

The calculation result shows that the weight of a 249-μm beam—285 pN—is a negligible contribution and will not be considered in further calculations.

Now the thermal component of residual stress may be calculated (the internal stress component for polysilicon is already given in Table 4.4). This calculation requires information about the gold evaporation temperature—typically about 60° C or 333 K [16]. The room temperature value used is 27° C or 300 K.

$$\begin{aligned}\sigma_{therm} &= E'_{gold}\left(\alpha_{poly}-\alpha_{gold}\right)\Delta T \\ &= \frac{74}{1-0.44}\text{x}10^{9}\,\frac{\text{N}}{\text{m}^2}\left(2.33\text{x}10^{-6}\text{K}^{-1}-14.3\text{x}10^{-6}\text{K}^{-1}\right)\left(300\text{K}-333\text{K}\right) \\ &= 52.2\text{x}10^{6}\,\frac{\text{N}}{\text{m}^2}\ (\text{T})\end{aligned} \tag{4.29}$$

The total residual stress due to fabrication effects, then, is:

$$\begin{aligned}\sigma_{res} &= \sigma_{poly}+\sigma_{therm} \\ &= -7.3\text{x}10^{6}\,\frac{\text{N}}{\text{m}^2}+52.2\text{x}10^{6}\,\frac{\text{N}}{\text{m}^2} \\ &= 44.9\text{x}10^{6}\,\frac{\text{N}}{\text{m}^2}\end{aligned} \tag{4.30}$$

Finally, the deflection due to residual stress in a 49-μm beam is calculated.

$$\begin{aligned}z &= \left.\frac{3t_{gold}\sigma_{res}L^2}{E'_p t^2_{poly}}\right|_{x=L} \\ &= \frac{3\left(0.5421\text{x}10^{-6}\text{m}\right)\left(44.9\text{x}10^{6}\,\frac{\text{N}}{\text{m}^2}\right)\left(49\text{x}10^{-6}\text{m}\right)^2}{\left(\frac{161}{1-0.23}\text{x}10^{9}\,\frac{\text{N}}{\text{m}^2}\right)\left(1.496\text{x}10^{-6}\text{m}\right)^2} \\ &= \boxed{0.375\text{x}10^{-6}\text{m}}\end{aligned} \tag{4.34}$$

$$\begin{aligned}\theta &= \frac{dz}{dx} = \frac{6t_{gold}\sigma_{res}}{E'_p t^2_{poly}}\,x \\ &= \frac{6\left(0.5421\text{x}10^{-6}\text{m}\right)\left(44.9\text{x}10^{6}\,\frac{\text{N}}{\text{m}^2}\right)}{\left(\frac{161}{(1-0.23)}\text{x}10^{9}\,\frac{\text{N}}{\text{m}^2}\right)\left(1.496\text{x}10^{-6}\text{m}\right)^2}\left(49\text{x}10^{-6}\text{m}\right) \\ &= \boxed{0.015\text{ rad}} \\ &= \boxed{0.876\text{ deg}}\end{aligned} \tag{4.35}$$

These calculations were put into a MatLab® m-file to observe the results of changing certain input values; the code is included in Appendix B.2. The results for several lengths are in Table 4.5 (deflection is emboldened for easier reference later).

Table 4.5. Analytical calculations of deflection for various gold-poly2 beam lengths.

Beam {μm}	Deflection {μm}	Angle {degrees}
49	**0.375**	0.876
99	**1.529**	1.770
149	**3.464**	2.664
199	**6.179**	3.558
249	**9.674**	4.452

The results from this simple model serve as a reliable baseline. This modeling technique is not suitable for irregularly shaped structures, however, such as microrobot wings. These are analyzed in a finite element modeling (FEM) software package. Nonetheless, the results from the simple cantilever model can be used to verify the accuracy of the FEM results.

4.4 CoventorWare® Finite Element Simulations of Cantilever Beams

There are two main objectives in finite element modeling: to predict initial deflection due to residual stress, and to predict downward deflection due to heating. Several structures are modeled, starting with the same rectangular cantilevers analyzed in the previous section. The finite element software package used in these simulations is CoventorWare®, a program tailored for MEMS device analysis [17]. In order to ascertain the accuracy of the Coventor® FEM results, a set of control structures is necessary. The modeled deflection results from the previous section, as well as the measured deflection results from gold-poly2 cantilevers fabricated in MUMPs® 66 (see Figure 4.1), serve this

purpose. Validating the FEM deflection values of simple cantilevers ensures that FEM deflection results in microrobot wings may also be trusted. The following sections describe the general steps in the FEM process.

4.4.1 Mesh Efficiency Study using Cantilever Beams

To optimize the simulation efficiency, a mesh efficiency study was conducted, which compared the accuracy of the simulation results of different mesh sizes. The Manhattan brick mesh is an ideal choice because the cantilevers are rectangular. First, meshes with a 10-μm width and a 0.75-μm thickness but varying lengths were compared to each other: small-sized (10 x 0.75 x 5 μm^3), medium-sized (10 x 0.75 x 10 μm^3), and large-sized (10 x 0.75 x 50 μm^3). It was found that there was only a 1.7% difference in deflection results between the largest mesh and the smallest mesh, yet the simulation time in the largest-sized mesh was significantly shorter. Additionally, 0.5-μm and 0.75-μm mesh thickness sizes were compared, yielding only a 0.036% difference. Thus, the larger-sized elements shown in Figure 4.3 were chosen to reduce simulation time.

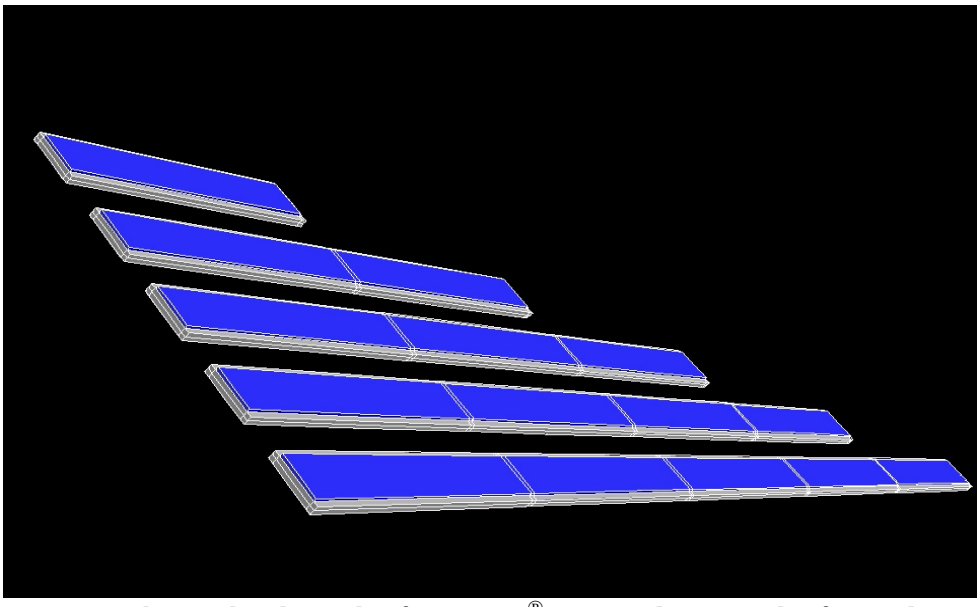


Figure 4.3: Manhattan brick mesh of MUMPs® 66 cantilevers. The finite element sizes are 10 x 0.75 x 50 μm^3, which yield accurate results with minimal simulation time expended.

4.4.2 Calibrating CoventorWare® using Cantilever Beams

Next, the material parameters from Table 4.4 were input into Coventor®, and a simple MemMech mechanical simulation was used to measure the vertical deflection. The only boundary condition was fixing one end of the cantilever, thus allowing the remainder of the cantilever to flex upwards. These preliminary results were nearly three orders of magnitude smaller than what was predicted. It appeared that Coventor® needed to be calibrated to MUMPs® run 66. By default in Coventor®, residual stress acts isotropically, yet the primary stress in MUMPs® is only in the x- and y-directions. Even with this change, the preliminary Coventor® deflection results were much lower than expected, warranting further calibration.

The next step in calibrating Coventor® was precisely measuring the five cantilevers fabricated, which was accomplished with a Zygo® interferometric microscope (IFM). Several measurements were made because stress varies from one wafer to the next, as well as from one die location to the next. Figure 4.4 illustrates the Zygo® IFM data of beams fabricated in MUMPs® run 66. Table 4.6 includes the measurements from four samples of these cantilever beams.

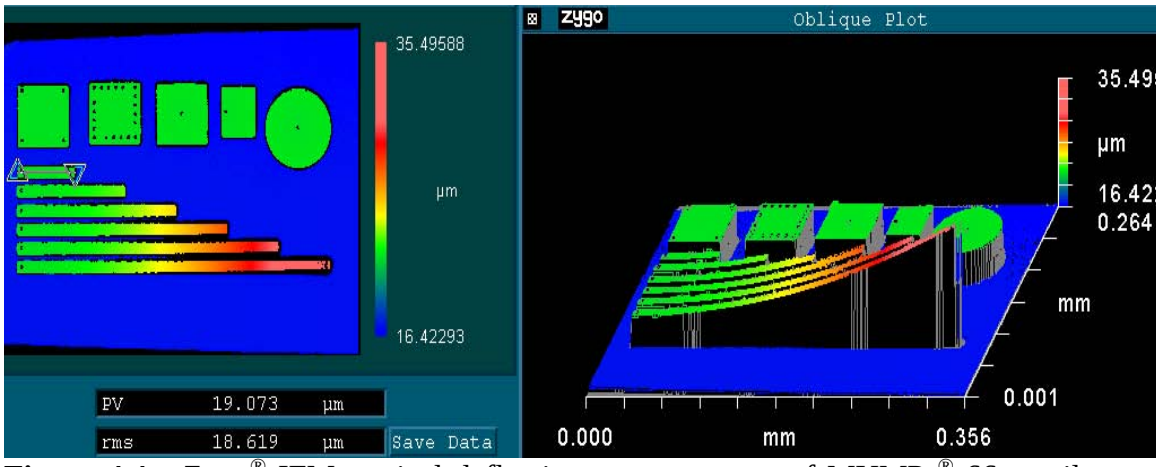


Figure 4.4: Zygo® IFM vertical deflection measurements of MUMPs® 66 cantilevers. The beams with lengths from 49 to 249 µm were measured; the longest beam exhibits the most deflection.

Table 4.6. Actual experimental deflection measurements of four samples of MUMPs® 66 cantilevers {all units in μm}. Beam lengths range from 49 to 249 μm. The average deflections are emboldened and color-coded for easy reference in later comparisons.

Beam	Sample A	Sample B	Sample C	Sample D	Average Deflection
49	0.3483	0.3730	0.3777	0.3423	**0.360**
99	1.4739	1.5091	1.5285	1.5322	**1.511**
149	3.3074	3.3487	3.8563	3.7924	**3.576**
199	5.9026	5.9316	6.6786	6.5514	**6.266**
249	9.0995	9.1729	10.298	10.101	**9.668**

Through an iterative process in which the residual stress values were varied, Coventor® eventually yielded results that matched the measurements. Stress and Young's modulus were the main contributing variables. Although Young's modulus for polysilicon varies widely among foundry processes, it was assumed to be 161 GPa (Table 4.1) [6]. Therefore, stress was the chosen parameter to vary. A comparison between the stress values reported in MUMPs® and the final calibrated values is given in Table 4.7.

Table 4.7. Comparison between preliminary MUMPs® 66 values and calibrated stress values used in Coventor®; also included are the directions in which the stress acts.

Material Layer	Poly 2		Gold	
Value Type	Preliminary	Calibrated	Preliminary	Calibrated
Residual Stress {MPa}	-7.3 (C)	-12 (C)	25.7 (T)	58 (T)
Stress Direction	σ_x, σ_y, σ_z	σ_x, σ_y	σ_x, σ_y, σ_z	σ_x, σ_y

The calibrated value of stress in gold is much greater than the preliminary value, yet the poly2 value is only slightly larger. The stress caused by uneven thermal expansion is not accounted for in Coventor® because the deposition temperatures are neglected. The high stress value in gold compensates for this. In addition, both the gold and poly2 are set to act in only the x- and y-directions, which is consistent with the

MUMPs® fabrication process. The simulation results using the calibrated values are illustrated in Figure 4.5, showing an 8.999-µm deflection in the 249-µm beam.

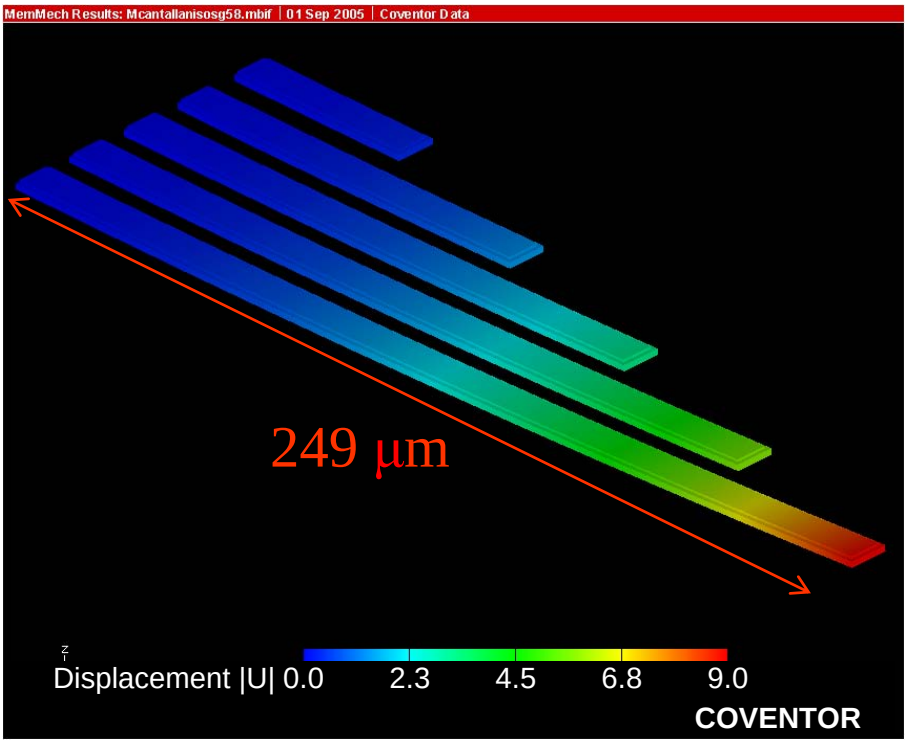


Figure 4.5: MemMech simulation results of cantilevers with calibrated stress values. Highlighted is the 249-µm beam with a vertical deflection of 8.999 µm.

4.4.3 Comparison of Cantilever Beam Deflection Values

The FEM simulation results for each beam length are given in Table 4.8. Also included are the color-coded results from the analytical predictions and experimental measurement averages. The results from the two modeling methods are compared with the experimental measurements to illustrate the accuracy of each method.

Table 4.8. Analytical, experimental, and simulated cantilever initial deflection results.

Beam Length {µm}	Analytical Predictions {µm}	Experimental Measurements {µm}	Simulated Results {µm}	**Experimental-Analytical** Difference	**Experimental-Simulated** Difference
49	**0.375**	**0.360**	**0.354**	4.07%	-1.70%
99	**1.529**	**1.511**	**1.437**	1.20%	-4.91%
149	**3.464**	**3.576**	**3.239**	-3.14%	-9.42%
199	**6.179**	**6.266**	**5.760**	1.39%	-8.08%
249	**9.674**	**9.668**	**8.999**	0.06%	-6.92%

The cantilever analytical prediction results (grey), the average experimental measurements (blue), and the Coventor® FEM simulated deflection results (green) are graphed in Figure 4.6. This graph illustrates that the analytical predictions are closer to the actual experimental deflection values than are the Coventor® results. Throughout the previously mentioned iterative process of adjusting stress values in Coventor®, these deflection values were the closest obtainable. Thus, there is a certain degree of inaccuracy in Coventor® that must be considered in the robot wing modeling.

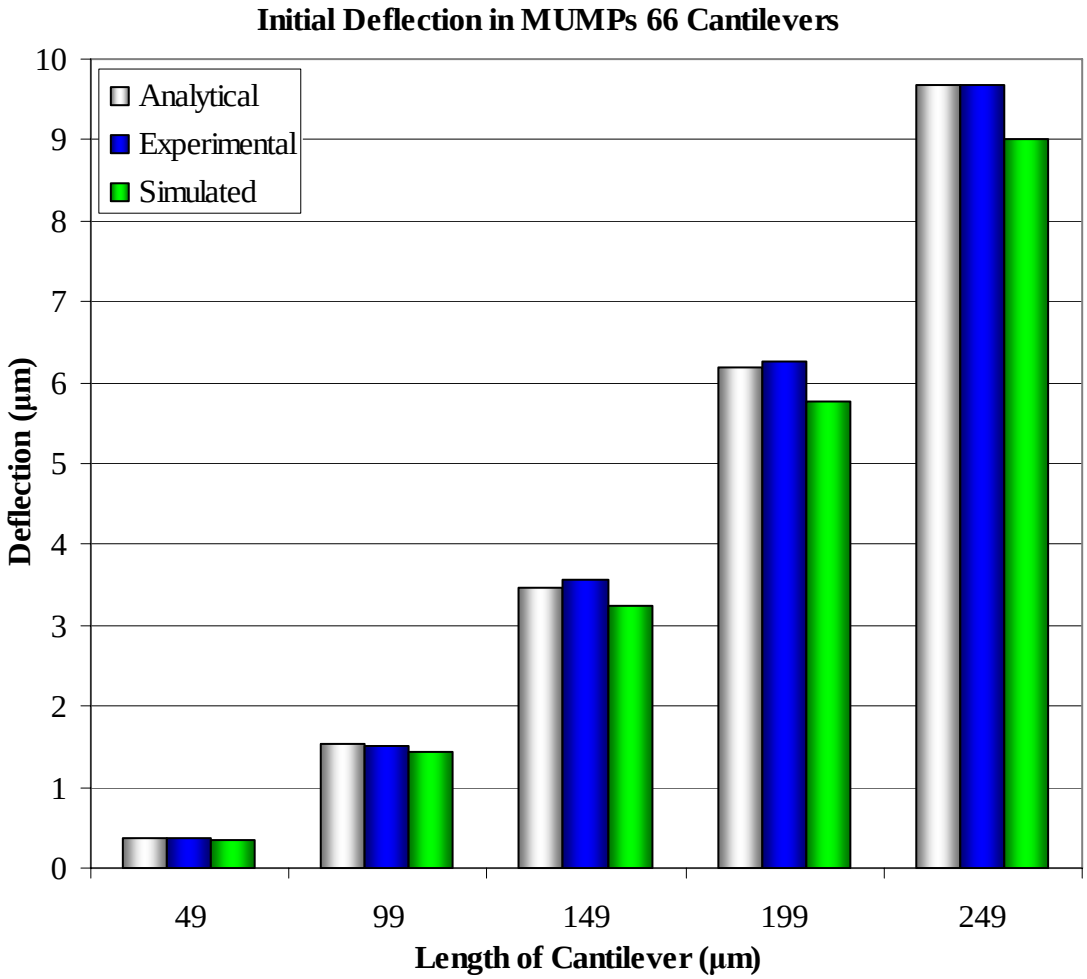


Figure 4.6: Graphed results from Table 4.8, illustrating the comparison among analytical, experimental, and simulated cantilever initial deflection results. The analytical approach, in general, is more similar to the actual measured results than the simulated results.

4.5 CoventorWare® Finite Element Simulations of Microrobot Wings

Relatively accurate simulation results of cantilever beams make it possible to determine the accuracy of modeled microrobot wings. The CoventorWare® software package is ideal for simulating irregularly shaped structures, such as microrobot wings. Using Coventor®, any microrobot wing can be modeled to predict the future performance of that wing. Among the many possible designs, a simple gold-poly2 wing with varying flexure widths is a good one to start with. Figure 4.7 illustrates a mask layout of a microrobot wing chosen for the simulation. While the details of the design are given in the next chapter, the basic components include: a light-absorbing, non-deflecting poly2 center; varying widths of expanding, deflecting gold-poly2 flexures; minimum-width gaps between the flexures; and an outer gold-poly2 rim to increase surface area. The radius of the poly2 center is 40 μm, and the wing length is 210 μm. An entire microrobot could consist of any number of these wings—a minimum of two and a maximum of eight.

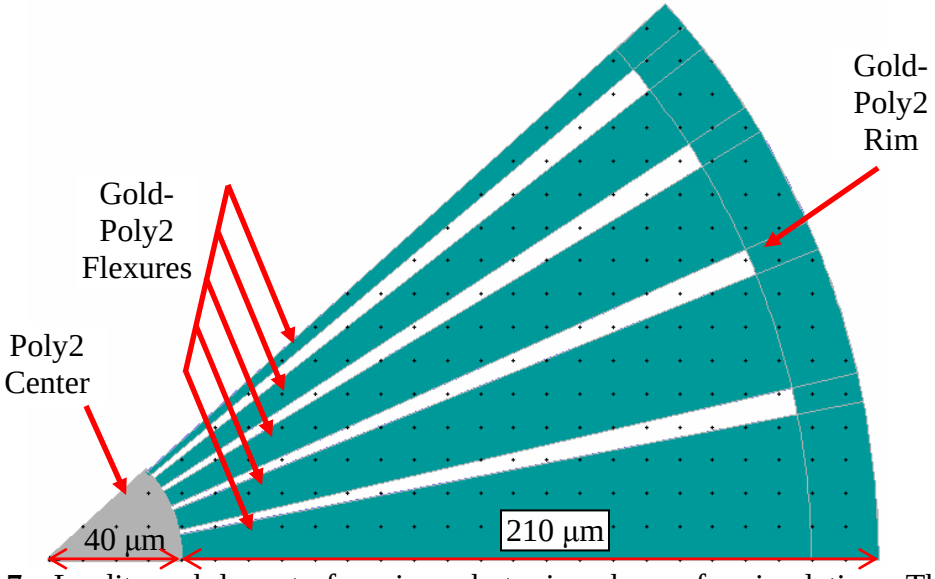


Figure 4.7: L-edit mask layout of a microrobot wing chosen for simulation. The gold-poly2 flexures are based on the cantilevers previously modeled. The 40-μm-radius poly2 center is not included in the FEM deflection simulations because it does not contribute to bending. The sections included in the model are the 210-μm-long gold-poly2 flexures and rim.

4.5.1 Microrobot Wing Model 1: The Separated Wing

It is always best to begin any simulation with a simplified model. Only the movable, expandable flexures are included in the first simplified model, which is called the "separated wing." This simplified model is illustrated in Figure 4.8, showing the extruded brick mesh. The maximum mesh size is 30 x 30 x 0.75 μm^3. These wing sections resemble the cantilevers modeled previously, as they are not attached to adjacent flexures. The MemMech deflection results are illustrated in Figure 4.9.

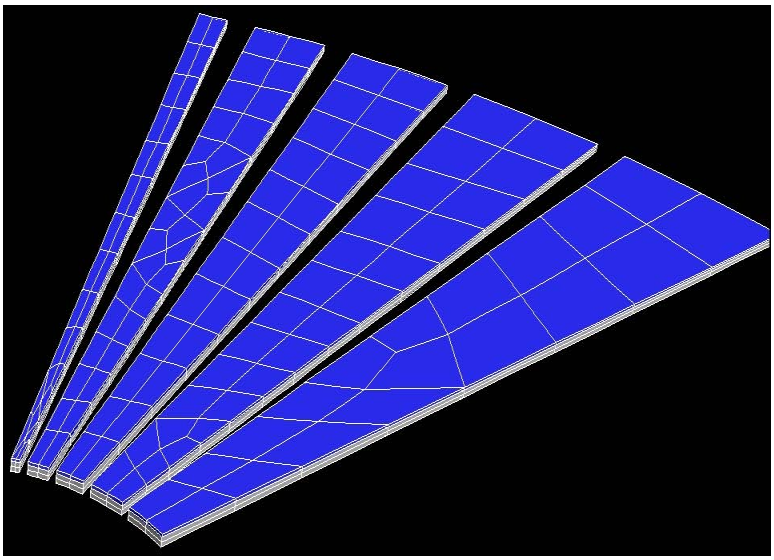


Figure 4.8: 3-D image of a 210-µm separated wing model with the extruded brick mesh.

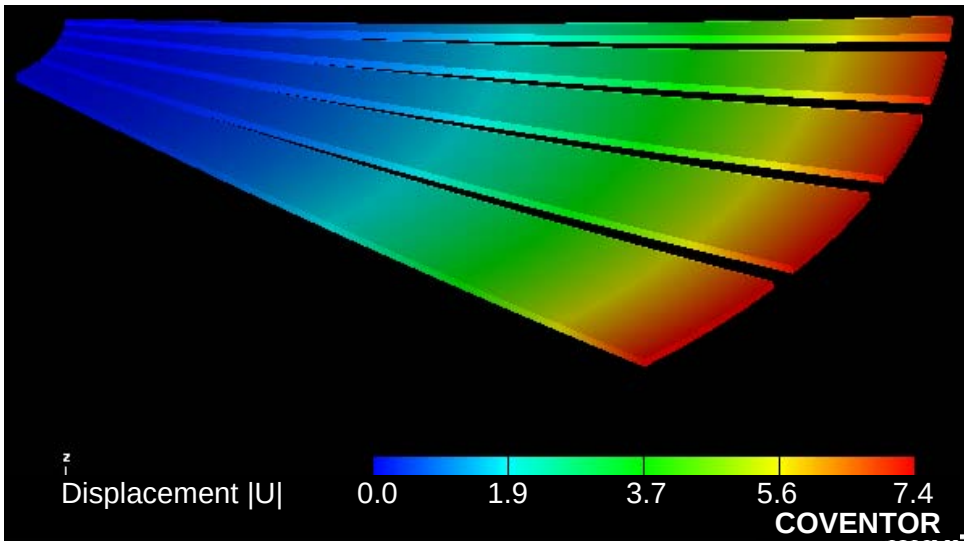


Figure 4.9: MemMech simulation results of a 210-µm separated wing showing a 7.4-µm tip deflection on all flexure widths.

4.5.2 Microrobot Wing Model 2: The Connected Wing

The second wing modeled was the connected wing version (illustrated in Figure 4.10). The included rim connects the flexures at the tip of the wing. A tetrahedral mesh fits this design best, with 30 x 30-μm^2 maximum lateral dimensions. The deflection measurements are identical to those of the separated wing (illustrated in Figure 4.11).

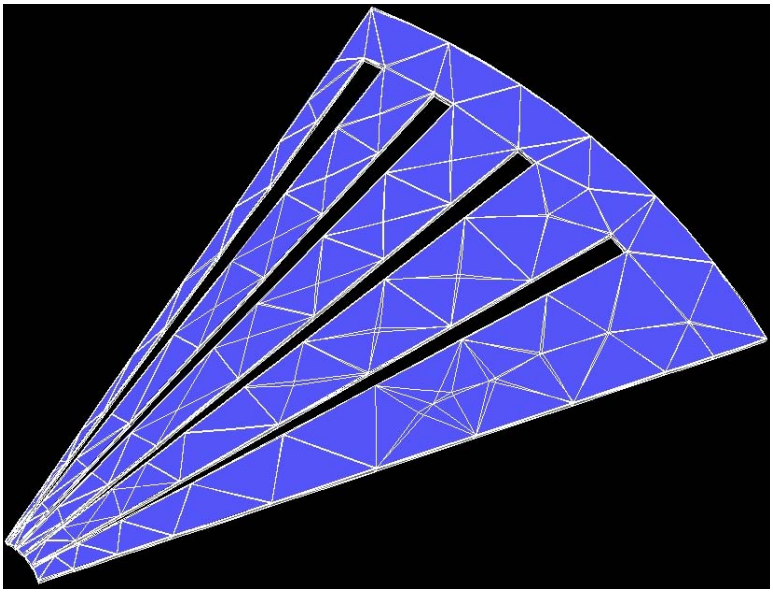


Figure 4.10: 3-D image of the 210-μm connected wing model with a tetrahedral mesh; the maximum element dimensions are 30 x 30 μm^2.

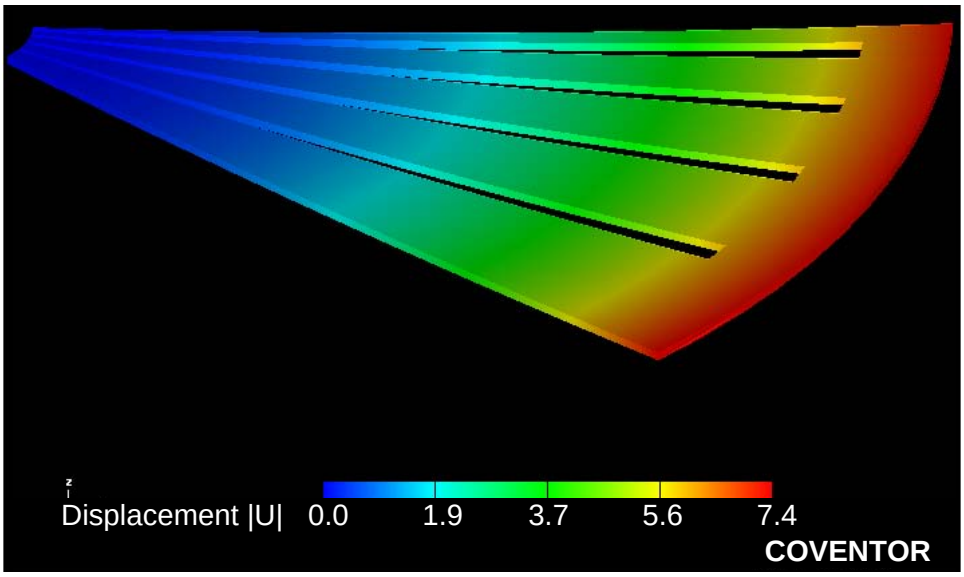


Figure 4.11: MemMech simulation results of a 210-μm connected wing showing a 7.4-μm tip deflection at all points around the rim.

4.5.3 Microrobot Wing Model 3: The Raised Wing

The final model includes an anchored poly1 layer under the three middle flexures of the wing (see Figure 4.12). The poly2 layer conforms to the poly1 spacer layer, but the two layers are not connected due to a thin removable layer between them. The purpose of the spacer is to direct the powered deflection downward; it could also cup more air under the wing. The tetrahedral mesh with 30 x 30-μm^2 maximum element dimensions is used (see Figure 4.13).

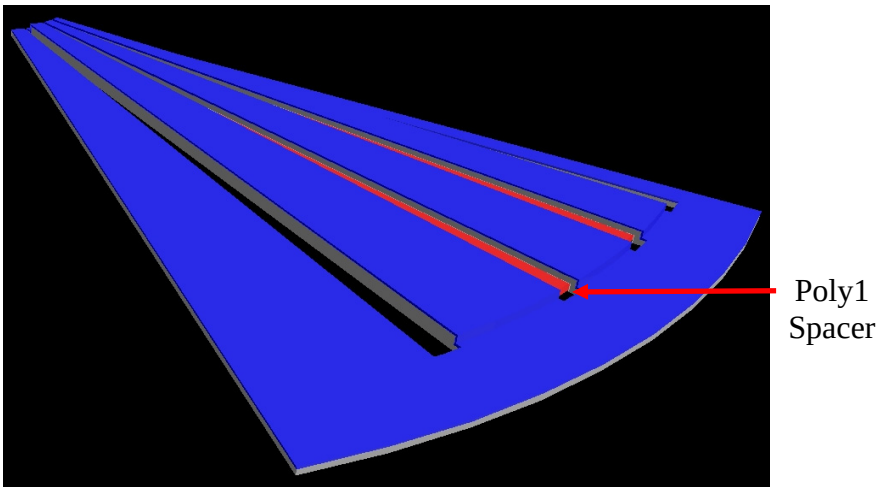


Figure 4.12: 3-D image of the 210-μm raised wing model that includes a poly1 spacer under the three center flexures. The spacer biases the powered deflection downward.

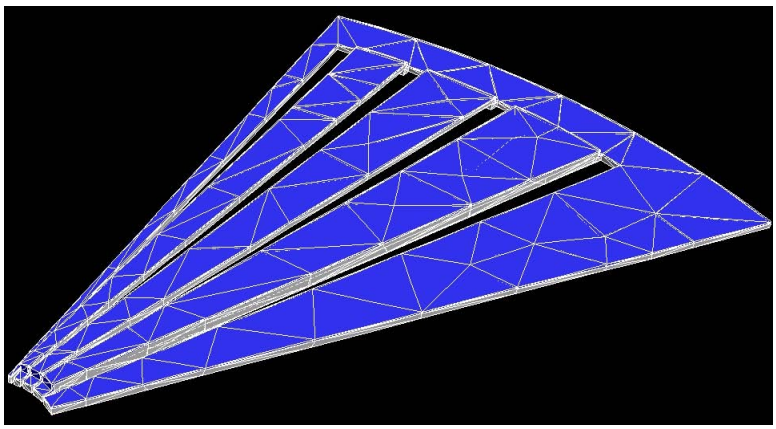


Figure 4.13: 3-D image of the raised wing model with a tetrahedral mesh; the maximum element dimensions are 30 x 30 μm^2.

The MemMech displacement simulation shows significantly lower deflection results (illustrated in Figure 4.14) than those obtained in the models without the spacer.

This final simulation indicates that the spacer significantly reduces initial deflection. The effect of the cupping shape on lift can only be determined experimentally.

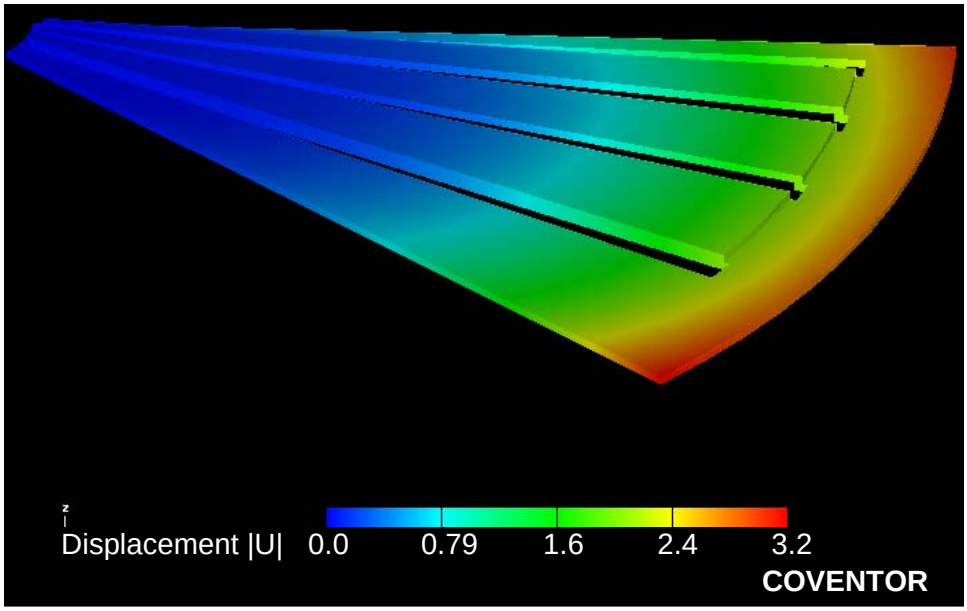


Figure 4.14: MemMech simulation results of the 210-μm raised wing model with the poly1 spacer. The highest deflection—3.2 μm—is at the tip of the wide flexure. The deflection in the center of the rim is 2.72 μm.

4.5.4 Summary of Microrobot Wing Deflection Values

The Coventor® simulation results of the three 210-μm microrobot wing models are given in Table 4.9. Although not described until Chapter 7, the measured deflection values of the MUMPs® 66 microrobot that matches the simulated designs are included for comparison. Again, the poly1 spacer under the raised wing decreases the initial deflection, which would limit the microrobot performance. Important to note is the percent difference in the measured and simulated values for the raised wing. This significant uncertainty in the accuracy of Coventor® justifies designing a copy of each robot—one with and one without the spacer—to verify the effect of this spacer. Also included in the table are the 199- and 249-μm simulated and measured cantilever values for comparison. As determined previously, deflection is directly proportional to structure length. It is interesting to note that a longer 210-μm raised wing yields less deflection

than a shorter 199-μm cantilever. This illustrates the effect of beam shape on deflection—another argument against using the poly1 spacer.

Table 4.9. Comparison of cantilever and robot wing deflections.

Device Structure	Deflection {μm}		Percent Difference
	Coventor	Measured	
210-μm separated wing	7.400	8.691	14.9%
210-μm connected wing	7.400	9.292	20.4%
210-μm raised wing	3.200	4.877	34.5%
199-μm cantilever	5.760	6.266	8.08%
249-μm cantilever	8.999	9.668	6.92%

4.6 Downward Deflection in Cantilevers

Downward deflection due to increased temperature is the second main modeling objective. Analytical expressions for the downward deflection in cantilevers as a function of temperature and power are included in the following subsections. These expressions are based on the simplifying assumption that temperature is constant throughout the beam—assuming constant heat generation throughout the beam as well as neglecting convection losses. Including convection losses and non-uniform heat generation is best achieved in a finite element analysis. Section 4.7 includes downward deflection modeling in Coventor® for a microrobot wing.

4.6.1 Temperature-Deflection Relationship in Cantilevers

A simplified model of a cantilever section including constant heat generation and no convection losses is illustrated in Figure 4.15. The device at the bottom is at a higher temperature than the top device ($T_{heated} > T_{RT}$). The increased temperature in the bottom device is a result of absorbed laser power and is colored red to reflect its higher temperature. The temperatures at both ends of the devices are constant.

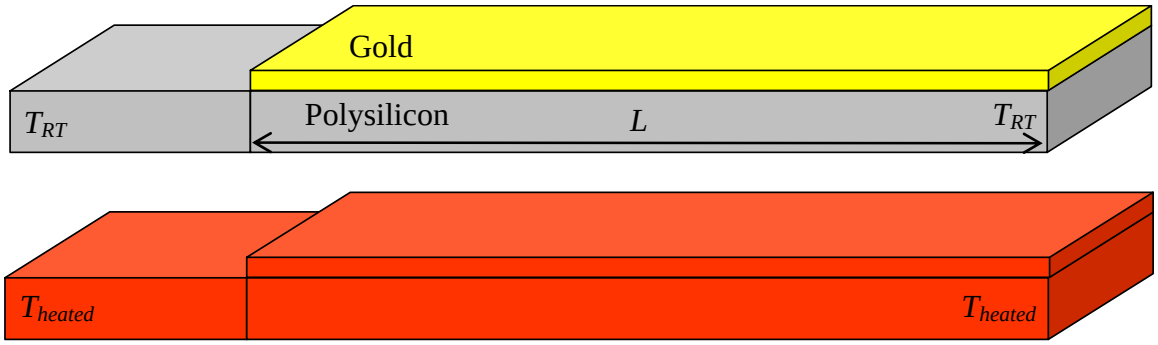


Figure 4.15: Diagrams of gold-poly2 cantilevers in a simple modeling case with constant heat throughout the device and no convection losses. The increased temperature in the bottom cantilever is due to the absorbed laser power; $T_{heated} > T_{RT}$.

The same equations used to determine initial deflection due to residual stress in cantilevers may be used to determine downward deflection as a function of temperature. The expression for residual stress,

$$\sigma_{res} = \sigma_{poly} + E'_{gold}\left(\alpha_{poly} - \alpha_{gold}\right)\left(T - T_{fab}\right), \tag{4.30}$$

is substituted into the deflection expression,

$$z = \frac{3t_{gold}\sigma_{res}L^2}{E'_{poly}t^2_{poly}}, \tag{4.34}$$

to yield:

$$z = \frac{3t_{gold}\left[\sigma_{poly} + E'_{gold}\left(\alpha_{poly} - \alpha_{gold}\right)\left(T - T_{fab}\right)\right]L^2}{E'_{poly}t^2_{poly}}. \tag{4.36}$$

The temperature of the device T depends on the temperature increase T_{inc} caused by heat generated in the device and the room temperature T_{RT} {all in K}:

$$T = T_{inc} + T_{RT}\,. \tag{4.37}$$

The downward deflection results from Equation 4.36 are plotted as a function of increased temperature T_{inc} and are given in Figure 4.16 (see Appendix B.3 for code). The deflection at the tip of each cantilever decreases linearly with increasing temperature. This model verifies the theory of downward deflection with increased temperature.

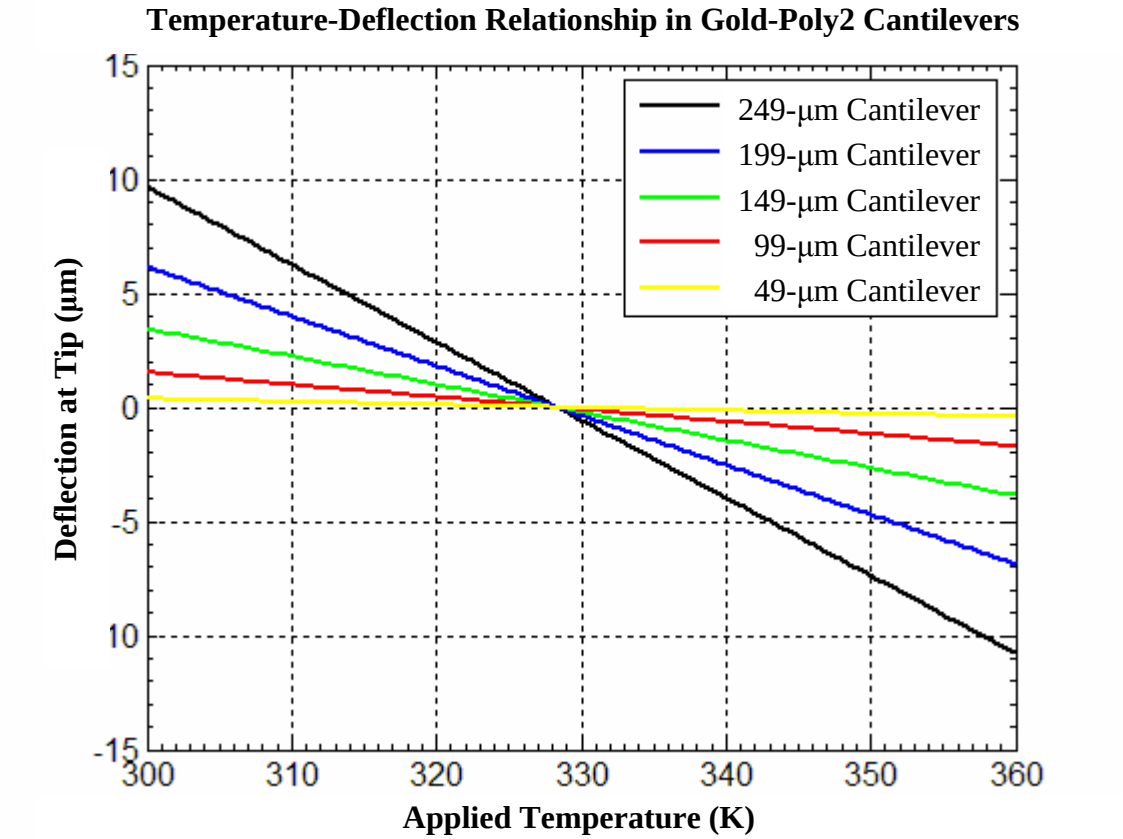


Figure 4.16: MatLab® plot of downward deflection as a function of temperature in several gold-poly2 cantilevers. This steady-state model assumes constant temperature throughout the beam; it also neglects convection heat loss.

4.6.2 Power-Deflection Relationship in Cantilevers

A power-deflection model is more useful than the temperature-deflection model since laser power, instead of temperature, is the known input variable. An expression for increased temperature as a function of absorbed laser power is given by the material heat capacity c {J·kg^{-1}·K^{-1}}. This property reflects the amount of energy required to raise a kilogram of material by one Kelvin. The temperature increase is given by:

$$T_{inc} = \frac{P_{abs}\tau}{mc}, \tag{4.38}$$

where P_{abs} {W} is the absorbed power, τ {s} is the pulse length or the amount of time the power is absorbed, m {kg} is the mass, and c {J·kg^{-1}·K^{-1}} is the heat capacity. The value for τ may seem quite arbitrary as it reflects the length of time the heat is nearly constant

in the device. This parameter could be interpreted as a fudge factor that accounts for convection losses, which are not included in this model. For this reason alone, it is imperative to expand the model to reflect the real conditions. This is addressed in the next section.

The increased temperature term is substituted into the temperature-deflection expression to yield a new power-deflection expression, which is given by:

$$z = \frac{3t_{gold}\left[\sigma_{poly} + E'_{gold}\left(\alpha_{poly} - \alpha_{gold}\right)\left(\frac{P_{abs}\tau}{mc} + T_{RT} - T_{fab}\right)\right]L^2}{E'_{poly}t^2_{poly}}. \qquad (4.39)$$

The plotted results are given in Figure 4.17 with the same assumptions as in the temperature-deflection model; the material properties are from Table 4.1 and Table 4.4.

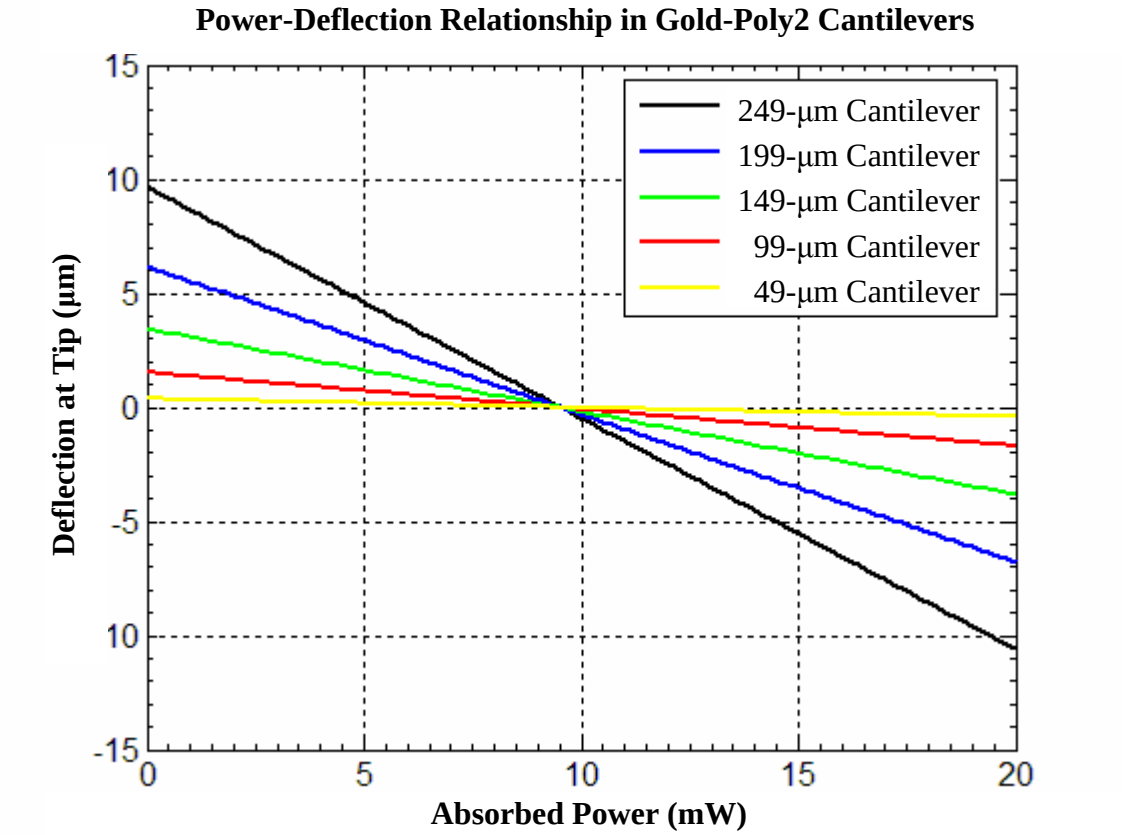


Figure 4.17: MatLab® plot of downward deflection as a function of absorbed power in several gold-poly2 cantilevers. This model assumes no heat loss from convection.

4.6.3 Non-Uniform Temperature Distribution

The assumptions in the previous model neglect two very important conditions in the device. The first condition is that the laser power is absorbed only in the center section and the heat is conducted into the flexing section. This localized absorption results in a monotonically decreasing temperature profile along the device flexure. The second neglected condition is that the heat losses from convection into the air also result in a decreasing temperature profile. The resulting deflection at each increment along the device would be slightly less than the adjacent, warmer increment. Thus, determining the effects of a non-uniform temperature on deflection would require this simple model to be broken into small elements and evaluated simultaneously. This type of complex analysis is best performed using a finite element modeling software package. Nonetheless, a qualitative understanding of the heat exchange principles can be obtained from simple diagrams and general expressions. Figure 4.18 illustrates a gold-poly2 device with a constant temperature T_1 in the poly2 center; the heat is from an impinging laser. The heat is conducted into the gold-poly2 flexure, and some heat is lost due to convection. The temperature at the end of the device T_2 is lower than that at the poly2 center T_1.

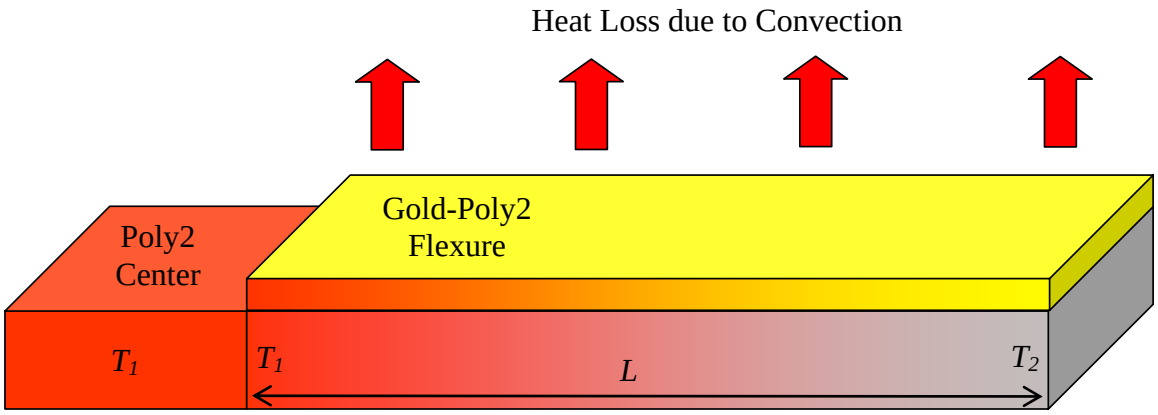


Figure 4.18: Diagram of a gold-poly2 device with non-uniform temperature distribution. The constant temperature T_1 of the poly2 center section is due to absorbed laser power. The laser does not illuminate the gold-poly2 flexure, but the heat in that section is conducted from the poly2 center. The heat loss due to convection occurs along the flexure length L, and the temperature at the end of the device T_2 is lower than T_1.

An expression for temperature distribution in a conduction-convection system, such as the one in Figure 4.18, has already been derived [18]. For each element of the system, the heat conducted in the left face must equal the heat conducted in the right face plus the heat lost from convection. This expression is comprised of Fourier's Law of Heat Conduction and Newton's Law of Cooling, which are, respectively:

$$q_{cond} = -kA\frac{dT}{dx}, \tag{4.40}$$

$$q_{conv} = hA\left(T_1 - T_\infty\right). \tag{4.41}$$

These two heat equations combine to yield the steady-state one-dimensional conduction-convection expression:

$$\frac{d^2T}{dx^2} - \frac{hP}{kA}\left(T - T_\infty\right) = 0, \tag{4.42}$$

where h {W·m^{-2}·K^{-1}} is the experimentally determined heat-transfer coefficient, P {m} is the perimeter around the cross-sectional element, k {W·m^{-1}·K^{-1}} is the thermal conductivity of the material, A {m^2} is the cross-sectional area of the element, T is the temperature at a given distance, and T_∞ is the ambient temperature {both in K}.

For a case with an infinitely long device, the solution to Equation 4.42 is:

$$\frac{T - T_\infty}{T_1 - T_\infty} = e^{-mx}, \tag{4.43}$$

where T_1 is the temperature at the left end of the device (x = 0), and m is defined as:

$$m = \sqrt{\frac{hp}{kA}}. \tag{4.44}$$

For the case of a finite-length device, the solution is:

$$\frac{T - T_\infty}{T_1 - T_\infty} = \frac{\cosh\left(m\left[L - x\right]\right) + \frac{h}{mk}\sinh\left(m\left[L - x\right]\right)}{\cosh\left(mL\right) + \frac{h}{mk}\sinh\left(mL\right)}. \tag{4.45}$$

In Figure 4.19, the temperature distribution for the gold-poly2 cantilever shown in Figure 4.18 is plotted for both the infinite and finite cases (see Appendix B.5 for code). The temperature at the left end of the device T_1 is 400 K, and the ambient temperature T_∞ is 300 K. The thermal conductivity used is the average k_{ave} of gold and poly2 from Table 4.1; the forced convection coefficient of 3850 $W \cdot m^{-2} \cdot K^{-1}$ is also used [18]. Notice that the temperature distribution in the finite beam is higher than that in the infinitely long beam, and the difference is more pronounced as the beam length increases.

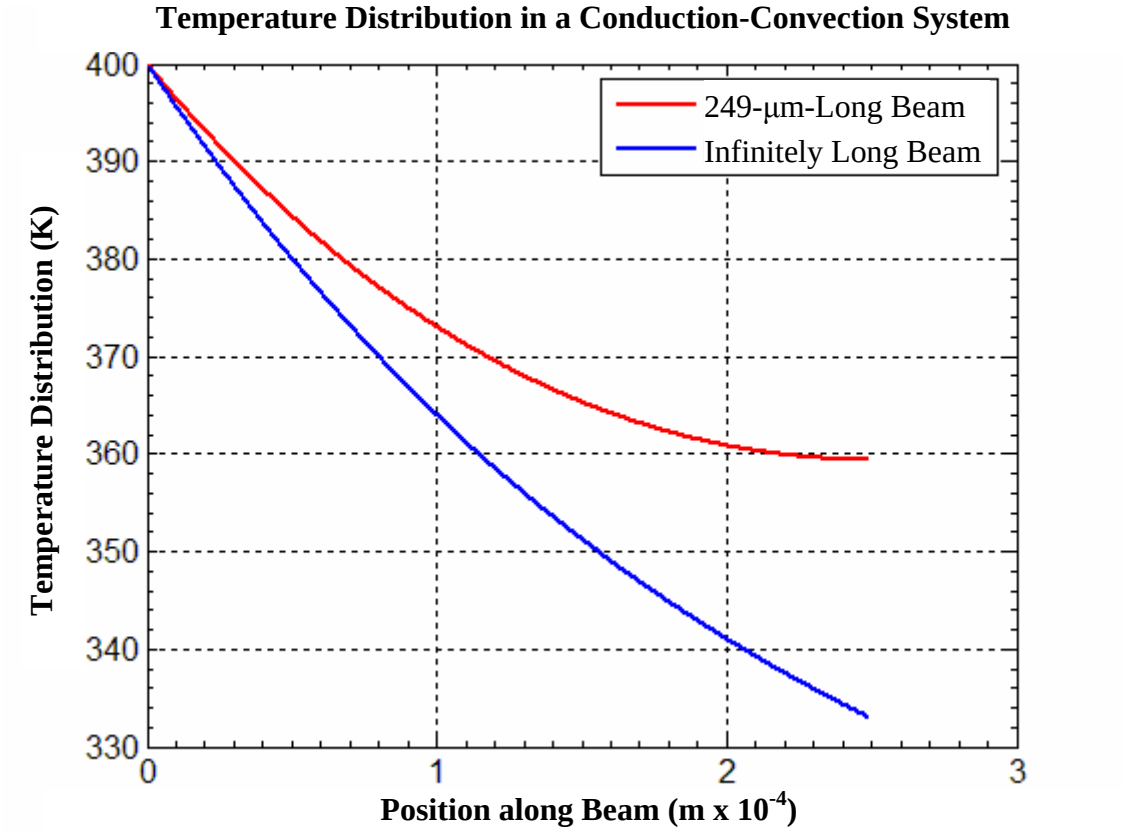


Figure 4.19: Graph of the temperature distribution for a 249-µm-long and an infinitely long gold-poly2 cantilever with 400-K end-tip and 300-K ambient temperatures. The decreasing temperature along the beam in this model most accurately represents the true device. The temperature is higher in the finite beam than in the infinitely long beam.

4.7 Downward Deflection in Microrobot Wings

As mentioned before, it would be very difficult to derive analytical expressions for the downward deflection in simple cantilevers given true conduction-convection conditions. It would be impossible to model irregularly shaped microrobot wings, given the same conditions, without a finite element package. Similar to the previous Coventor® models and simulations, this simulation is also simplified. It assumes steady-state temperature conditions in order to determine total static deflection instead of transient behavior. A constant temperature is applied at the narrow end of the wing—the place where the laser energy would be absorbed and conducted into the wing. Also, a 0.6-m/s airflow is applied as a forced convection condition. This airflow accounts for the movement the wing undergoes during deflection, assuming a maximum 1-kHz wing movement. This simulation was completed for each of the three wing model types. The results show increased downward deflection with increased applied temperature. The connected wing model is shown in Figure 4.20 with the results in Figure 4.21.

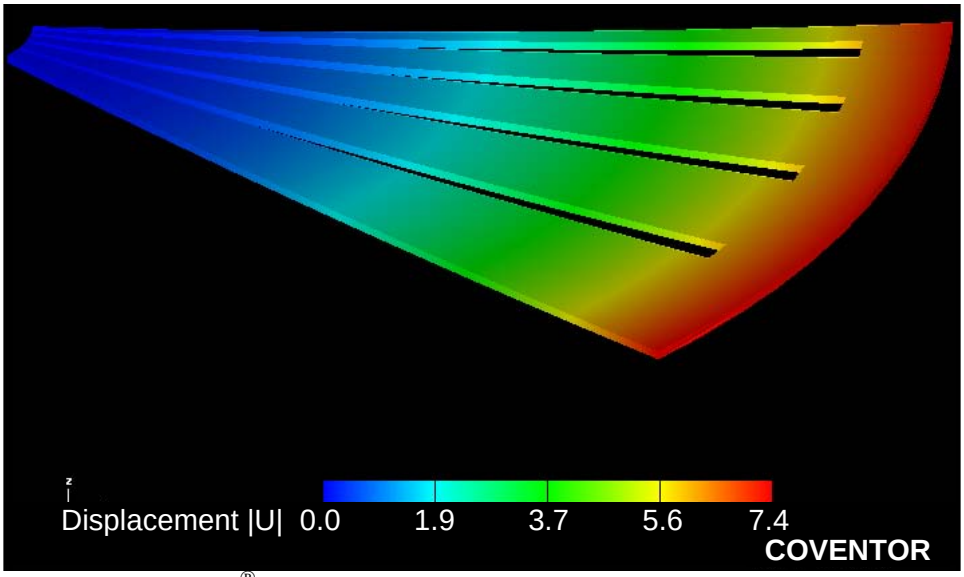


Figure 4.20: Coventor® image of the connected wing model in the steady-state incremental temperature analysis. The downward deflection is shown in Figure 4.21.

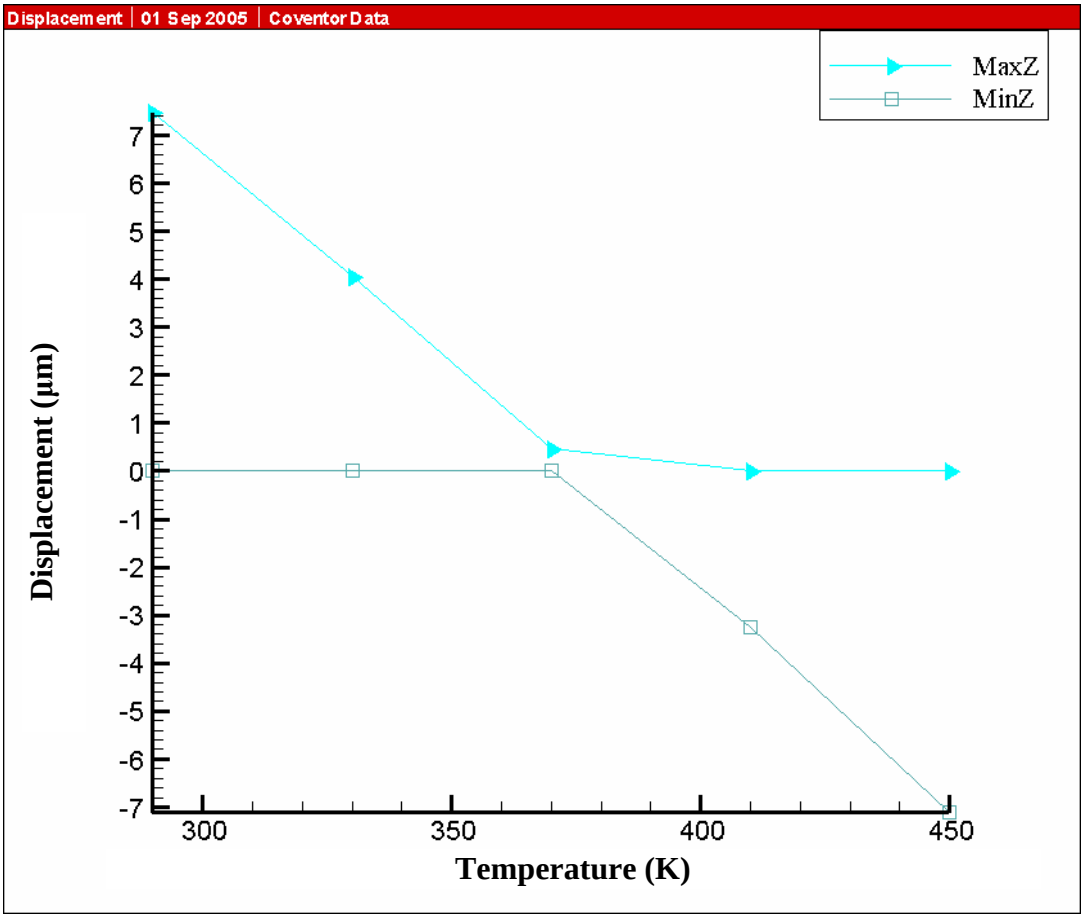


Figure 4.21: Thermal simulation of the connected wing model with an applied incremental steady-state temperature; a 0.6-m/s airflow is applied to account for forced convection losses during wing movement. The wing deflects downward {in µm} as the temperature {in K} increases, which verifies the downward deflection theory.

4.8 Modeling to Predict Performance

Coventor® could be used to predict future performance of device designs. Since it takes almost two months and several thousand dollars to fabricate each MUMPs® run, it would be possible to save time and money using Coventor®. However, for devices based on residual stress for their fundamental operation—cantilevers and robots—it should be noted that predicting future performance may be uncertain due to the variability of residual stress from run to run. Figure 4.22 and Figure 4.23 illustrate the mean, standard deviation σ, and sample variance σ^2 in poly2 and gold layers from MUMPs® 5–69.

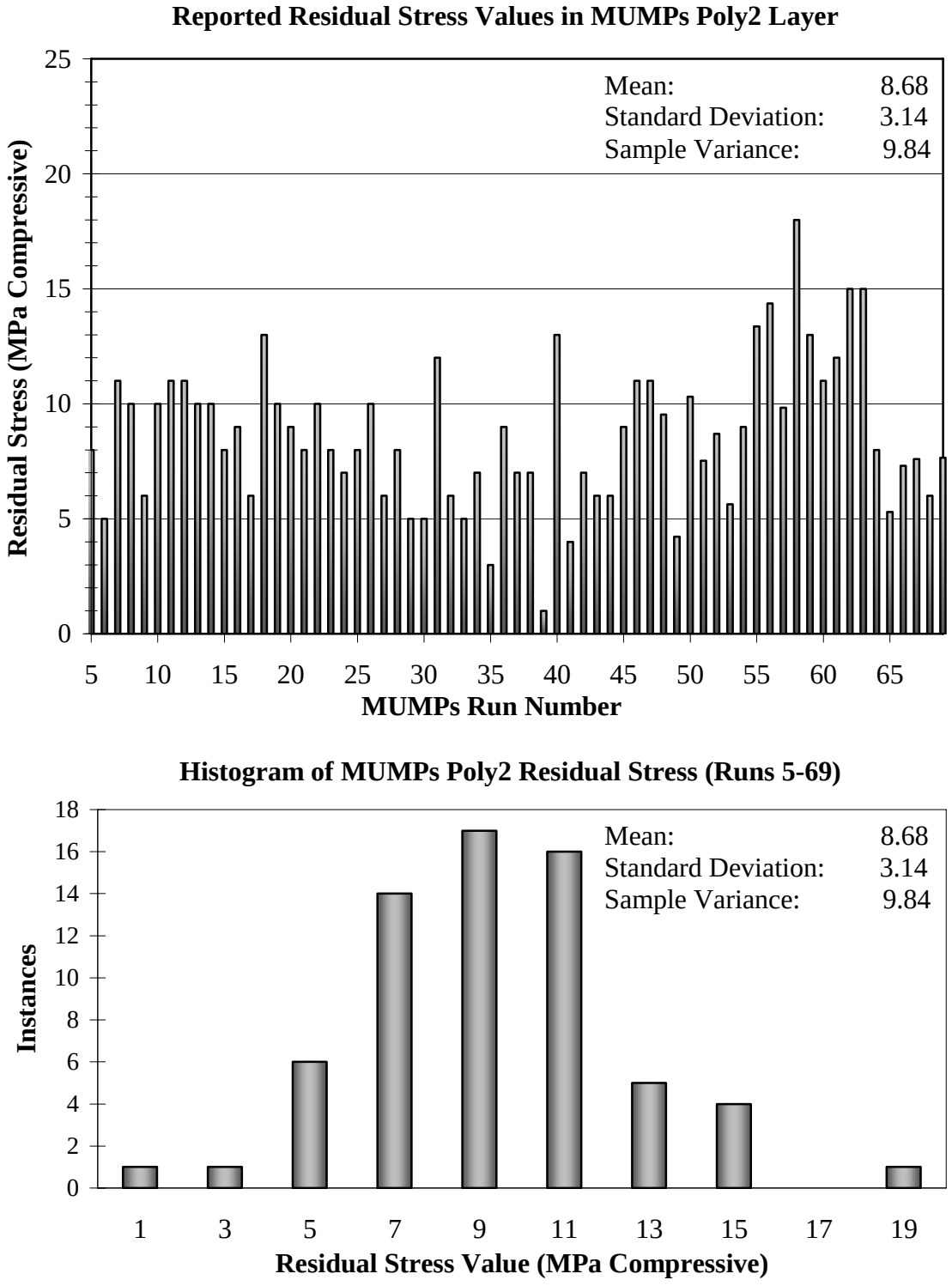


Figure 4.22: Reported residual stress values in PolyMUMPs® poly2 layer. The histogram shows a normal distribution with a mean of 8.68 MPa and standard deviation σ of 3.14 MPa. About 68% of the values fall between 5 and 12 MPa.

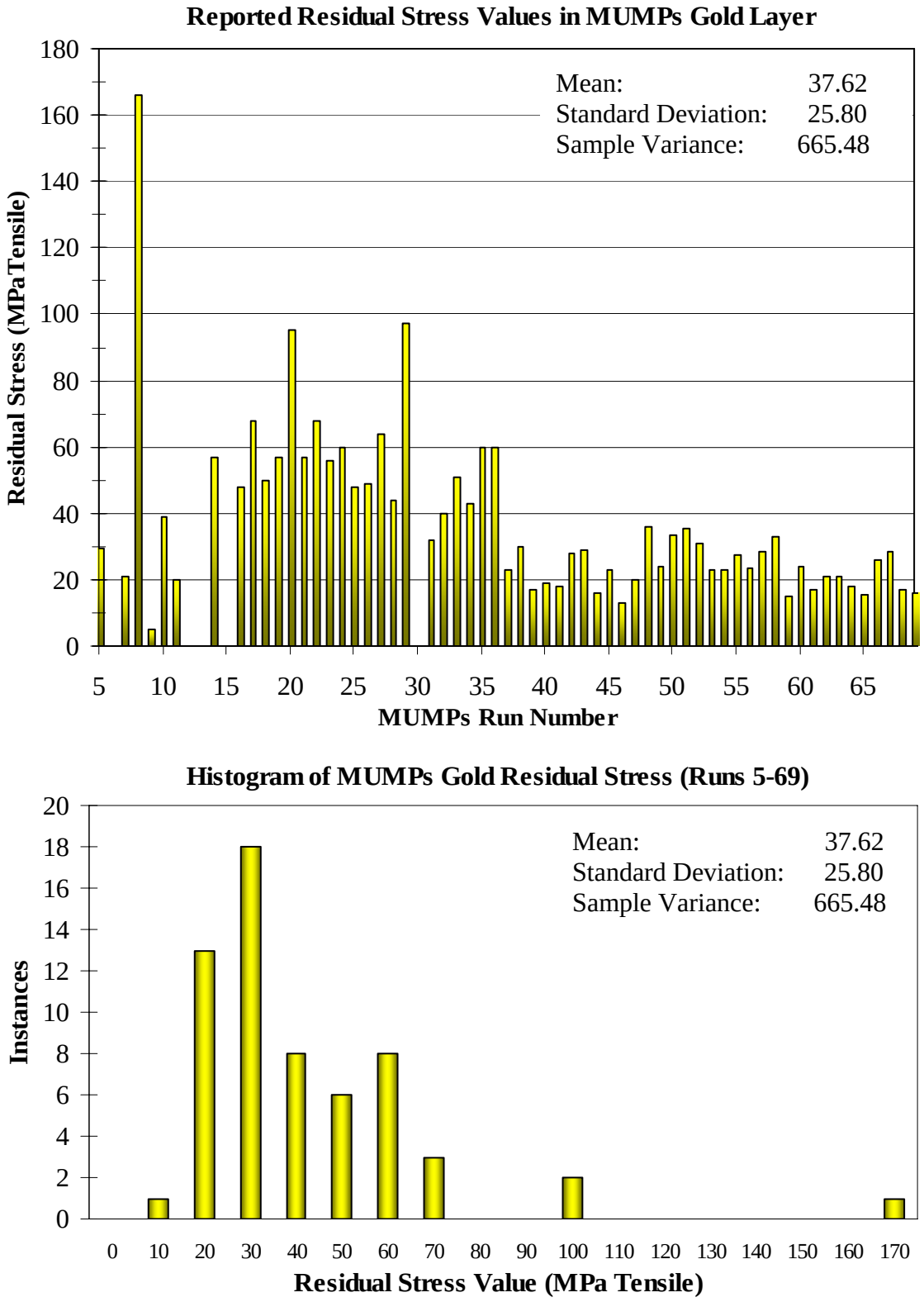


Figure 4.23: Reported residual stress values in PolyMUMPs® gold layer. The gold distribution is exceptionally more varied than the poly2 distribution because of the first several runs. The stress in later runs shows a more normal distribution with less variance.

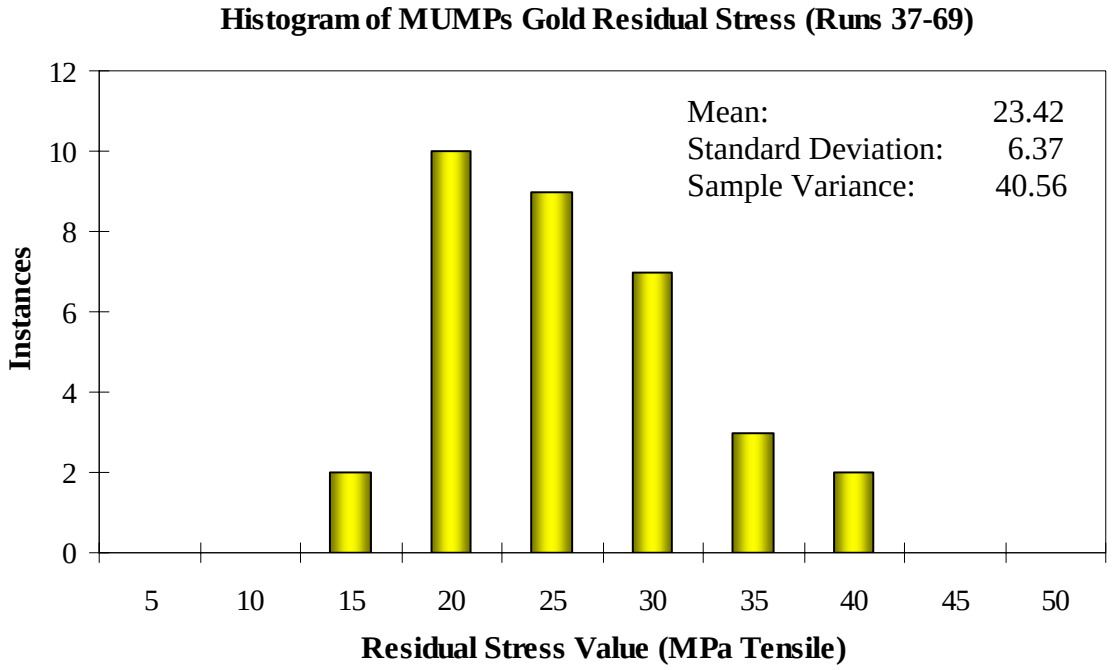


Figure 4.24: Reported residual stress values in PolyMUMPs® poly2 layer from runs 37–69. The histogram shows significantly less variance and a lower mean than those in Figure 4.23. About 68% of the stress values fall between 17 and 30 MPa.

From runs 5–69, the stress values in the poly2 layer have an 8.68-MPa average and a 3.14-MPa standard deviation, meaning about 68% of the values fall between ± one standard deviation—5–12 MPa. The poly2 component of future device performance can be predicted by using the poly2 mean residual stress value from runs 5–69.

The gold residual stress values do not exhibit the same consistency throughout the fabrication history as those from poly2. From runs 5–69, the stress values in the gold layer have a 37.62-MPa average and 22.5-MPa standard deviation, which is a significant amount of variability. The reason for such variance in the metal layer is that the MUMPs process underwent some initial tweaking. The metal used in PolyMUMPs® run 3 was aluminum, but this was found to be etched away by hydrofluoric acid (HF) during the release process. The metal was copper for run 4, but this was found to have oxidation problems. Gold was chosen for run 5 and is still used today because of its superior

fabrication and post-processesing compatibility [19]. After the first few runs, the process seemed to be more stable. From runs 37–69, the stress values in gold have a 23.42-MPa average and a 6.37-MPa standard deviation, meaning about 68% of the values fall between 17 and 30 MPa. This is significantly less variance than in the previous runs. Future device performance can be accurately predicted using the mean residual stress values for gold from runs 37–69.

4.9 Chapter Summary

This chapter incorporated the theory from Chapter 3 into several models to describe two aspects of novel flying MEMS robots: the initial deflection due to residual stress and downward deflection due to laser heating. Both cantilevers and robot wings were modeled through analytical expressions and through the CoventorWare® finite element modeling package. The cantilever model served as a baseline for comparison with the microrobot wings. Temperature-deflection and power-deflection relationships were derived for cantilevers. The ability to predict future performance through modeling was proposed. The mean residual stress values reported for PolyMUMPs® runs can be used as a guideline for future device performance. The device concepts modeled in this chapter will be described in detail in Chapter 5. Chapter 6 and Chapter 7 give the procedures for testing the devices and the results of those tests, respectively.

4.10 References

[1] J. D. Anderson, *Fundamentals of Aerodynamics* (3rd Edition), Boston: McGraw-Hill, 2001, pp. 85–86.

[2] G. T. A. Kovacs, *Micromachined Transducers Sourcebook*, Boston: McGraw-Hill, 1998, pp. 79–81.

[3] J. W. Gardner, V. K. Varadan, and O. O. Awadelkarim, *Microsensors MEMS and Smart Devices*, Chichester, England: John Wiley and Sons, 2001, Appendix G.

[4] J. W. Gardner, *Microsensors: Principles and Applications*, New York: Wiley, 1994, pp. 69–71.

[5] M. J. Madou, *Fundamentals of Microfabrication: The Science of Miniaturization* (2nd Edition), Boca Raton, FL: CRC Press, 2002, p. 294.

[6] L. A. Starman, *Characterization of Residual Stress in Microelectromechanical Systems (MEMS) Devices Using Raman Spectroscopy*. Air Force Institute of Technology (AU), Wright-Patterson Air Force Base OH, 2002 (AD-A402559).

[7] H.-C. Tsai, J. M.-L. Tsai, H.-C. Chang, and W. Fang, "A Reliable Test Key for Thin Film Mechanical Properties Characterization," *The 12th International Conference on Solid State Sensors, Actuators and Microsystems—Transducers '03*, pp. 452–455, Boston, MA, 8–12 Jun. 2003.

[8] W. N. Sharpe, Jr., "Mechanical Properties of MEMS Materials," in *The MEMS Handbook*, Ed. M. Gad-El-Hak. Boca Raton, FL: CRC Press, 2002.

[9] Y. Laghla and E. Scheid, "Optical Study of Undoped, B or P-doped Polysilicon," *Thin Solid Films*, vol. 306, pp. 67–73, 1997.

[10] D. Koester, A. Cowen, R. Mahadevan and B. Hardy, *PolyMUMPs Design Handbook: A MUMPs® process* (Revision 10.0), MEMSCAP®. www.memscap.com/memsrus/docs/PolyMUMPs.dr.v10.pdf, 2003.

[11] Y. Laghla, E. Scheid, H. Vergnes, and J. P. Couderc, "Electronic Properties and Microstructure of Undoped, and B- or P-Doped Polysilicon Deposited by LPCVD," *Solar Energy Materials and Solar Cells*, vol. 48, pp. 303–314, 1997.

[12] "Gold." *Webelements™ Periodic Table: Professional Edition*. Excerpt from an online database. n. pag. www.webelements.com. 26 Jan. 2006.

[13] S. M. Sze, *Semiconductor Devices: Physics and Technology* (2nd Edition), New York: John Wiley and Sons, 2002, pp. 349–351.

[14] PolyMUMPs® Fabrication Data from runs #66-69. Excerpt from an online database. n. pag. http://www.memsrus.com/nc-pmumps.refs.html. 15 Jan. 2006.

[15] J. E. Shigley, C. R. Mischke, and R. G. Budynas, *Mechanical Engineering Design* (7th Edition), Boston: McGraw-Hill, 2004, p. 970.

[16] K. D. Leedy. Senior Material Research Engineer, Multi-Chip Integration Branch, Aerospace Components and Subsystems Division, Sensors Directorate, Air Force Research Laboratory (AFRL/SNDI), Wright-Patterson AFB, OH. Personal Correspondence. 5 Jan. 2006.

[17] *CoventorWare ANALYZER™ Tutorials* (Version 2004, Revision A). Coventor®. http://www.coventor.com. 16 Mar. 2004.

[18] J. P. Holman, *Heat Transfer* (9th Edition), Boston: McGraw-Hill, 2002, pp. 11, 43–4.

[19] J. H. Comtois, *Structures and Techniques for Implementing and Packaging Complex, Large Scale Microelectromechanical Systems Using Foundry Fabrication Processes*. Air Force Institute of Technology (AU), Wright-Patterson Air Force Base OH, 1996 (AD-A310747).

V. Designs and Fabrication

5.1 Chapter Introduction

The designs of novel ornithoptic polysilicon-based microrobots are described in this chapter. The inspiration for the designs comes from sponsor requirements, insect studies, and from theory and modeling principles. 129 different microrobots were designed and fabricated in the commercially available PolyMUMPs® process. Because the design concepts are entirely original, several design iterations were required to optimize certain elements of performance. The post-fabrication processing required to test the microrobot performance is given in Chapter 6, and the results are in Chapter 7.

5.2 Design Inspiration

The designs of the microrobots in this chapter were inspired by the sponsor's requirements, insect characteristics, and the principles from Chapter 3 and Chapter 4.

5.2.1 Sponsor Requirements

The sponsor requested a microrobot capable of demonstrating some predictable, repeatable behavior—e.g. moving towards a target. This very open-ended problem can be interpreted very differently in terms of the level of complexity in the end product. A satisfactory, yet, simple solution would be a robot that moves in a straight line and happens to be directed towards a target. Another satisfactory yet very advanced solution would be a robot that senses the target and strategically maneuvers towards it. The robots in this thesis are designed to ascend from the substrate towards a laser power source.

Another design requirement is that the largest dimension of the robot must be less than 1 mm. The project sponsor initially desired an even smaller robot with dimensions

on the order of 500 x 500 μm^2 [1]. Most of the robots in this chapter are 500 µm in diameter and a few are 990 µm.

5.2.2 Inspiration from Insects

Since the advance of the microrobotics field, entomology is no longer an obscure bug-collecting profession. Top scientists are studying insect behavior—flying, communicating, responding, and adapting—to enable engineers in developing devices that mimic their biologically superior performance [2]–[11]. The Mechanical Flying Insect project of Chapter 2 epitomizes this biomimetics principle.

A trend in wing flapping frequency has been observed in small insects. As the insect mass decreases, the flapping frequency increases. This is illustrated in Figure 5.1, which was adapted from [2].

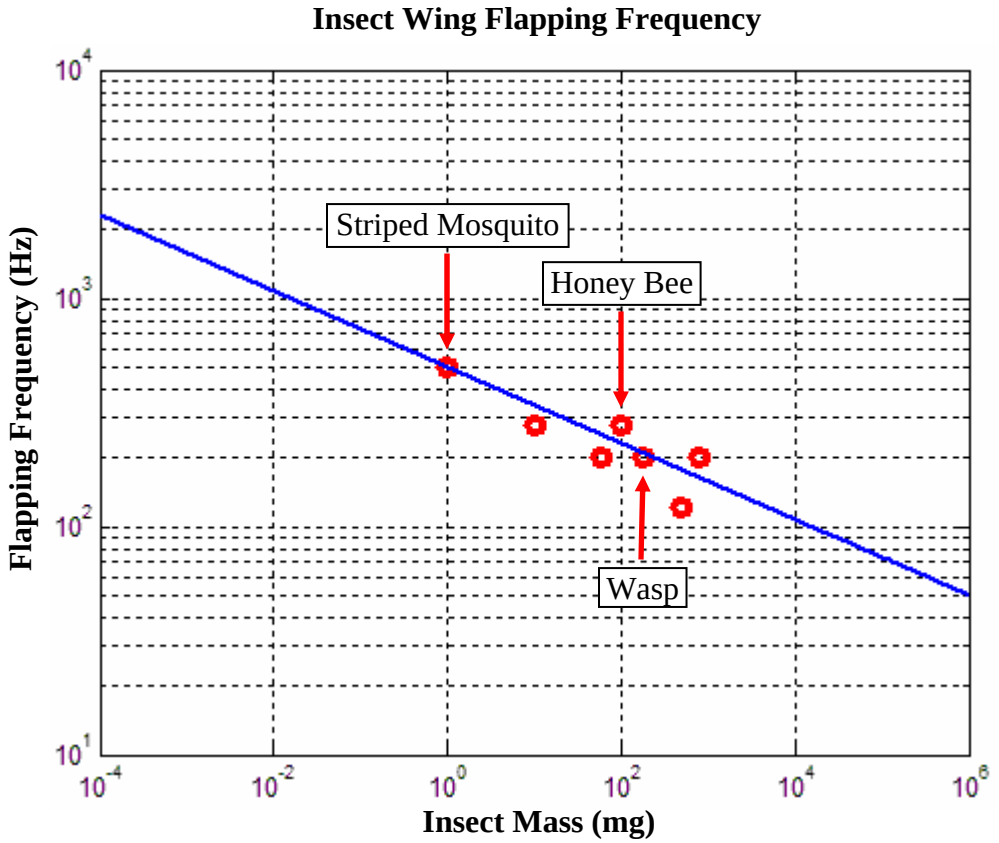


Figure 5.1: Illustration of the trend in insect wing flapping frequency versus mass. Smaller insects tend to flap faster than larger insects (adapted from [2]).

Flight at smaller scales is based on different mechanisms than those of the larger scale, such as lift from curved airfoils. Tiny insects such as the parasitic wasp *Encarsia formosa*, greenhouse white-fly *Trialeurodes vaporariorum*, and some other larger insects use a "fling motion" to generate lift [3]. Each wing cycle involves slapping two wings together to create bound vortices that create lift at a scale traditionally considered impossible. This fling motion is an attractive technique for microrobot engineers, but it is not yet practical with current fabrication and actuation techniques. Extra lift can be gained instead using larger wings or a faster wing-beat frequency [3]. The size should be kept on the order of 1 mm, but the wing-beat frequency can be maximized with the knowledge from the theory and modeling chapters.

5.2.3 Inspiration from Theory and Modeling

The first criterion in realizing a downward-flapping robot is reducing the energy required to actuate the wings up and down. As mentioned in Chapter 3, the inherent residual stress in MUMPs® polysilicon and gold layers results in an upward position at room temperature. Once deflected downwards, gold-polysilicon wings would return to their starting position without being powered. This obvious advantage is the reason for designing gold-polysilicon robot wings. Yet many structures exhibit similar elasticity. A two-by-four piece of lumber, for example, bends back into place when deflected, but it is very difficult to deflect initially.

This leads to the second criterion: the wings must bend easily both downward and upward. Given the vertical deflection equation derived in Chapter 4,

$$z = \frac{M_{res} L^2}{2EI_y}, \tag{5.1}$$

there are two design options for maximizing deflection: increasing the structure length L, and reducing moment of inertia about the axis of bending I_y. The other terms in Equation 5.1—the moment due to residual stress M_{res} and Young's modulus E—are material-dependent properties that cannot be altered. The moment of inertia, which describes the ease of bending, is given by:

$$I_y = \frac{wt^3}{12}, \tag{5.2}$$

where w and t are the width and thickness of the structures. Reducing the thickness by one unit reduces the moment of inertia by a power of three. Reducing the width also improves the ease of bending, but only by a smaller degree. It is clear that the wings should be made of long, thin polysilicon and gold layers.

Making the layers thin would result in less energy being absorbed from the laser. As described in Chapter 3, the amount of laser power that contributes to heating can be increased by making the absorbing layer thick. A thin layer would actually transmit energy, which decreases the device efficiency. A compromise between bending and energy absorption can be made by making a thick non-deflecting target area for the laser while keeping the deflecting wings thin.

Power consumption and ease of bending are not the only design criteria. The wings must also flap rapidly. Though thermal actuation yields more force and is generally simpler to implement than other actuation techniques, a significant disadvantage is its relatively slow response time. In laser-powered thermal actuation, the devices are heated during the on-phase of the laser pulse cycle; they cool during the off-phase as their heat is lost through convection. It has been demonstrated that convective cooling is slower than absorptive heating, which means that the maximum wing-beat

frequency is limited primarily by the cooling process [12]–[15]. Minimizing the cooling time can be achieved by maximizing convective heat transfer rate given in Chapter 3: $q_{conv} = hA(T_0 - T_\infty)$. This is best accomplished by maximizing the wing surface area *A*. The heat-convection coefficient *h* and ambient temperature T_∞ are dependent on the environment and are not design elements. A summary of these design elements and requirements is given in Table 5.1.

Table 5.1. Summary of design elements and requirements for a flying microrobot.

Design Element	Purpose	Method
Reduce overall size to less than 1 mm	Satisfies sponsor requirement	Use MEMS fabrication processes
Maximize wing size	Creates more lift	Maximize wing area
Maximize wing-beat frequency	Creates more lift	Minimize cooling time by maximizing surface area
Maximize deflection	Creates more lift	Increase wing length, reduce wing stiffness, increase gold
Minimize wing stiffness	Reduces power required for actuation	Minimize thickness in flexures
Minimize power for actuation	Enables wireless flight	Use polysilicon and gold to naturally force wings upward
Maximize power absorption	Increases device efficiency	Maximize thickness in area for laser energy absorption

5.2.4 The Dominant Design Elements

In order to determine which design element has the greatest effect on microrobot flight, it is necessary to examine the forces involved. From a study on insect-based microrobots, it has been determined that insects fly by viscous forces—that is, drag (instead of lift) dominates insect flight [2]. The force due to drag is given by:

$$F_D = C_D \frac{1}{2} \rho U^2 A, \tag{5.2}$$

where C_D is the coefficient of drag and has been assumed to be 2 for small insects [2]; U {m/s} is the wingtip velocity; A {m^2}is the wing area; and ρ {kg/m^3} is the density of air, which is 1.168 kg/m^3 at 25 °C and standard atmospheric pressure (100 kPa). The wingtip velocity U is given by:

$$U = \frac{\theta L}{\tau} = \frac{\delta}{\tau}, \tag{5.3}$$

where θ {radians} is the deflection angle, L {μm} is the wing length, τ {s} is the time required to complete a full down-up deflection cycle, and δ {μm} is the amount of downward deflection. Since the microrobot wings are initially in an upward position, the downward deflection is measured from that initial deflection to the farthest downward position, as illustrated in Figure 5.2.

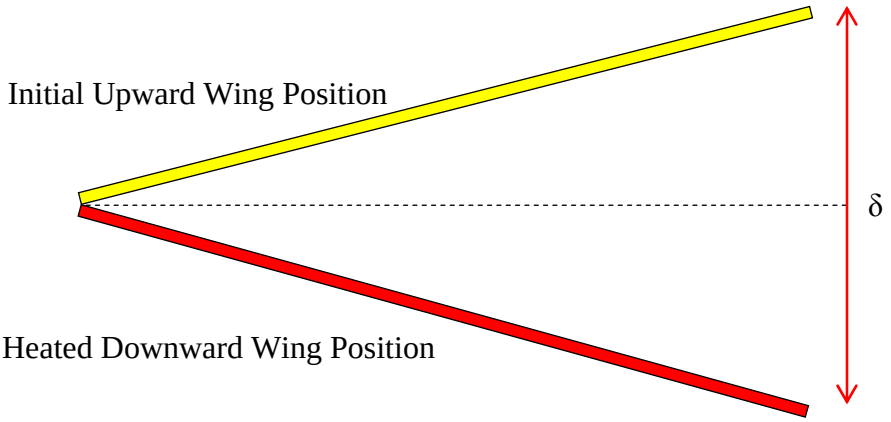


Figure 5.2: Diagram illustrating the downward deflection in a microrobot wing. The top beam represents the initial position of each wing, and the heated bottom beam represents the downward deflection position.

From Equation 5.2, it is clear that wing-tip velocity U is the most important term in generating downward force because it is raised to the power of two. Maximizing the velocity results in a maximum downward force; this is achieved by maximizing downward deflection and minimizing deflection time. As mentioned in the previous section, the time required to complete an entire cycle is dominated by the cooling time.

It has been determined that the temperature $T(\tau)$ during the cooling cycle of MEMS devices is given by [12]:

$$T(\tau) = T_{\max} \exp\left(-\frac{hA_T}{mc}\tau \right) + T_a , \tag{5.4}$$

where T {K} is the temperature in the device with respect to time; T_{max} {K} is the maximum temperature achieved during the heating cycle of the laser; h {W·m^{-2}·K^{-1}} is the experimentally determined convection coefficient; A_T {m^2} is the total device area (approximately twice the area for lift A); m {kg} is the device mass; c {J·kg^{-1}·K^{-1}} is the specific heat of the material; τ {s} is the time variable; and T_a {K} is the ambient temperature. Solving Equation 5.4 for the time required to cool τ yields:

$$\tau = \frac{mc}{hA_T} \ln\left(\frac{T_{\max}}{T - T_a} \right). \tag{5.5}$$

As the device temperature approaches T_a, the time required to cool approaches infinity, which is not practical. For the robot to return to a temperature within 1 K of ambient temperature, the time required is:

$$\tau = \frac{mc}{hA_T} \ln\left(T_{\max} \right). \tag{5.6}$$

From Equation 5.6, it is clear that minimizing cooling time is achieved by minimizing mass m and maximizing total surface area A_T. This trend is also important in overcoming the weight of the microrobot, which is described next.

In order for the microrobot to overcome its own weight, the force from the downward stroke must be greater than the force due to gravity:

$$C_D \frac{1}{2} \rho U^2 A > mg , \tag{5.7}$$

where, m {kg} is the robot mass and g {m/s^2} is the acceleration due to gravity.

It is clear from Equation 5.4 that surface area must be maximized and the mass must be minimized in order for the microrobot to lift off. However, the mass is directly proportional to the area:

$$m = At\rho\,, \tag{5.8}$$

where A {m^2} is the area, t {m} is the layer thickness, and ρ {kg/m^3} is the material density. Thus, the mass cannot be reduced without also reducing the area. The mass of a robot is the sum of the masses of each layer:

$$m_{robot} = A_{gold}t_{gold}\rho_{gold} + A_{poly}t_{poly}\rho_{poly}\,. \tag{5.9}$$

Although the thickness of the poly2 layer is 3 times the thickness of the gold layer in PolyMUMPs®, the density of gold is 8 times the density of polysilicion: 8/11 or 73% of the total mass of a gold-poly2 structure comes from the gold layer. One way to reduce mass without reducing the surface area is to decrease the amount of gold that covers the polysilicon structure. Unfortunately, this would also decrease initial deflection, according to the modeling from Chapter 4.

In order to sustain flight, the force during the downward stroke must be greater than both the force during the upward stroke and the force due to gravity:

$$C_D\frac{1}{2}\rho\Delta U^2 A \geq mg\,, \tag{5.10}$$

where ΔU is the difference in the upward and downward flapping velocities. It is given in Equation 5.11:

$$\Delta U = \delta\left(\frac{1}{\tau_{down}} - \frac{1}{\tau_{up}}\right) = \delta\left(\frac{\tau_{up} - \tau_{down}}{\tau_{down}\tau_{up}}\right), \tag{5.11}$$

where δ is the downward deflection, τ_{down} is the time required to deflection downward, and τ_{up} is the time required to return to the initial position—i.e., the cooling time.

The asymmetry required to hover could be achieved by varying the wing area, but this would be difficult to accomplish with current MEMS fabrication technologies. Since the cooling time is longer than heating time in thermal actuators, it is easiest to let the velocity be asymmetric between the upward and downward strokes.

To summarize, important design elements are deflection, surface area, and mass. By increasing the wing deflection by one unit, the downward stroke force increases by a power of two. Therefore, deflection is the most important element, and it should be maximized with every available means. In addition, it is important to maximize surface area while minimizing mass, which is possible only by using a less dense or thinner material. More surface area increases thrust and decreases the time required for cooling. A shorter cooling time allows the microrobot to respond to high-frequency input pulses, which increases the downward thrust.

However, in order for the microrobot to sustain flight, there must be some asymmetry between the upward and downward strokes. This naturally occurs in thermal actuators due to the slower upward velocity caused by a longer cooling time. Decreasing the drag on the upward stroke is also an alternative, which could be accomplished in one of two ways: decreasing the wing area on the upward stroke; or making the wing cup-shaped so that it is less aerodynamic on the downward stroke than on the upward stroke. Curved structures are difficult to fabricate due to the planar nature of the fabrication process. Changing the area during the flapping cycle could be achieved using fold-down hinges, but this would add complexity and weight to the devices.

5.3 PolyMUMPs® Fabrication Process

The microrobots can be fabricated in PolyMUMPs®—Polysilicon Multi-User MEMS Processes—which is a commercially available process. This process is used most often by universities and researchers in order to prove the efficacy of a particular device concept. Its thin polysilicon and gold layers make it ideal for fabricating flying microrobots. The available PolyMUMPs® layers are illustrated in Figure 5.3.

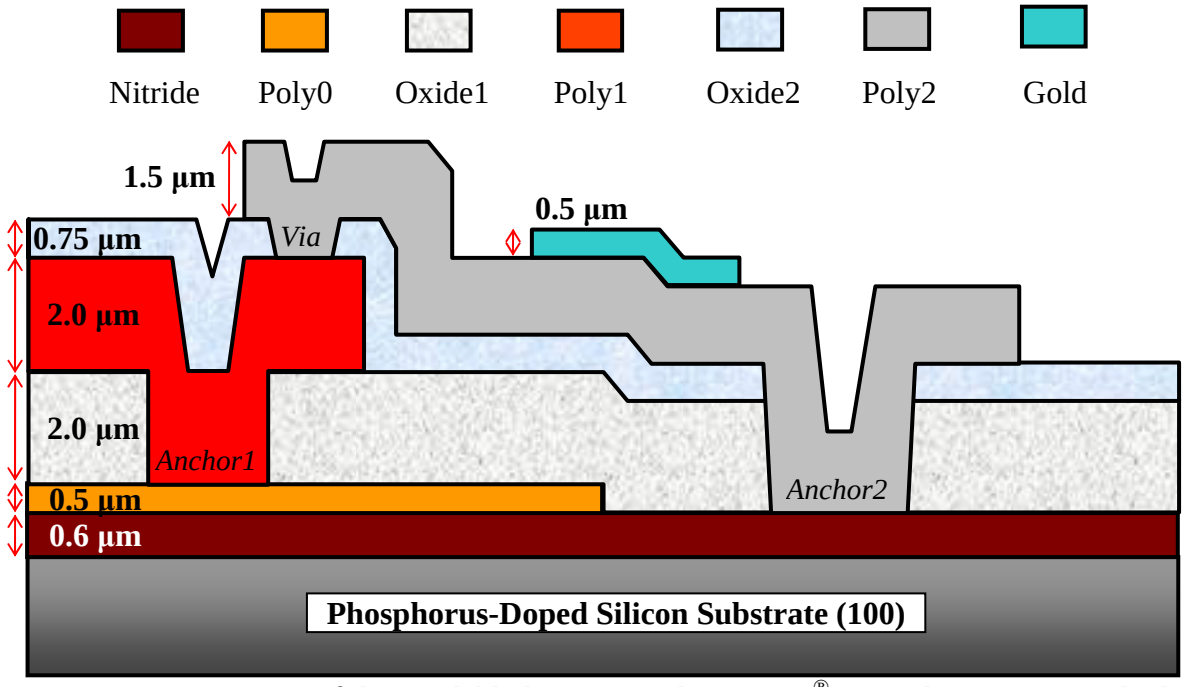


Figure 5.3: Diagram of the available layers in PolyMUMPs®. Nitride is a 0.6-µm-thick insulating layer; poly0 is a 0.5-µm-thick non-releasable polysilicon layer; poly1 is a 2.0-µm-thick and poly2 is a 1.5-µm-thick releasable polysilicon layer; gold is a 0.5-µm-thick layer deposited only on poly2; oxide1 is a 2.0-µm-thick and oxide2 is a 0.75-µm-thick highly doped silicon dioxide layer. Anchor1, anchor2, and via are oxide etches.

The PolyMUMPs® fabrication process starts with an n-type silicon wafer oriented in the (100) plane, and the process follows in this sequence: a 0.6-µm-thick silicon nitride layer (nitride) is deposited on the substrate using LPCVD (low pressure chemical vapor deposition); a 0.5-µm-thick LPCVD polysilicon layer (poly0) is deposited and lithographically patterned; a 2.0-µm-thick phosphorus-doped sacrificial oxide layer

(oxide1) is deposited and etched; a 2.0-μm-thick LPCVD polysilicon layer (poly1) is deposited and patterned; a 0.75-μm-thick oxide layer (oxide2) is deposited and etched; a 1.5-μm-thick LPCVD polysilicon layer is deposited and patterned; and, finally, a 0.5-μm-thick gold layer is deposited by electron-beam evaporation and patterned by a lift-off technique [16]. As illustrated in Figure 5.3, the deposited layers conform to the layers underneath. There are four oxide etches in this process: anchor1, anchor2, via, and dimple (not shown). Anchor1 and anchor2 allow poly1 and poly2, respectively, to be anchored to the substrate, and the via etch allows poly1 and poly2 to be connected. Dimple is 0.75-μm-deep etch into oxide1; this yields bumps or dimples in the poly1 layer, which reduces stiction. Refer to [17] for more details of the fabrication process.

The cost of one fabrication run is $3,200, and the product package includes 15 copies of a 1 x 1-cm^2 die. The fabrication time of a MUMPs® run is approximately seven weeks. After fabrication, the chips may be subdiced. Following this, the sacrificial oxide must be released to free the poly1 and poly2 structural layers. The release process is described in Chapter 6. The relatively low cost and short fabrication time are advantages to using PolyMUMPs®.

5.4 Microrobot Design Concept

It is clear from Table 5.1 that certain trade-offs must be made in the design. The microrobot designs must be focused on maximizing deflection since it is the most important design element. This can be achieved in two ways: by depositing two materials with a large coefficient of thermal expansion difference between them, and by reducing wing stiffness. Gold and polysilicon are commercially available and meet this criterion. As mentioned previously, the residual stress in the two materials results in a

natural upward deflection. This simplifies the flapping process by requiring only one direction for actuation. Reducing stiffness is achieved by making long, thin structures, but these would have little area for generating thrust. A bi-mutual trade-off can be made by making flexures with a narrow base for easier bending and a wide end for increased area. This shape resembles a piece of a pie, and the natural configuration for combining all the flexures is a circle. This design is illustrated in Figure 5.4.

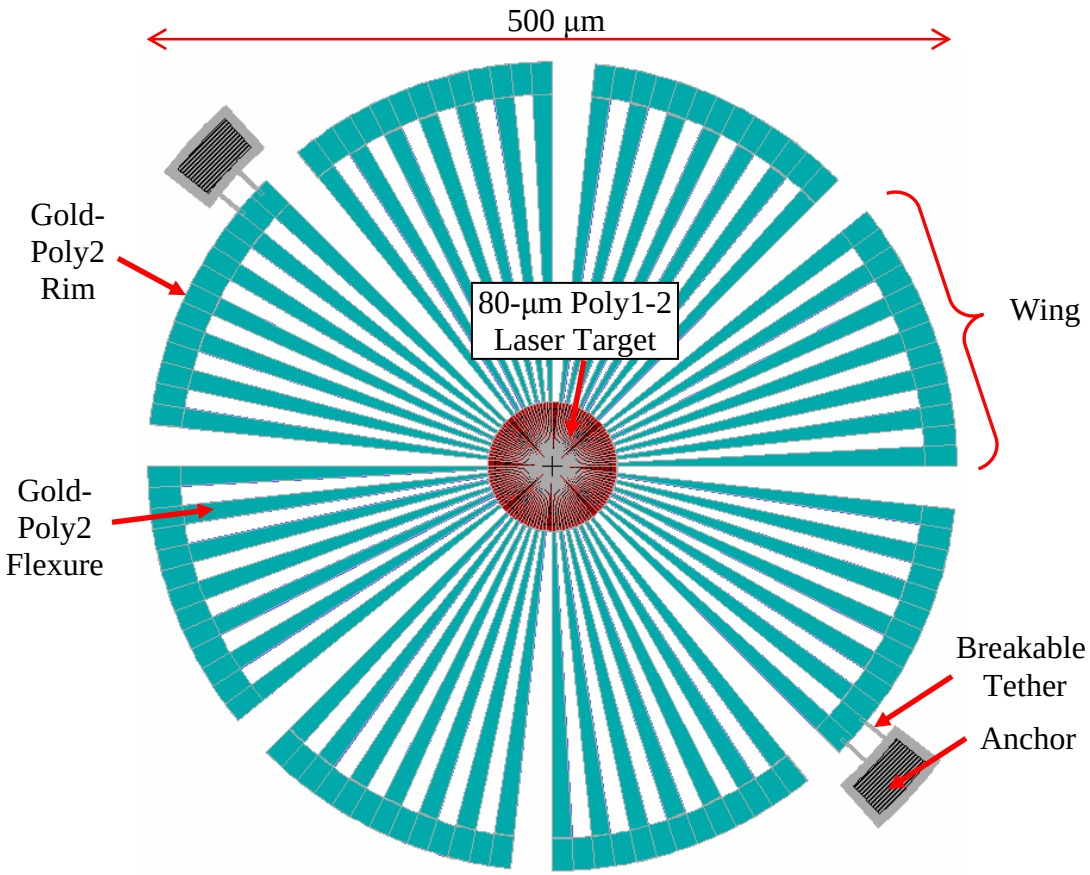


Figure 5.4: Diagram of an eight-wing 500-µm gold-polysilicon microrobot concept. The aqua-colored areas represent gold deposited over poly2. The red center area represents an 80-µm laser target that is made of stacked poly1 and poly2 layers without gold. To reduce stiffness, each wing flexure is made of poly2, which is thinner than poly1; the flexures are narrow at the center of the microrobot and become wider away from the center in order to increase area. Gold-poly2 structures deflect upward due to stress in the layers. The microrobot is anchored to the substrate through breakable tethers.

Each microrobot component is labeled in Figure 5.4. The entire 500-µm-diameter microrobot is composed of poly2 and gold, except for the 80-µm-diameter center that

receives the laser energy. In order to maximize laser energy absorption, this laser target area should be made of thick, non-reflective polysilicon; thus it is made of poly1 and poly2 but not gold. The gold layer is deposited over the rest of the microrobot—the flexures and the rim—to maximize initial vertical deflection. Unfortunately, this large amount of gold significantly increases the microrobot mass. Narrow, thin flexures help maximize deflection and minimize mass. However, narrow flexures reduce surface area.

One method to reduce the mass of the microrobot is to reduce the number of wings, but this also reduces the amount of surface area. The gaps between the wing flexures can be filled with polysilicon and not gold; this increases surface area with an only slight increase in mass. The ends of the flexures near the laser target are kept narrow to reduce bending stiffness. Since the laser energy is at its highest concentration near the center, this is the most critical area for bending. A four-wing, 500-µm microrobot following this design concept is illustrated in Figure 5.5.

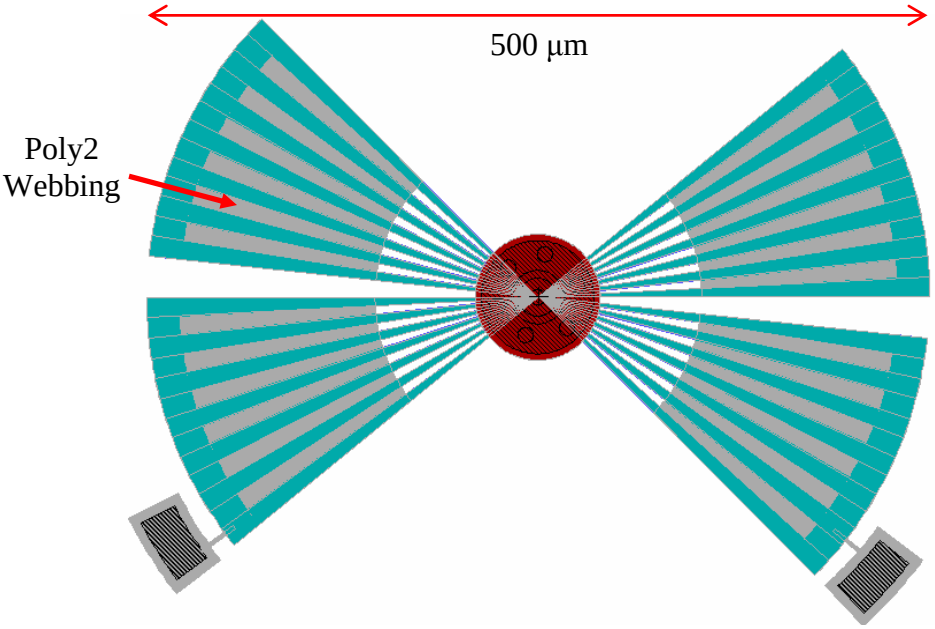


Figure 5.5: Diagram of a four-wing 500-µm gold-polysilicon microrobot design concept. The number of wings is reduced in order to reduce mass, but this also reduces surface area. To compensate, polysilicon is used to fill the gaps between the gold-poly2 flexures. All the other components are identical to the previous microrobot.

5.5 Microrobot Design Details

Scanning-electron microscope (SEM) images of microrobots fabricated in MUMPs® are given in Figure 5.6 and Figure 5.7. These correspond to the design concepts from Figure 5.4 and Figure 5.5. The images were taken following the sacrificial oxide release. Clearly visible are the gold-poly2 flexures, the poly2-poly1 center laser target, and the poly2 substrate anchors. Dimples in the laser target prevent the microrobot from sticking to the surface. Also noticeable are gold stringers that were caused by intentionally depositing gold too close to the poly2 edge. The purpose of this design rule violation is to maximize initial deflection by increasing the amount of gold.

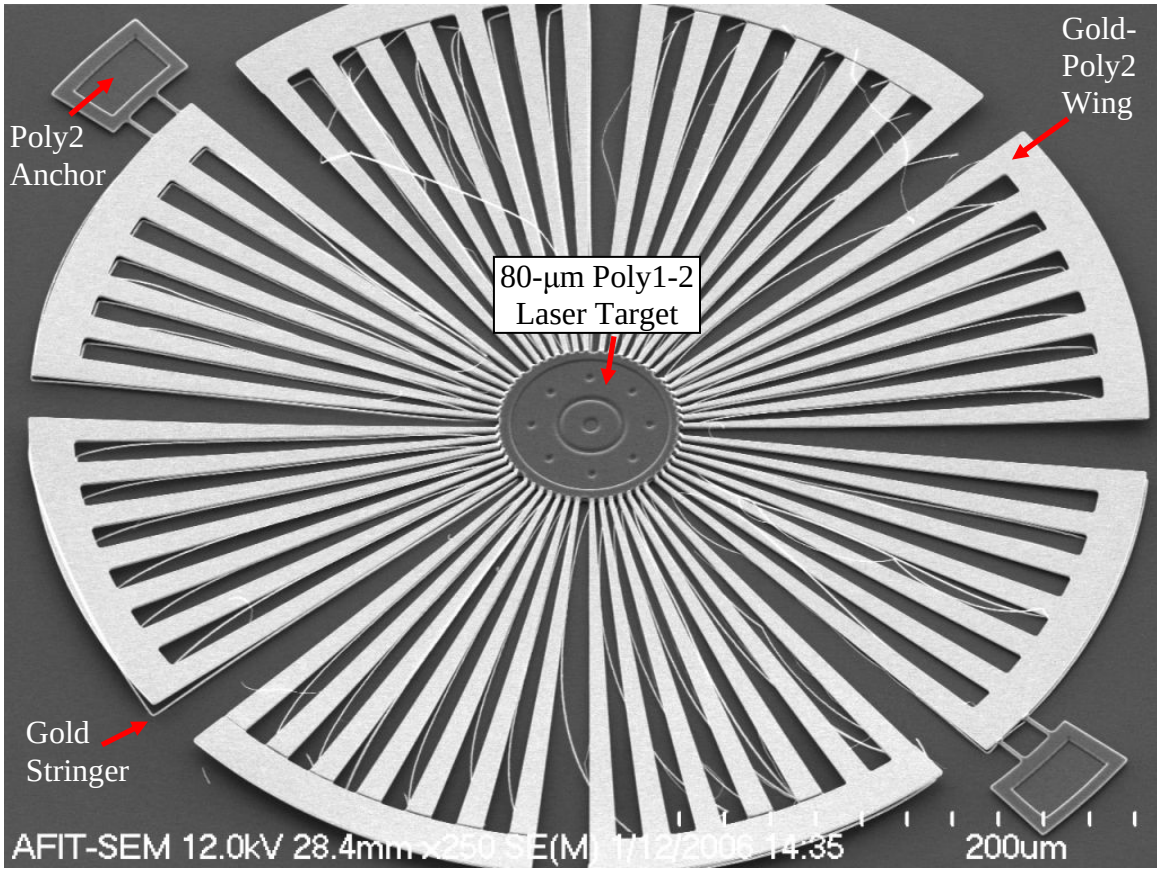


Figure 5.6: SEM micrograph of an eight-wing 500-μm gold-polysilicon microrobot fabricated in MUMPs®. The space between each pair of tick marks on the scale is 20 μm. This microrobot corresponds to the diagram in Figure 5.4. The gold stringers resulted from depositing gold too close to the poly2 edge.

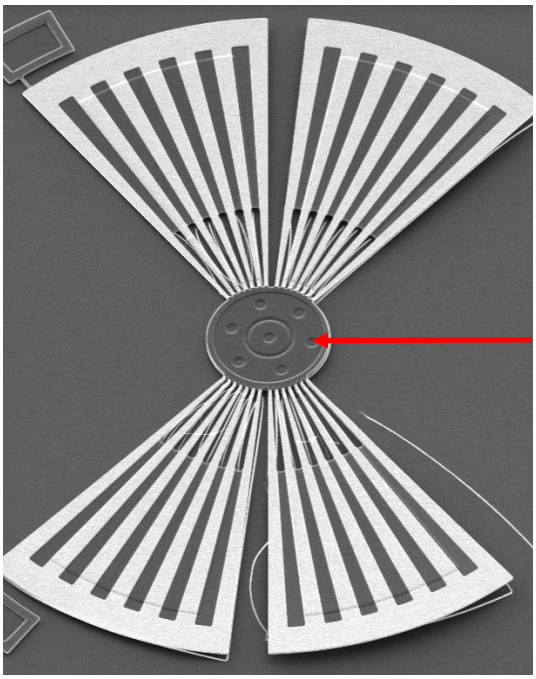


Figure 5.7: SEM micrograph of a four-wing 500-μm gold-polysilicon microrobot fabricated in MUMPs®. Notice the dimples in the poly1-poly2 laser target area, which prevent the center from sticking to the substrate. This design corresponds to Figure 5.5.

Throughout this thesis research, 129 different microrobots were designed and fabricated in PolyMUMPs®. The purpose of fabricating so many microrobots was to determine which design elements contributed to maximum deflection. Many test structures were also fabricated to isolate particular design elements. Each die from PolyMUMPs® was sub-diced into 25 2 x 2-mm^2 chips. An overview of the 27 chips fabricated for this thesis is given in Table 5.2. An SEM micrograph of an entire 2 x 2-mm^2 microrobot chip is given in Figure 5.8.

Table 5.2. Overview of the 27 microrobot and test-structure chips of this thesis.

MUMPs® Run	# of Microrobot Chips	Microrobot Design Types	# of Test-Structure Chips
66	1	8-wing 500-μm robots	1
67	2	8-wing and 4-wing 500-μm robots	1
68	8	8-wing and 4-wing 500-μm robots	1
69	12	8-wing and 4-wing 500-μm robots, 2-wing 990-μm robots	1

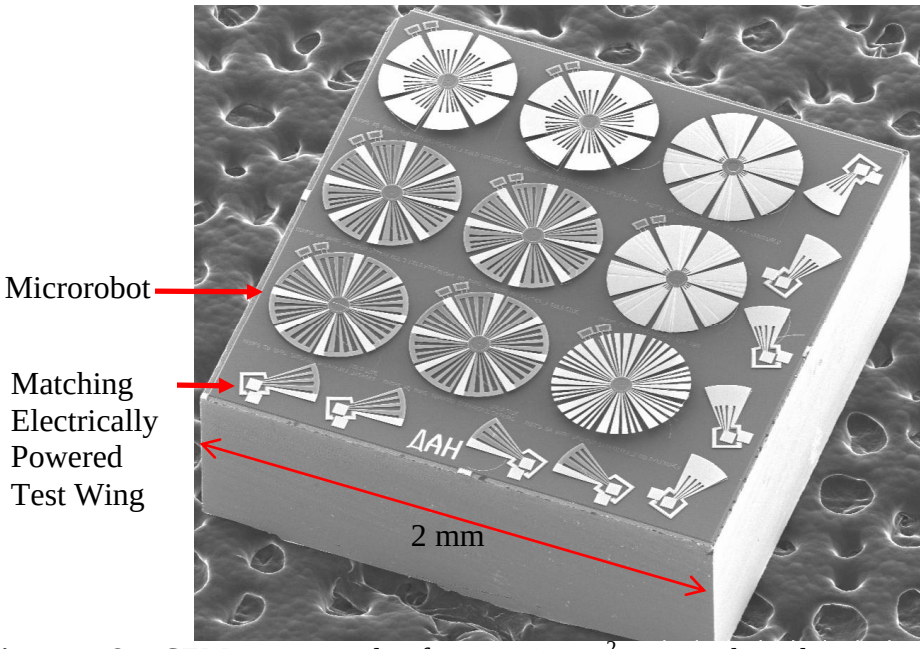


Figure 5.8: SEM micrograph of a 2 x 2-mm^2 microrobot chip containing 9 500-µm robots and matching electrically powered test wings.

As indicated in Table 5.2, not all the microrobots fabricated were 500 µm in diameter. Taking inspiration from insect studies, a few 990-µm microbots were also designed and fabricated. One is illustrated in Figure 5.9.

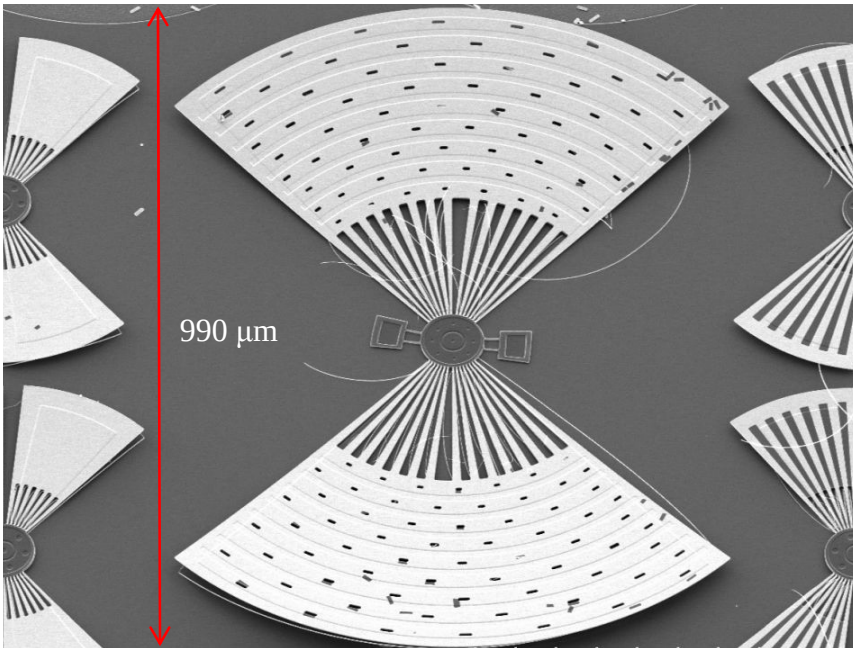


Figure 5.9: SEM micrograph of a two-wing 990-µm microrobot surrounded by 500-µm microrobots. This larger microrobot was designed based on an insect study that recommended using only two wings and making the surface area as large as possible.

One reason so many microrobots were fabricated was to improve certain features. For example, the microrobots need to be anchored to the substrate until they are ready for testing. The position of the anchors proved to be significant during the release, drying, and measuring processes. Figure 5.10 shows SEM micrographs of a poly2 substrate anchor attached to one side of a microrobot. Anchors on one side of the microrobot result in fragile, vulnerable devices, especially during the release and drying steps. A Zygo® data image of the microrobots is given in Figure 5.11, and Figure 5.12 illustrates how several microrobots anchored on one side were destroyed in the drying chamber.

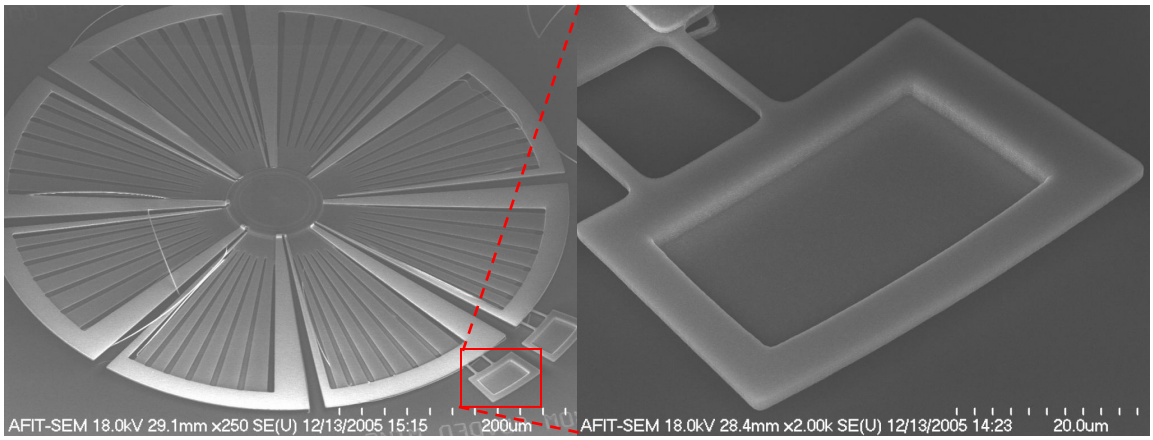


Figure 5.10: SEM micrographs of (left) a microrobot with the anchors on one side and (right) a poly2 substrate anchor with breakable tethers.

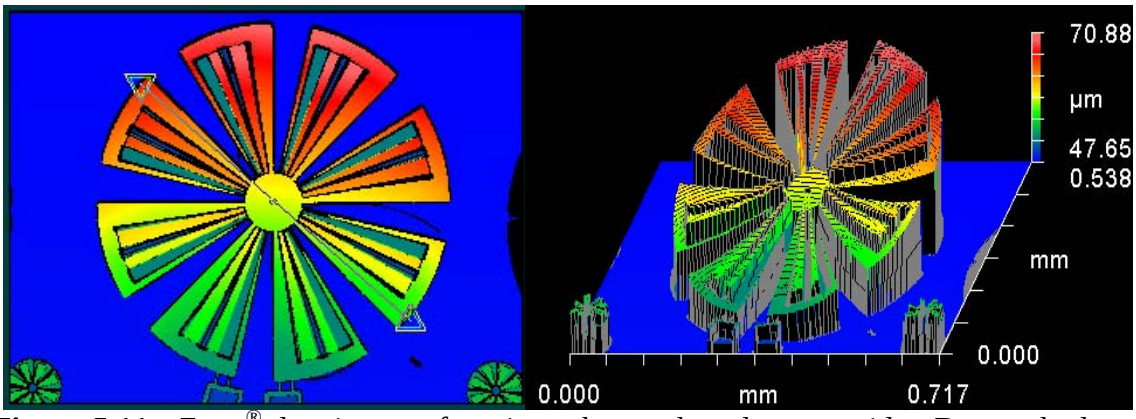


Figure 5.11: Zygo® data image of a microrobot anchored on one side. Due to the large surface area of the robot, the large deflection, and the thin tethers, microrobots anchored on one side are fragile and vulnerable to the turbulent drying process.

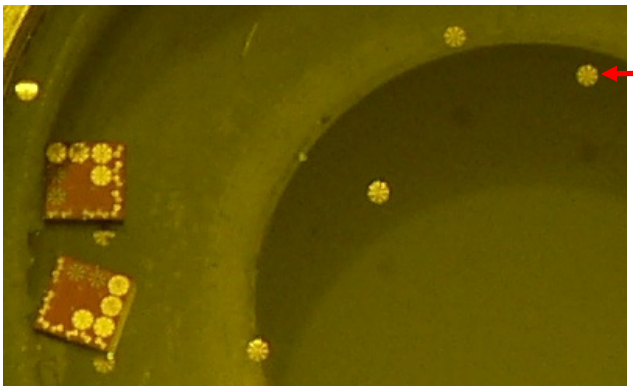


Figure 5.12: Photograph of microrobots that were destroyed in the drying chamber.

One solution to this problem is to use more anchors, but a better solution is to put anchors on opposite sides of the microrobot. Figure 5.13 and Figure 5.14 illustrate how anchors on both sides improve device security and ease of measuring the deflection.

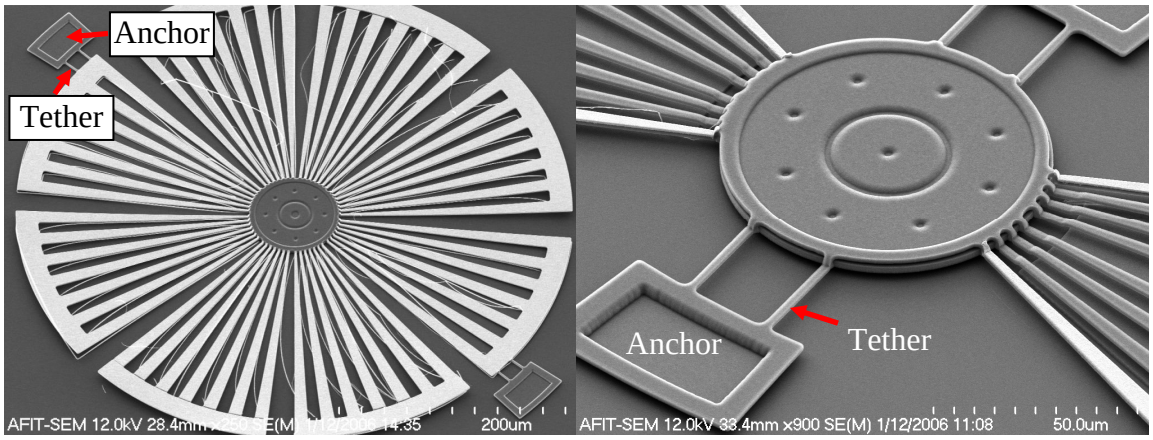


Figure 5.13: SEM micrographs of microrobots with tethers on opposite sides of the device. In this configuration, the microrobots are less vulnerable to the drying process.

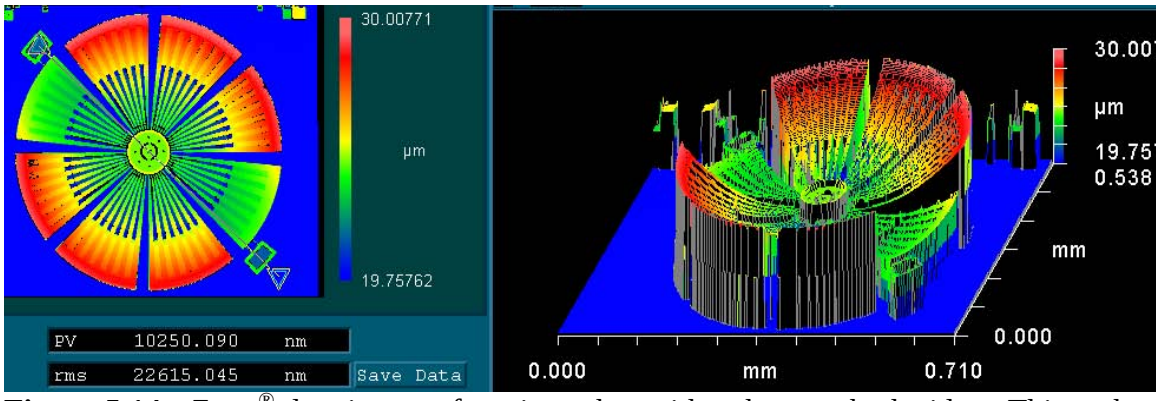


Figure 5.14: Zygo® data image of a microrobot with tethers on both sides. This makes the microrobots less vulnerable to drying turbulence, and it also facilitates measuring deflection.

Another design iteration included making the laser target area thick to increase the energy absorption. Before the optical absorption theory was understood, the centers of early microrobot designs were made of only poly2. In later designs, the center laser target thickness was increased by depositing poly1 under the poly2 and connecting the two layers with a via etch. The thicker poly1-poly2 center absorbs more photon energy, which generates more heat for downward deflection. Figure 5.15 illustrates both designs.

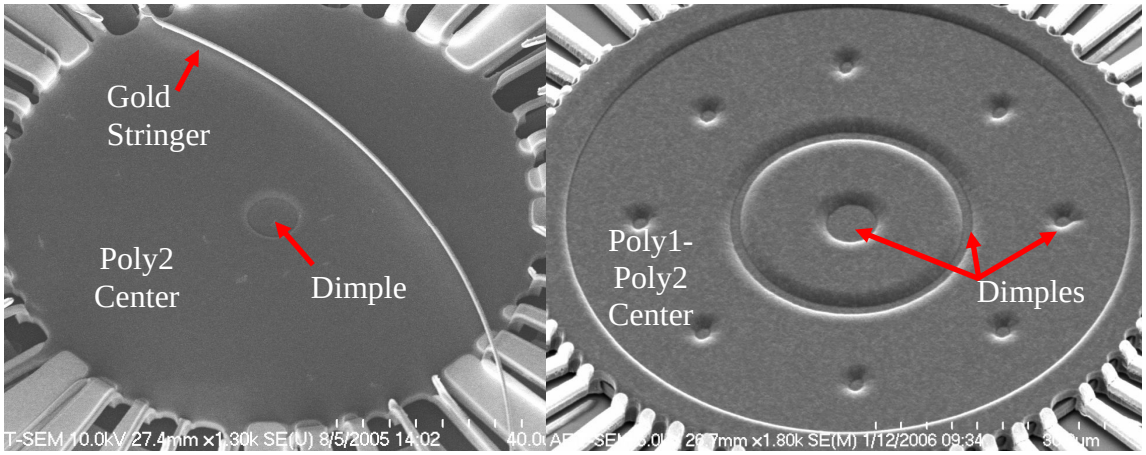


Figure 5.15: SEM micrographs of (left) a microrobot center with just poly2, and (right) poly1-poly2 center connected through a via oxide etch. The thicker poly1-poly2 center allows the microrobot to absorb more laser energy than does the thinner center. Notice the dimples that help prevent the device from sticking to the substrate.

The main reason so many microrobots were designed and fabricated was to determine how certain design elements affected initial deflection. These elements include varying flexure width and spacing, adding an unattached spacer layer under the wings to improve wing aerodynamics, and varying the amount of gold on each wing. As will be reported in Chapter 7, hundreds of initial deflection measurements were taken with the Zygo®. These deflection measurements helped determine the optimum design solution—the one that yielded the most initial deflection and surface area while minimizing mass. Closely examining the microrobots using the SEM also identified ways to improve the designs.

In determining the effect of flexure width and spacing on deflection, both extremely narrow flexures and narrowly spaced flexures were fabricated. The SEM illustrated poor gold adhesion to the poly2 layer in extremely narrow flexures. This is a problem because the device cannot deflect up or down as much unless the two layers remain connected. In narrowly spaced flexures, the poly2 layer of each flexure merged with the adjacent flexures. This resulted in one very wide flexure instead of narrower, individual flexures. Both cases are illustrated in Figure 5.16.

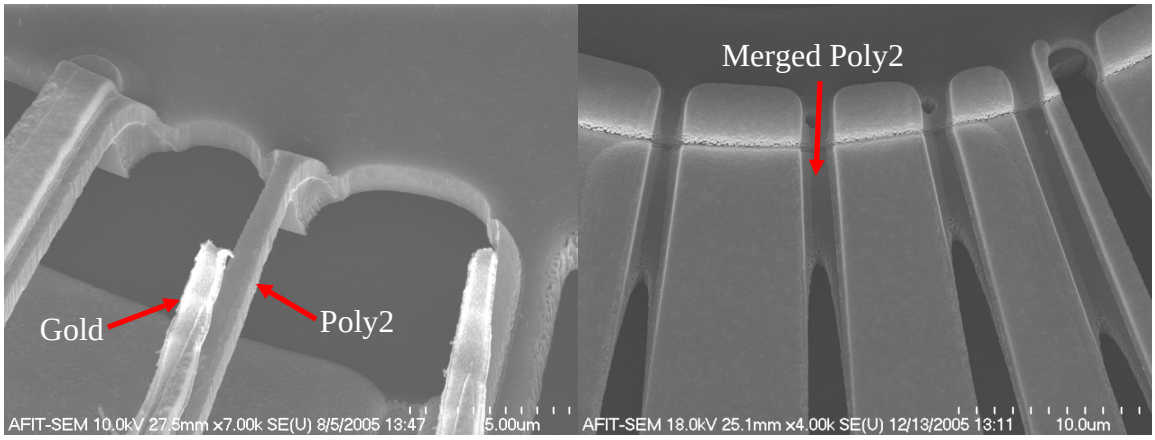


Figure 5.16: SEM micrographs of (left) the poor gold adhesion that results from making the gold-poly2 flexures too narrow; (right) the merging poly2 flexures that results from making the flexure spacing too close. The solution to these problems is to make the flexures just wide enough so that the gold adheres and making the spacing just close enough so that the poly2 does not merge. The effect of flexure width and spacing on initial deflection is examined in detail in Chapter 7.

In an attempt to improve the wing aerodynamics, a layer of poly1 was deposited and anchored to the substrate. Poly2 was deposited over this layer but not connected to it. Due to the conformal nature of the LPCVD process, the poly2 is molded by whatever lies beneath it. The result is a cupping shape in the wing, which could slightly increase drag on the downward wing stroke and reduce drag on the upward stroke. It was found, however, that the poly1 layer was restricting the microrobot from being moved around the chip due to the thickness of poly1. An alternative approach is to use the thinner poly0

layer. The microrobots with poly0 were easily movable. Both are illustrated in Figure 5.17. The disadvantage, however, of using poly0 is it does not raise the flexures as much as the poly1 layer. The flexures are raised 2 μm by poly1 and 0.5 μm by poly0. The effect of these spacer layers on initial deflection is reported in Chapter 7.

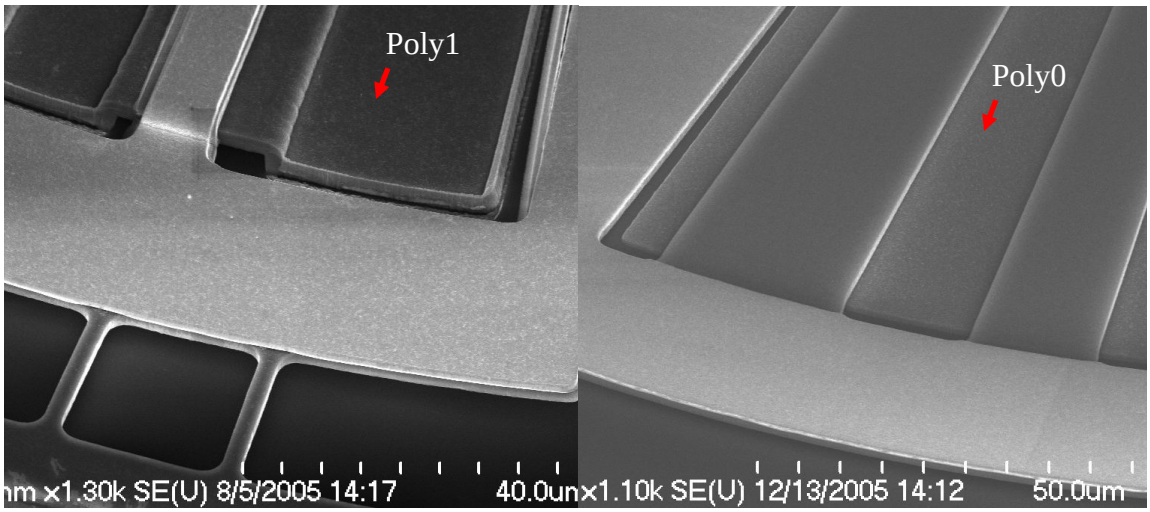


Figure 5.17: SEM micrographs of (left) the unattached poly1 spacer under the center of the wing and (right) that poly0 spacer. The poly1 layer raises the flexures by 2 μm, but it prevents the microrobot from moving around the chip; the poly0 layer raises the flexures by only 0.5 μm, but it allows the microrobot to be moved. The effect of these spacer layers on initial deflection is given in Chapter 7.

As will be discussed later, it is impossible to measure laser-powered deflection with the Zygo®. Therefore, it is impossible to achieve precise laser-powered downward deflection measurements. There needs to be a benchmark for comparing the power-deflection relationship among the different devices. This is possible by making electrically powered wings that are testable with the Zygo®. These test wings match the design configurations of the laser-powered microrobots. By applying a voltage potential across each test wing, current flows throughout the wings according to Ohm's Law. This current results in Joule heating within the polysilicon, and the heat imitates the heat absorbed from the laser. Figure 5.18 illustrates a chip full of electrically powered test wings corresponding to 500-μm and 990-μm microrobots.

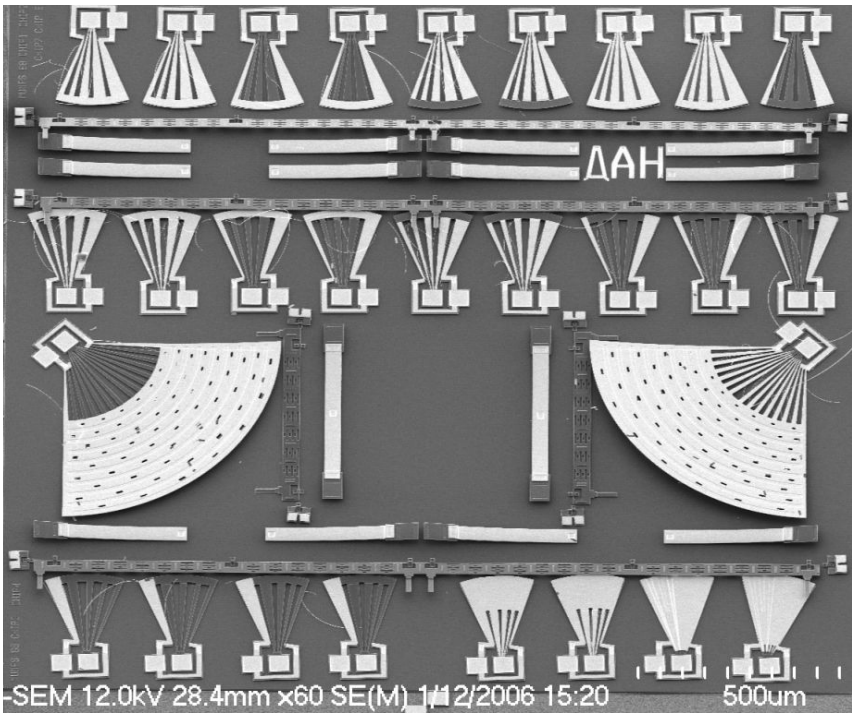


Figure 5.18: SEM micrograph of electrically powered test wings for several microrobot wing configurations. By applying a voltage at each probe pad, a current flows throughout the wing according to Ohm's Law and heats up the device. The heat causes the device to deflect downward in the same manner as the laser energy.

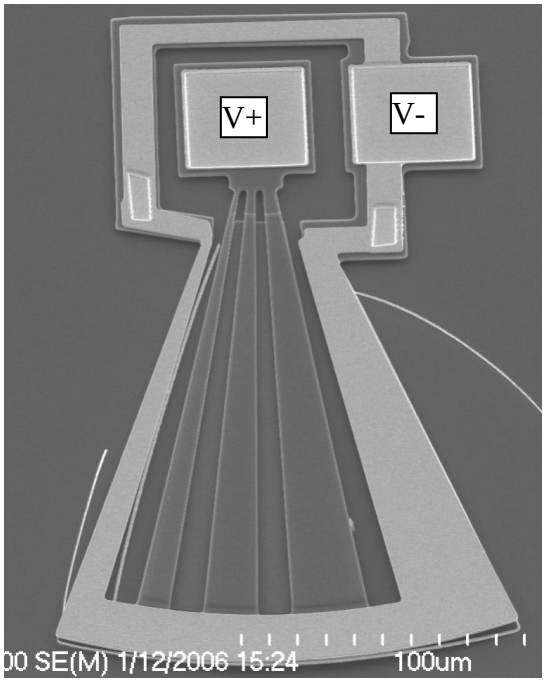


Figure 5.19: Close-up SEM micrograph of an electrically powered test wing corresponding to a 500-μm microrobot. The voltage potential is applied at each probe pad which allows current to flow and heat up the device. The downward deflection can then be measured under the Zygo®.

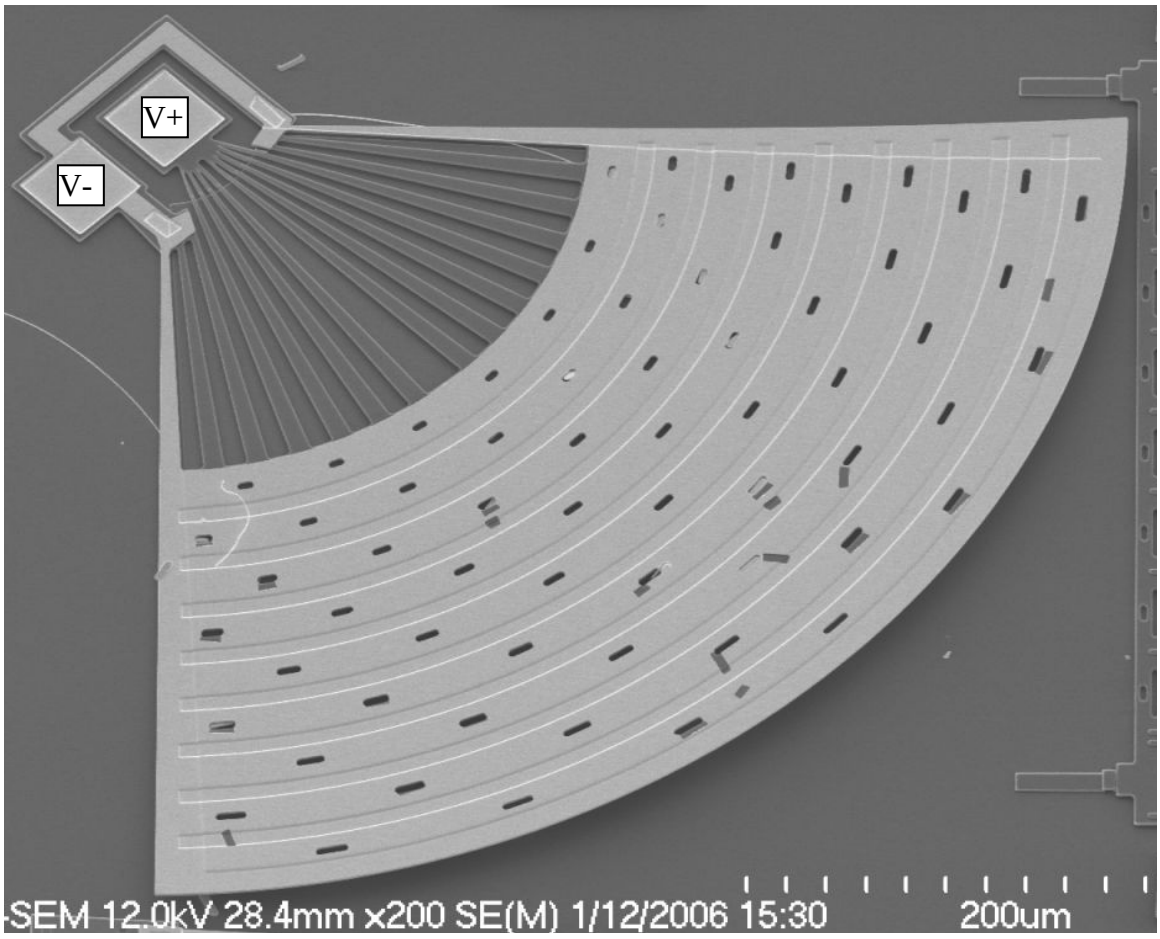


Figure 5.20: Close-up SEM micrograph of an electrically powered test wing corresponding to a 990-μm microrobot. The voltage potential is applied at each probe pad which allows current to flow and heat up the device. The downward deflection can then be measured under the Zygo®.

5.6 Summary

This chapter explained the device concept for 500-μm and 990-μm ornithoptic microrobotics. Inspiration for the designs came from insect studies, theory, modeling, and the sponsor's requirements. It was determined that maximizing wing deflection and area while minimizing mass are the key ingredients for a flying microrobot. The most important of these elements is initial deflection, and over 100 microrobots were designed and fabricated to investigate how to maximize initial deflection. The results are given in Chapter 7.

5.7 References

[1] F. R. Szabo, *Demonstrating Optothermal Actuators for an Autonomous MEMS Microrobot*, MS thesis, AFIT/GE/ENG/04-23. School of Engineering and Management, Air Force Institute of Technology (AU), Wright-Patterson AFB OH, March 2004 (AD-A426469).

[2] I. Shimoyama, "Scaling in Microrobots," *Proceedings of the IEEE*, pp. 208–211, 1995.

[3] C. P. Ellington, "The Novel Aerodynamics of Insect Flight: Applications to Micro-Air Vehicles," *Journal of Experimental Biology*, vol. 202, pp. 3439–3448, 1999.

[4] R. Ramamurti and W. C. Sandberg, "A Three-Dimensional Computational Study of the Aerodynamic Mechanisms of Insect Flight," *Journal of Experimental Biology*, vol. 205, pp. 1507–1518, 2002.

[5] S. P. Sane, "The Aerodynamics of Insect Flight," *Journal of Experimental Biology*, vol. 206, pp. 4191–4208, 2003.

[6] L. A. Miller and C. S. Peskin, "When Vortices Stick: An Aerodynamic Transistion in Tiny Insect Flight," *Journal of Experimental Biology*, vol. 207, pp. 3073–3088, 2004.

[7] F. Togashi, Y. Ito, M. Murayama, K. Nakahashi, and T. Kato, "Flow Simulation of Flapping Wings of an Insect using Overset Unstructured Grid," *Proceedings of the 15th AIAA Computational Fluid Dynamics Conference*, AIAA 2001-2619, Anaheim, CA, 11–14 Jun. 2001.

[8] J. Szmelter and R. Zbikowski, "Progress in Aerodynamic Studies of Micro Air Vehicles Based on Insect-Like Flapping Wings," *Proceedings of the 41st Aerospace Sciences Meeting and Exhibit*, AIAA 2003-419, Reno, NV, 6–9 Jan. 2003.

[9] D. Lentink and M. Gerritsma, "Influence of Airfoil Shape on Performance in Insect Flight," *Proceedings of the 33rd AIAA Fluid Dynamics Conference and Exhibit*, AIAA 2003-3447, Orlando, FL, 23–26 Jun. 2003.

[10] A. Muniappan, V. Baskar, and V. Duriyanandhan, "Lift and Thrust Characteristics of Flapping Wing Micro Air Vehicle (MAV)," *Proceedings of the 43rd AIAA Aerospace Sciences Meeting and Exhibit*, Reno, NV, 10–13 Jan. 2005.

[11] B. Singh, M. Ramasamy, I. Chopra, and J. G. Leishman, "Experimental Studies on Insect-Based Flapping Wings for Micro Hovering Air Vehicles," *Proceedings of the 46th AIAA/ASME/ASCE/AHS/ASC Structures, Structural Dynamics and Materials Conference*, AIAA 2005-2293, Austin, TX, 18–21 Apr. 2005.

[12] S. Baglio, S. Castorina, L. Fortuna, and N. Savalli, "Development of Autonomous, Mobile Micro-Electro-Mechanical Devices," *Proceedings of the 2002 IEEE International Symposium on Circuits and Systems—ISCAS 2002*, vol. 4, pp. 285–288, Phoenix-Scottsdale, AZ, 26–29 May 2002.

[13] S. Baglio, S. Castorina, L. Fortuna, and N. Savalli, "Technologies and Architectures for Autonomous 'MEMS' Microrobots," *Proceedings of the 2002 IEEE International Symposium on Circuits and Systems—ISCAS 2002*, vol. 2, pp. 584–587, Phoenix-Scottsdale, AZ, 26–29 May 2002.

[14] S. Baglio, S. Castorina, L. Fortuna, and N. Savalli, "Novel Microactuators Based on a Photo-Thermo-Mechanical Actuation Strategy," *Proceedings of the 1st IEEE Conference on Sensors*, vol. 1, pp. 192–197, Orlando, FL, 12–14 Jun. 2002.

[15] S. Baglio, S. Castorina, L. Fortuna, and N. Savalli, "Modeling and Design of Novel Photo-Thermo-Mechanical Microactuators," *Sensors and Actuators A: Physical*, vol. 101, pp. 185–193, 2002.

[16] W. D. Cowan, V. M. Bright, M. K. Lee, J. H. Comtois, and M. A. Michalicek, "Design and Testing of Polysilicon Surface-Micromachined Piston Micromirror Arrays," *Proceedings of SPIE*, vol. 3292, pp. 60–70, April 1998.

[17] D. Koester, A. Cowen, R. Mahadevan and B. Hardy, *PolyMUMPs Design Handbook: A MUMPs® Process* (Revision 10.0), MEMSCAP®. www.memscap.com/memsrus/docs/PolyMUMPs.dr.v10.pdf, 2003.

VI. Experiments and Procedures

6.1 Chapter Introduction

Descriptions of three major experiments comprise this chapter: optimizing the laser experiment used to power MEMS robots, performing the post-fabrication sacrificial oxide release of the microrobot chips, and measuring microrobot performance. Concise, repeatable procedures of these experiments are also included for follow-on researchers.

6.2 660-nm Laser Diode Operation

The laser used to test the microrobots is a 660-nm AlGaInP laser diode with a 40-mW continuous-wave (CW) optical power output; for pulsed operation, the maximum power is 60 mW. This laser diode, with all its required operating hardware, was used in previous microrobotics research [1]. The details of the laser operation hardware are included in Table 6.1, and photographs of the devices are shown in Figure 6.1.

Table 6.1. Laser diode and hardware required for continuous and pulsed operation.

Item	Relevant Specifications	Function
Thorlabs® ML101J8 Laser Diode	660 nm; single mode; 5.6 mm; AlGaInP; 40-mW (CW), 60-mW (pulse) max output power; 53-mA threshold current; 109-mA operating current	Produces laser beam
Thorlabs® TCLDM9 Diode Mount and Collimating Lens	Holds 5.6 or 9 mm diodes; 0 to 70 °C temp range; 2-A max laser current; 20-W cooling capacity; uses AD592 IC temp sensor or 10-kΩ thermistor	Holds diode; collimates laser beam
Thorlabs® TEC 2000 Temp. Controller	-40 °C to +150 °C temp control range; supports IC temp. sensors/thermistors; 10-min warm-up	Controls diode temp.
Thorlabs® LDC 500 Diode Controller	500-mA max output current; powers laser diodes/ photodiodes; CW and pulsed; 10-min warm-up	Powers diode
Thorlabs® LG4 Safety Glasses	3+ optical density (< 0.1% transmission) between 625 and 830 nm	Protects eyes
Agilent® 33250A Function Generator	80-MHz bandwidth; arbitrary sine, square, ramp, triangle, noise, DC, and pulse waveforms	Pulses diode

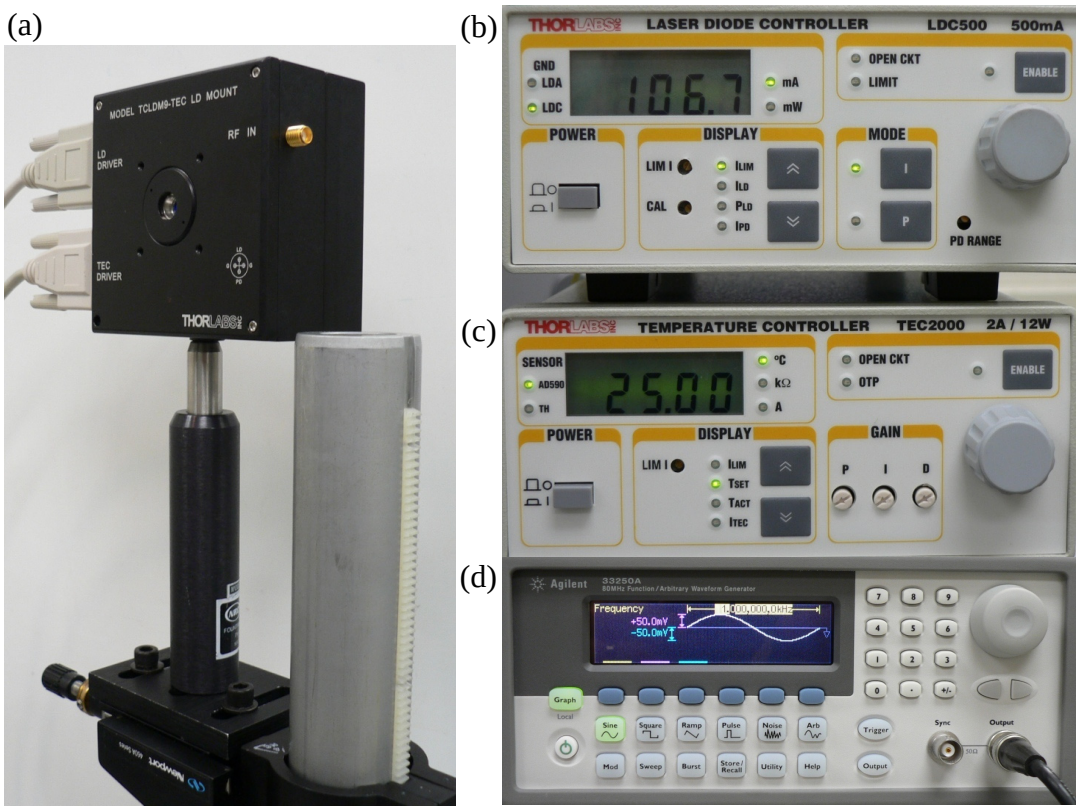


Figure 6.1: Photographs of laser operating equipment. (a) The ML101J8 laser diode is inside the TCLDJ8 diode mount; (b) the LDC 500 diode controller powers the diode; (c) the TEC 2000 temperature controller ensures the diode temperature is constant; (d) and the 33250A function generator modulates the LDC 500 controller for pulsed operation.

The laser diode is a class III device, which can cause serious damage to the unprotected eye. Safe operating procedures must be followed to avoid permanent injury. These procedures are contained in Appendix C, and simplified operating procedures for each device are contained in Appendix D.

6.3 Laser Diode Characterization

6.3.1 Current-Power Relationship

Each laser diode is manufactured to perform within a certain tolerance. Because of this variability, each diode needs to be characterized before use. This is accomplished by comparing measured optical output power with input current. In addition, like most semiconductor devices, laser diode performance is temperature-dependent. The power-

current relationships for several temperatures should also be accomplished to determine the diode sensitivity to temperature. Acquiring this data requires only a simple optical power meter and a digital multimeter (DMM), which are illustrated in Figure 6.2.

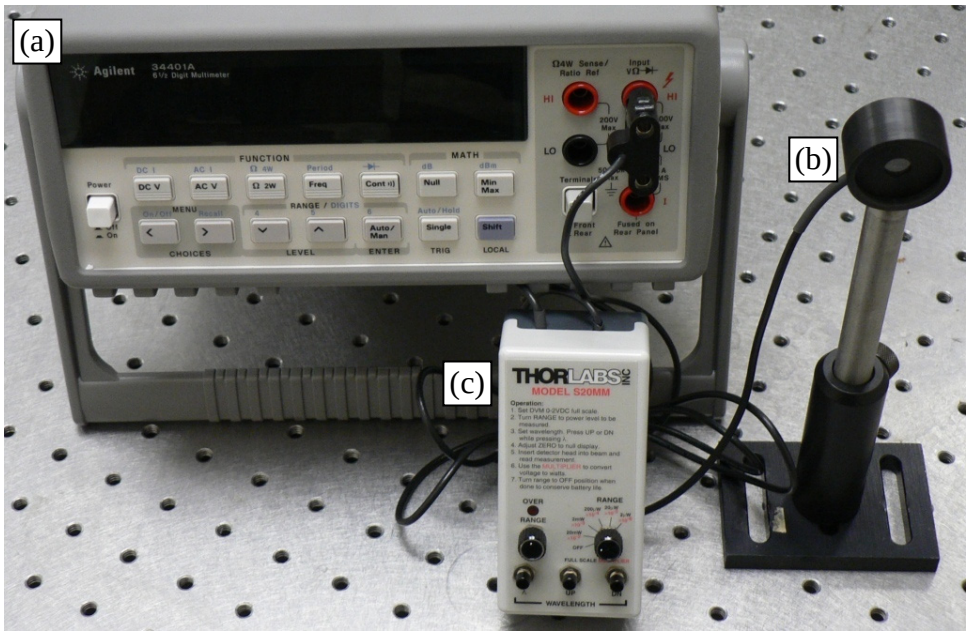


Figure 6.2: Photograph of equipment used to measure laser power. (a) The Agilent® 34401A digital multimeter displays the power values from (b) the Thorlabs® S20MM silicon power meter head and (c) the meter controller. Not shown are the absorptive neutral density filters that attach to the power meter for high-power measurements.

The power measuring limit of the silicon meter is 20 mW. Therefore, at least one absorptive neutral density (ND) filter must be added to characterize the entire 40-mW laser diode range. The power absorbed in the ND filter must be accounted for when recording the DMM readings. In addition to the standard laser operating equipment listed in Table 6.1, the equipment used to characterize the laser includes:

- Thorlabs® S20MM silicon power meter
- Thorlabs® absorptive neutral density filter ND = 0.3 (50 % transmission)
- Agilent® 34401A digital multimeter (DMM)

A simple procedure to characterize the power-current relationship is given in Table 6.2.

Table 6.2. Procedures for characterizing the diode power-current relationship.

- Turn on the laser temperature controller according to the TEC 2000 temperature controller operation procedures (Appendix D.1)
- Set T_{SET} to the desired diode operating temperature
- Turn on the laser diode controller according to the LDC 500 laser diode controller operation procedures (Appendix D.2)
- Turn on the DMM and set to measure voltage (0-2 V range)
- Turn on and zero the silicon power meter according to the S20MM power meter operation procedures (Appendix D.3)
- Record the DMM readings for each driver current value

The DMM displays the input signals from the power meter in volts. Converting the reading to milliwatts requires multiplying the voltage reading by the factor listed on the power meter. The characterization results for temperatures of 5, 15, 24.66 (average room temperature), and 35 °C throughout the diode range are plotted in Figure 6.3.

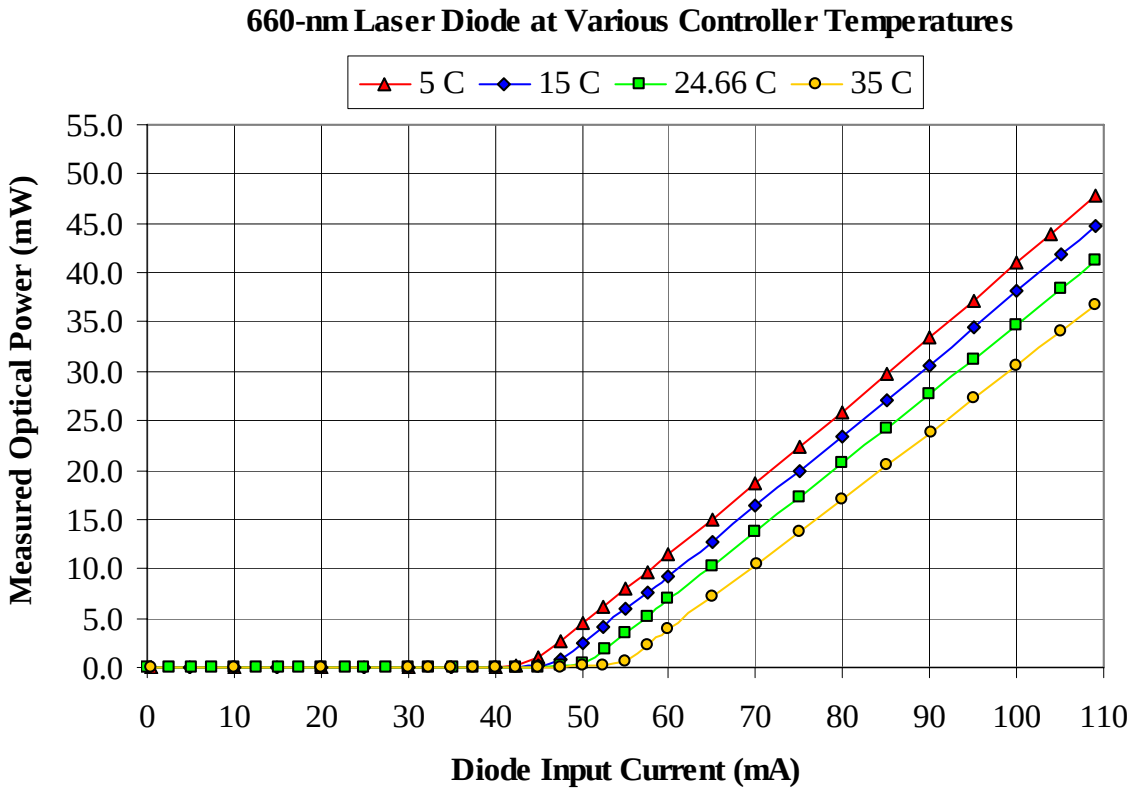


Figure 6.3: Graph of the measured current-power relationship for the 660-nm laser diode for various operating temperatures. Output power decreases with increased temperature, and threshold current increases with increased temperature.

The temperature sensitivity from Figure 6.3 is clear: for each 10-degree increase in temperature, the output power decreases by approximately 4 mW. Also evident in the graph is that the threshold current—the current required for lasing—increases by approximately 3–4 mA for each 10-degree increase in operating temperature.

6.3.2 Spot Size Characterization

The laser diode current-power relationship from the previous section is necessary to safely operate the device. With this data, other characterization experiments can be performed, such as determining the relationships between propagation distance and spot size as well as output power and spot size. These experiments are critical in order to minimize the power lost in directing and focusing the laser beam onto the robot. Otherwise, the performance of a successful robot could be limited by the laser test apparatus. A basic overview of Gaussian beam propagation is presented first.

6.3.2.1 Gaussian Beam Propagation Model

Most laser beams can be modeled as a Gaussian beam [2], where the beam radius $W(z)$ {mm} is a function of the propagation distance z {mm}:

$$W(z) = W_0 \left[1 + \left(\frac{z}{z_0} \right)^2 \right]^{\frac{1}{2}}. \tag{6.1}$$

The beam waist is the plane $z = 0$ where the beam radius assumes its minimum value W_0. The value W_0 {mm} is the waist radius, and the waist diameter $2W_0$ is called the spot size. The variable z_0 {mm} is the Rayleigh range, which is a measure of beam divergence: the smaller the Rayleigh range, the more the beam diverges. As given in Equation 6.1, the value of the beam radius at the Rayleigh range ($z = z_0$) is $1.414W_0$. Equation 6.1 also demonstrates that as the distance away from the beam waist ($z = 0$) increases, the beam radius increases, which is illustrated in Figure 6.4.

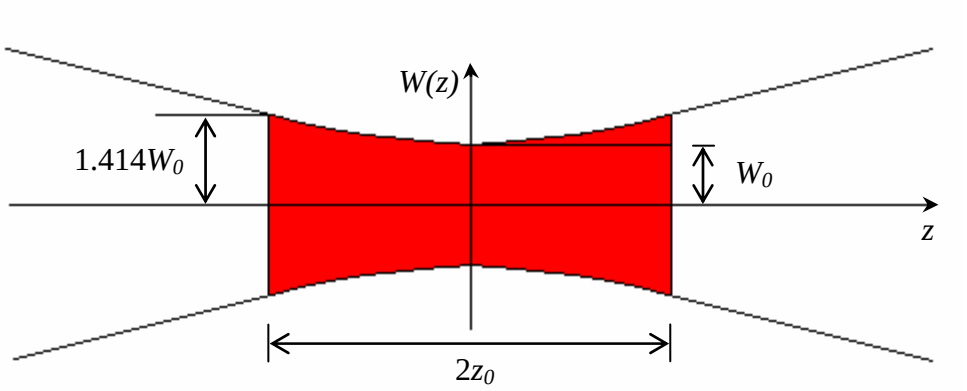


Figure 6.4: Diagram of a Gaussian beam propagating along the *z*-axis. The beam waist is located at $z = 0$, where the beam radius assumes its minimum value W_0, called the waist radius. The waist diameter $2W_0$ is the spot size. At the Rayleigh range ($z = z_0$), the beam radius is 1.414 times the waist radius ($1.414W_0$). Small Rayleigh range values correspond to highly diverging beams.

The depth of focus of a Gaussian beam is an important parameter that indicates the range within which the beam is in focus—it is illustrated in Figure 6.4 by the red section. A beam with a small depth of focus is difficult to keep focused. The depth of focus is twice the Rayleigh range ($2z_0$), and it is directly proportional to the waist radius W_0 and inversely proportional to the laser wavelength λ:

$$2z_0 = \frac{2\pi W_0^2}{\lambda}. \tag{6.2}$$

This equation shows that a narrowly focused beam—one with a small beam radius W_0—has a very small depth of focus. On the other hand, the depth of focus increases for short-wavelength laser beams, which are more easily focused.

The relationship between laser beam intensity and propagation is illustrated in Figure 6.5, which shows the normalized beam intensity at three distances: $z = 0$, $z = z_0$, and $z = 2z_0$. The maximum normalized intensity occurs at the beam waist ($z = 0$) and decreases as the beam diverges. Though the intensity decreases, energy is conserved and the power remains constant as the beam propagates [2].

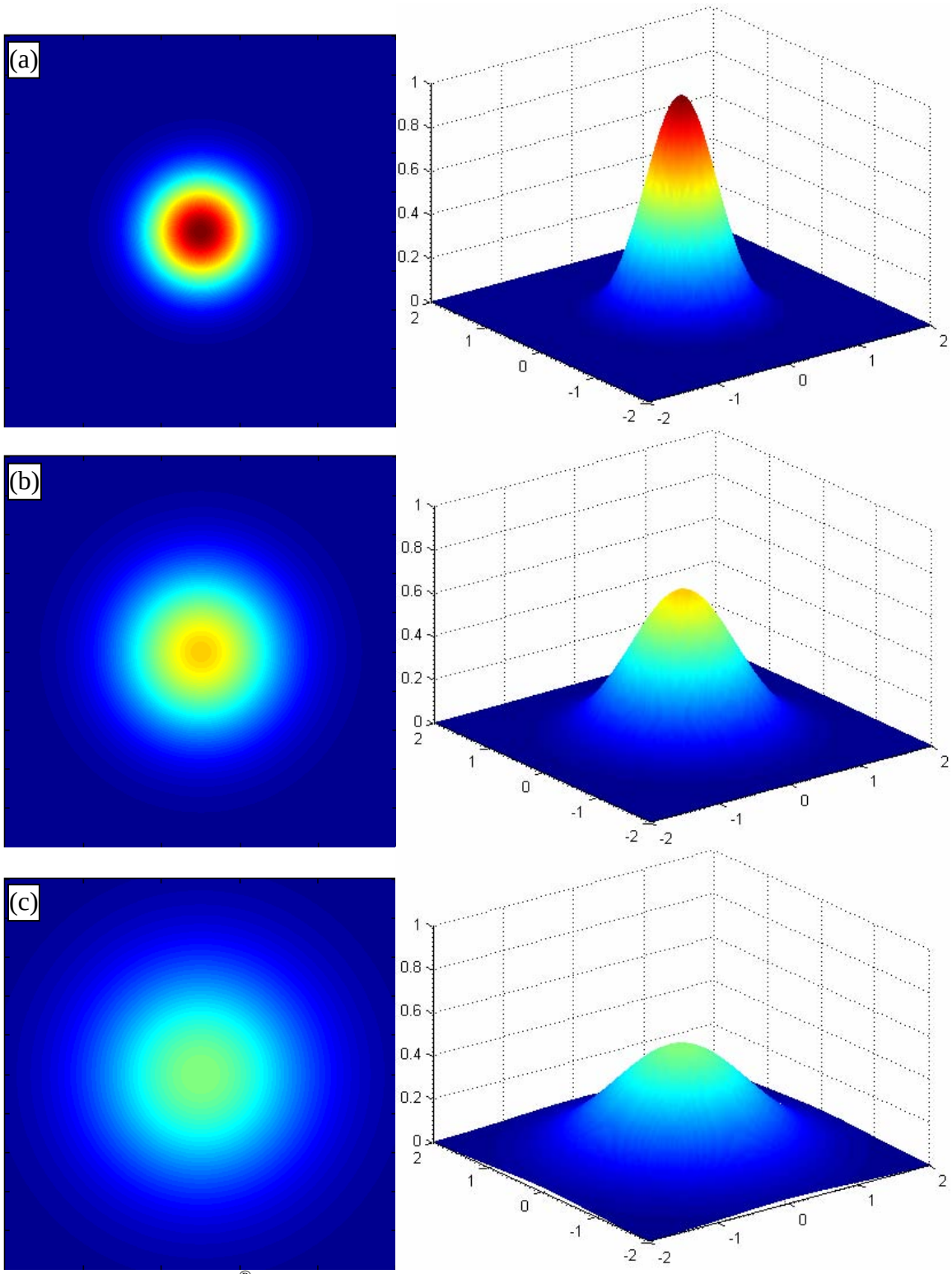


Figure 6.5: MatLab® model of a normalized Gaussian beam intensity at increasing distances from the laser source: (a) beam waist $z = 0$; (b) Raleigh range $z = z_0$; (c) $z = 2z_0$. The 2-D plots on the left correspond to the 3-D plots on the right. At increased distances, the beam diverges and the intensity decreases, but the power remains constant. The intensity is highest at the beam waist (a). The code is available in Appendix B.6.

Laser diodes by nature are highly divergent—that is, they have a very small Rayleigh range. In order to be useful for practical laboratory applications, laser diode mounts are usually equipped with a collimating lens to reduce this divergence. As noted in Table 6.1, the laser diode mount used in this thesis is equipped with a collimating lens. However, the focal distance of the collimating lens and the corresponding beam waist are unknown. Characterizing the spot size at various distances from the laser output yields the beam waist location as well as needed spot size information.

6.3.2.2 Laser Diode Propagation at Threshold and Maximum Current

Measuring the laser beam spot size requires a simple charge-coupled device (CCD) camera with at least two ND filters, as shown in Figure 6.6.

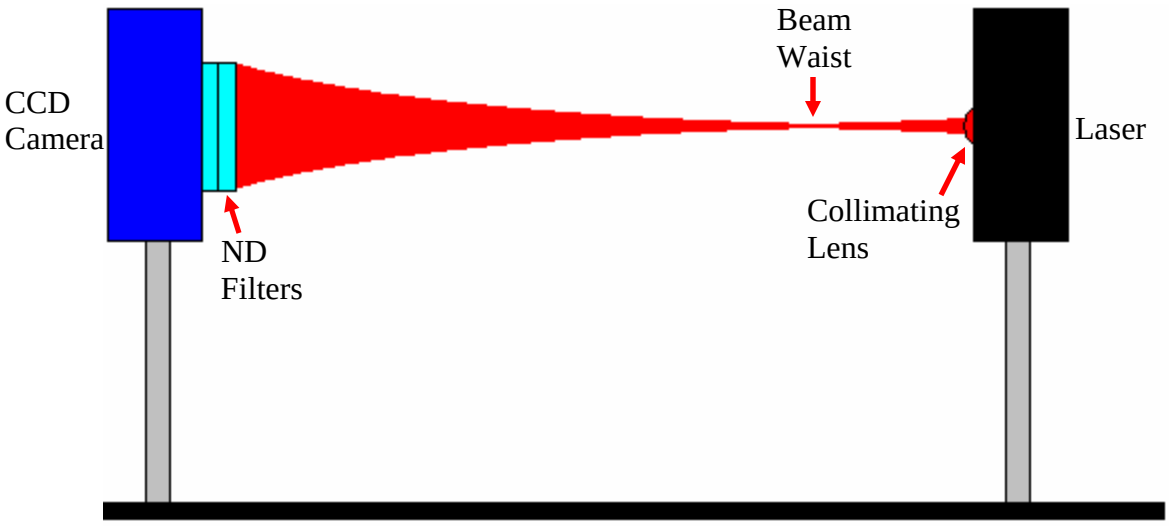


Figure 6.6: Diagram of the experiment used to measure the laser beam spot size. The laser diode is on the right and a CCD camera with two ND filters is on the left. The collimating lens on the laser diode mount focuses the beam at the beam waist; at farther distances the beam continues to diverge.

Figure 6.7 and Figure 6.8 illustrate the spot sizes at 50- and 109-mA driving currents at three distances from the laser output: 1, 6.5, and 11 inches. The beam converges at the beam waist (6.5 inches from the output) and then continues to diverge. The intensity is highest at the beam waist and decreases as the beam diverges.

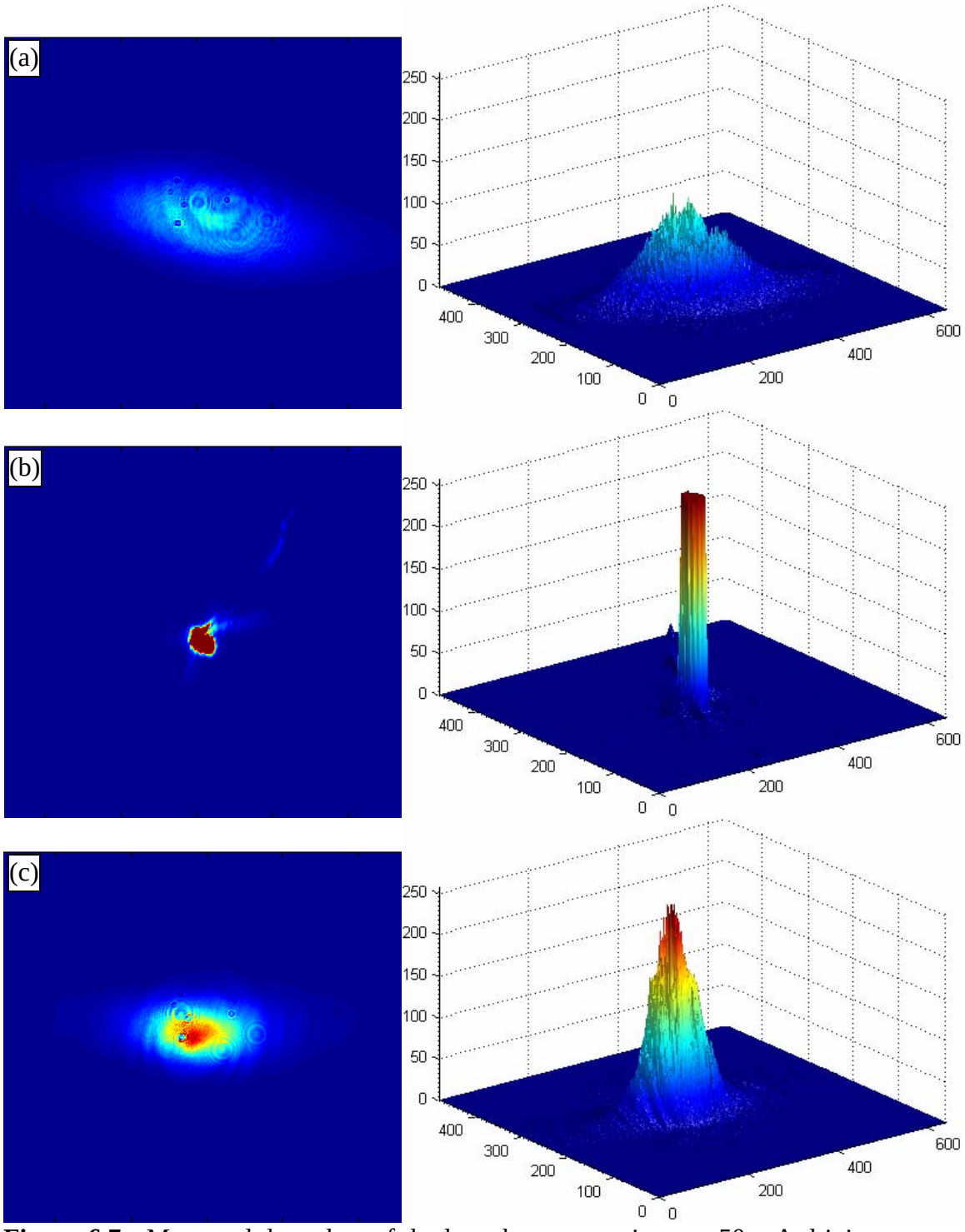


Figure 6.7: Measured data plots of the laser beam spot size at a 50-mA driving current for various distances from the laser: (a) at 1 in (2.54 cm); (b) at the beam waist 6.5 in (16.51 cm); (c) and at 11 in (27.94 cm). The beam converges at the beam waist, where the intensity is the greatest. The intensity decreases as the beam diverges, but the power remains constant. Each image on the left was captured with a CCD camera and imported into MatLab® plots. The code is available in Appendix B.7.

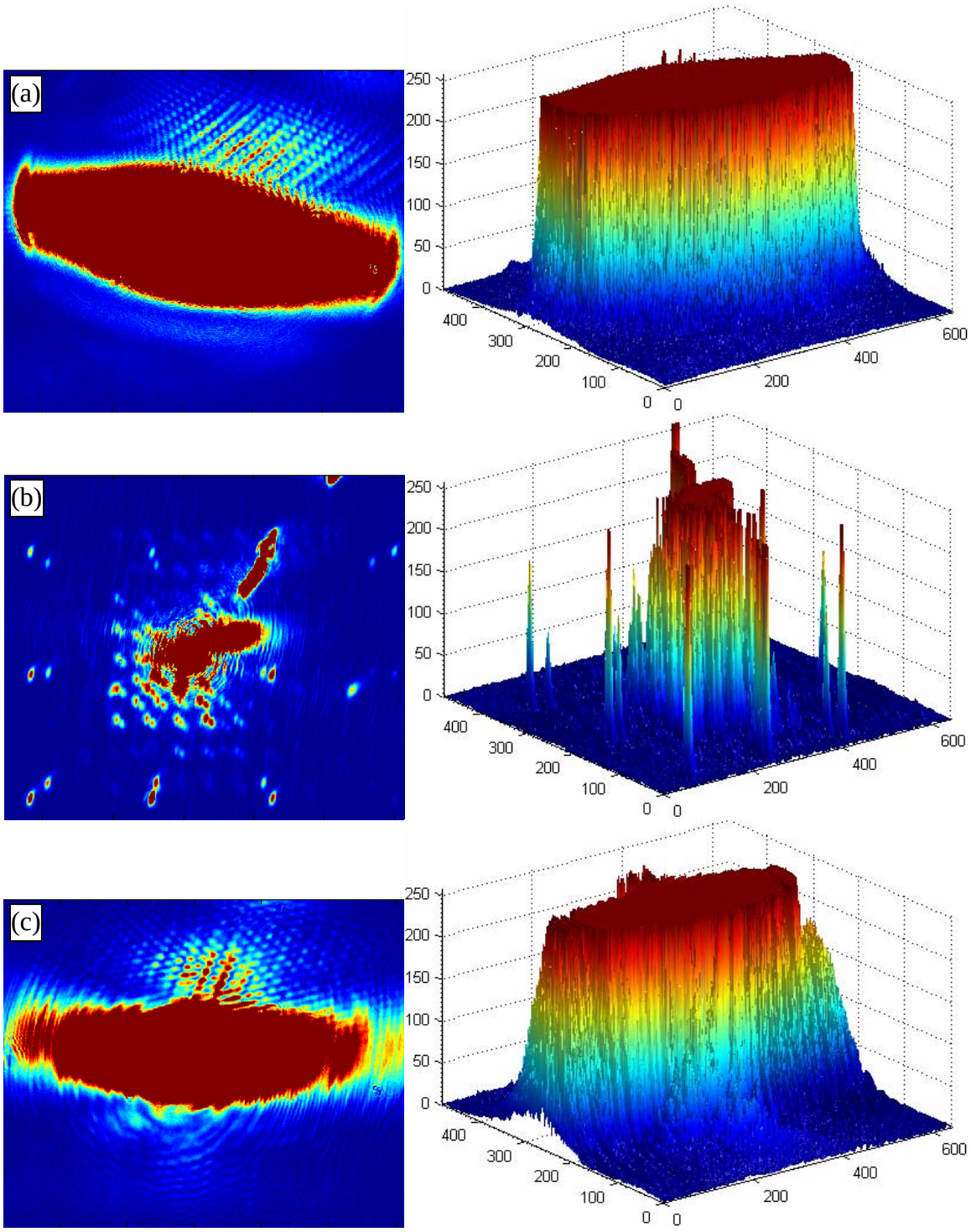


Figure 6.8: Measured data plots of the laser beam spot size at a 109-mA driving current for various distances from the laser: (a) at 1 in (2.54 cm); (b) at the beam waist 6.5 in (16.51 cm); (c) and at 11 in (27.94 cm). Just as in the previous experiment, the beam converges at the beam waist, where the intensity is the greatest. The intensity decreases as the beam diverges, but the power remains constant.

A trend evident in Figure 6.7 and Figure 6.8 is that both the spot size and the intensity increase for increased laser power. This trend is shown in Figure 6.9.

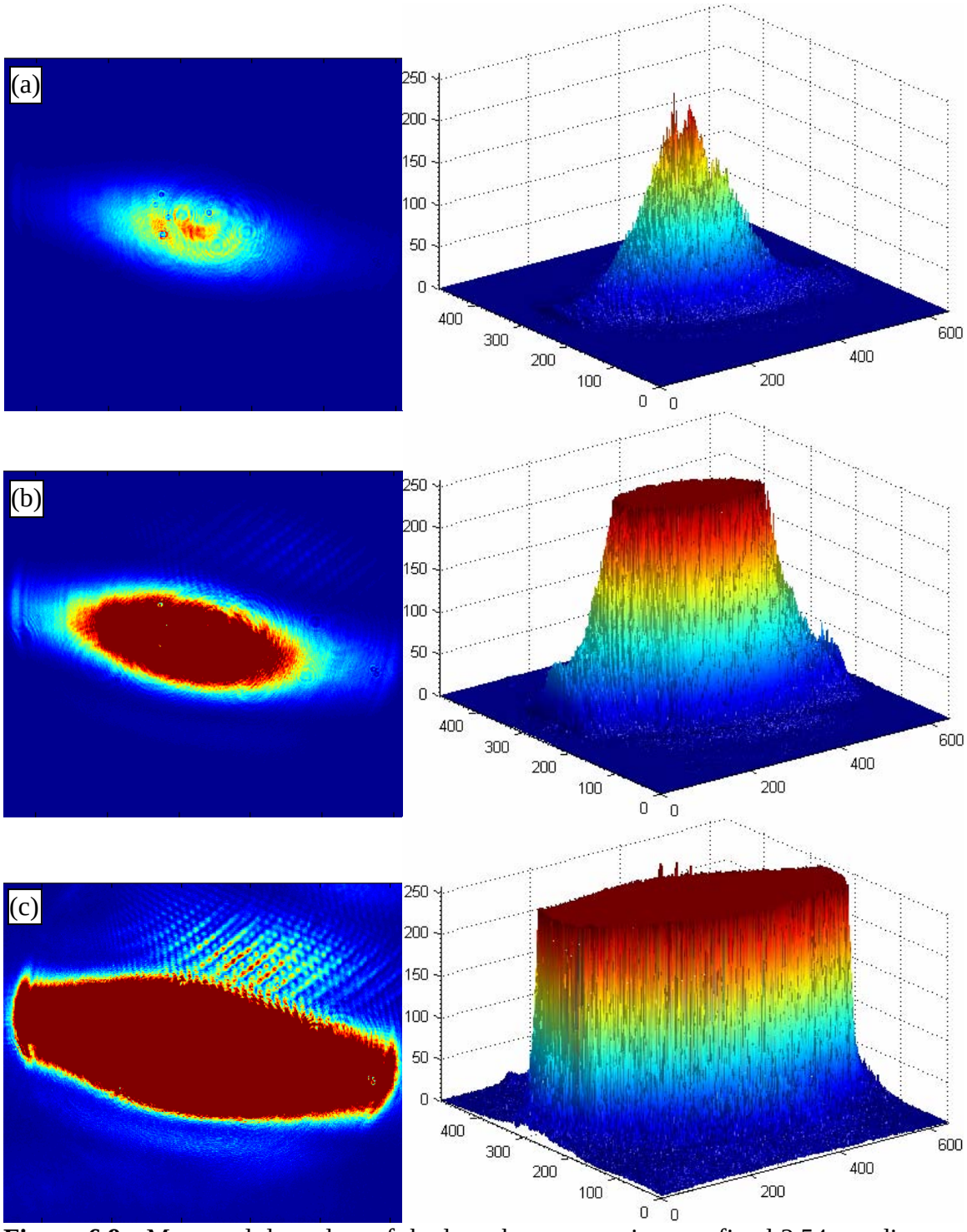


Figure 6.9: Measured data plots of the laser beam spot size at a fixed 2.54-cm distance between the CCD and the laser for increasing power values: (a) 51-, (b) 55-, (c) and 109-mA driving currents. The spot size and intensity increase with increased power.

The results from Figure 6.9 are important because aligning and focusing the beam is done at a low, eye-safe power (usually 50 mA or 1 mW for an operating temperature of 25 °C). However, the spot size at the maximum operating power (109 mA or 40 mW) is much larger than the spot size at 50 mA. Without compensating for this increase in spot size, much of the laser power is wasted if the spot size exceeds the diameter of the optical elements—mirrors, lenses, etc. A discussion of system optimization follows.

6.4 Laser Setup Optimization

In order to deliver maximum power to the robot, the laser beam must be focused onto the polysilicon center of each robot. The laser beam spot size can be focused with a simple bi-convex lens according to the following expression:

$$W_1 = \frac{\lambda f}{\pi W_0}, \tag{6.3}$$

where W_1 {μm} is the focused waist radius, λ {μm} is the laser wavelength, f {mm} is the lens focal length, and W_0 {μm} is the input beam waist [2]. This expression shows that it is easier to obtain a small focused beam waist as the input beam waist is large. Also, a small lens focal length yields a small beam waist.

Equation 6.3 describes the size of the waist radius. The location of the focal point is given by:

$$\frac{1}{s_o} + \frac{1}{s_i} = \frac{1}{f}, \tag{6.4}$$

where s_o {mm} is the distance from the unfocused beam waist to the lens, s_i {mm} is the distance from the lens to the focused beam waist, and f {mm} is the focal length of the lens. As s_o increases, s_i approaches the lens focal length f. Both the focusing distance and the spot size must be considered when positioning the laser and the lens.

The efficiency of an optical system decreases with the addition of each optical element. The laser setup used to power MEMS robots in previous research efforts was quite inefficient. The components of the setup included a beam expander used to increase the beam divergence; a spatial filter to remove the fringes from the laser beam; a lens to focus the beam; and a mirror that directed the beam at a 45-degree incidence angle onto the robot chips [1].

Given the naturally high beam divergence, a beam expander is not necessary. While a spatial filter improved beam quality, it sacrificed a large amount of power. Power measurements with the silicon power meter showed a 41% loss in optical power after the spatial filter and beam expander in the previous research. Maximizing power is more important than beam quality, so the spatial filter, too, is not necessary. The total loss in the previous optical setup was 46%, meaning only 54% of the laser power output ever made it to the robots. Moreover, the polysilicon reflectivity at a 45-degree incidence angle is 0.3 instead of 0.2 for a normal or 0-degree incidence angle (see Figure 3.9). The resulting total heat-conversion efficiency at this angle is 26.6% instead of 30.4% for 0 degrees (see Table 3.3). The combined efficiency of 54% and 26.6% is only 14% for that optical setup. The previous researcher recommended buying a more powerful laser, but an alternative solution is to improve the efficiency of the optical setup.

An improved optical setup includes a 25.4-mm-diameter mirror and a 12.7-mm-diameter lens with a 12.7-mm focal length. The beam expander and spatial filter are not used in this setup. The beam is directed at normal incidence to the robot surface to minimize reflection losses. Figure 6.10 is a diagram of this improved optical setup, and Figure 6.11 shows the measured losses at each step. At higher powers, the laser spot size

exceeds the mirror and lens diameters, which decreases efficiency. The total power loss in this optical setup is 37%, meaning only 63% of the power makes it to the robots.

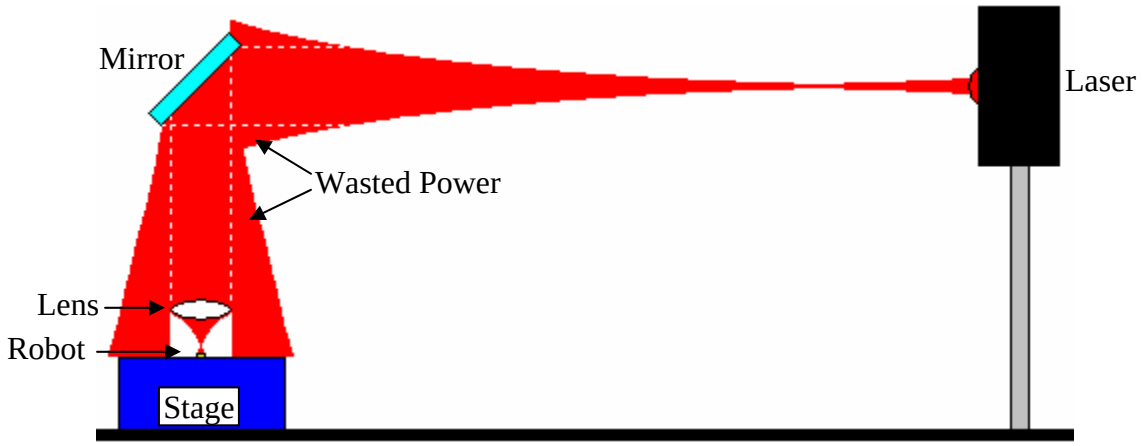


Figure 6.10: Diagram of an improved optical setup with just a mirror and a lens. As shown, the spot size exceeds the mirror and lens diameters at higher powers, which reduces the system efficiency; the laser power outside the dashed marks is wasted.

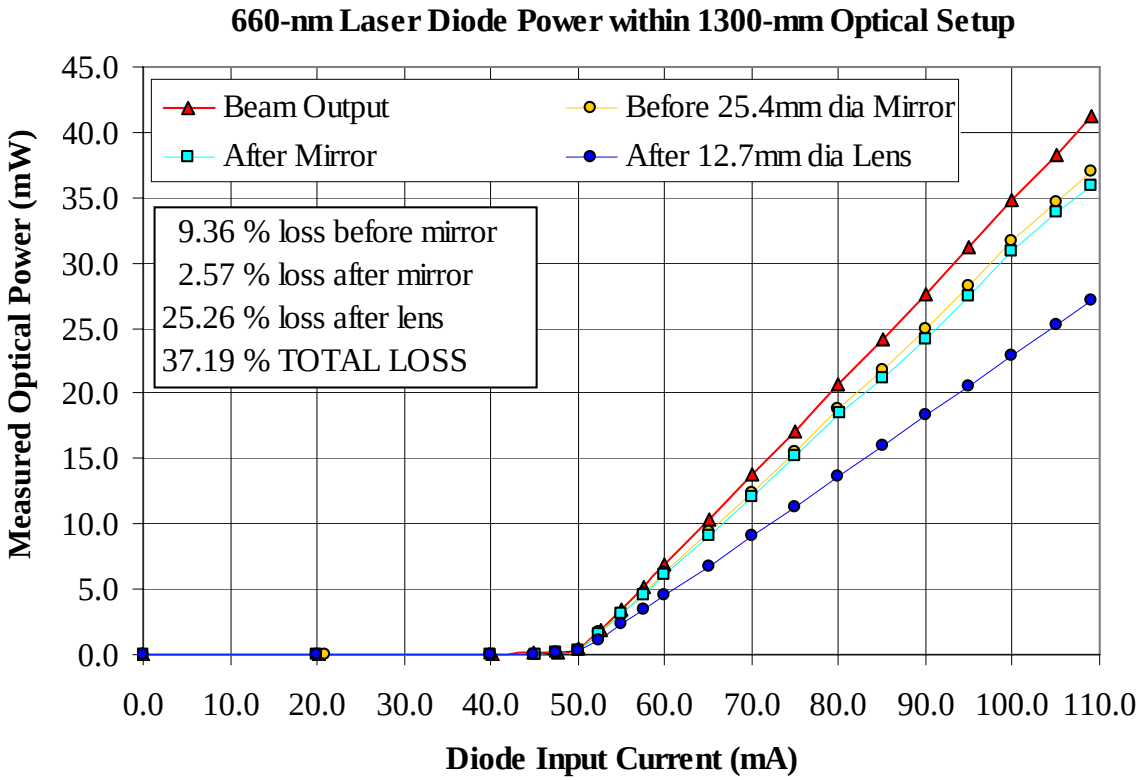


Figure 6.11: Graph of measured laser power after each element in the 1300-mm optical setup (1300 mm represents the distance from laser to robot). The greatest losses occur before the mirror and after the lens because the spot size at those points exceeds the diameters of the optical elements. There is a finite (2.57%) absorption loss in the mirror. The 37% total power loss is less than the 46% loss achieved in previous research.

The total 37% loss in the 1300-mm optical setup (distance from laser to robot) is better than the 46% loss from previous research. However, optimizing the optical setup is easily done by reducing the laser-to-robot distance to 650 mm. Reducing this distance also reduces the spot size to match the diameter of the lens. Figure 6.12 illustrates the smaller setup, and Figure 6.13 shows the optimized 6.2% total power loss.

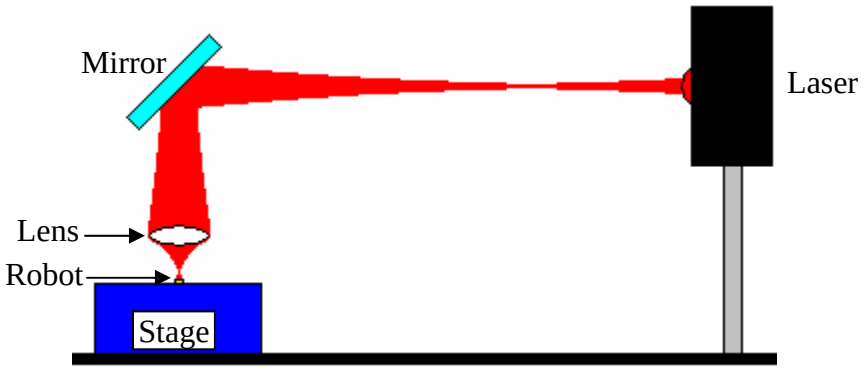


Figure 6.12: Diagram of an optimized optical setup with the same components as those in Figure 6.10. Very little power is wasted as the spot size matches the lens diameter.

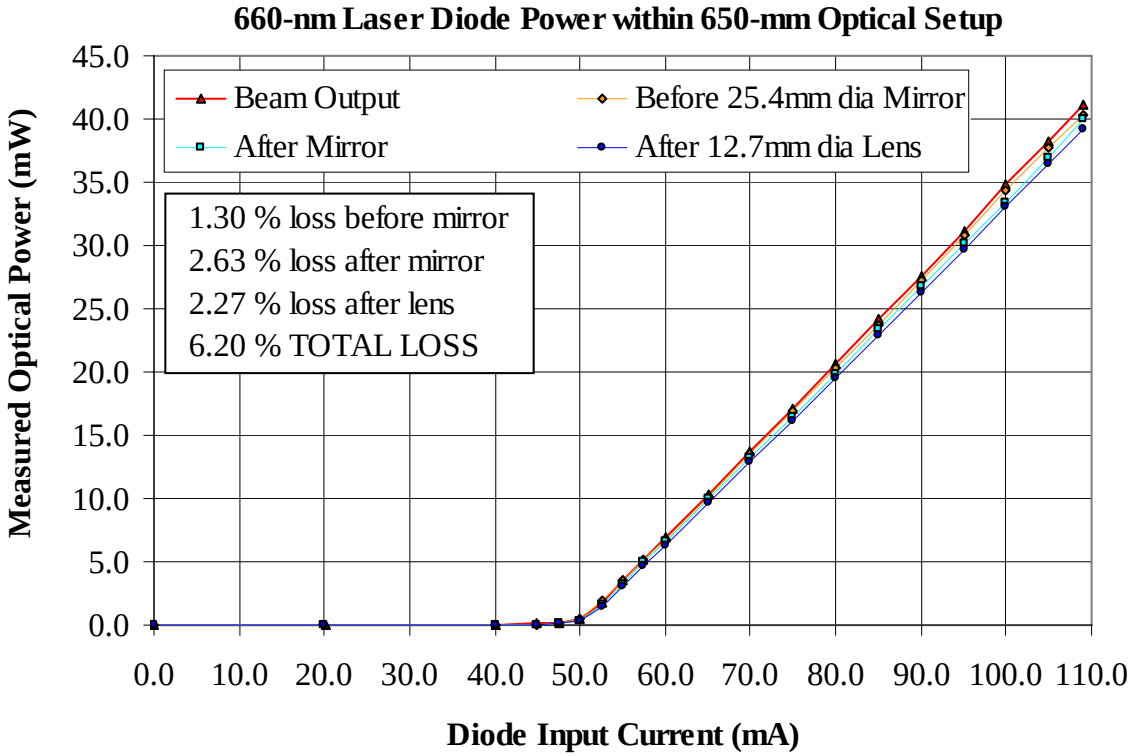


Figure 6.13: Graph of measured laser power in the optimized 650-mm optical setup. Power losses are minimized by matching the spot size with the lens diameter.

Photographs of the optimized optical setup are given in Figure 6.14.

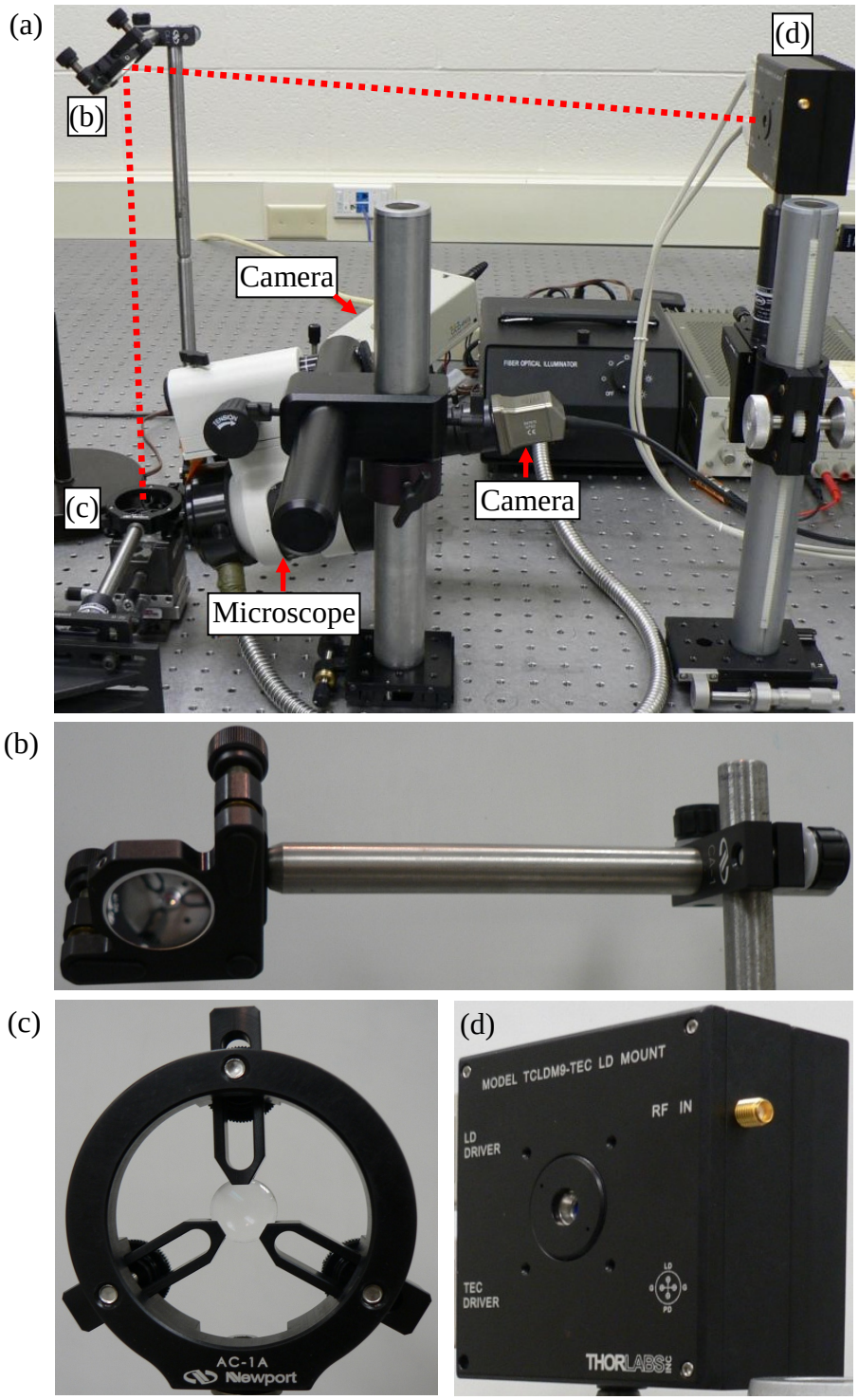


Figure 6.14: Photographs of the optimized 650-mm laser test setup: (a) the entire laser setup including a microscope and two cameras; (b) 25.4-mm-diameter mounted mirror; (c) 12.7-mm-diameter mounted lens (f = 12.7 mm); (d) laser diode and mount. The letters in picture (a) correspond to the individual pictures. The efficiency of this optical setup is 93.8% (only 6.2% power is lost).

A top view of the optical setup that clearly illustrates the cameras, mirror, and lens is given in Figure 6.15. The close view of the stage area is given in Figure 6.16.

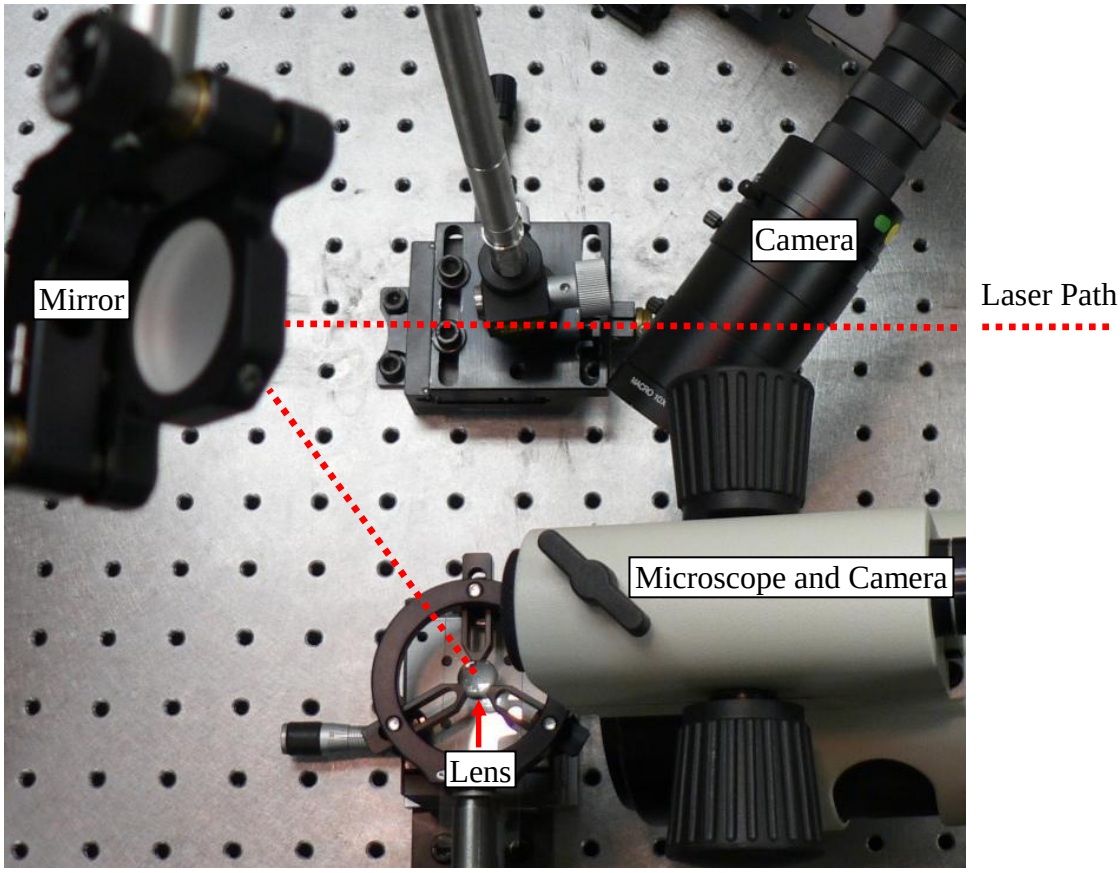


Figure 6.15: Photograph of the top view of the optimized 650-mm optical setup.

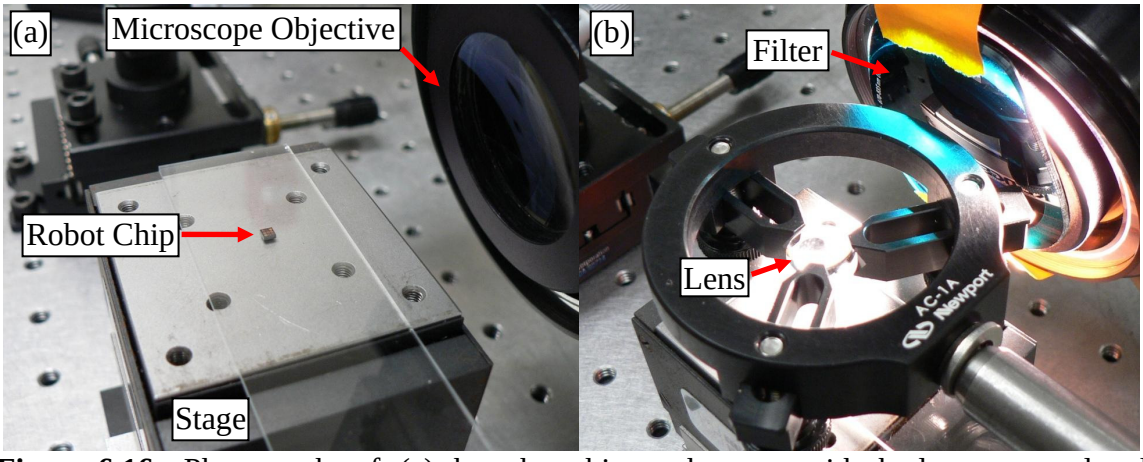


Figure 6.16: Photographs of: (a) the robot chip on the stage with the lens removed and the microscope light off; (b) the lens replaced with the camera light on. An eyepiece from the laser safety glasses is attached to the microscope objective in order to filter the laser light. Without this filter, the laser light would saturate the attached CCD camera.

The two cameras illustrated in Figure 6.15 and Figure 6.16 give complementary views of the robot chip. The camera attached to the microscope provides a close side view of the robots. The 50X microscope objective is sufficient to quantify the downward deflection of each wing. The laser light must be filtered to prevent saturating the image. This is accomplished by attaching an eyepiece from a pair of laser safety glasses. The other camera gives a view of the entire chip without filtering the laser. This global view is helpful in aligning the laser to the chip and verifying the laser operation status.

The digital signals from the cameras are displayed in standard video monitors. It is important to emphasize that laser safety glasses must be worn during laser operation. However, the glasses completely filter the laser beam. The only view of the laser beam is on the monitor connected to the unfiltered global-view camera. The microscope camera is usually connected to video capturing equipment for later analysis.

6.5 PolyMUMPs® Sacrificial Oxide Release

As described in Chapter 4 and Chapter 5, each PolyMUMPs® run includes two silicon dioxide sacrificial layers that must be removed to allow the devices to move. After the chips are returned from the foundry and the subdicer, they are sorted, put into gel boxes, and stored in a humidity-free nitrogen storage container. This moisture-free atmosphere is necessary to prevent MEMS structures from sticking to the surface of the chip. Figure 6.17 illustrates several 2 x 2-mm^2 diced chips aligned in a gel box; one of the chips is enlarged to show the relative size of the devices. These chips are unreleased—that is, the movable structures are still surrounded by the releasable sacrificial oxide.

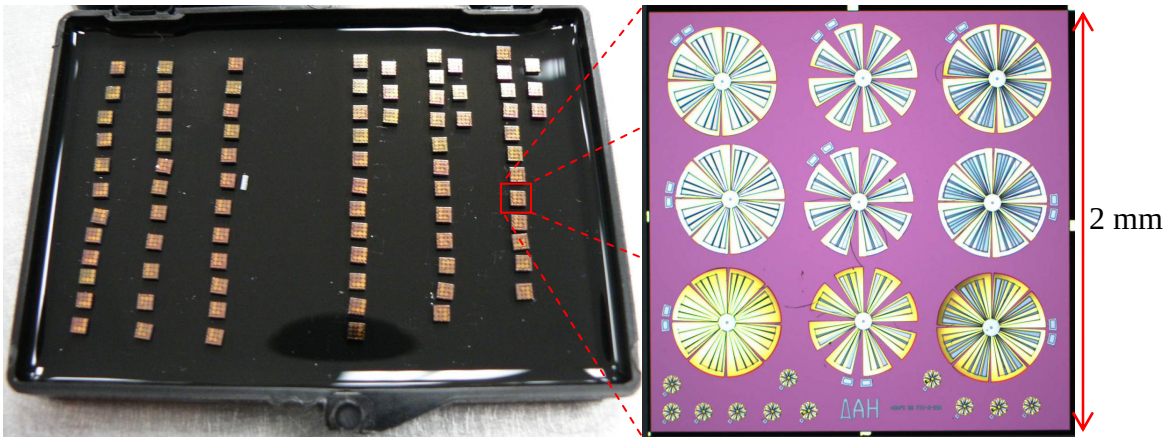


Figure 6.17: Photograph of a gel box with six columns of unreleased chips (left) and a magnified image of one chip (right).

The procedures for the sacrificial oxide release are given in three major steps: preparatory, release, and drying and storage steps. The procedures used in this thesis are given in detail in Table 6.3.

Table 6.3. PolyMUMPs® sacrificial oxide release procedures (adapted from [1]).

Preparatory Steps

A1. Clean a pair of acid-resistant tweezers initially and periodically by
- Blowing with N_2
- Rinsing with methanol
- Rinsing with de-ionized water (DIW)
- Drying with N_2

A2. Clean six acid-resistant[1] beakers by
- Blowing with N_2
- Rinsing with acetone, methanol, or DIW depending on the liquid to be used[2]

A3. Prepare Autosamdri-815 critical-point CO_2 dryer (see instruction manual)

Release Steps

B1. Place chips in ~25 mL of acetone for 10 minutes to remove bulk photoresist
B2. Place chips in ~25 mL of acetone for 10 minutes to remove residual photoresist
B3. Place chips in ~25 mL of methanol for 5 minutes to remove residue from B2
B4. Place chips in ~25 mL of DIW until ready for the HF step (B5)
B5. Place chips in ~25 mL of 48% HF for 3–5 minutes[3] to remove sacrificial oxide
B6. Place chips in ~25 mL of DIW for 10 seconds to stop the HF reaction
B7. Place chips in ~25 mL of methanol until ready for the CO_2 dryer

Drying and Storing Steps

C1. Place chips in chamber and ensure chips are submerged[4] in methanol
C2. Close metal chamber, place in CO_2 dryer, and proceed to dry[5]
C3. Inspect with microscope once chips are dried
C4. Place chips in a dry gel pack and store in a humidity-free N_2 storage bin

Notes

1. Acid-resistant beakers are required only for the HF steps (B5 and B6) but may be used throughout.
2. Rinse with the same liquid that will later be used to fill the beaker; for the HF beaker, rinse with DIW.
3. The HF etch time depends upon the structure design. Care must be taken to avoid over- or under-etching.
4. In order to prevent stiction in the PolyMUMPs devices, the chips must be submerged in methanol while waiting to dry. Extra methanol may need to be added since it evaporates quickly at room temperature.
5. If the Autosamdri-815 is not available, the chips may be dried on a 110-ºC hotplate for 10-15 minutes. Some structures with large surface area, such as cantilevers, do not dry well with the hotplate. Stiction will likely result.

The chemicals used in the release process—methanol, acetone, and hydrofluoric acid (HF)—are illustrated on a scale in Figure 6.18. HF is a highly corrosive chemical that can cause serious damage to the body. Proper training is required prior to use.

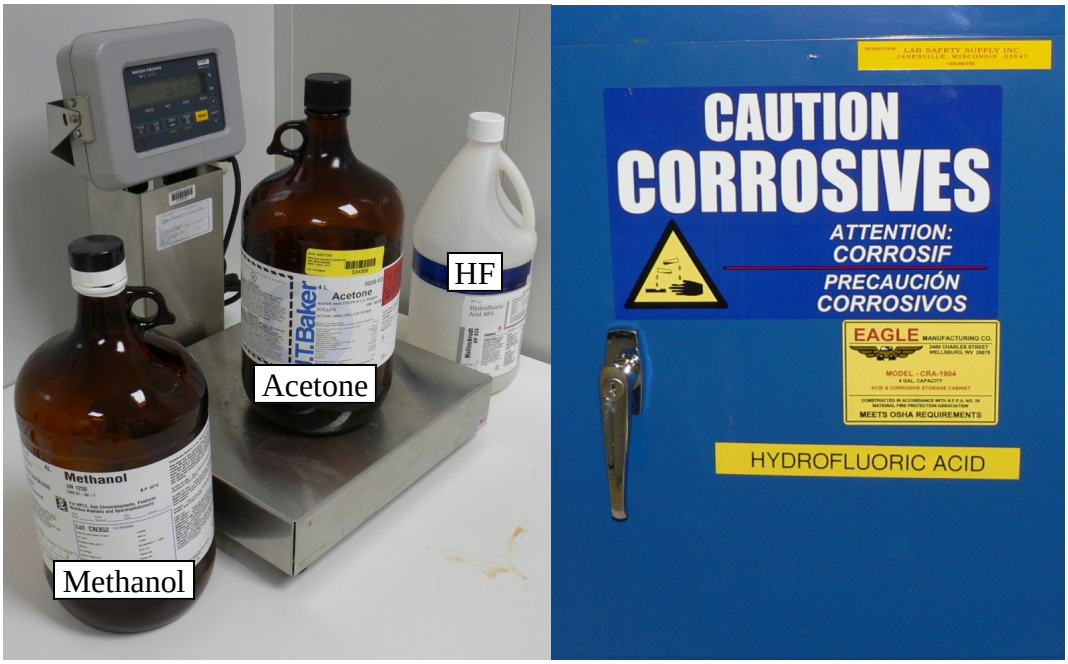


Figure 6.18: Photographs of the three chemicals used in the release procedure—methanol, acetone, and hydrofluoric acid (HF)—on a weighing scale (left) and the separate storage unit for the highly corrosive HF (right).

The seven steps of the release are shown in Figure 6.19. To prevent mistakes during the release, each step is labeled on clean room paper as shown in Figure 6.20.

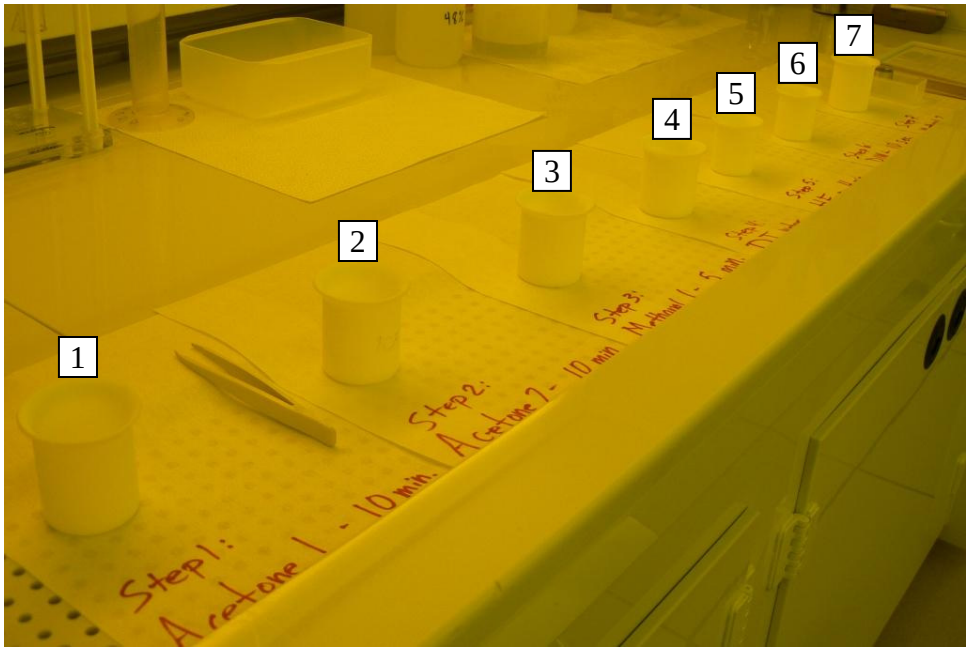


Figure 6.19: Photograph of the beakers and labels of the seven-step release process: (1) first acetone bath, (2) second acetone bath, (3) first methanol bath (4) first de-ionzed water rinse (5) HF release, (6) second de-ionized water rinse, and (7) final methanol bath.

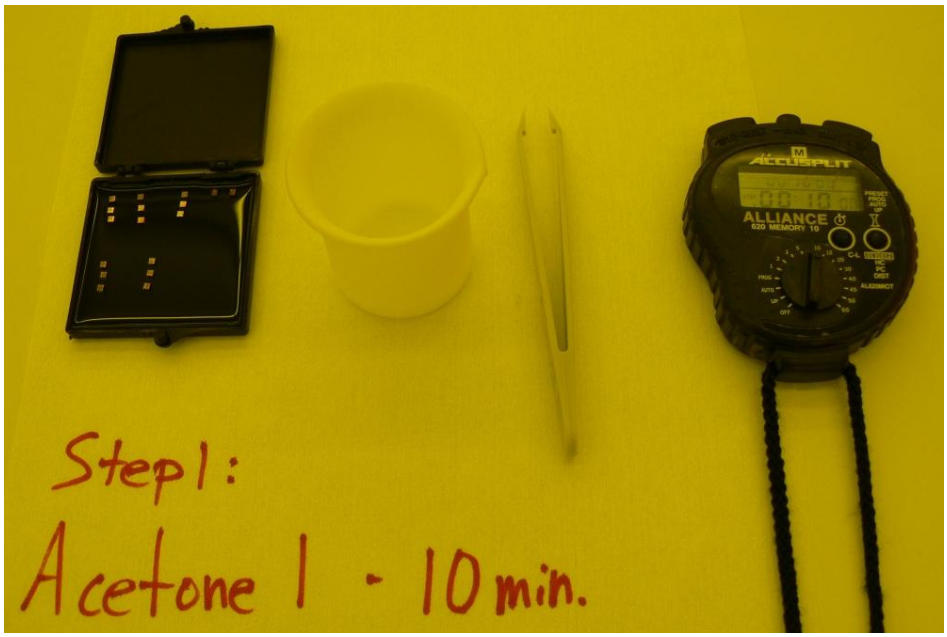


Figure 6.20: Photograph of the first step in the release process—a 10-minute acetone bath. Shown are the chips, an acid-resistant beaker, acid-resistant tweezers, a stopwatch, and a piece of labeled clean room paper. Labeling the paper helps prevent mistaking de-ionzied water with HF, for example.

Some microrobots, especially those with large wings and no etch holes, did not release completely even after 4.5–5 minutes in HF (see Figure 6.21 and Figure 6.22).

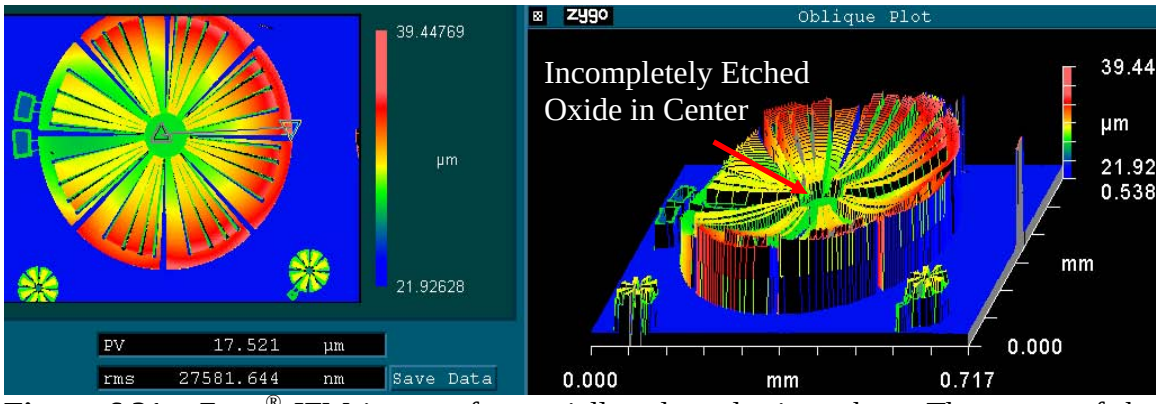


Figure 6.21: Zygo® IFM image of a partially released microrobot. The center of the microrobot is unintentionally attached to the substrate by incompletely etched oxide.



Figure 6.22: Diagram of the side view of: (left) a microrobot chip before performing an HF release; (right) an incompletely etched chip showing an attached oxide post.

One would assume that the solution to this under-etching is to etch longer, but this should be avoided as longer exposure to HF destroys narrow polysilicon structures. The solution is to gently agitate the HF beaker every 15–30 seconds, which replenishes fresh HF into the unetched oxide regions. Figure 6.23 shows a Zygo® IFM image of a completely released microrobot that is intentionally anchored on its left side.

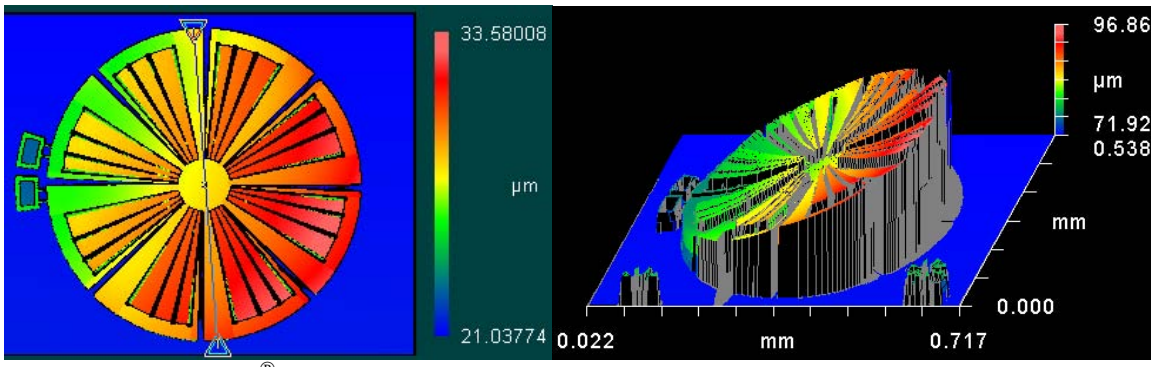


Figure 6.23: Zygo® IFM image of a completely released microrobot. Gently agitating the HF beaker replenishes fresh HF in the oxide regions, achieving a complete release.

MEMS structures must be dried following the wet chemical release process. If allowed to evaporate on its own, the surface tension in the liquid is sufficiently strong to pull the MEMS structures towards the substrate and become stuck. Flat, thin structures on a flat substrate are impossible to separate without destroying the structures. Figure 6.24 is a Zygo® IFM image of a microrobot that was allowed to dry on a hotplate.

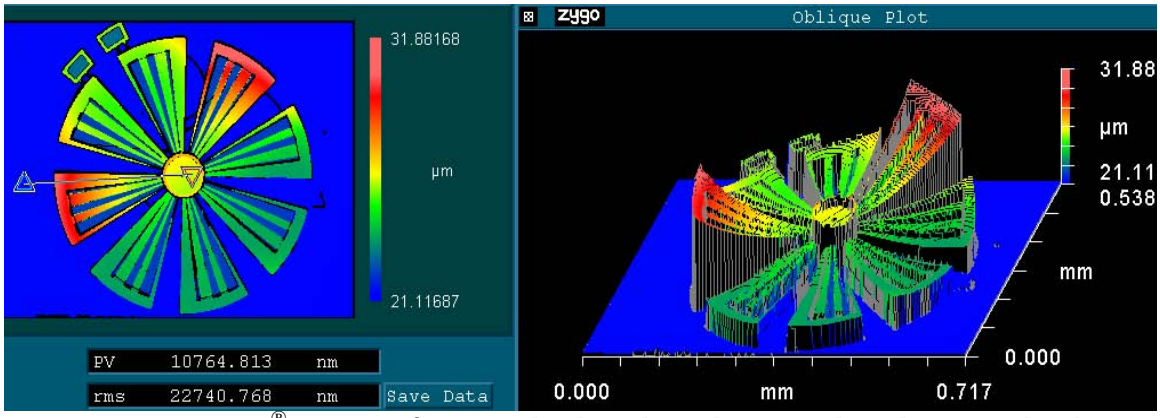


Figure 6.24: Zygo® image of a completely released microrobot that was dried on a hotplate at 110 °C. The wings are stuck to the substrate due to surface tension following methanol evaporation. Robots dried on a hotplate are entirely unusable once stuck.

This "stiction" phenomenon can be overcome using a supercritical carbon dioxide (CO_2) dryer. The CO_2 drying process begins by filling the dryer chamber with methanol and placing the MEMS chips inside. Once the chamber is well sealed, the methanol is cooled to at least 10 °C. Then, the chamber temperature and pressure are both increased as liquid CO_2 fills the chamber. For approximately 10 minutes, the methanol is purged and replaced by the liquid CO_2. The chamber temperature and pressure continue to increase until the CO_2 reaches its supercritical region, where it is in both liquid and gas form. The pressure decreases and the CO_2 becomes strictly a gas as it leaves the supercritical region. The gas is vented prior to the temperature and pressure returning to ambient conditions. (Refer to [3] for detailed operating instructions of the CO_2 dryer.) The supercritical CO_2 dryer was absolutely essential in this research (see Figure 6.25).

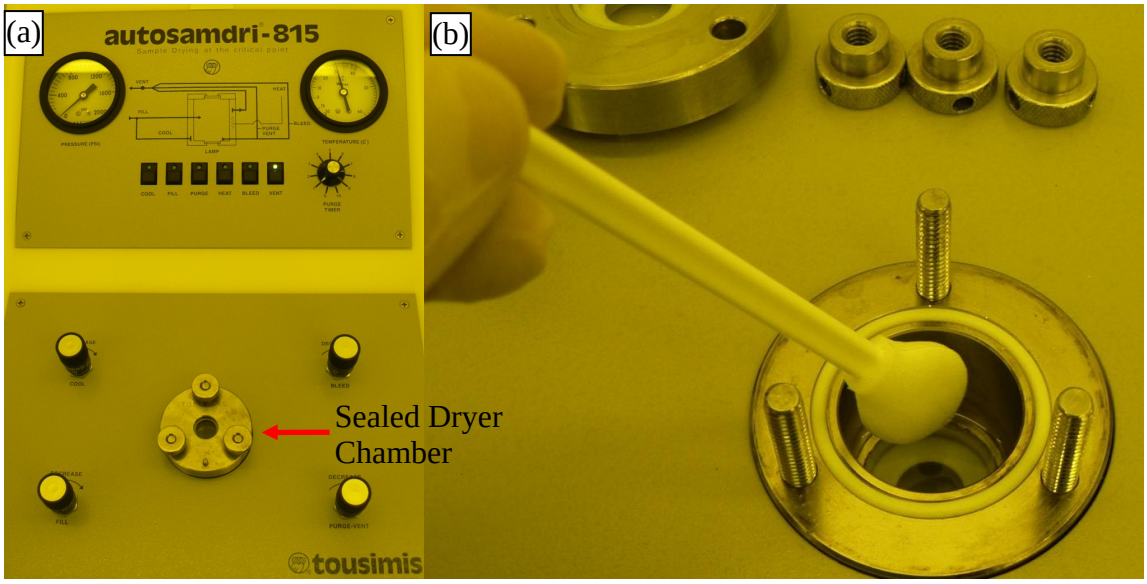


Figure 6.25: Photographs of (a) the entire supercritical CO_2 dryer unit, and (b) the required pre-run chamber cleaning. Because it prevented stiction in the microrobot wings, the CO_2 dryer was an essential element of this research.

6.6 Microrobot Characterization

6.6.1 Initial Deflection Measurements

Once the chips are released and successfully dried, it is possible to characterize, image, probe, and test the microrobots. Characterizing the initial vertical deflection in each microrobot is a principal element of this thesis because maximizing both upward and downward deflection is necessary for successful flapping flight. Measuring the initial vertical deflection of each robot is the first step in determining the optimum robot design—the one with the greatest chance of taking flight.

The instrument of choice for precise vertical measurements is the Zygo® interferometric microscope (IFM). This instrument uses non-contact white light interferometry to acquire images with nanometer vertical resolution. It can scan structures up to 5 mm tall with a 10-μm/sec vertical scan rate. The Zgyo used in this research is illustrated in Figure 6.26, and pertinent operation steps are given in Table 6.4 (for more details, refer to [4]).

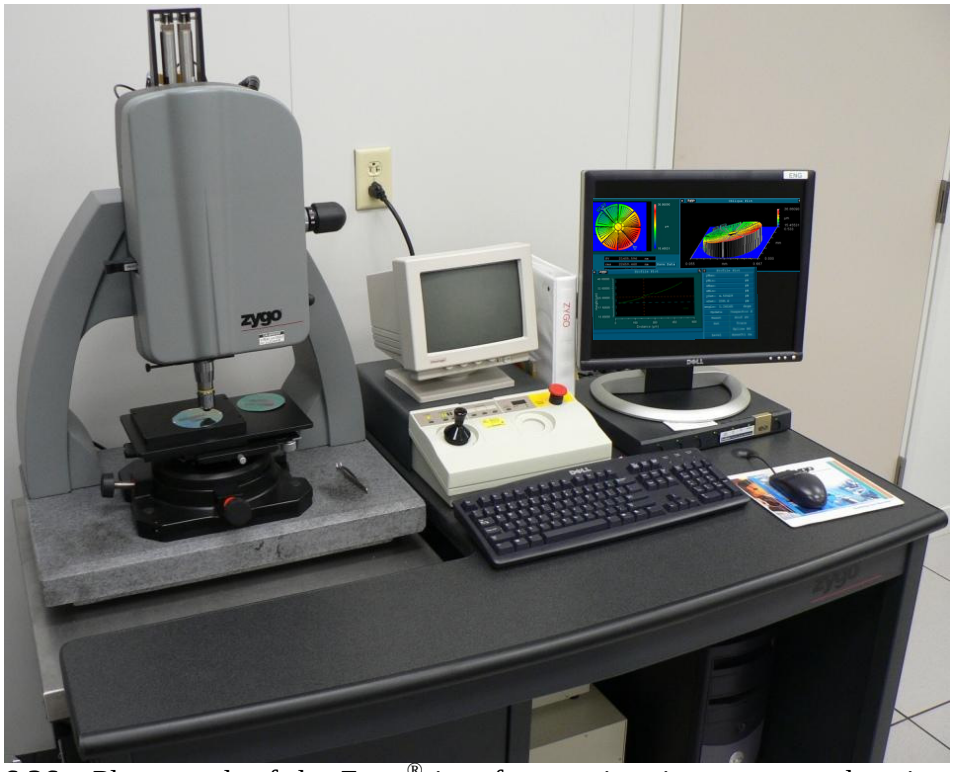


Figure 6.26: Photograph of the Zygo® interferometric microscope workstation used to precisely measure microrobot vertical deflection.

Table 6.4. Abbreviated operating instructions for the Zygo® IFM.

- Turn the machine on and select the "Micro2.App" application in the Zygo® menu
- Select the objective label that corresponds with the microscope objective in use
- Place the sample on the stage
- Focus on the surface of the chip by using the joystick to move the stage up and down (an object is in focus when the fringe lines rest on that object)
- Level the sample by adjusting the level knobs until there is only one broad fringe line on the surface of the chip
- Ensure the sample is never saturated with light by moving the focus from the substrate to the highest object to be measured
- Return the focus to the substrate, select the desired scan length (about twice the height of the highest object), and measure the sample

A successful Zygo® image is one that includes all the pertinent data from the device. Three cases illustrate when data could not have been collected: the Zygo® light intensity is too high and saturates the image; the measured sample dimensions exceed the Zygo® scan length; or the measured sample is tilted beyond the detection range of the

Zygo®. The first two reasons are easily correctable. The third, however, presents a problem when measuring highly deflecting microrobots that are anchored only on one side. Figure 6.27 shows two Zygo® scans of microrobots: one with all the data captured and the other with a section of the data missing. The Zygo® could not measure a section of the large-deflecting microrobot because of the high deflection angle. The white light in that region is reflected away from the Zygo® sensor. The best way to correct this problem is to design microrobots with one anchor on each side of the device.

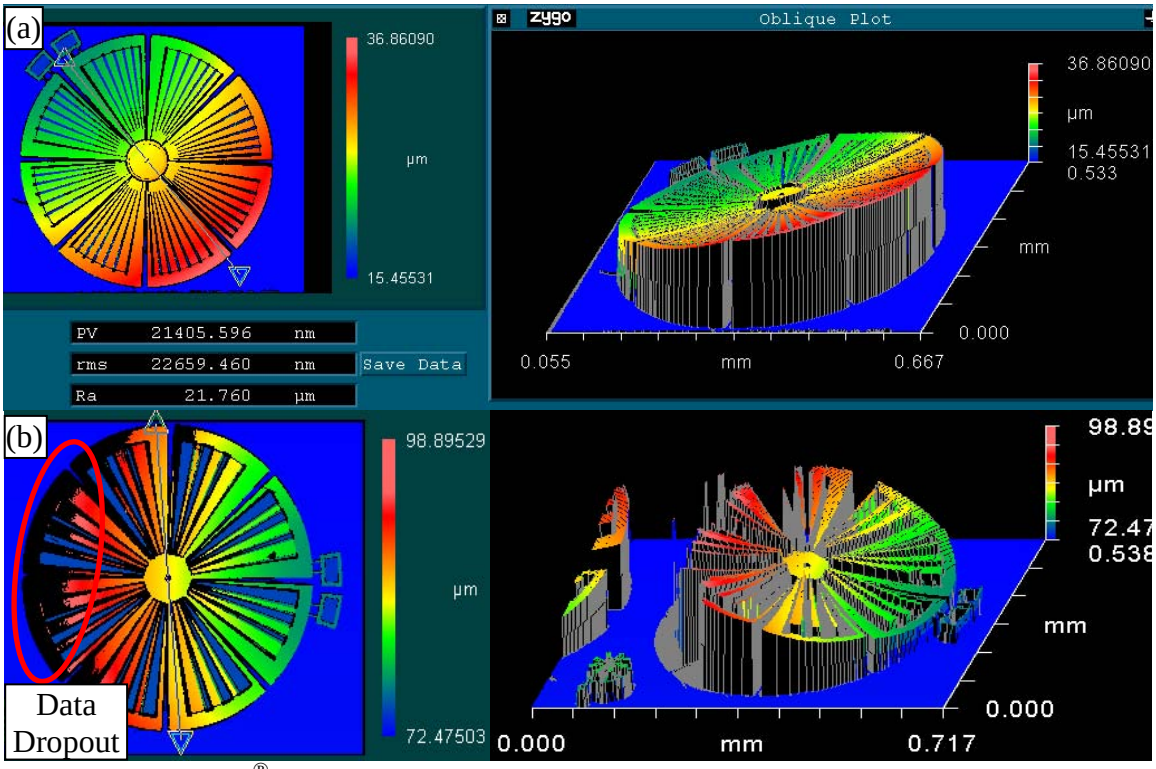


Figure 6.27: Zygo® IFM images of (a) complete vertical deflection data in a microrobot, and (b) incomplete data. The incomplete data results from a deflection angle that exceeds the detection scope of the Zygo®.

The Zygo® is very sensitive to external lighting, as too much light can saturate the image. For this reason, the Zygo® cannot be used to measure the downward deflection of microrobot wings powered by laser energy. Some other technique must be developed to achieve precise vertical deflection measurements. The Zygo® can, however, be used to

measure static deflection of electrically powered wings. A scan is performed at each voltage increment. Figure 6.28 shows a Zygo® image of an electrically powered test wing with no power applied.

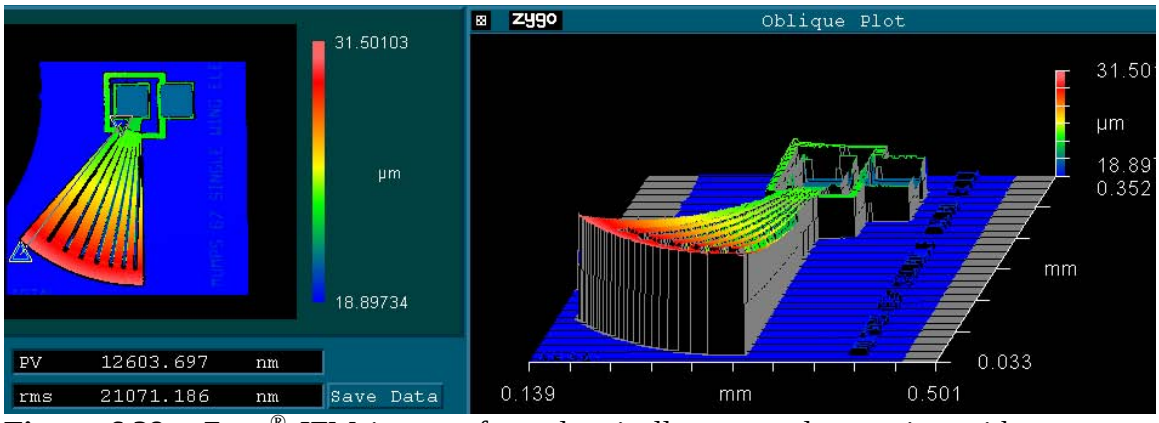


Figure 6.28: Zygo® IFM image of an electrically powered test wing with no power applied. The Zygo® can be used to measure static deflection in this device. The Zygo® cannot be used to test laser-powered robots because the laser would saturate the image.

6.6.2 Microrobot Imaging

An absolutely essential piece of equipment for working with MEMS structures is a probe station with a microscope. Probes are often necessary to inspect, apply power to, and manually manipulate MEMS samples. In this research, the microrobots are anchored to the substrate through 2-µm-wide tethers that are easily broken with probe tips. Probes are also necessary to power the electrically testable wings shown in Figure 6.28.

Figure 6.29 illustrates the Micromanipulator® probe station (with video capture equipment) used throughout this research. Features of the probe station include a nitrogen floating table, a powered and manual X-Y-Z translatable stage with a vacuum suction to hold the chips in place, X-Y-Z translatable probes that remain in place with a vacuum suction, X-Y-Z translatable microscope with a mounted video camera. The camera attaches to video capture equipment for later analysis and presentations.

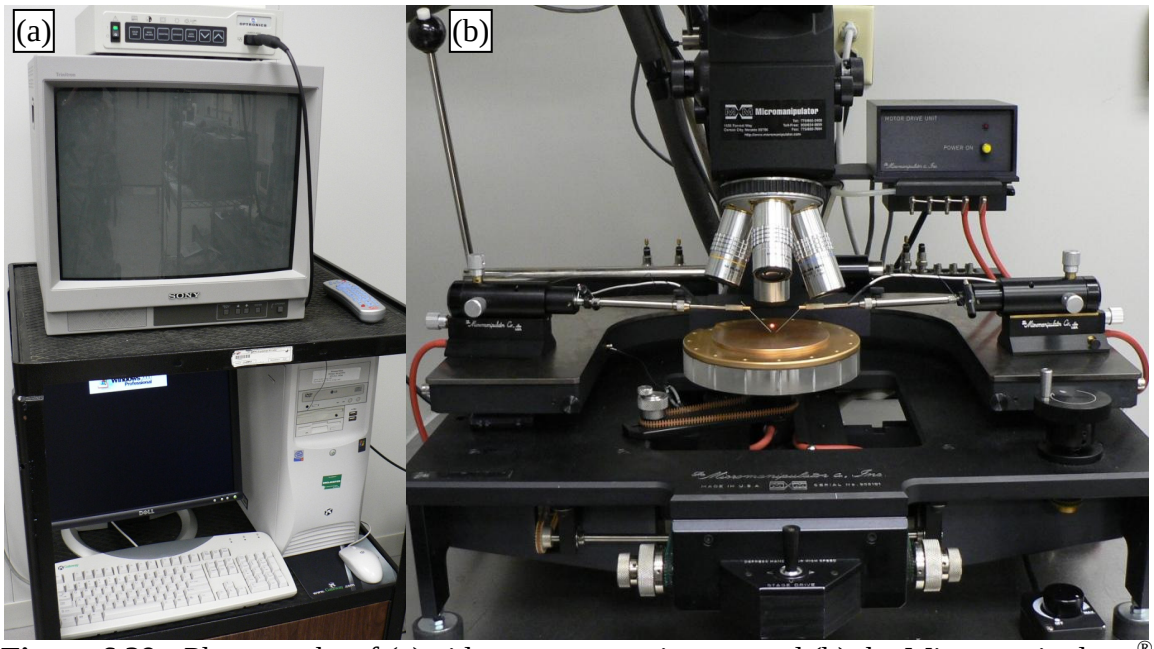


Figure 6.29: Photographs of (a) video capture equipment and (b) the Micromanipulator® probe station used for inspecting, applying power to, and probing MEMS samples.

High-resolution images with a large depth of focus are attainable with a scanning electron microscope (SEM). The SEM used is illustrated in Figure 6.30.

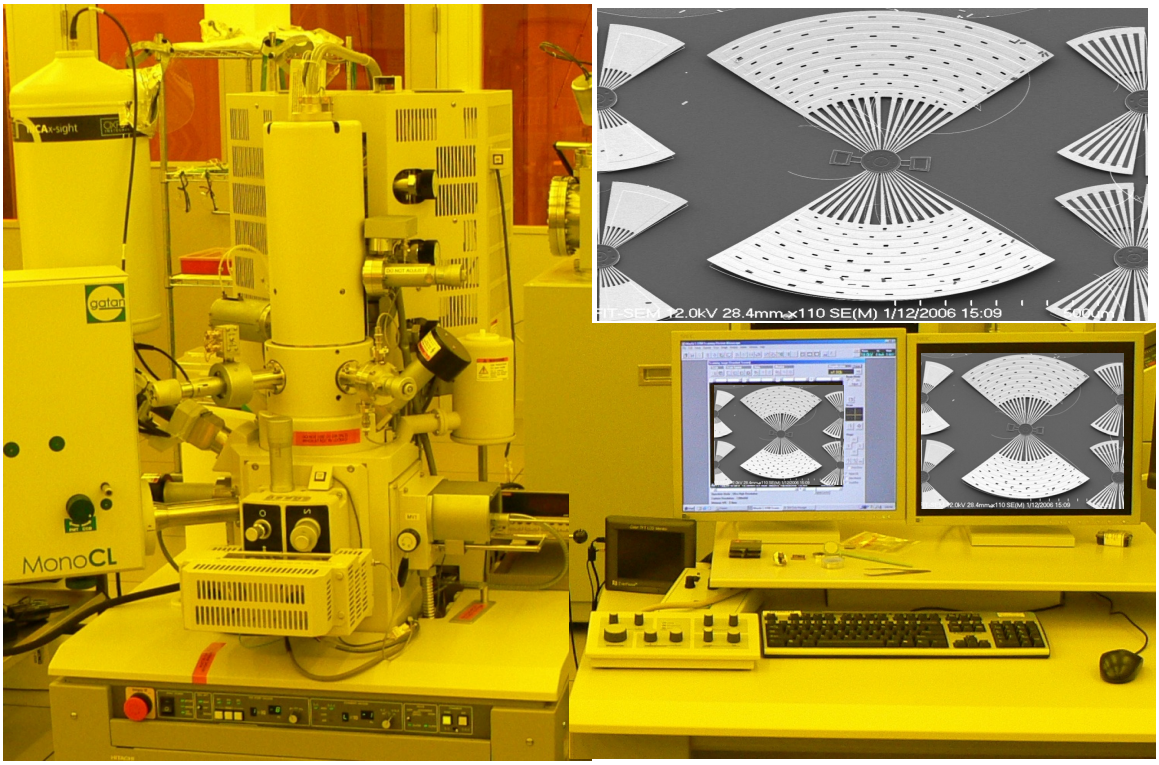


Figure 6.30: Photograph of the scanning electron microscope (SEM) used for high-resolution imaging. A scanned microrobot is featured.

6.7 Microrobot Performance

6.7.1 Challenges in Testing Laser-Powered Deflection

Testing laser-powered deflection in microrobots is difficult for a few reasons. First, the Zygo® IFM cannot be used to measure laser-induced downward deflection. Some other measuring paradigm must be used, but the accuracy and ease of this paradigm would be inferior to that of the Zygo®. Second, once the tethers binding the microrobots to the substrate are severed, the robots are not oriented in an ideal take-off position. Usually, they are either flat on the substrate or tilted against some residual object. In these positions, the flapping motion of the wing is obstructed by the substrate or by some other object. Moreover, laser heat is lost when the microrobot touches another object, which reduces the amount of available power for deflection. These challenges must be overcome to realize a successful, flying microrobot.

6.7.2 Solutions to Testing Challenges

Providing an alternative power-deflection measuring paradigm for laser-induced operation is necessary. One solution is to design measuring devices to be fabricated on the microrobot chip. The poly0 layer in PolyMUMPs® has often been used successfully for planar deflection measurements, but it cannot be used to measure vertical deflection. A hinged flip-up ruler made from releasable layers is the best option. Figure 6.31 and Figure 6.32 illustrate the details of a novel ruler fabricated in MUMPs® run 69. The ruler pivots inside a poly2 staple hinge; there is sufficient room between the poly1 pivot and the poly2 staple to allow the ruler to rotate upwards. Gold-poly2 cantilevers provide an initial vertical boost to the ruler, and locking tabs are positioned to hold the ruler in place. The measuring portion is made by etching 3-μm-wide holes in the poly1 layer. Figure 6.33 illustrates the locking mechanism in a vertical beam.

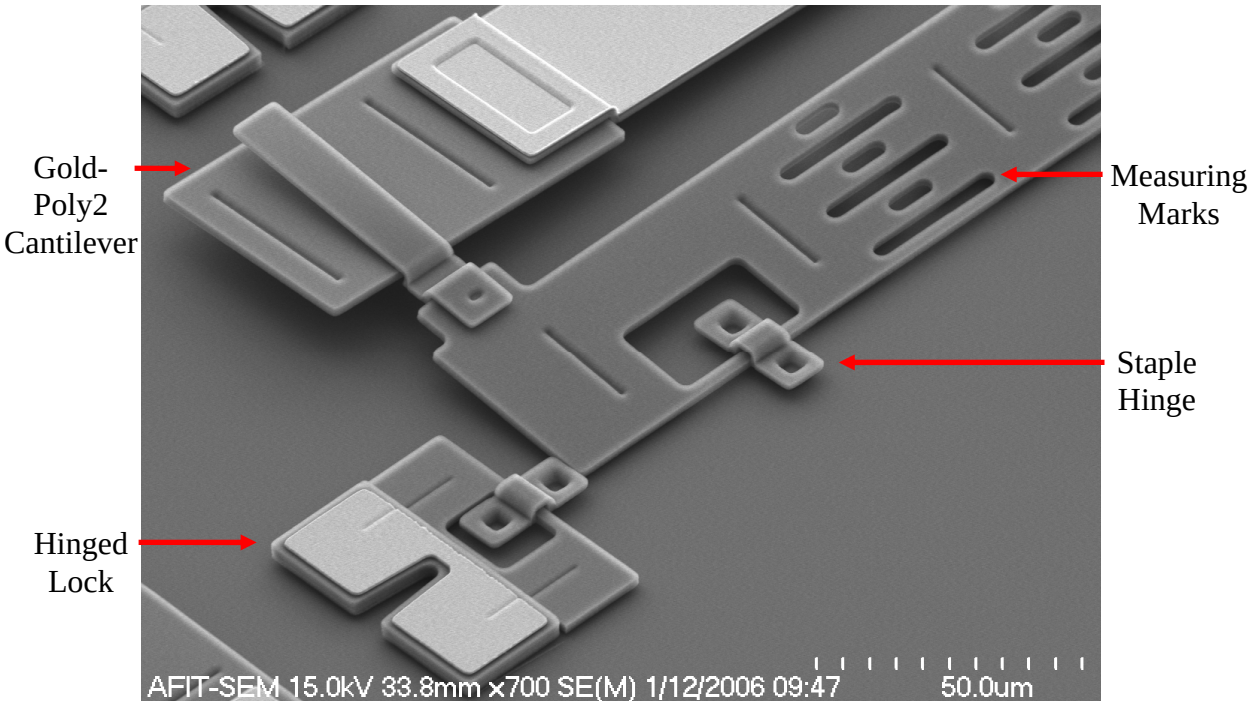


Figure 6.31: SEM image of a hinged flip-up ruler used to measure the downward vertical deflection of laser-powered microrobots. The ruler has regularly spaced etch holes for the measurement marks, and the ruler pivots inside a poly2 staple hinge. The ruler is boosted upwards by a gold-poly2 cantilever and can be locked into place.

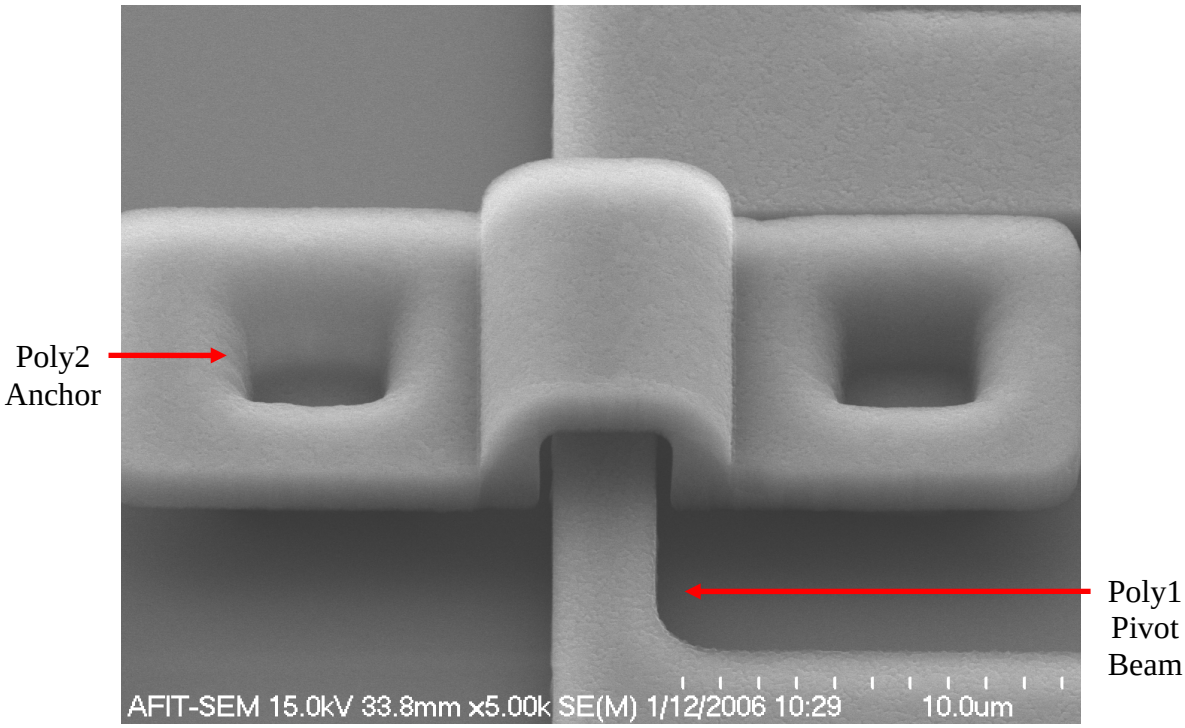


Figure 6.32: A close-up SEM image of the poly2 staple hinge for the flip-up ruler used to measure downward deflection in laser-powered robots.

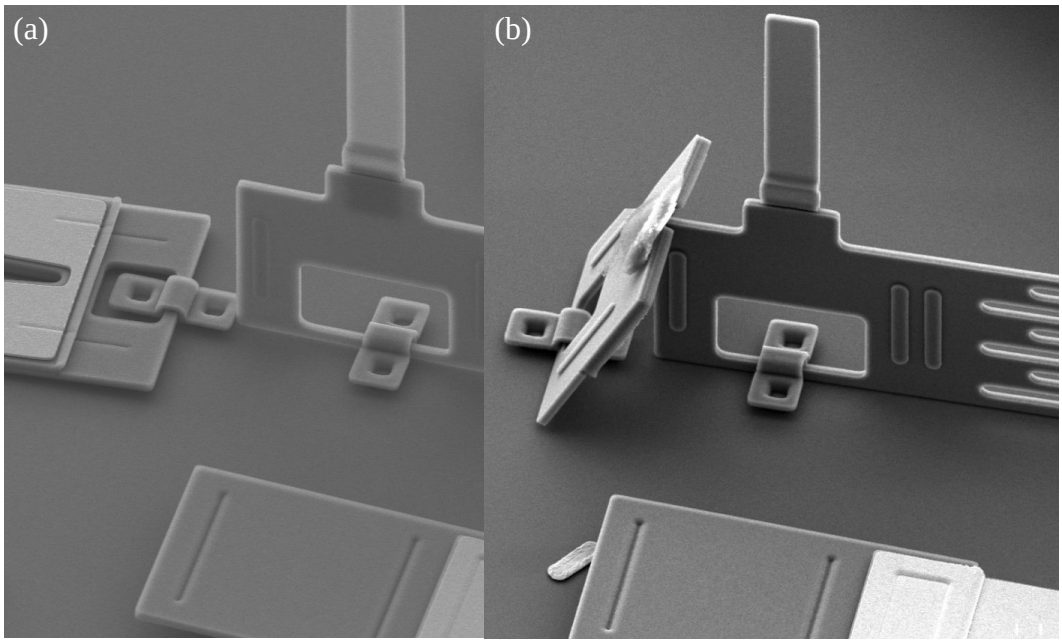


Figure 6.33: SEM images of a flip-up ruler in its: (a) unlocked and (b) locked positions.

The solution to the second issue is to design a novel launch pad. One viable design is a post, on which the microrobots could be positioned. The height of the post should be sufficient to allow full downward deflection of the wings. To minimize heat conduction from the microrobot into the substrate, the post should be thin, with only a very small amount of contact area on the top. It is possible to lift a released microrobot onto the post using a couple of probes, though this is very tedious.

Two different launch pads were fabricated. The first was accomplished by back-side etching a MUMPs® chip using a focused ion beam (FIB). The FIB etches structures with accelerated gallium ions at a very slow etch rate: 4 nm per minute for a 360-μm-diameter circle. It required nearly 40 hours of etching to achieve a depth of 23 μm for the launch pad shown in Figure 6.34 [5]. The center of the microrobot would rest on the hollow cylindrical post. The contact area is minimized to reduce heat conduction losses from the robot. An insulating layer could be deposited to further minimize heat loss.

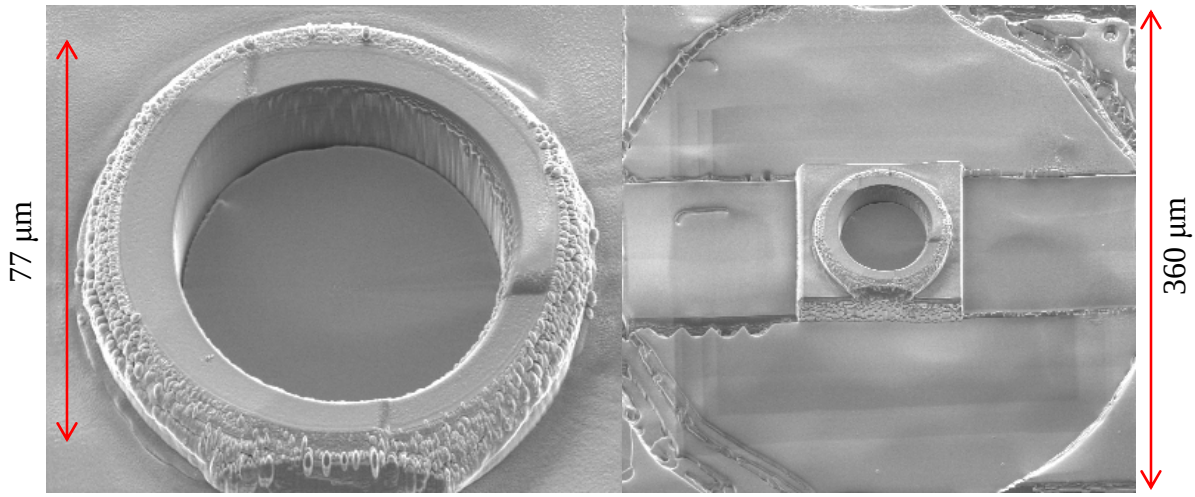


Figure 6.34: SEM images of a microrobot launch pad formed by back-side etching a MUMPs® chip. The launch pad was patterned and etched using a focused ion beam (FIB) machine. The center post diameter is 77 µm and is 23 µm deep [5].

The second launch pad was formed through both subtractive and additive techniques in PolyMUMPs®. A circular pit was etched into the nitride layer and substrate by applying every etchant available in PolyMUMPs®. The post was formed using every layer, including trapped oxide. A 10-µm-tall, 75-µm-wide post is shown in Figure 6.35.

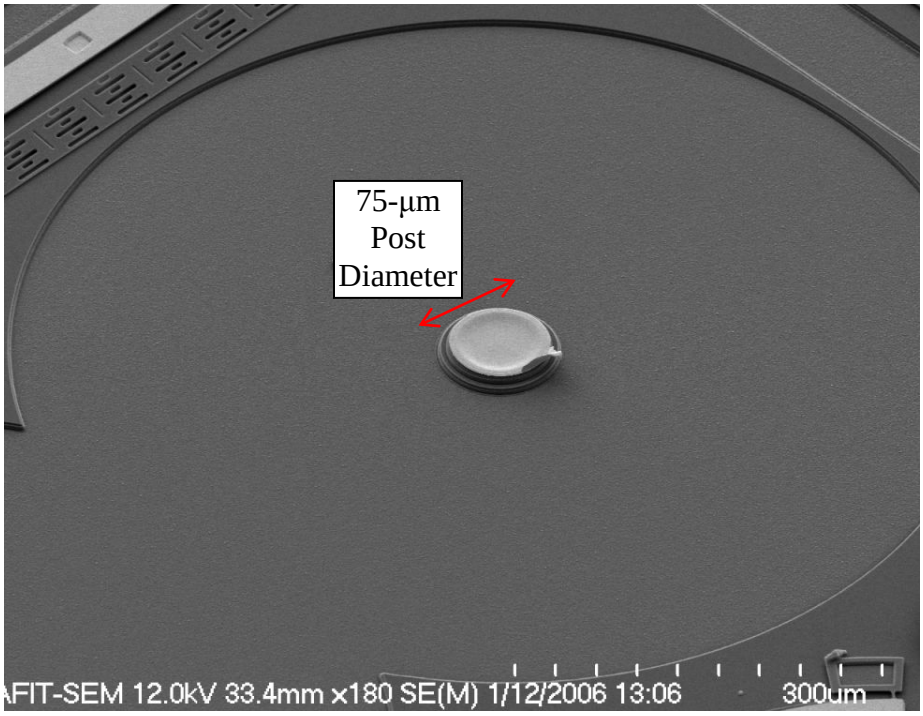


Figure 6.35: SEM image of a microrobot launch pad formed by etching a pit into the substrate and by stacking every PolyMUMPs® layer to form a post.

Gold was not supposed to remain on the posts, but, as evident in Figure 6.35, the gold did not successfully lift off during fabrication. This gold residue is the result of both maximizing the post height and minimizing the contact area on the top of the post. Flip-up rulers and microrobots were fabricated adjacent to the launch pads in order to facilitate positioning the robots on the launch pads and measuring downward deflection (see Figure 6.36). Figure 6.37 is a Zygo® image illustrating the 10-µm post height.

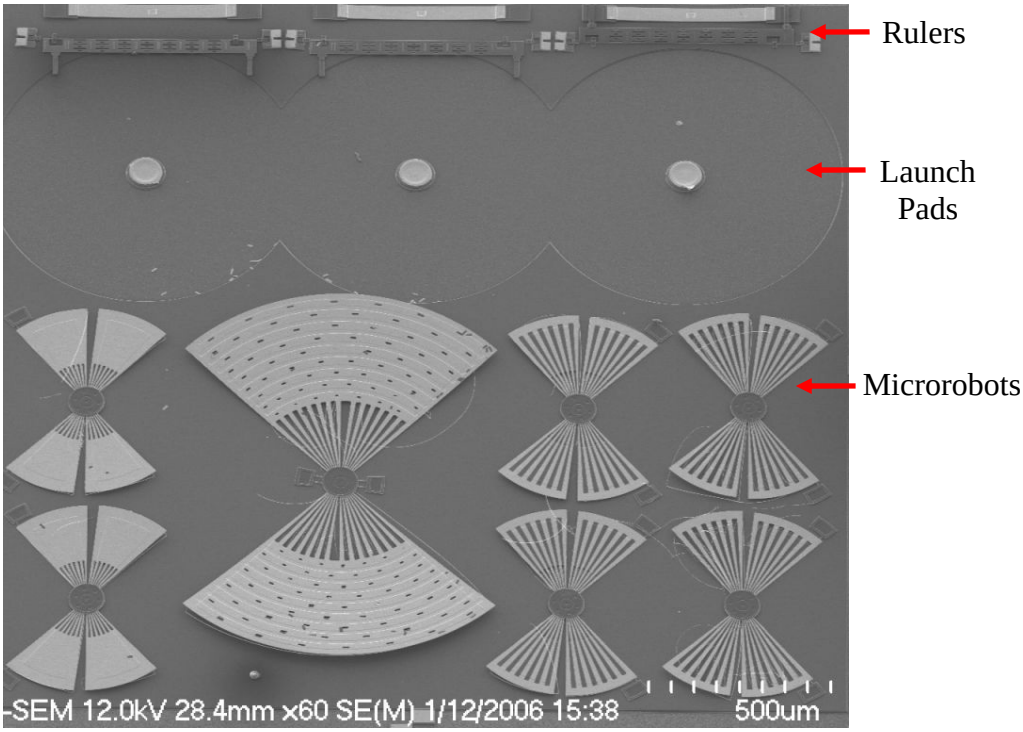


Figure 6.36: SEM image of rulers, launch pads, and microrobots.

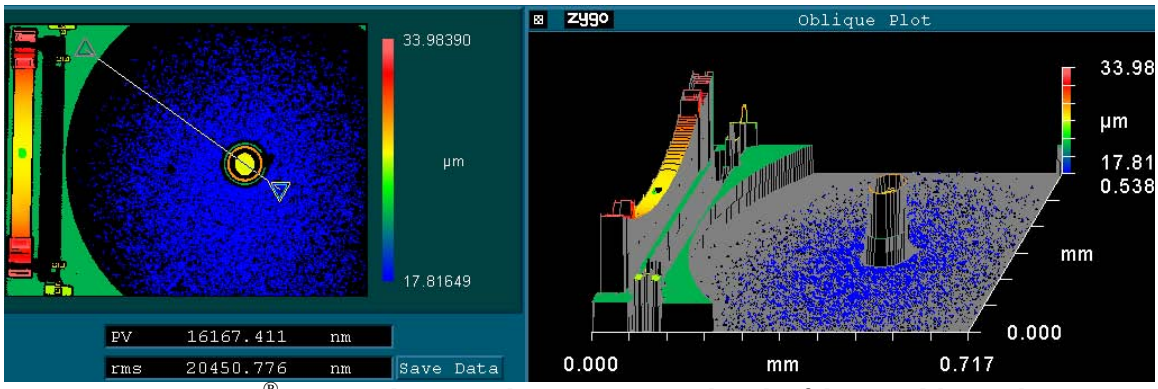


Figure 6.37: Zygo® image showing the 10-µm post height fabricated by etching 4 µm into the substrate and by stacking every PolyMUMPs® layer into a 6-µm post.

The novel flip-up rulers and launch pads are satisfactory solutions to the challenges encountered in measuring laser-induced downward deflection in microrobots. It would require months to test every fabricated microrobot with the laser setup. The focus must be on the robots with the most probable chance of taking flight. These are best identified by looking at the initial deflection results presented in the next chapter.

6.8 Summary

This chapter thoroughly described the three major experiments performed in this thesis: optimizing the laser setup used to power the microrobots, performing successful sacrificial oxide releases of the microrobot chips, and measuring the performance of the microrobots. The information contained in this chapter is invaluable to researchers in laser-powered microrobots as well as to MEMS researchers in general.

Chapter 7 presents the results of the robot performance experiments. The focus is on initial deflection because of its relation to downward deflection. While it is impossible to test the scores of different microrobots designed and fabricated in this thesis, it is possible to test those with greatest probability of taking flight. These are identified by initial deflection values given in the next chapter.

6.9 References

[1] F. R. Szabo, *Demonstrating Optothermal Actuators for an Autonomous MEMS Microrobot*, MS thesis, AFIT/GE/ENG/04-23. School of Engineering and Management, Air Force Institute of Technology (AU), Wright-Patterson AFB OH, March 2004 (AD-A426469).

[2] B. E. A. Saleh and M. C. Teich, *Fundamentals of Photonics*, New York: John Wiley and Sons, 1991, pp. 83-95.

[3] *Autosamdri®-815 Series B User Manual*. Rockville, MD: Tousimis®, 2003.

[4] *New View 5000™ User Manual*. Middlefield, CT: Zygo®, 2001.

[5] S. Apt. Focused Ion Beam and Scanning Electron Microscope Technical Expert, Materials Directorate, Air Force Research Laboratory (AFRL/MLLN), Wright-Patterson AFB, OH. 28 Nov. 2005–5 Jan. 2006.

VII. Results and Analyses

7.1 Chapter Introduction

The results from the microrobot performance experiments described in Chapter 6 are reported here. The entire initial deflection results for cantilevers are presented, and only trends in microrobot deflection measurements are presented. The deflection values from various microrobot design configurations are analyzed to determine which elements contribute the most to deflection. Downward deflection results in electrically powered test wings are also included. Based on these results, the most optimized microrobot designs are identified. The thrust-to-weight ratio of these microrobots is given and analyzed. Finally, the results of laser-powered downward deflection tests are presented.

7.2 Cantilever Initial Deflection

Identical cantilevers of varying lengths were fabricated in MUMPs® runs 66, 68, and 69. The initial deflection due to residual stress in these cantilevers serves as a control element from run to run. Figure 7.1 illustrates a Zygo® image of gold-poly2 cantilevers.

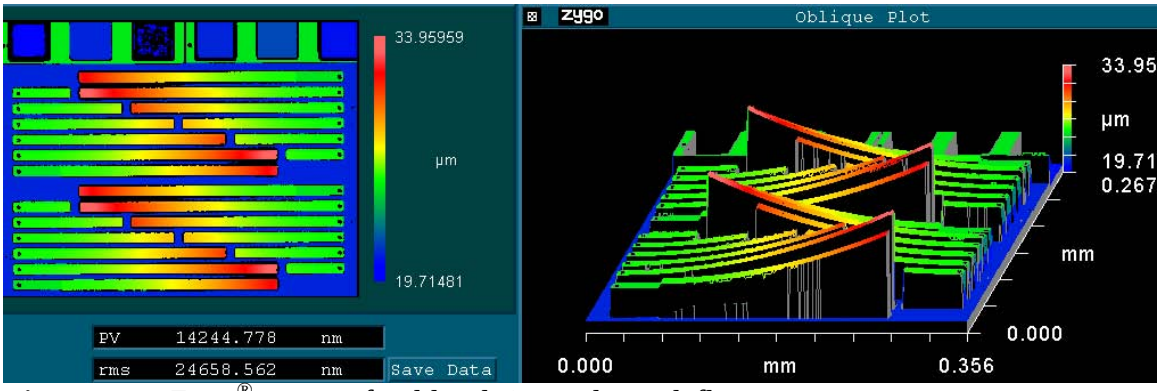


Figure 7.1: Zygo® image of gold-poly2 cantilever deflection measurements.

The deflection measurements for cantilevers fabricated in MUMPs® runs 66, 68, and 69 are given in Figure 7.2 and in Table 7.1, Table 7.2, and Table 7.3 (cantilevers

were not included in MUMPs® run 67). The cantilever lengths vary from 49 to 249 μm and all are 10 μm wide. The nanometer vertical resolution of the Zygo® IFM provides precise data for measurements in the micrometer range. Thus, the measurement error is assumed negligible for this data. However, the standard deviation values are included in the tables since several measurements were made for each cantilever.

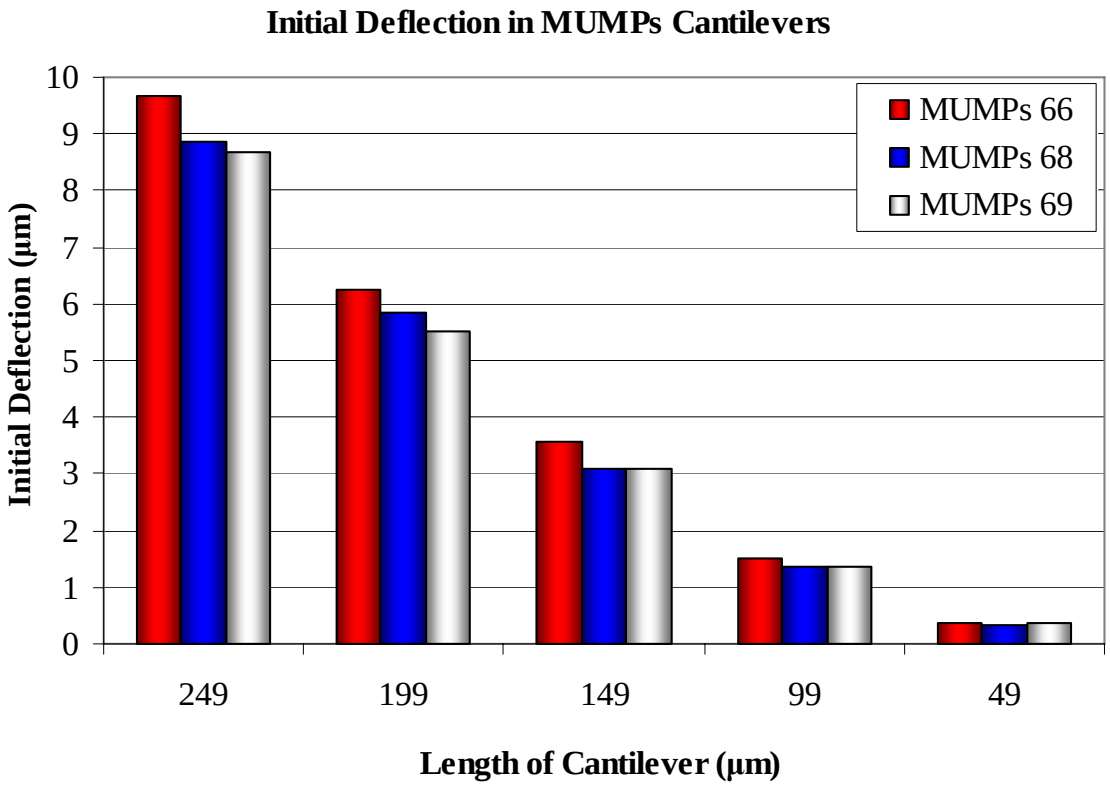


Figure 7.2: Graphed data of gold-poly2 cantilever deflection measurements from MUMPs® runs 66, 68, and 69. The cantilever dimensions are identical from run to run. No cantilevers were fabricated in run 67. This data illustrates that the initial deflection was the greatest for run 66 and the least for run 69.

Table 7.1. MUMPs® 66 cantilever deflection measurement values {all units in μm}.

Cantilever Length	Average Deflection	Standard Deviation
249	9.668	0.620
199	6.266	0.406
149	3.576	0.288
99	1.511	0.027
49	0.360	0.018

Table 7.2. MUMPs® 68 cantilever deflection measurement values {all units in μm}.

Cantilever Length	Average Deflection	Standard Deviation
249	8.866	0.139
199	5.841	0.123
149	3.075	0.104
99	1.362	0.043
49	0.338	0.014

Table 7.3. MUMPs® 69 cantilever deflection measurement values {all units in μm}.

Cantilever Length	Average Deflection	Standard Deviation
249	8.681	0.169
199	5.500	0.108
149	3.099	0.059
99	1.351	0.045
49	0.354	0.024

The cantilever deflection values are the greatest in MUMPs® run 66 and the lowest in run 69. However, the standard deviation among the cantilever measurements in run 66 is also the greatest, while the deviations in runs 68 and 69 are generally less. As was demonstrated in Chapter 4, deflection is directly proportional to residual stress in the material layers. The reported residual stress values for poly2 and gold are given in Table 7.4. As compressive and tensile stress act in opposite directions, the difference between the stress values for the two layers is also calculated. At 18.40 MPa (T), the difference is the greatest for run 66 and the lowest at 8.10 (T) for run 69. This trend matches the deflection results given.

Table 7.4. Reported residual stress data for MUMPs® poly2 and gold layers [1].

MUMPs® Run	66	67	68	69
Poly2 Residual Stress {MPa}	7.30 (C)	7.60 (C)	6.00 (C)	7.66 (C)
Gold Residual Stress {MPa}	25.70 (T)	20.10 (T)	17.13 (T)	15.76 (T)
Difference {MPa}	18.40 (T)	12.50 (T)	11.13 (T)	8.10 (T)

7.3 Trends in Microrobot Initial Deflection

As determined in the design chapter, microrobot flight can be achieved by maximizing deflection and surface area while minimizing mass. In the MUMPs® process, the layer thicknesses and materials are fixed. The only way to reduce mass without simultaneously reducing surface area is to either make the layers thinner or use less dense materials. Therefore, the focus for this chapter is maximizing upward and downward deflection. The various design elements examined include the amount of gold, flexure width and spacing, the spacer layer, and other wing configurations.

Measuring initial deflection on the Zygo® was explained in Chapter 6. Figure 7.3 illustrates a Zygo® IFM image of a microrobot, including the deflection profile. The 7.47179-µm initial deflection is measured along the white cursor. At least three samples of each microrobot were measured individually in this manner.

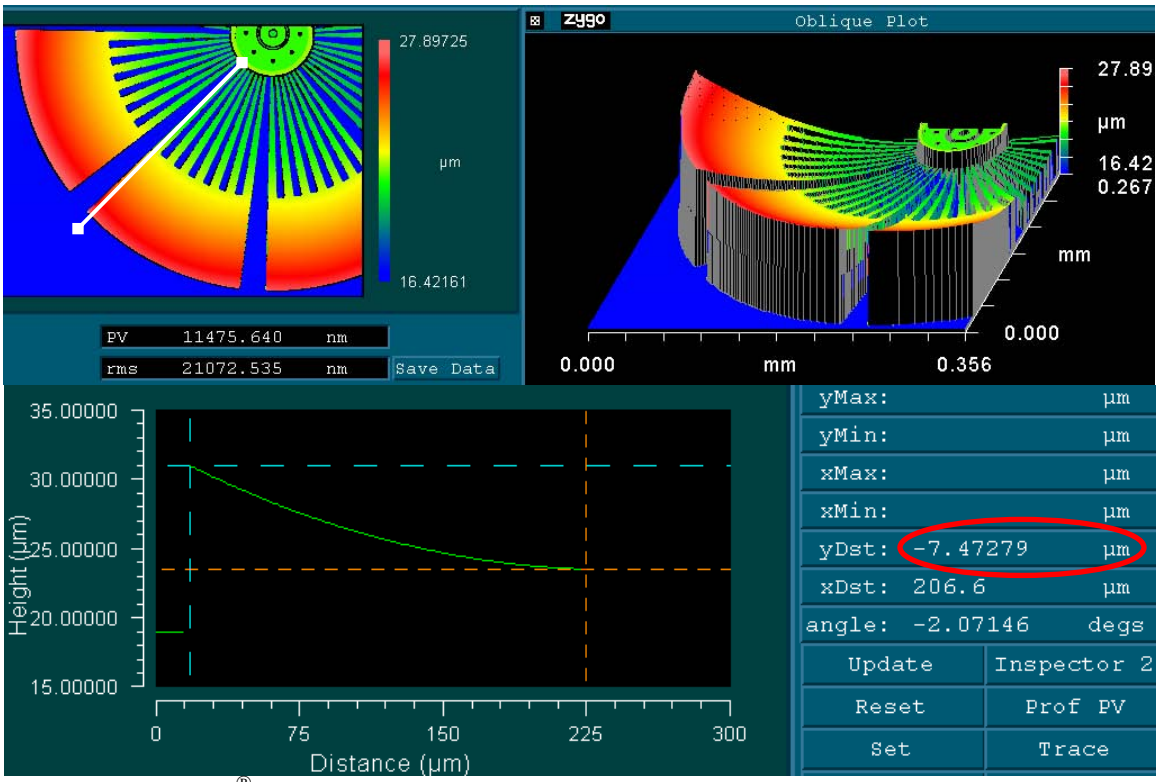


Figure 7.3: Zygo® data showing a microrobot surface map and deflection profile. The initial deflection of this microrobot is 7.47279 µm for a 206.6-µm wing length.

The following sections highlight the important trends in the microrobot initial deflection results. The complete results of each microrobot fabricated in this thesis are given in Appendix E. In MUMPs® runs 66–69, 129 different microrobots were fabricated on 23 separate chips. In order to maximize chip real estate, the order in which the microrobots were positioned was often not ideal. Therefore, a clear numbering scheme has been adopted to reference the designs: for the microrobot in the 9th position on the first robot chip in MUMPs® 67, the scheme is M67rob1pos9. This scheme allows the avid reader to refer to either Appendix A or E to see any design in more detail.

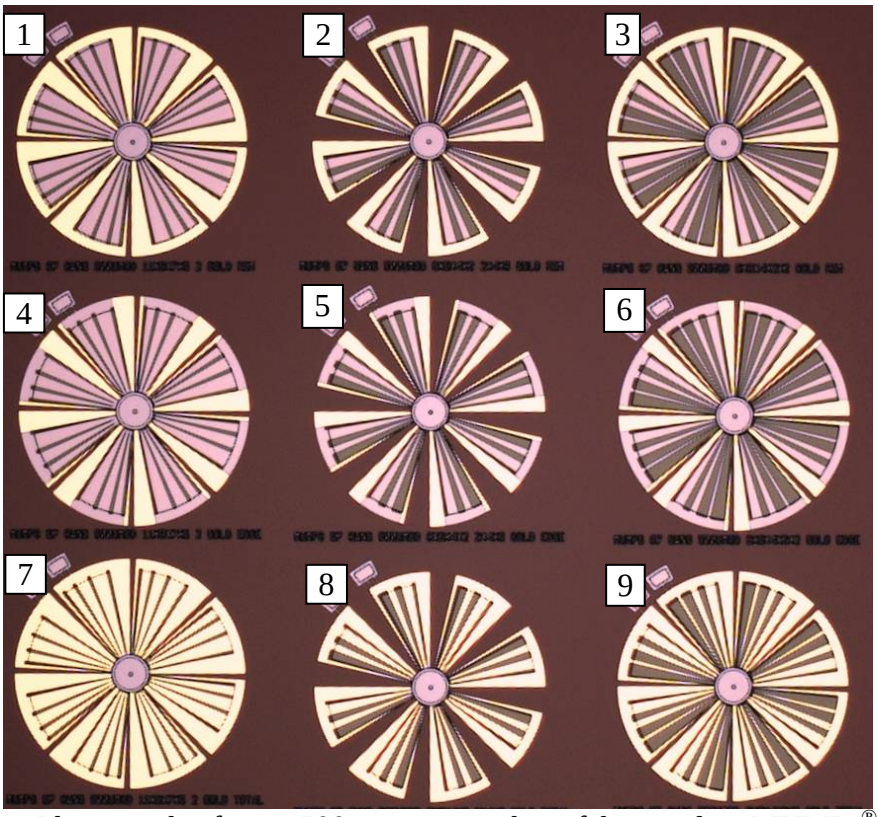


Figure 7.4: Photograph of nine 500-μm microrobots fabricated in MUMPs® 67. Each chip is divided into a 3x3 grid and numbered sequentially from left to right, top to bottom. This is the first robot chip in MUMPs® run 67, so the robot in the ninth position is labeled M67rob1pos9.

Due to their efficient organization, two particular microrobot chips illustrate most of the trends from the design elements. These two chips—MUMPs® 68 robot chip 1

(M68rob1) and MUMPs® 68 robot chip 2 (M68rob2)—are given in Figure 7.5. SEM images of a robot from M68rob1 and M68rob2 are given in Figure 7.6.

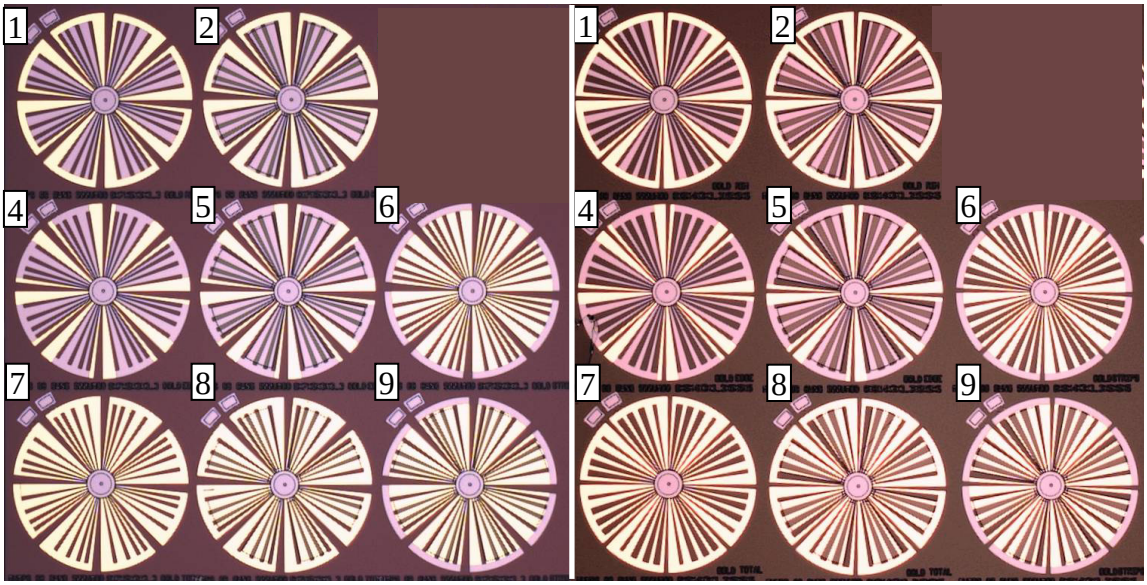


Figure 7.5: Photographs of (left) the M68rob1 chip, and (right) the M68rob2 chip. The only difference between the two chips is the poly2 wing pattern: the robots on M68rob1 have closely spaced flexures and the robots on M68rob2 have larger gaps between each flexure. There are four basic gold patterns on the robots. Each robot on a chip is duplicated so that four robots have a poly0 spacer under them (2, 5, 8, and 9) and four do not (1, 4, 6, and 7). The same is true for the other chip: the same four microrobots have the poly0 spacer under their wings and four do not.

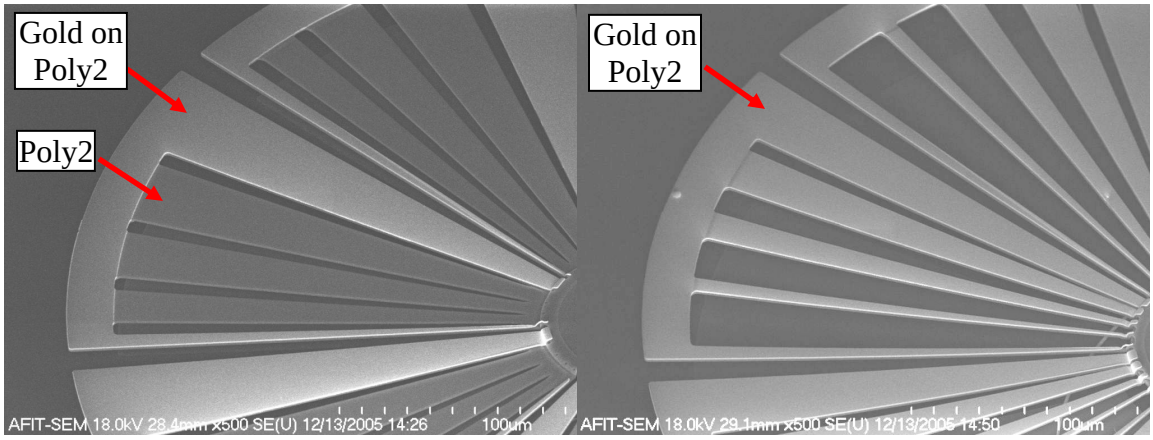


Figure 7.6: SEM images of the two different microrobot wing configurations from Figure 7.5. The image on the left has relatively wide flexures that are narrowly spaced; this corresponds to the M67rob1 chip in Figure 7.5. The image on the right has relatively narrow flexures with incrementally varying gaps between each flexure; this corresponds to the M67rob2 chip in Figure 7.5. Notice that the image on the left has gold only around the wing edges while the image on the right has gold over the entire wing.

The poly2 microrobot wing configurations between the two chips are different. On M68rob1, each robot has relatively wide flexures and equal gaps between each flexure. On M68rob2, each robot has relatively narrow flexures and incrementally varying gaps between each flexure. This is the only difference between the two chips.

Both chips have four different gold configurations on each wing. Robots in positions 1 and 2 have gold around the edge of the wing; robots in positions 4 and 5 have gold only on the left and right edges of each wing, but none around the outside rim; robots in positions 7 and 8 have gold everywhere; and robots in positions 6 and 9 have gold everywhere except on the outside rims. The robots in the first column (1, 4, 7) are duplicates of the robots in the second column (2, 5, 8); the only difference is the robots in the first column do not have a poly0 spacer under their wings while those in the second column do. Positions 6 and 9 are duplicates; 6 does not have poly0 but 9 does. The poly0 spacer is visible in the L-edit® layout, where poly0 is colored brownish-orange.

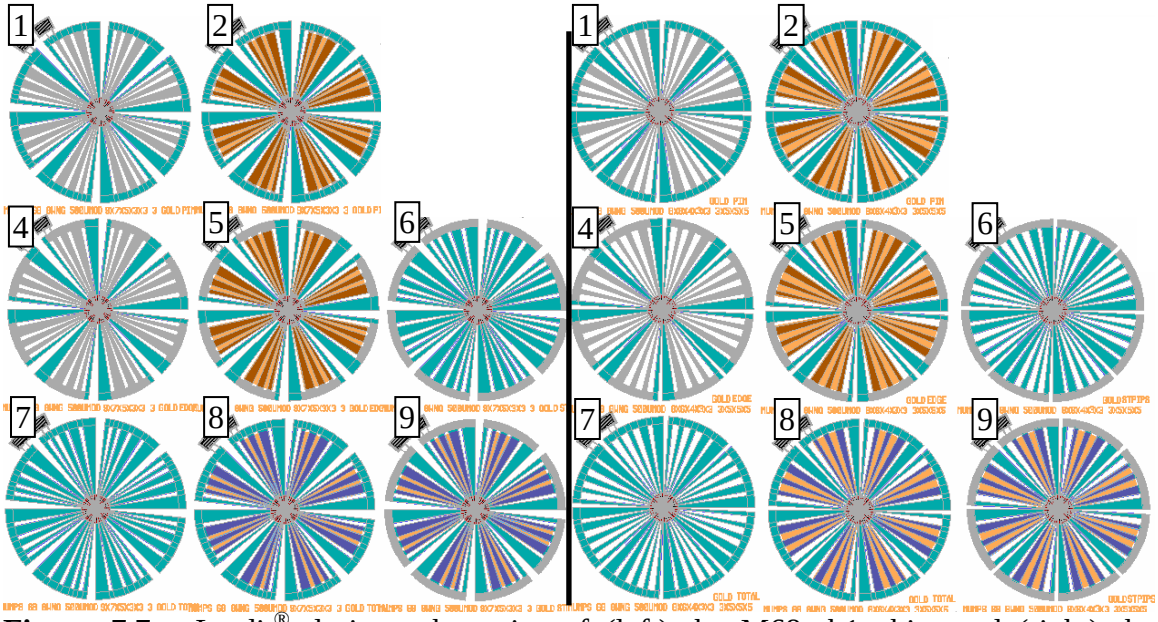


Figure 7.7: L-edit® design schematics of (left) the M68rob1 chip, and (right) the M68rob2 chip. Each robot on both chips has a duplicate pair. In each pair, half have a poly0 spacer under them and half do not; the poly0 layer is colored brownish-orange.

The deflection results for the robots in these two chips are presented in Figure 7.8.

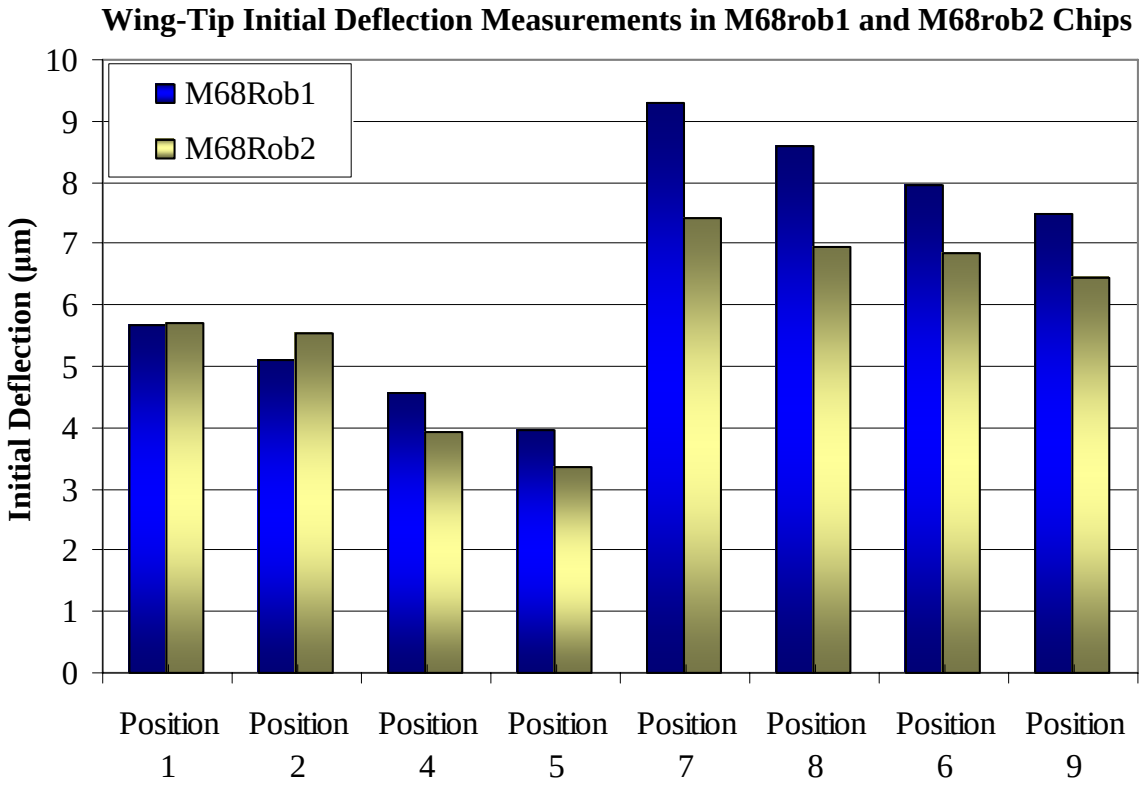


Figure 7.8: Wing-tip deflection measurements of microrobots in the M68rob1 and M68rob2 chips. Except for positions 1 and 2, the deflection in M68rob1 is greater.

A few trends in the data are immediately evident. The first is the relationship between the amount of gold and deflection. The microrobot pairs put in descending order from most to least deflection are: 7-8, 6-9, 1-2, and 4-5. This trend exactly matches the amount of gold each microrobot has: 7-8 with the most, 6-9 with a little less, 1-2 with even less, and 4-5 with the least amount of gold. Therefore, the results confirm the theory that deflection is directly proportional to gold quantity.

Another trend is that, except for the 1-2 position pair, the amount of microrobot deflection in the M68rob1 chip is greater than that the M68rob2 chip. This leads to a relationship between flexure width and deflection: wider gold flexures deflect more than narrower gold flexures.

The final trend from the deflection data is the effect of the poly0 spacer on deflection. In each pair, the microrobot without the poly0 spacer layer under the wings shows more deflection than the microrobot with the spacer. Thus, the spacer inhibits deflection, and its only benefit is a slight cupping shape.

The calculated mass and surface area values for each microrobot are compared with deflection in Table 7.5 and Table 7.6. This data shows that the microrobots with the most deflection and surface area are also the most massive.

Table 7.5. Measured deflection compared with calculated mass and surface area in M68rob1 microrobots. The maximum deflection and surface area values and minimum mass values are in bold. The microrobot pairs are arranged together.

Position	Deflection	Mass	Surface Area
1	5.66 μm	1.12 μg	0.286 mm^2
2	5.09 μm	1.12 μg	0.286 mm^2
4	4.57 μm	**0.94 μg**	0.286 mm^2
5	3.97 μm	**0.94 μg**	0.286 mm^2
7	**9.29 μm**	1.70 μg	**0.291 mm^2**
8	8.59 μm	1.70 μg	**0.291 mm^2**
6	7.97 μm	1.44 μg	**0.291 mm^2**
9	7.50 μm	1.44 μg	**0.291 mm^2**

Table 7.6. Measured deflection compared with calculated mass and surface area in M68rob2 microrobots. The maximum deflection and surface area values and minimum mass values are in bold. The microrobot pairs are arranged together.

Position	Deflection	Mass	Surface Area
1	5.72 μm	1.08 μg	0.269 mm^2
2	5.55 μm	1.08 μg	0.269 mm^2
4	3.93 μm	**0.87 μg**	0.268 mm^2
5	3.37 μm	**0.87 μg**	0.268 mm^2
7	**7.41 μm**	1.53 μg	**0.273 mm^2**
8	6.94 μm	1.53 μg	**0.273 mm^2**
6	6.85 μm	1.25 μg	**0.273 mm^2**
9	6.44 μm	1.25 μg	**0.273 mm^2**

The trends highlighted in the M68rob1 and M68rob chips are consistent with all the microrobots fabricated from MUMPs® runs 66 to 69. The complete set of data is available in Appendix E. This data shows a satisfying design trend. From run 66 to run 69, the residual stress values in gold and poly2 decreased as did the measured cantilever deflection (see Figure 7.2, Table 7.1, Table 7.2, and Table 7.3). It was determined in the modeling chapter that deflection is directly related to stress. Despite this decrease in stress, the microrobot deflection continued to increase from run to run. The increased microrobot deflection is attributed to optimized designs.

It should be noted here that the deflection in the 990-μm robots was three times the deflection of the best 500-μm robot. Thus, a very effective method of increasing deflection is by increasing the wing length. The microrobot deflection results from the four MUMPs® runs are concisely summarized in Table 7.7, in which the advantages and disadvantages of each design elements are also given.

Table 7.7. Microrobot design element advantages and disadvantages.

Design Element	Advantages	Disadvantages
More Gold	More Deflection	More Mass
More Surface Area	Faster Cool Time More Lift More Deflection	More Mass
No Spacer Layer	More Deflection	Same Mass
Wider Flexures	More Deflection More Surface Area	More Mass
Longer Wings	More Deflection More Surface Area	More Mass

It is obvious that tradeoffs must be made between deflection, surface area, and mass for each design element except the spacer layer—eliminating it improves deflection without any significant negative consequences. The robots with the most deflection and

surface area yet least mass would be the most successful flyers. It could be assumed that initial deflection is equivalent to powered downward deflection. However, this assumption may not be true. The relationship between downward deflection and power can be determined with electrically powered test wings.

7.4 Powered Deflection in Microrobot Test Wings

The electrically testable wings from MUMPs® 69 that were chosen for this test are illustrated in Figure 7.9. The wing in position (1) is covered in gold and has a poly0 spacer underneath. The wing in position (2) is the same as (1) except it lacks the poly0 spacer. The wing in position (3) has gold around the edges but not on the middle flexures; it also has a poly0 spacer under it. Downward deflection is achieved by applying incremental voltages to the test wings through probes. A Zygo® measurement is then made at each voltage increment. Figure 7.10 shows Zygo® images at 0.0 V and 2.0 V, and Figure 7.11 shows the results.

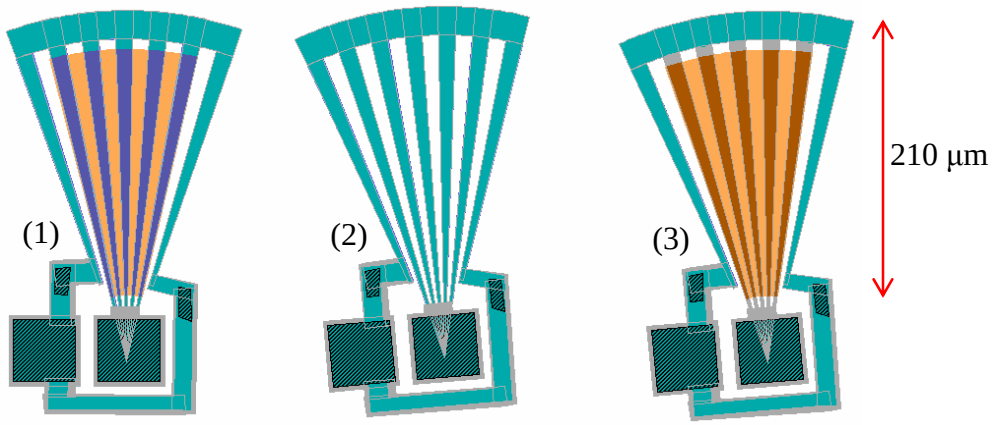


Figure 7.9: L-edit® schematic of three 210-μm electrically testable wings from 500-μm microrobots fabricated in MUMPs® 69. The wing in (1) has gold everywhere and a poly0 spacer layer under it (poly0 is colored brownish-orange). The wing in (2) is the same as (1) except for the poly0 spacer. The wing in (3) is the same as (1) except is does not have gold on the middle flexures. A positive voltage is applied to one probe pad while ground is applied to the other. The resulting current flow creates heat in the device and causes downward deflection.

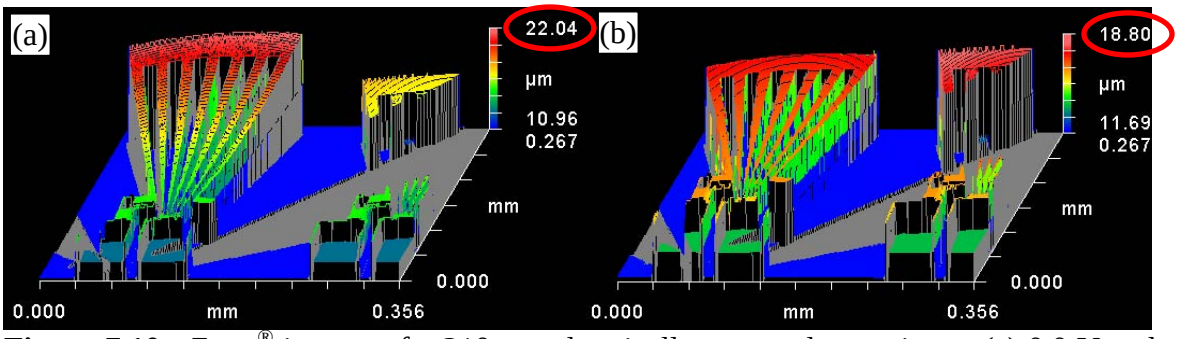


Figure 7.10: Zygo® images of a 210-µm electrically powered test wing at (a) 0.0 V and (b) 2.0 V. The test wing imitates the laser-powered microrobots by deflecting downward from (a) 22.05 µm to (b) 18.80 µm when power is applied.

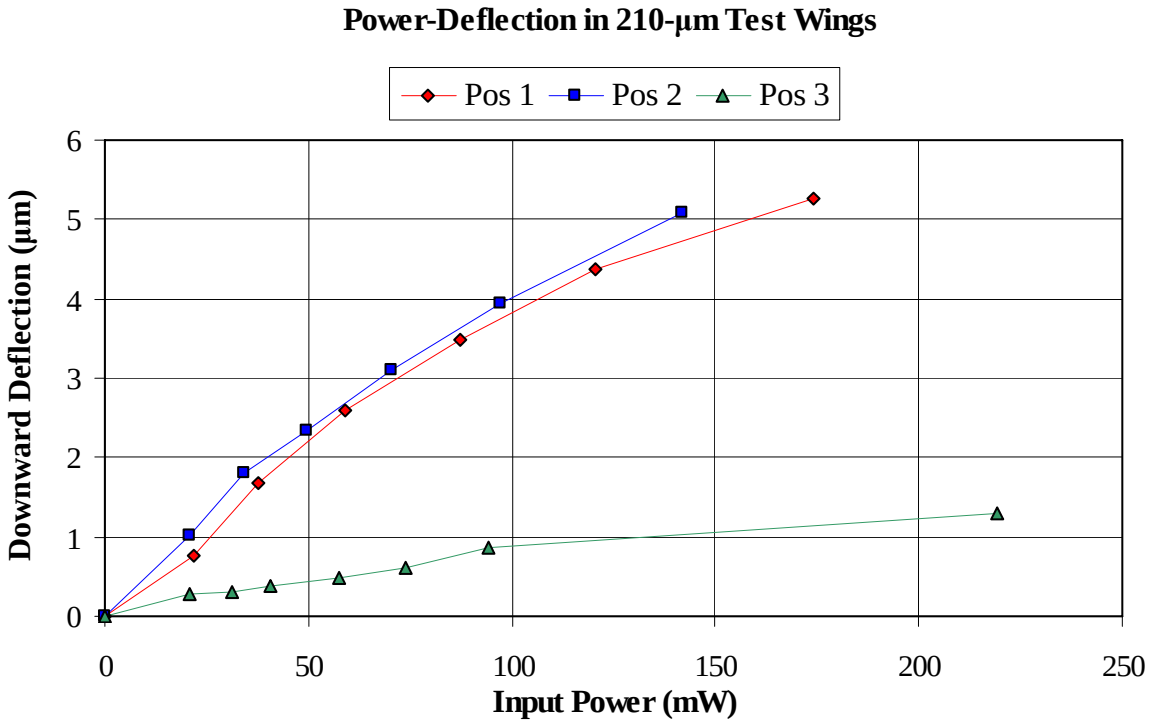


Figure 7.11: Powered deflection in three 210-µm electrically powered test wings at increasing input power levels. The positions correspond to the numbers in Figure 7.9. The all-gold wing without the poly0 spacer has the best deflection-power ratio.

The powered deflection results from Figure 7.11 clearly illustrate that the all-gold wings have a better deflection-power ratio than the wing with gold only on the outside edges. This test indicates that the microrobots with the best laser-powered deflection are the ones with all-gold flexures. Thus, the microrobot flexures without gold will not yield efficient downward deflection. Challenges in this test are described in Appendix F.

The downward deflection in a 420-µm test wing from a 990-µm microrobot was also tested. The wing is illustrated in Figure 7.12, and the deflection results are given in Figure 7.13. Also shown are the results from the position-1 test wing from Figure 7.11.

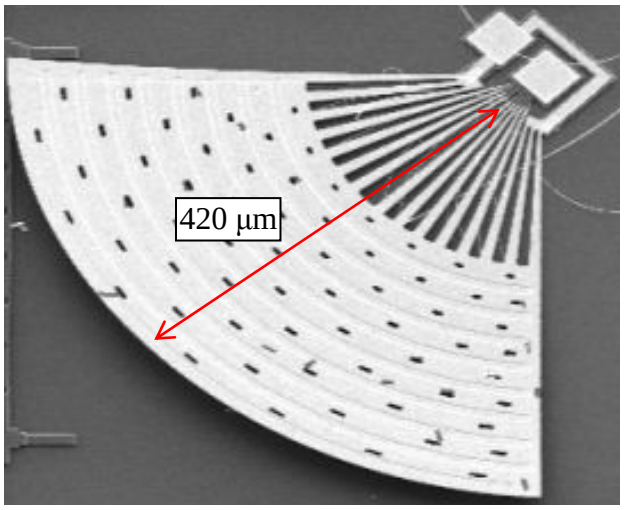


Figure 7.12: SEM image of a 420-µm electrically testable wing from a 990-µm microrobot fabricated in MUMPs® 69.

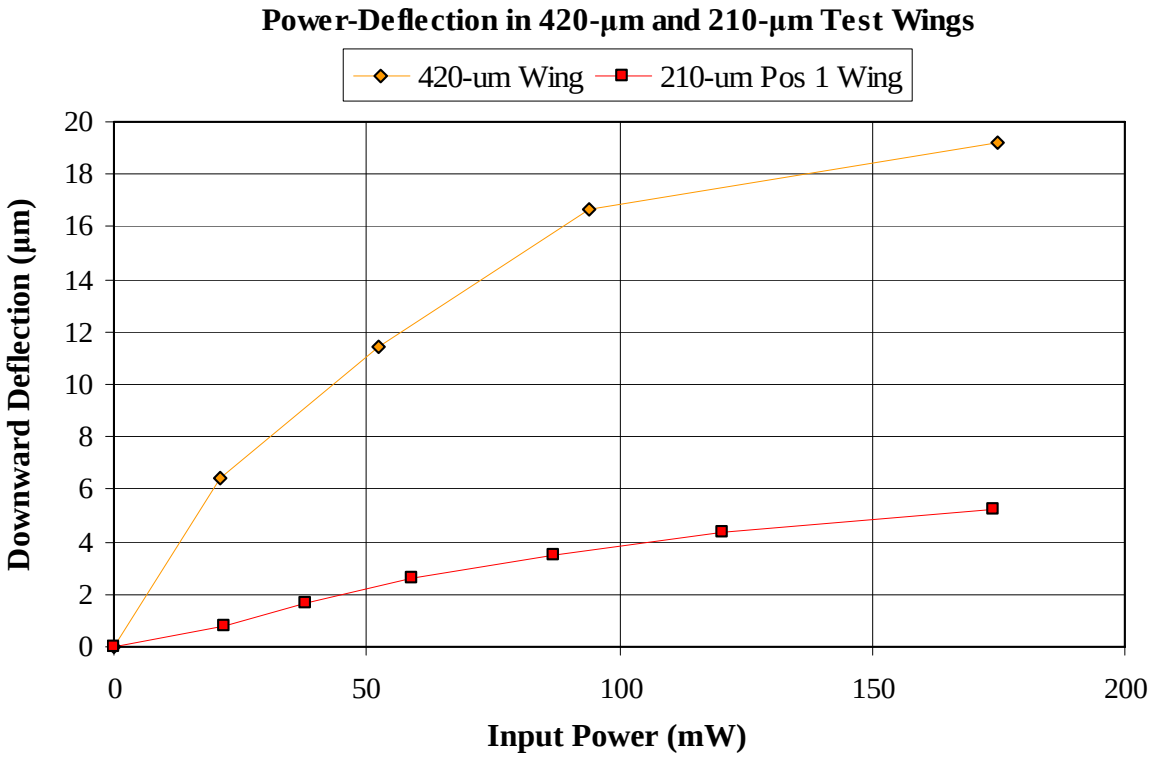


Figure 7.13: Powered deflection of a 420-µm electrically testable wing from a 990-µm microrobot compared with the 210-µm wing from Figure 7.9. The 420-µm has a greater deflection-power ratio.

It is clear that the test wing from the 990-μm microrobot has a better deflection-power ratio than test wings from the 500-μm microrobots. With the power-deflection results, it is possible to determine which microrobots have the greatest potential for flight.

7.5 Optimized Microrobot Design Results

The microrobots with the greatest chance of taking flight are those with the following characteristics: the greatest upward and downward deflection, the greatest surface area, and the least amount of mass. Because of design trade-offs and the constraints of the PolyMUMPs® process, it is impossible to maximize deflection and surface area without also increasing mass. However, in other processes—MEMS Exhange®, Mosis®, etc.—it could be possible to increase surface area without increasing mass by reducing layer thicknesses and by using less dense materials.

The 500-μm microrobots with the highest combined deflection-mass and area-mass ratios from this thesis are identified; these are illustrated in Figure 7.14 and in Table 7.8. Only three 500-μm microrobots were selected as their deflection-mass ratio exceeded 5 and their area-mass ratio exceeded 0.2. All the other microrobots exceeded only one of the ratios—either 5 or 0.2 but not both.

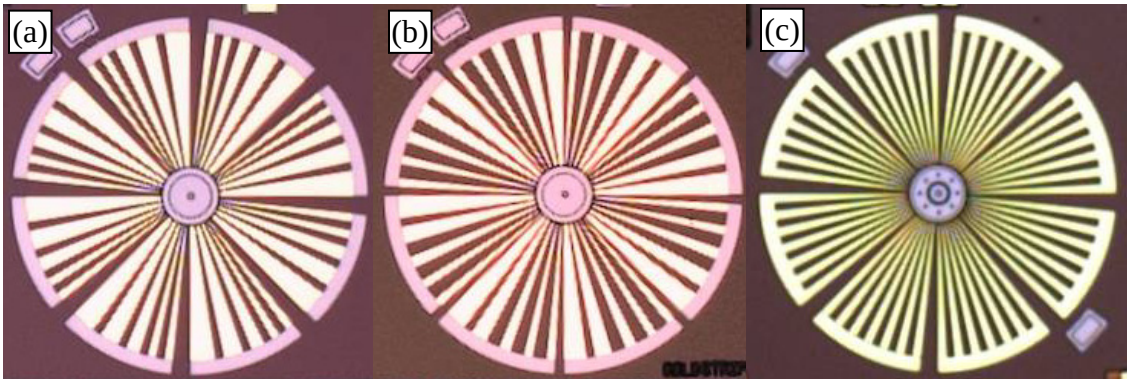


Figure 7.14: Photographs of the 500-μm microrobots with the highest combined deflection-mass and area-mass ratios: (a) is M68rob1pos6; (b) is M68pos2pos6; and (c) is M69rob1pos8.

Table 7.8. The 500-μm microrobots with the best combined deflection-mass and area-mass ratios. These microrobots have the greatest chance of taking flight due to their large deflection and surface area yet relatively low mass. (The letters match Figure 7.14.)

Microrobot	Deflection-Mass Ratio	Area-Mass Ratio
(a) M68rob1pos6	5.535	0.202
(b) M68rob2pos6	5.480	0.218
(c) M69rob1pos8	5.545	0.204

The microrobots highlighted in Figure 7.14 and in Table 7.8 exemplify the best balance in the design trade-offs. Common in their designs are gold flexures and the lack of the poly0 spacer. Also, the gold rim is missing in (a) and (b), which indicates that the mass it contributes does not match its deflection contribution. The microrobot in (c) could be improved by removing the gold rim.

Observing the deflection data from all the microrobots designed in this thesis yields important design trends. While the robots with the greatest deflection had the widest flexures, their mass was also very high, resulting in a low deflection-mass ratio. Also, the robots with the least amount of gold had the greatest area-mass ratio, but their lack of gold resulted in a very low deflection. Achieving the best combined deflection-mass and area-mass ratios is a balancing act that is best illustrated in the microrobots from Figure 7.14.

The thrust calculations for these microrobots show a disappointing result. The requirement for flight given in Chapter 5 is that downward force must exceed the force due to gravity. The equations are repeated here and the calculations follow:

$$C_D \frac{1}{2} \rho U^2 A > mg \,, \tag{7.1}$$

$$U = \frac{\theta L}{\tau} = \frac{\delta}{\tau} \,, \tag{7.2}$$

$$\tau = \frac{mc}{hA_T} \ln\left(T_{\max}\right). \tag{7.3}$$

The deflection, surface area, and mass values for each of the microrobots in Figure 7.14 are used; the constants are taken from Chapter 4 and Chapter 5. It is assumed that total deflection is twice the upward initial deflection. It is also assumed that the deflection time is determined by the time required for cooling, and the heating time is assumed to be instantaneous. The maximum operating frequency is the inverse of the cooling time. Also, it is assumed that only a portion of the entire microrobot mass heats up—the portion closest to the laser target area. Thus, only a fraction of the entire microrobot mass must be cooled, which reduces cooling time. It is assumed that only one half of the microrobot mass heats up.

Table 7.9. Calculations of thrust and weight from the microrobots in Figure 7.14.

Property	Value	Reference	
Coefficient of Drag, C_D {unitless}	2	From Chap 5	
Density of Air, ρ {kg/m^3}	1.168	From Chap 5	
Specific Heat, c {J·kg^{-1}·K^{-1}}	129 (Gold)	From Chap 4	
Convection Coefficient, h {W·m^{-2}·K^{-1}}	3850	From Chap 4	
Maximum Device Heat, T_{max} {K}	360	From Chap 4	
	M68rob1pos6	M68rob2pos6	M69rob1pos8
Microrobot Mass, m {kg}	1.44 x 10^{-9}	1.25 x 10^{-9}	1.34 x1 0^{-9}
Microrobot Area, A {m^2}	0.1455 x 10^{-6}	0.1365 x 10^{-6}	0.137 x 10^{-6}
Total Area for Convection, A_T {m^2}	0.291 x 10^{-6}	0.273 x 10^{-6}	0.274 x 10^{-6}
Cooling Time, τ {s}	216 x 10^{-6}	200 x 10^{-6}	213 x 10^{-6}
Max. Operating Frequency, f {Hz}	4636	5010	4690
Downward Deflection, δ {m}	7.97 x 2 x 10^{-6}	6.85 x 2 x 10^{-6}	7.43 x 2 x 10^{-6}
Wing-Tip Velocity, U {m/s}	73.9 x 10^{-3}	68.6 x 10^{-3}	69.7 x 10^{-3}
Force due to Drag, F_D {N}	**0.928 x 10^{-9}**	**0.751 x 10^{-9}**	**0.777 x 10^{-9}**
Force due to Gravity, F_g {N}	**14.1 x 10^{-9}**	**12.3 x 10^{-9}**	**13.1 x 10^{-9}**
Force Ratio, F_D/F_g {unitless}	**0.0658**	**0.0613**	**0.0592**

From the calculations given in Table 7.9, the force due to drag generated by the microrobots is lower than the microrobot weight. In order to fly, the force ratio must be greater than unity, but for these devices it is less than one. These thrust-weight calculations were done for every microrobot in this thesis, and the three microrobots in this table yielded the best thrust-weight ratio. Just as expected, the deflection-mass and area-mass ratios indicate which microrobot has the greatest chance of taking flight.

Though the M68rob1pos6, M68rob2pos6, M69rob1pos8 designs are the most optimized, they still cannot generate sufficient force to fly. Higher deflection, shorter cooling time, more area, and less mass would allow the microrobots to fly. Ignoring the maximum frequency response of each microrobot, these exact devices could produce enough thrust to overcome their weight if they could flap approximately four times as fast, or 20 kHz.

Based on the deflection results of the all-gold 990-μm microrobot, the thrust-weight ratio is calculated to be 0.1, which is closer to unity than thrust-weight ratios of the best 500-μm microrobots. In order to overcome its weight, the 990-μm microrobot would need to flap at approximately 11 kHz.

It should be noted here that the deflection in the four-wing 500-μm microrobots is the same as the deflection in the eight-wing 500-μm robots. By reducing the number of wings by one half, the mass and surface area values are both reduced by one half. The only possible advantage of the four-wing microrobots is their downward deflection could be greater than that in the eight-wing robots—the same amount of laser energy would power half the number of wings, resulting in more downward deflection per wing.

7.6 Laser-Powered Deflection

Despite the thrust-weight calculations, several microrobots were tested under the laser setup to determine if they were indeed capable of taking flight. When powered by the laser described in Chapter 6, each microrobot wing deflected downward. Also, the microrobot wings flapped up and down as the laser was pulsed. At approximately 60 Hz, the camera could no longer detect wing motion due to its limited frame capture rate. At this point, it was difficult to determine whether the microrobot wings could respond fast enough to the pulse frequency. A high-speed camera could be used for the frequency response. The laser was pulsed at full power between 1 Hz and 10 kHz, but none of the robots achieved flight. Due to time constraints after the last fabrication run (in which the flip-up rulers were fabricated), it was not possible to quantify the amount of laser-induced downward deflection.

7.7 Towards a Flying Microrobot

As mentioned previously, in order for the microrobots to achieve flight, they must maximize wing speed and area while minimizing mass. High wing speeds are achieved by maximizing deflection and minimizing the time required to deflect. Methods for maximizing deflection were successfully demonstrated in this chapter. But due to the fabrication constraints in the MUMPs® process, increasing wing area is impossible without also increasing mass. In order to achieve flight, this must be overcome.

One method is to cover the gaps between each flexure with a very thin, less dense material, similar to thin insect wings. The density of polysilicon is relatively low, which keeps it a good candidate for the bottom structure. A less dense material with a high coefficient of thermal expansion would be better than the very dense gold layer. But if

depositing other layers is not feasible, then decreasing the gold layer thickness would suffice. Alternate processes should be examined in more detail.

Of course, flying microrobots must be wireless, and attaching a massive battery would weigh the robot down. At the present time, demonstrating wireless microrobotic flight is most simply achieved using optothermal actuation. Unfortunately, the response time in thermal actuators is slow due to the heat exchange phenomenon. The deficiency in response time must be compensated for in deflection and surface area to achieve successful flight.

7.7 Summary

The initial deflection results from each microrobot fabricated in this thesis yield a few useful relationships among design elements: gold quantity, surface area, spacer layer, flexure width, and wing length, deflection, and mass. These are summarized in Table 7.7. In order to design a microrobot capable of successful flight, certain trade-offs must be made to maximize deflection and surface area while minimizing mass. Based on these results as well as powered deflection tests, three of the 500-μm microrobots with the best performance were identified. Each of the thrust-to-weight ratios of these robots was less than unity, which means they are too heavy to take flight. When powered by the laser that was demonstrated in Chapter 6, none of the robots achieved flight as of yet. Some useful conclusions about this research are given in Chapter 8.

7.8 References

[1] PolyMUMPs® Fabrication Data from runs #66-69. Excerpt from an online database. n. pag. http://www.memsrus.com/nc-pmumps.refs.html. 15 Jan. 2006.

VIII. Conclusions and Recommendations

8.1 Chapter Introduction

This chapter summarizes the major accomplishments presented in previous chapters, and it makes important conclusions about this research. Some recommendations for future work are also given.

8.2 Thesis in a Nutshell

Chapter 1 introduced the development of flying microrobots. It was argued that they could solve certain modern warfare issues. Several problems in fabricating microrobots exist due to the limitations in MEMS fabrication technologies. A solution to these problems is a flying (instead of walking) microrobot that scavenges power from the environment.

Chapter 2 presented the history of microrobots and expounded on the potential microrobot applications. A comprehensive critical review of all the known walking and flying miniature robots was presented. There currently exists only one untethered microrobot that demonstrated controlled walking movement. All the rest were larger, tethered, or could not demonstration movement. A flying microrobot still does not exist, although significant advances are being made on a centimeter-sized insect-based flying robot.

In Chapter 3, the theory of heat transfer, thermal expansion, optical absorption, and powered deflection was presented. For polysilicon structures, it was determined that the energy from shorter-wavelength lasers generates the most amount of heat in a device.

The modeling and simulations presented in Chapter 4 illustrated several important trends: initial deflection is based on the amount of residual stress in deposited layers as well as the coefficient of thermal expansion difference between two layers. It was predicted that deflection is proportional to length and the amount of gold deposited on a device. The initial deflection in cantilevers and microrobot wings was modeled and simulated. It was determined that increasing device temperature would cause the microrobot wings to deflect downward. Also, an important power-deflection relationship was developed. It was determined that laser-powered deflection was achievable in microrobot wings.

Chapter 5 illustrated several entirely original 500-μm and 990-μm microrobot designs. It highlighted the design elements that would be investigated in Chapter 7. Images of the fabricated microrobots illustrated how to optimize certain design features. The objective in designing so many robots was to determine which design elements would maximize initial and downward deflection. It was determined that maximizing deflection and surface area while minimizing mass would yield a successful flying microrobot.

Chapter 6 described the major experiments from this thesis. The laser setup used to power the microrobots was optimized. By reducing the number of optical elements and taking advantage of the laser beam characteristics, it was possible to minimize the amount of power lost in the setup. This allowed more power to be delivered to the microrobots. The microrobot post-processing procedures and measuring techniques were also included.

The results of the experiments were presented in Chapter 7. Certain trends in maximizing deflection in these novel microrobot wings were clearly demonstrated. The most optimized microrobots were identified, but the thrust calculations showed that these would be too heavy to take flight. Several microrobots were powered with the laser, and each responded to the pulse by flapping its wings. However, none achieved flight. The results showed very important trends that will enable a future researcher to develop a successful microrobot.

8.3 Novel Contributions of this Thesis

Novelty is a requirement in graduate and doctoral research, and this thesis contains several novel contributions.

1. Designed a novel integrated micro-sized actuator-wing that flaps downwards
2. Characterized and optimized the micro actuator-wing
3. Combined the actuator-wings to form a wireless microrobot (smaller than 1 mm x 1 mm x 1 mm^3)
4. Optimized the laser test setup to maximize power delivered to chip
5. Identified and demonstrated trends to maximize microrobot wing deflection
6. Demonstrated wireless flapping motion in several microrobots by scavenging power from a laser

This research has already resulted in one published IEEE conference presentation and paper:

D. J. Denninghoff, L. A. Starman, C. E. Perry, and P. E. Kladitis, "Autonomous Power-Scavenging MEMS Robots," *48th International IEEE Midwest Symposium on Circuits and Systems—MWSCAS 2005*, pp. 367–370, Cincinnati, OH, 7–10 Aug. 2005.

This research has been accepted for both a regular and an invited oral presentation at the *2006 SPIE Conference on Nano- and Microphotonics: Materials, Devices, Processing, and Applications*. This is part of the *Great Lakes Photonics Symposium* scheduled for 12–16 June 2006 in Dayton, Ohio. The titles of each presentation are: "Optothermally Actuated Microwings for an Autonomous Flying Microrobot," and "Performance and Optimization of Optothermal Microwings for an Autonomous Flying Microrobot." The papers are to be submitted into the SPIE *Optical Engineering Letters*.

8.4 Recommendations

Several recommendations for future research were briefly mentioned in preceding chapters, and they are presented in more detail here.

Micro-sized power sources for MEMS applications are currently being developed. However, the mass of these microbatteries would be too great for a microrobot, but they could be used in centimeter-sized aerial vehicles. Since onboard power sources would be too heavy and attached wires would restrict flight, the best solution for flying microrobots is to scavenge power from the environment. Scavenging power from a remote source has been demonstrated in solar-powered and laser-powered devices. The weight of solar panels is too great for a flying microrobot, but solar panels certainly could be used for walking or centimeter-sized flying robots. Thus, optothermal actuation remains the best choice for powering flying microrobots.

The easiest, most effective method to improve device performance is to power the microrobots with a shorter-wavelength laser. From the discussion in Chapter 3, not only does energy absorption increase at smaller wavelengths, both the gold and polysilicon reflectivity values decrease. This results in less reflection losses at the surface.

Moreover, the heat-conversion process is more efficient for lasers of a smaller wavelength because more absorbed energy is turned into heat. In addition, smaller-wavelength lasers are more easily focused into small spot sizes (see Chapter 6).

8.4.1 Recommendations for Flying Microrobots in PolyMUMPs®

Though the PolyMUMPs® microrobots presented in this thesis had thrust-weight ratios of less than unity, they should not be discarded. The PolyMUMPs® fabrication process alone cannot yield a successful microrobot, but a few post-processing steps on MUMPs® chips certainly could. It is left to the follow-on researchers to find a material with a very low density that could be deposited and patterned onto polysilicon and gold layers. This material must also withstand the chemical etching from the sacrificial oxide release (described in Chapter 6). This thin material—similar to insect wings—would increase wing surface area without increasing mass, which would improve the thrust-weight ratio. A possible choice for this material is some type of polyimide or thick photoresist.

The most successful microrobots identified in Chapter 7 could be used as the frame and muscles for a micro-sized flying robot. The M68rob1pos6 500-μm microrobot had the best thrust-weight ratio compared to all other 500-μm microrobots. By using this wing configuration for the actuators; using only two wings (similar to most flying insects); extending the wing span to 990 μm with very narrow, poly2 flexures; and increasing the surface area to 0.7 mm^2 with the light-weight film; the microrobot would need just 20-μm of initial deflection to achieve a thrust-weight ratio of 1.5. This microrobot would certainly be able to generate sufficient thrust to lift off. In order to hover, force generated on the downward stroke must exceed the weight as well as the counter-acting force from the upward stroke. There are two simple ways to achieve this

asymmetry: increasing the velocity of the downward stroke; and making the coefficient of drag greater on the downward stroke than on the upper stroke. By making the light-weight film slightly rounded on the top surface, the cup-shaped wings would have a higher coefficient of drag on the downward stroke than on the upward stroke.

A conceptual diagram of this microrobot design is given in Figure 8.1. This two-wing 990-µm microrobot is based on the M68rob1pos6 design, in which gold-poly2 flexures are used as optothermal actuators in each wing.

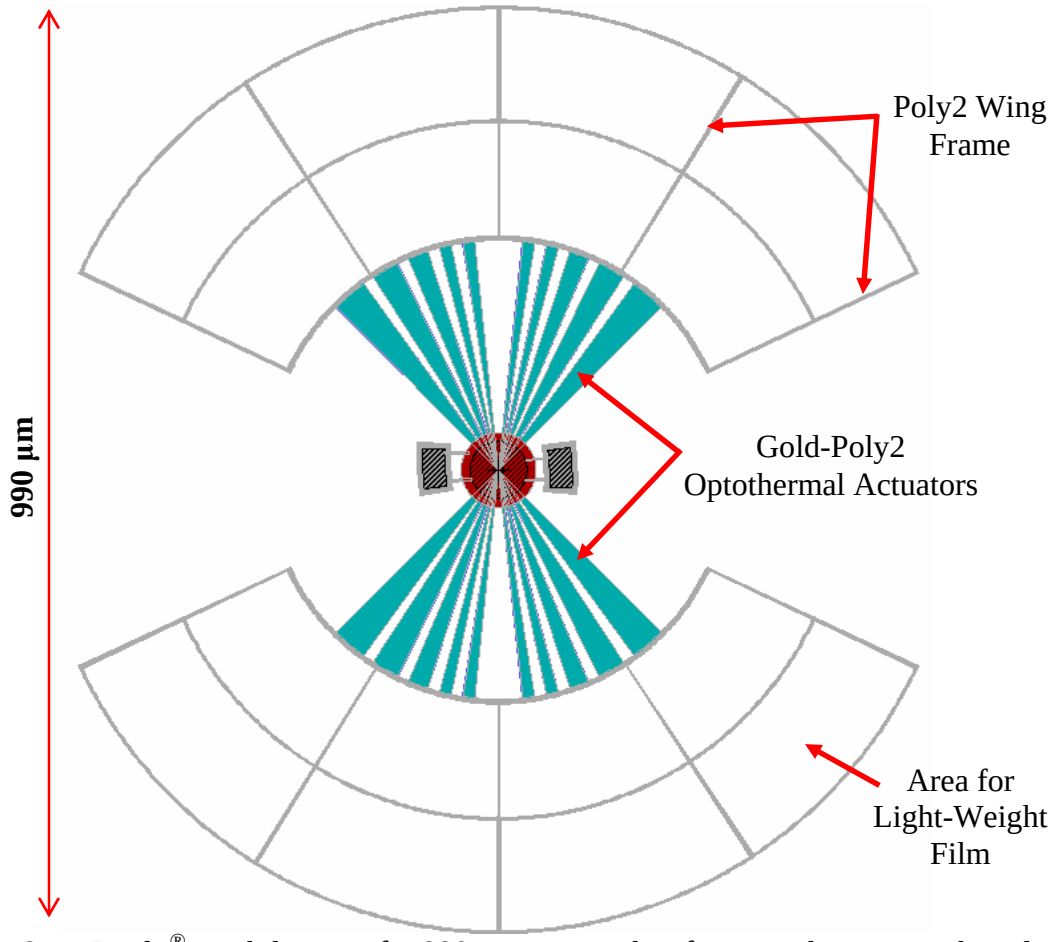


Figure 8.1: L-edit® mask layout of a 990-µm microrobot frame with actuators based on the most successful 500-µm robot fabricated in this thesis. The wings are extended using very narrow poly2 strips. A thin, light-weight film similar to insect wings could be deposited over this frame to give it more surface area without increasing the mass. A possible choice for this film is a type of polyimide that would be HF-resistant. Such a microrobot would have a 1.5 thrust-weight ratio and would be capable of flight.

As shown in Figure 8.1, the wing length is extended with very narrow poly2 flexures that provide a structural frame without increasing the mass significantly. Notice there is no gold on the poly2 because that would cause the wings to be bowed upwards. Poly2 has been found in this research to bow downward slightly, and the cup-shaped wing can be achieved in this design. The gaps between the poly2 extensions must be filled with a light-weight film, such as a type of polyimide, in order to increase surface area without increasing mass. The center laser target area is thick in order to increase laser absorption.

Another method of improving the flight performance of this microrobot is varying the area between the upward and downward wing strokes. Using a poly1-poly2 downward-folding scissor hinge between the flexures and the extended wing frame would allow the wing area to be large and on the downward stroke and small on the upward stroke. Though this addition would add weight and complexity, it is worth consideration as a test structure, as a minimum.

8.4.2 Recommendations for Flying Microrobots in other Processes

The microrobot given in Figure 8.1 could be improved using materials from other processes. Not only could the layers be thinner in a custom process, bi-layer flexures could have a greater coefficient of thermal expansion (CTE) difference between them. This would result in more deflection with less input energy. For example, aluminum has twice the CTE value as gold; aluminum is also eight times less dense. Both these characteristics would make aluminum an ideal replacement for gold in the actuators. The follow-on researcher should be aware of the significant cost and fabrication time required in custom fabrication processes. If the microrobots were to be fabricated in a custom process, the time required for fabrication may exceed the limited time available for a

master's student at AFIT. Regardless of the process, the ultimate objective is to minimize the weight of the microrobot structure while maximizing wing surface area and deflection.

8.4.3 Words of Wisdom

The conversations with both MEMS and non-MEMS students proved invaluable throughout this research. For example, several students from other departments suggested that insect studies be pursued. The results of the insect studies were a better understanding of insect flight and a better wing desings. There are certain benefits from conversations with non-MEMS students: commonly accepted assumptions are challenged; principles are explained with greater clarity; and alternate ideas often arise. With such a topic as flying microrobots, it would be wise to consult and collaborate with aeronautical engineering students, in particular. In addition, the writing process elucidated many principles in this thesis. It is recommended to write as soon as possible.

8.5 Summary

The microrobots designed in this thesis showed very important trends that will help future researchers achieve the first flying microrobot. The trends identified in this thesis demonstrate how to maximize wing deflection and area while minimizing mass. Novel upward- and downward-flapping actuators that are powered by a remote laser have been demonstrated in this thesis. These actuators can now be integrated into light-weight wings as part of an ornithoptic microrobot capable of flight. It is recommended that the power-scavenging concepts developed in this thesis be continued because onboard power supplies are too heavy for microrobots. Alternative fabrication processes could be customized to better meet the needs of this research.

Appendix A: L-edit Mask Layouts for PolyMUMPs® Fabrication

This appendix comprises all 27 thesis-specific designs that were submitted for fabrication in PolyMUMPs®, listed in order from run 66 to run 69. Unless otherwise annotated, each chip constitutes original work. The rationale for documenting every chip here—even those with the inevitable design flaws—is to present a comprehensive compendium of the work made towards this flying robot thesis project. Moreover, it is critical to identify and explain the merits, functions, purposes, and testing methods of each chip as well as the flaws. This is done to enable future researchers to review and resume this work exactly where it was finished and to help them avoid perhaps many of the mistakes that were made.

The images on the following pages are the mask layout designs from the MEMSPro L-edit® layout editor. For MUMPs® runs 66–69, the AFIT MEMS group purchased a single 1 x 1-cm^2 die site, which was subdivided into 25 chips with dimensions of 1900 x 1900 μm^2. (The extra 50-μm-wide perimeter around each chip was allocated for sub-dicing.) The L-edit® color scheme used to distinguish the several mask layers is given in Figure A.1 below. When masks are overlapped the colors are mixed, so the individual layers in resulting images are not always easily discernible. Figure A.2 illustrates all the possible overlapping layers used in these designs. The block where two arrows converge represents the overlapping of the two layers from which the arrows are drawn. For example, gray Poly2 and blue Gold overlap to form the aqua-colored block representing Gold over Poly2. Refer to chapter 4 of this thesis for detailed descriptions of the most important and successful designs.

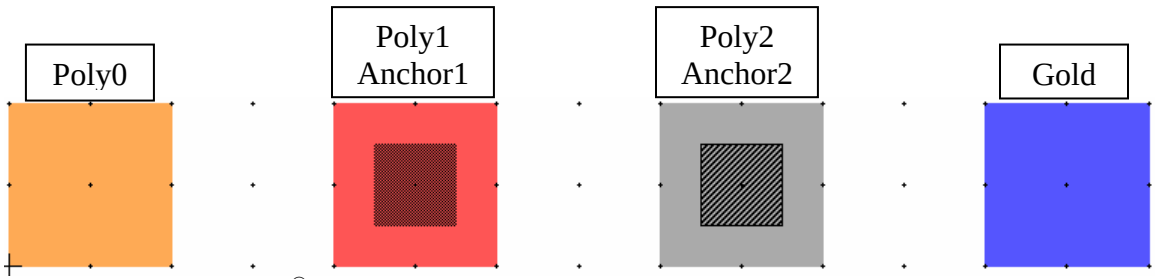


Figure A.1: L-edit® color scheme for identifying the mask layers available for photolithographic patterning in PolyMUMPs®. From left to right: Poly0; Poly1 and Anchor 1; Poly2 and Anchor 2; and Gold.

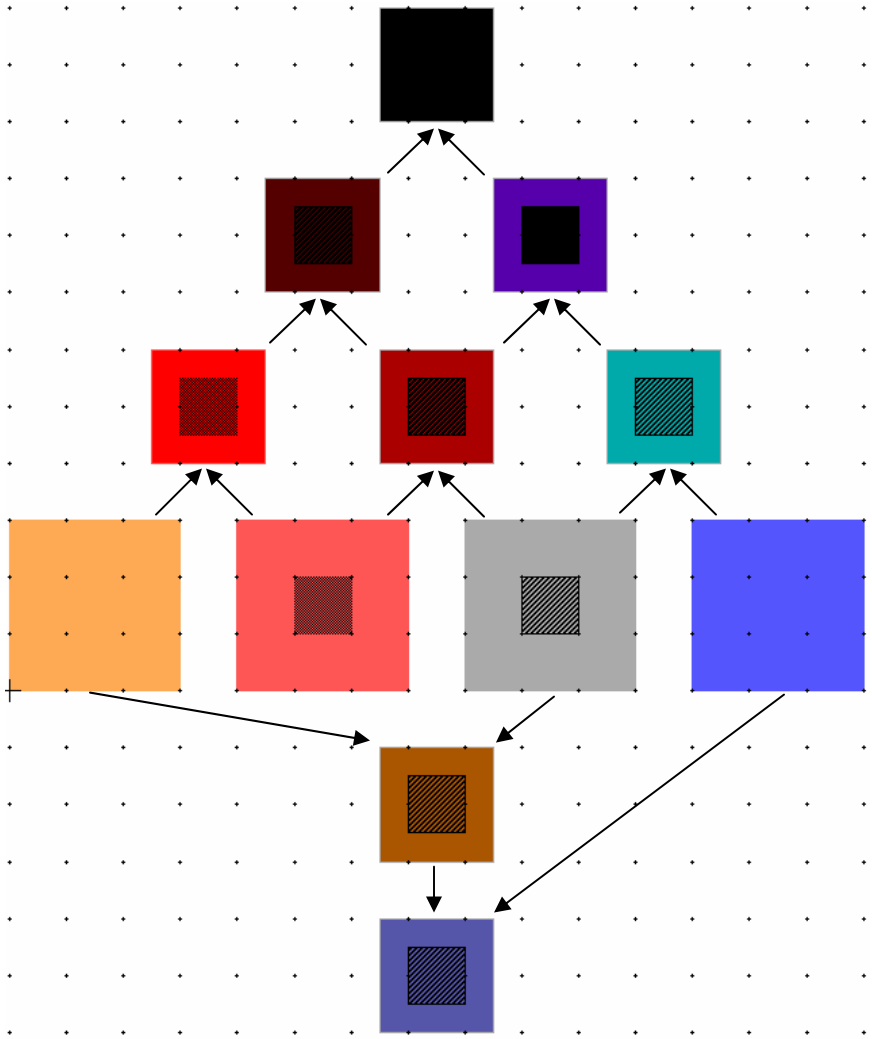


Figure A.2: L-edit® color mixing scheme of all the possible overlapping mask layers, starting from Poly0/Poly1/Poly2/Gold row and moving in the direction of the arrows. The block where two arrows converge represents the overlapping of the two layers from which the arrows are drawn.

A.1 MUMPs® Run 66 Masks

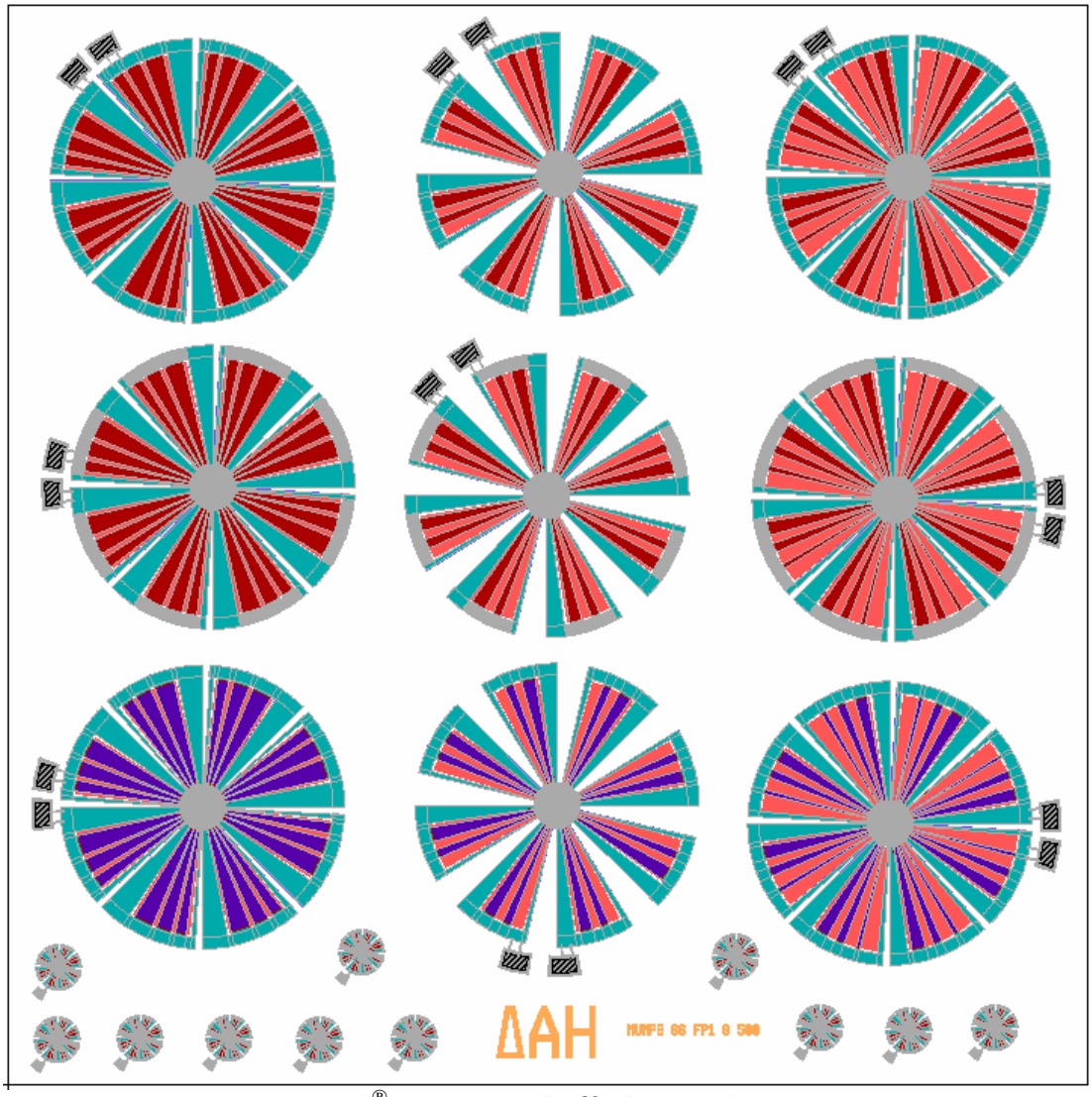


Figure A.3: MUMPs® 66 Denninghoff Chip1 Robots

MUMPs® run: 66 (original designs)
Layout: 9 different 500-µm outer-diameter and 80-µm inner-diameter pinwheel robots anchored on one side; robots in each column have the same wing configuration; robots in each row have the same gold configuration; 11 copies of a single 80-µm-diameter robot
Actuation: Optothermal downward deflection (660-nm laser diode)
Testing method: Measure initial vertical deflection due to residual stress with Zygo Interferrometric Microscope (IFM); focus 660-nm laser diode on the center of each robot; pulse the laser with a 50% duty-cycle or less square wave; increase the frequency for faster flapping
Comments: The 500-µm robots all deflect downwards when pulsed; the 80-µm robots did not fabricate properly; the Poly1 spacers under each wing prevent the entire robots from rotating or being easily moved around the chip; Poly1 is replaced by Poly0 in future designs

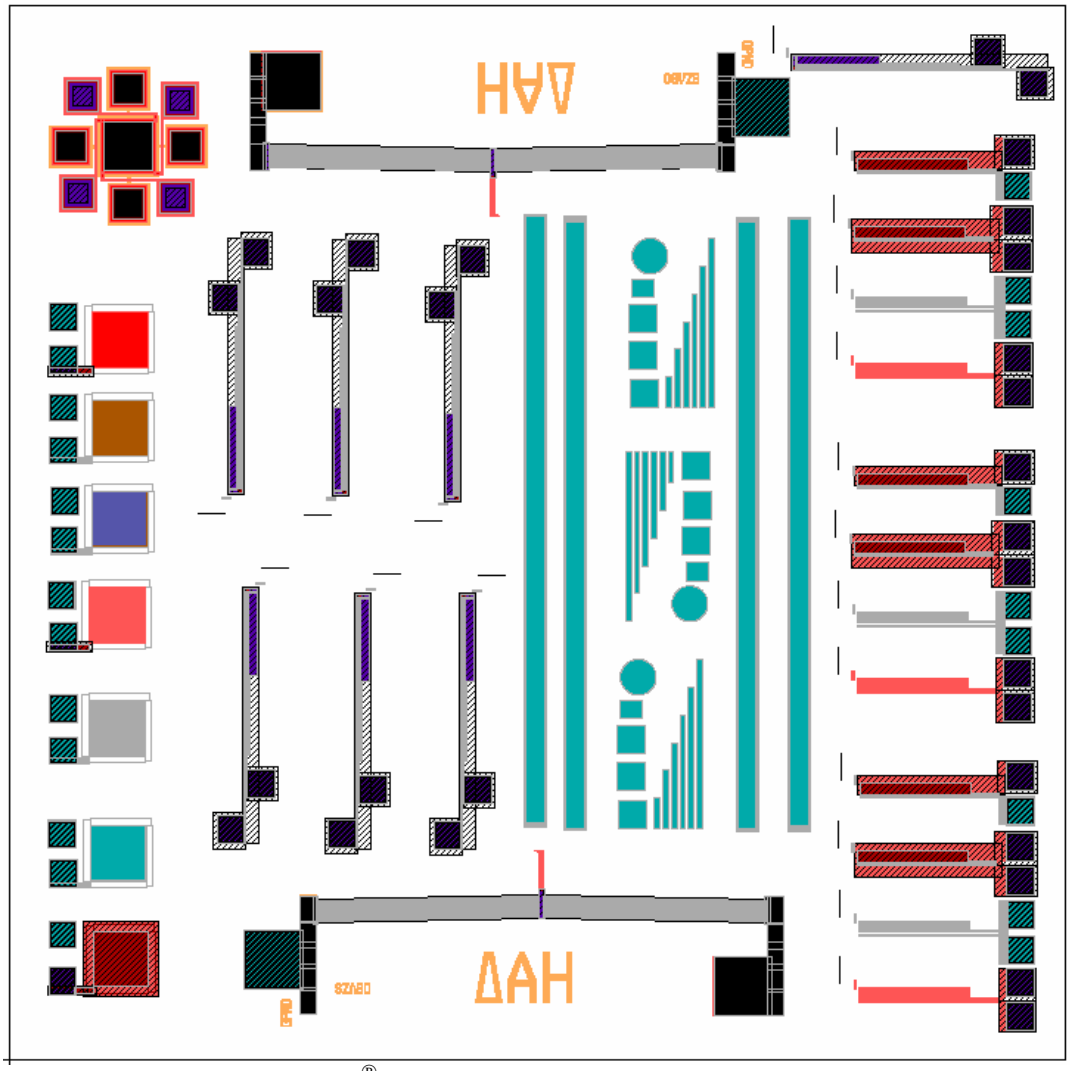


Figure A.4: MUMPs® 66 Denninghoff Chip2 Test Structures

MUMPs® run: 66 (half original designs and half designed by Frank R. Szabo)
Layout: Residual stress cantilevers; single-hot-arm thermal actuators; double-hot-arm actuators (FRS); chevron actuators (FRS); vertically deflecting electrostatic micromirrors
Actuation: Eletrothermal and electrostatic
Testing method: Cantilevers—measure initial vertical deflection with Zygo IFM; Electrothermal actuators—apply voltage from power supply to each probe pad and monitor deflection under micrscope; Electrostatic actuators—apply voltage from power supply to each probe pad and monitor deflection under microscope or IFM
Comments: Cantilevers deflected properly; Szabo's chevron actuators worked properly; double-hot-arm not tested; my poly2 thermal actuators worked properly, but my Poly1 versions were not anchored; my Poly2 electrostatic actuators worked properly, but the Poly1 actuators were cleaved between the probe pad and flexure

A.2 MUMPs® Run 67 Masks

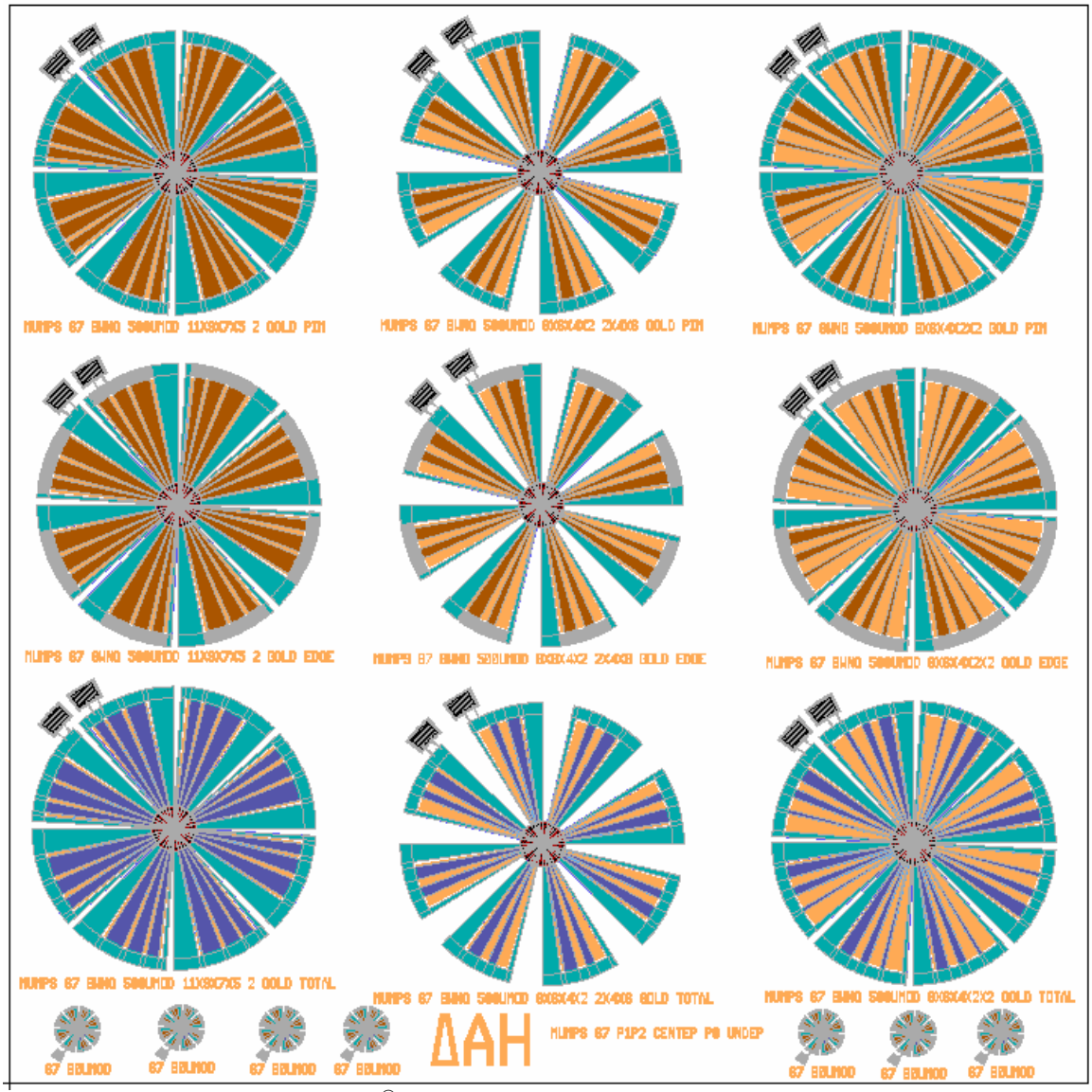


Figure A.5: MUMPs® 67 Denninghoff Chip1 Robots1

MUMPs® run: 67 (original designs)
Layout: 9 different 500-µm-diameter pinwheel robots anchored on one side
Wing and gold configurations are identical to MUMPs® 66 chip 1
Actuation: Optothermal downward deflection (660-nm laser diode)
Testing method: See MUMPs® 66 chip 1 testing procedures
Comments: These designs are modified from MUMPs® 66 robots with Poly0 replacing the Poly1 spacer and Poly1 is added to the center section for better power absorption; the 500-µm robots all deflect downwards when pulsed; from a qualitative perspective the Poly1/Poly2 center stack did absorb more energy in the laser testing; the 80-µm robots did not fabricate; *the performance of these robots was greatly improved over their run 66 counterparts*

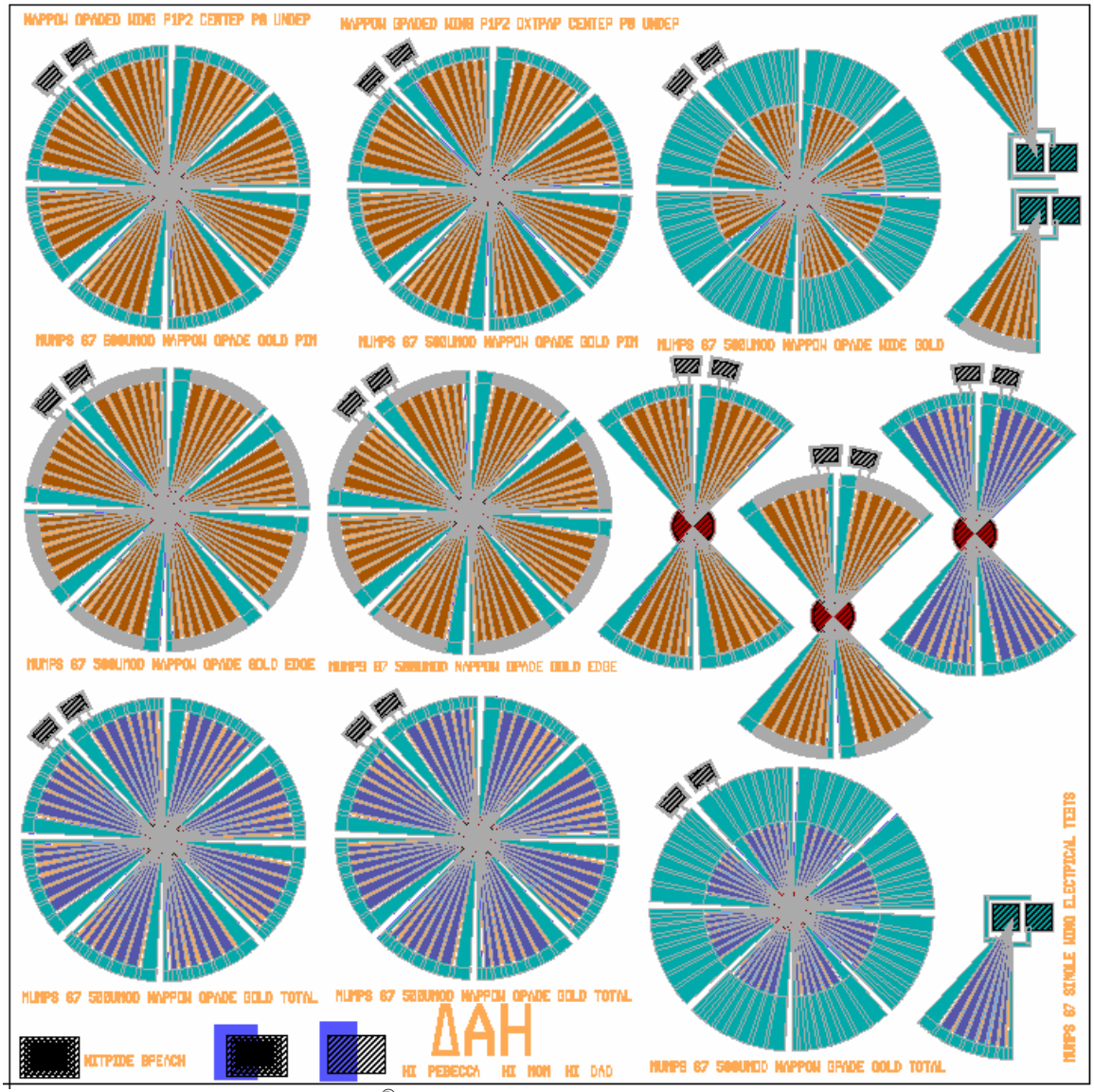


Figure A.6: MUMPs® 67 Denninghoff Chip2 Robots2

MUMPs® run: 67 (original designs)
Layout: 8 different 500-µm-diameter pinwheel robots anchored on one side
The spacing between flexures in each wing is minimized to maximize surface area; the first and second columns are identical except for a trapped oxide layer in the center of each device in the second column; the top and bottom robots in the third column are identical to those in the first except for more wing surface area
3 different insect-shaped robots with corresponding test wings
Actuation: Optothermal (660-nm laser diode) and electrical
Testing method: Standard optothermal testing; test wings could be electrically actuated just like standard thermal actuators
Comments: These robots proved stiffer than previous ones; the close spacing was a design rule violation, and the electrical wings did not fab

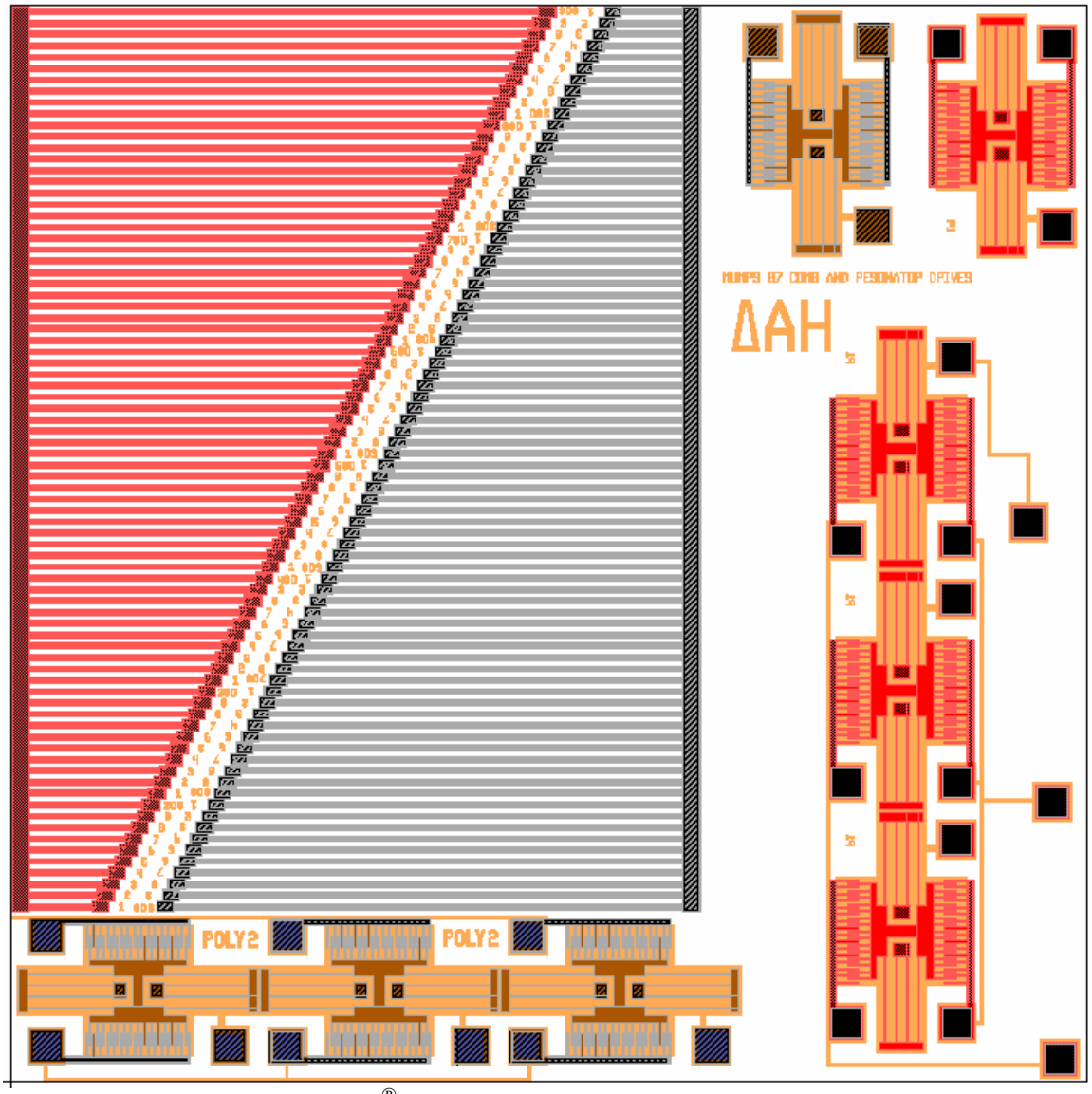


Figure A.7: MUMPs® 67 Denninghoff Chip3 Test Structures

MUMPs® run: 67 (designs provided by LaVern A. Starman)
Layout: Poly1 and Poly2 fixed beams; Poly1 and Poly2 comb resonators
Actuation: Electrostatic
Testing method: Beams—monitor vertical buckling with Zygo IFM; Resonators—apply an AC signal to one set of fingers, apply a DC bias to the other set, and ground the center shuttle; or apply an AC signal with a DC bias to one set of fingers, use the other set for sensing, and ground the center shuttle
Comments: With the devices on this chip, values for residual stress and Young's modulus of both Poly1 and Poly2 layers may be determined; all devices fabricated and functioned properly; a high-voltage power supply may be required to align the comb fingers

A.3 MUMPs® Run 68 Masks

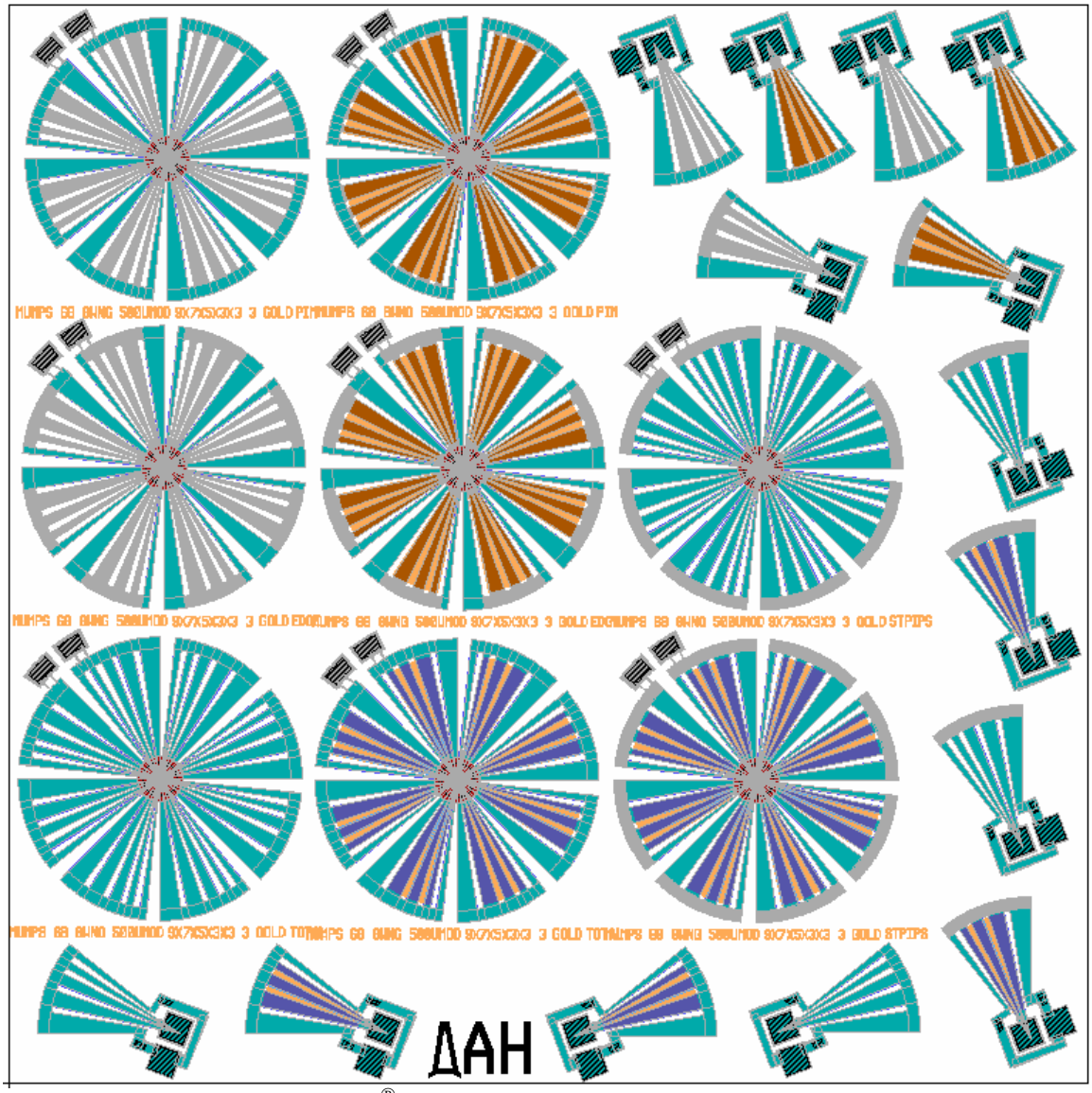


Figure A.8: MUMPs® 68 Denninghoff Chip1 Robots1 T

MUMPs® run: 68 (original designs)
Layout: 8 different 500-µm-diameter pinwheel-shaped robots with a standard Poly1/Poly2 stack in the center and *flexures in each wing that obey the design rules*; corresponding test wings of each robot
Actuation: Optothermal (660-nm laser diode) and electrical
Testing method: Standard optothermal testing for robots; two-probe electrical testing for wings; downward deflection observable with Zygo IFM
Comments: These designs are based on the first column of chip 1 of MUMPs® 67; the difference is the flexures obey the design rules; each robot has the same graded wing flexure and constant spacing configuration; half have Poly0 spacers and half do not in order to determine if the spacers reduce deflection or enhance it

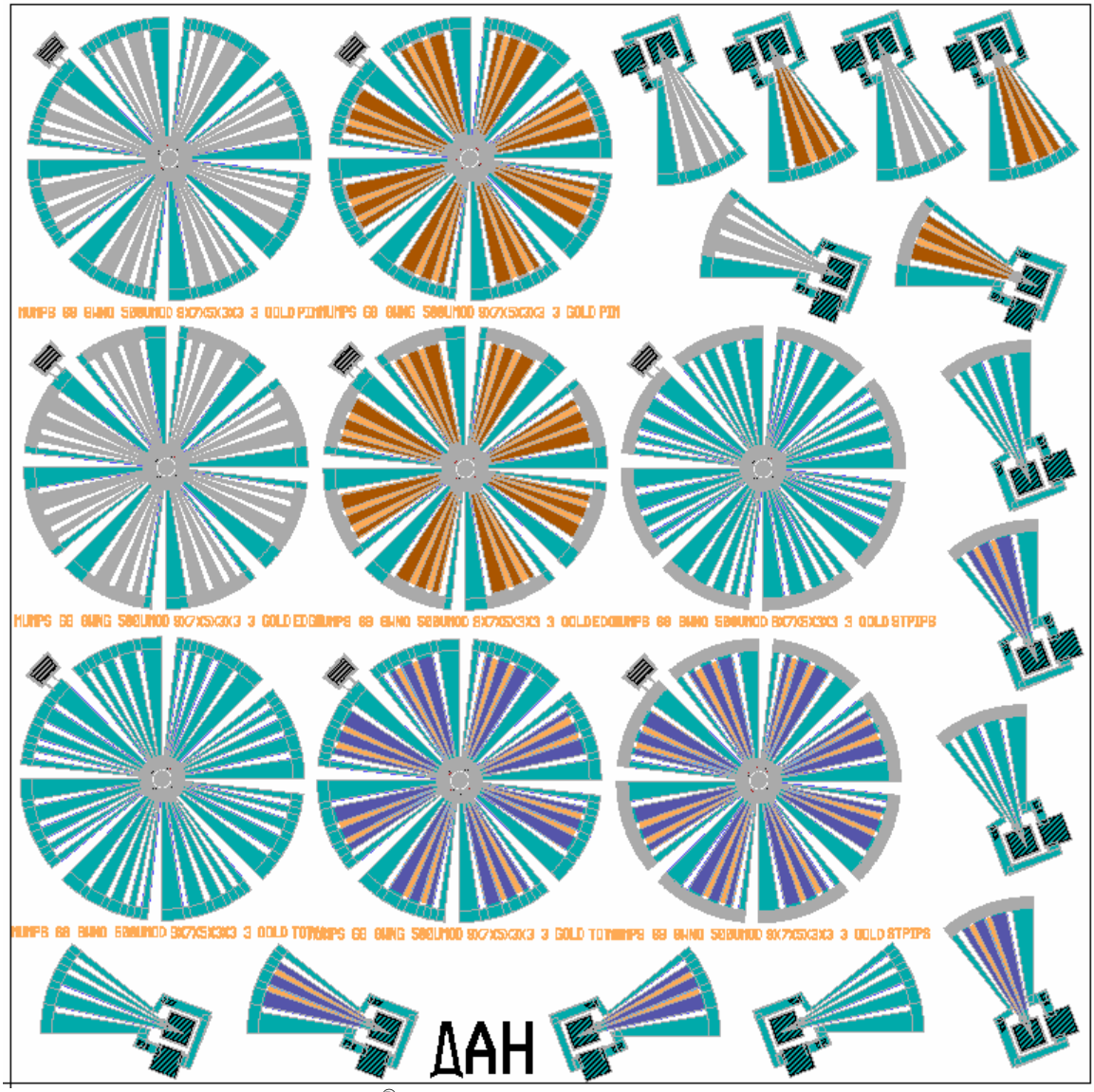


Figure A.9: MUMPs® 68 Denninghoff Chip2 Robots1 R

MUMPs® run: 68 (original designs)

Layout: Identical to 'tethered' designs of previous chip except for a 50-µm center 'rotor' pin that allows the robots to spin in place; test wings are identical to those of the previous chip

Actuation: Optothermal (660-nm laser diode) and electrical

Testing method: Standard optothermal testing for robots; two-probe electrical testing for wings; downward deflection observable with Zygo IFM

Comments: These robots were designed based on the presumption that the wings would deflect faster at the thinner edge than at the thicker edge, creating a canted or fan-blade shape; the 50-µm center rotor pin would the guide the robots in their rotating motion; the rotor pin latches the robots so they cannot take flight, so the designs on this chip are not practical but could prove the rotating concept

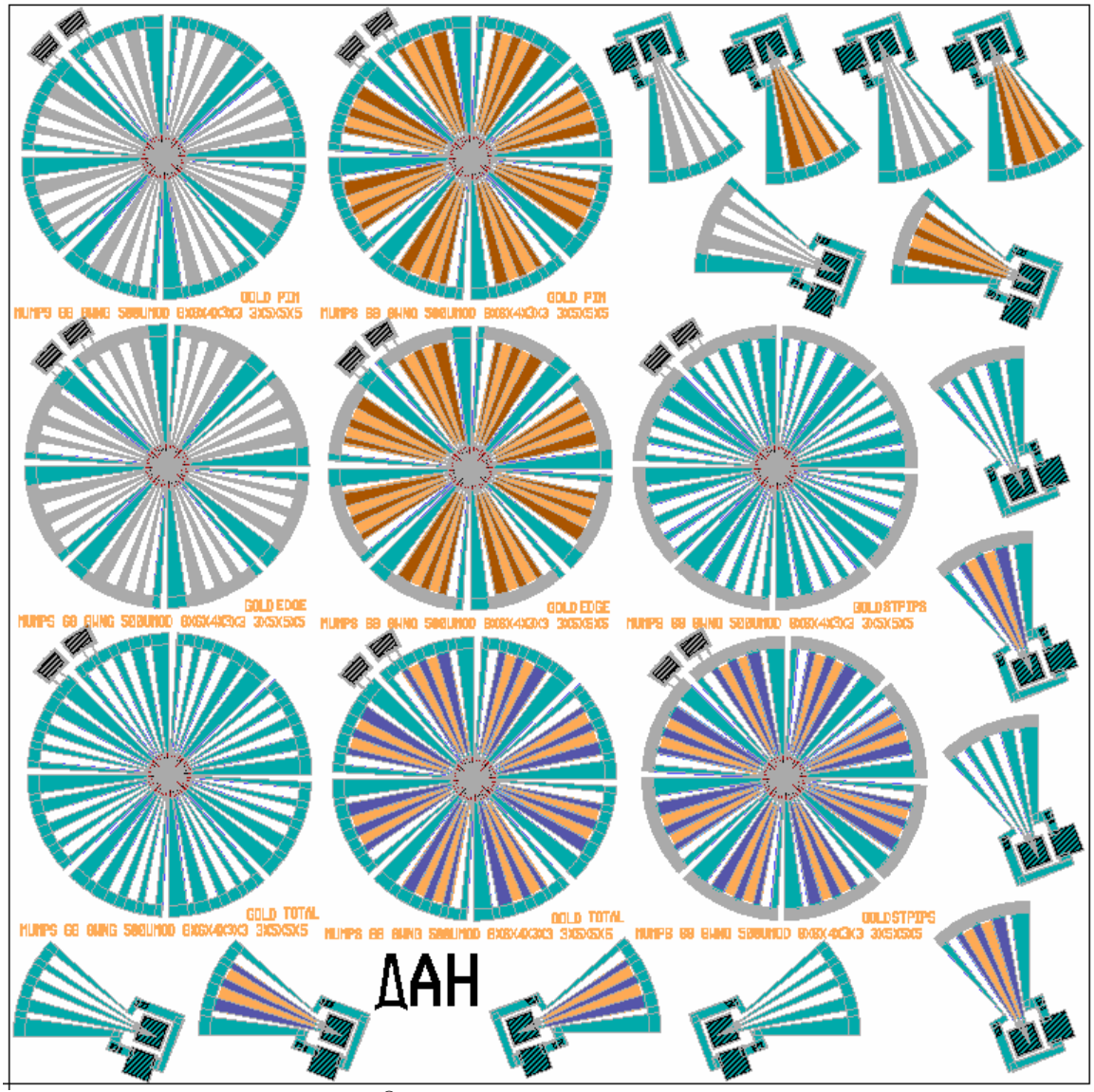


Figure A.10: MUMPs® 68 Denninghoff Chip3 Robots2 T

MUMPs® run: 68 (original designs)

Layout: 8 different 500-µm-diameter pinwheel-shaped robots with a standard Poly1/Poly2 stack in the center and flexures in each wing that obey the design rules; *spacing between flexures is graded*; corresponding test wings of each robot

Actuation: Optothermal (660-nm laser diode) and electrical

Testing method: Standard optothermal testing for robots; two-probe electrical testing for wings; downward deflection observable with Zygo IFM

Comments: These designs are based on the robots in the third column of chip 1 of MUMPs® 67; the main difference is the flexures obey the design rules; each robot has the same graded wing flexure and graded spacing configuration; half have Poly0 spacers and half do not in order to determine if the spacers reduce deflection or enhance it

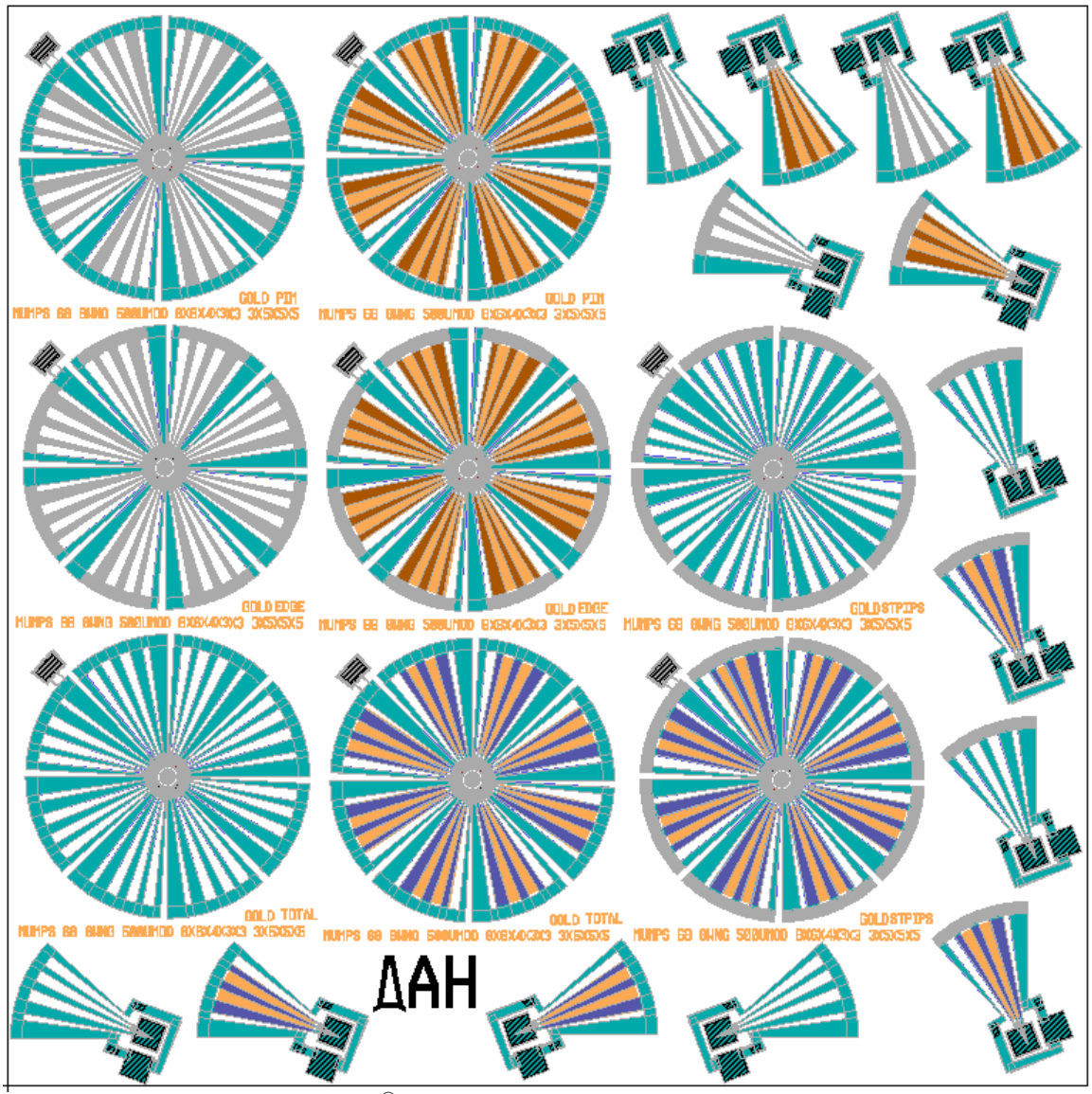


Figure A.11: MUMPs® 68 Denninghoff Chip4 Robots2 R

MUMPs® run: 68 (original designs)

Layout: Identical to 'tethered' designs of previous chip except for the same 50-µm center 'rotor' pin as in chip 2; same test wings as chip 3

Actuation: Optothermal (660-nm laser diode) and electrical

Testing method: Standard optothermal testing for robots; two-probe electrical testing for wings; downward deflection observable with Zygo IFM

Comments: Like those robots in chip 2, these robots were designed based on the presumption that the wings would deflect faster at the thinner edge than at the thicker edge, creating a canted or fan-blade shape; the 50-µm center rotor pin would the guide the robots in their rotating motion; the rotor pin latches the robots so they cannot take flight, so the designs on this chip are not practical but could prove the rotating concept

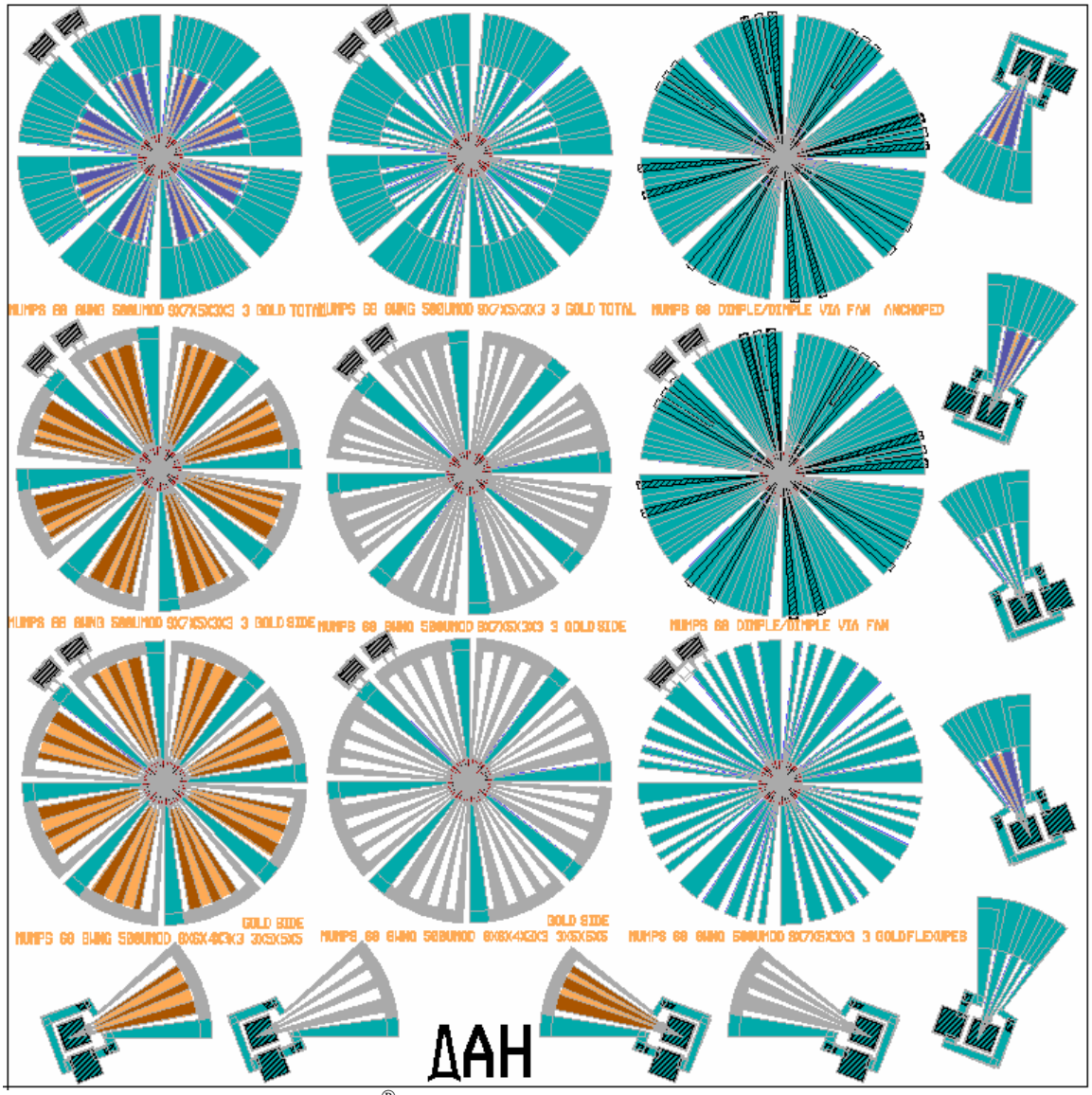


Figure A.12: MUMPs® 68 Denninghoff Chip5 Robots3 T

MUMPs® run: 68 (original designs)

Layout: 9 different 500-µm-diameter pinwheel-shaped robots with a standard Poly1/Poly2 stack in the center and experimental gold and wing patterns; corresponding test wings of each robot

Actuation: Optothermal (660-nm laser diode) and electrical

Testing method: Standard optothermal testing for robots; two-probe electrical testing for wings; downward deflection observable with Zygo IFM

Comments: 7 of these designs are based on the robots in chip 1 of this MUMPs® run and the bottom left two are based on chip 3; experimental gold and wing patterns were designed with lift characteristics in mind; the top robots have more surface area and the bottom left four have canted features; the bottom right one is just a shot in the dark

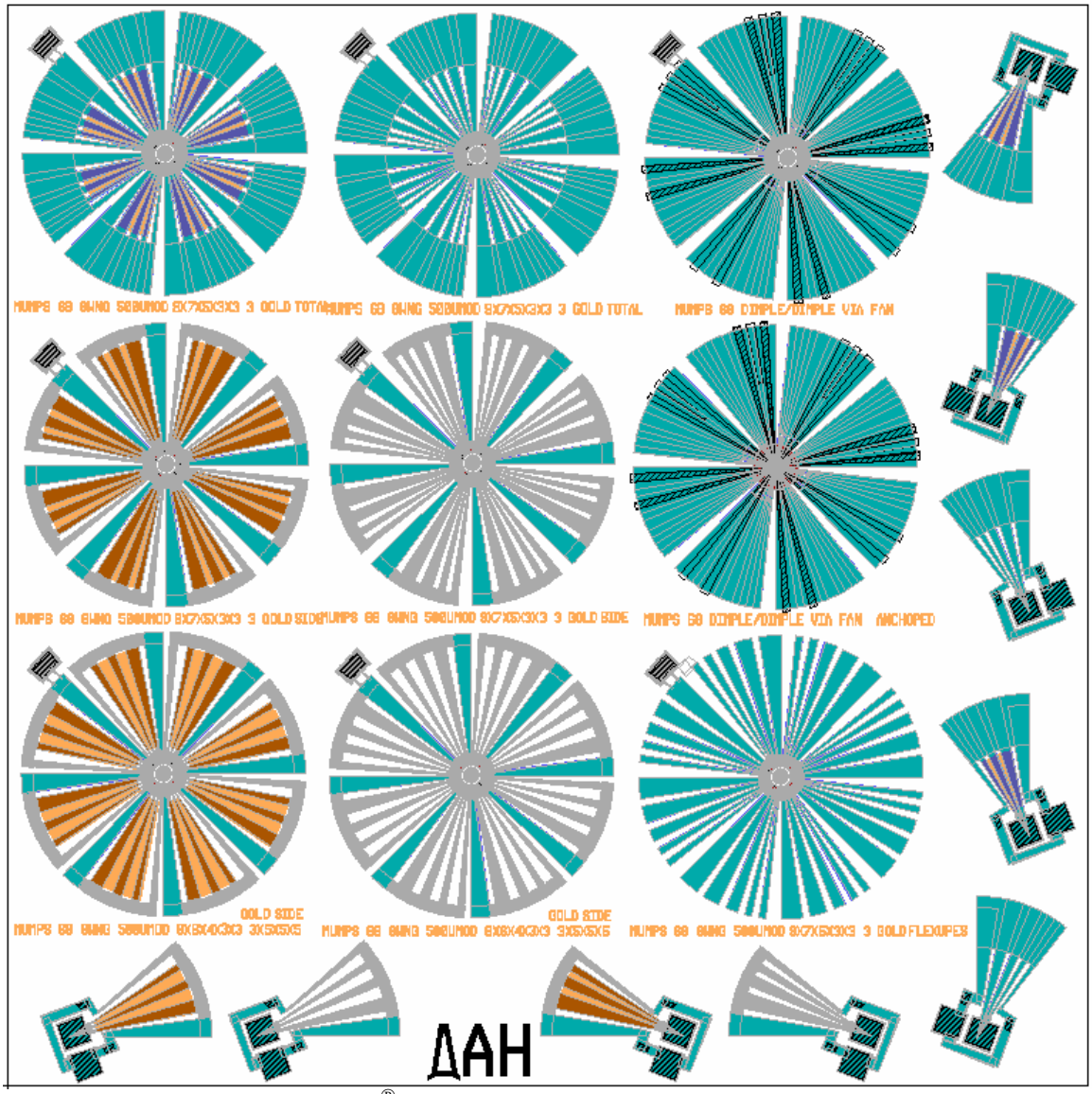


Figure A.13: MUMPs® 68 Denninghoff Chip6 Robots3 R

MUMPs® run:	68 (original designs)
Layout:	Same designs as previous chip except for the same 50-µm center 'rotor' pin as in chips 2 and 4; same test wings as previous chip
Actuation:	Optothermal (660-nm laser diode) and electrical
Testing method:	Standard optothermal testing for robots; two-probe electrical testing for wings; downward deflection observable with Zygo IFM
Comments:	Just like in previous 'rotor' versions, these robots differ in that the center is pinned with a 50-µm rotor that will guide the anticipated rotating motion caused by the canted deflection of the wings

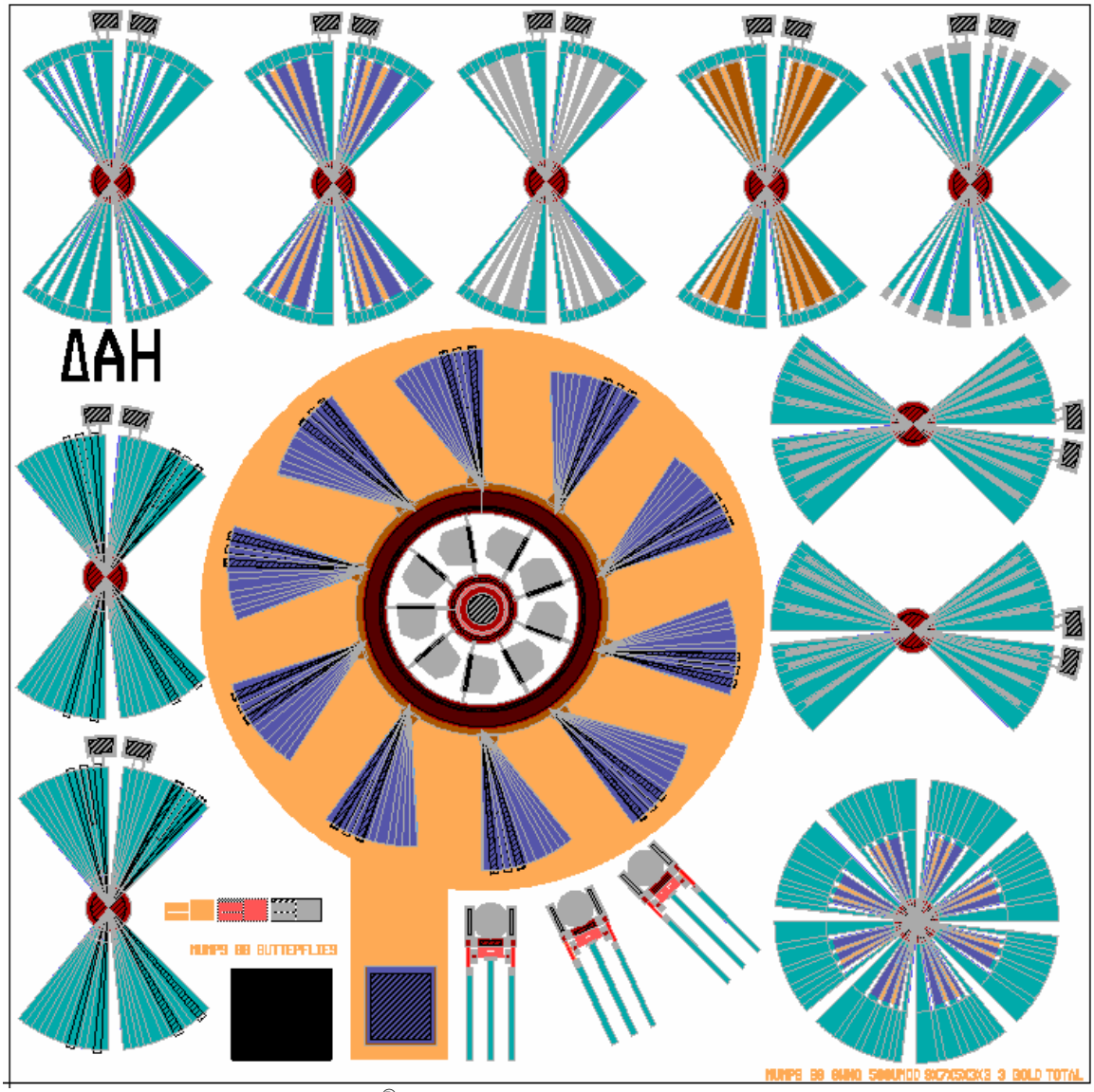


Figure A.14: MUMPs® 68 Denninghoff Chip7 Insects T

MUMPs® run: 68 (original designs)
Layout: 7 different (and two copies) 500-µm-diameter insect-shaped robots with a standard Poly1/Poly2 stack in the center and *the flexures in each wing obey the design rules*; a scratch drive with wings; 3 flip-up Fresnel lenses; one pinwheel robot is anchored in the center
Actuation: Optothermal (660-nm laser diode) and electrical
Testing method: Standard testing for insects; AC voltage signal for scratch drive
Comments: These insect robots are identical to the ones in the following chip except for their centers; here the standard center was used just in case the experimental pinned rotor idea of the following chip did not work; the wings are the same, which provides a control element between the two chips; the scratch drive is a in essence a fan with curled Poly2/Gold blades

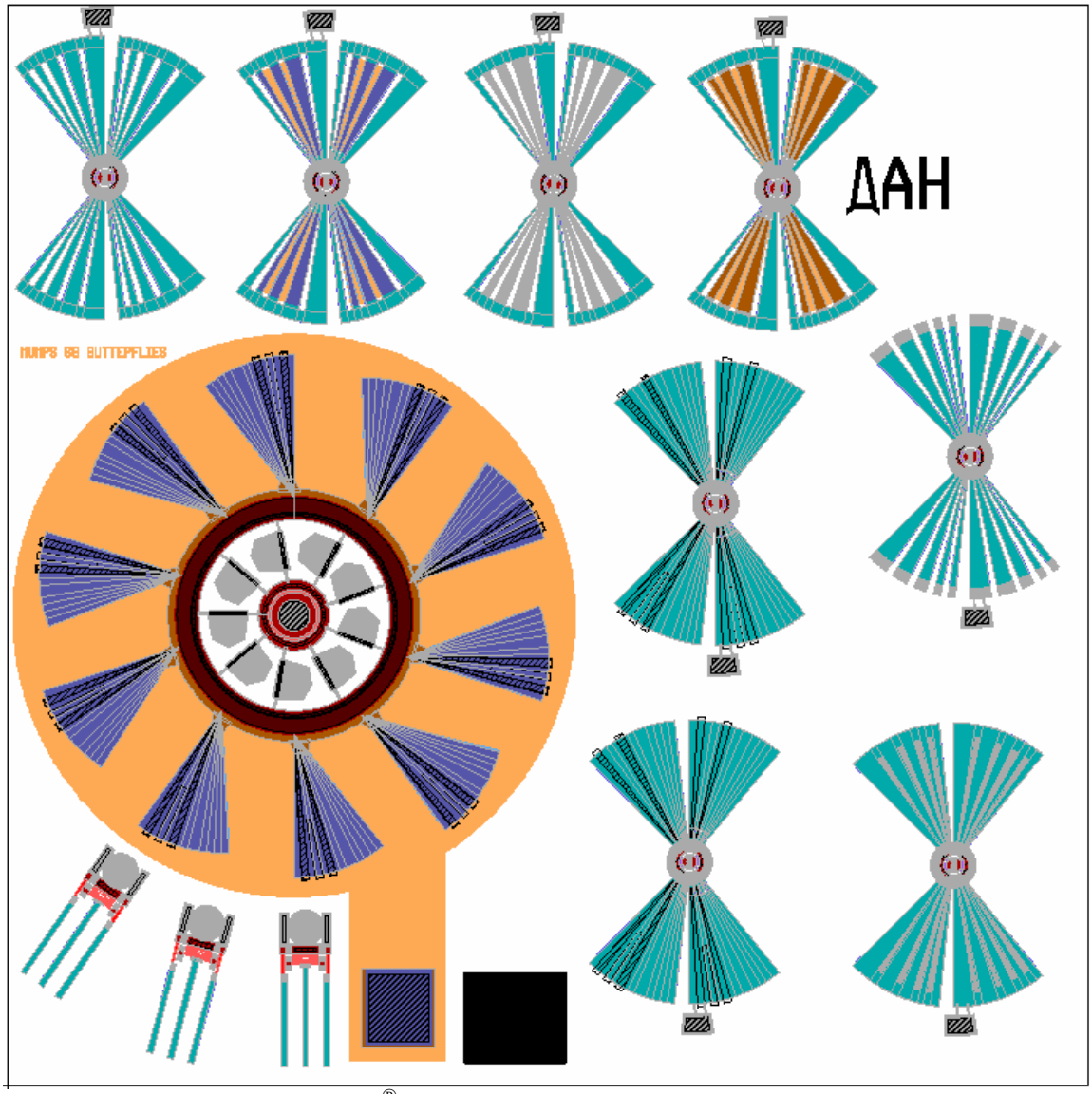


Figure A.15: MUMPs® 68 Denninghoff Chip8 Insects R

MUMPs® run: 68 (original designs)
Layout: Same devices as in the previous chip except for the same 50-µm center 'rotor' pin as in chips 2, 4, and 6; same scratch drive and Fresnel lenses
Actuation: Optothermal (660-nm laser diode) and electrical
Testing method: Standard testing for insects; AC voltage signal for scratch drive
Comments: Just like in previous 'rotor' versions, these insects differ in that the center is pinned with a 50-µm rotor that will guide the anticipated rotating motion caused by the canted deflection of the wings

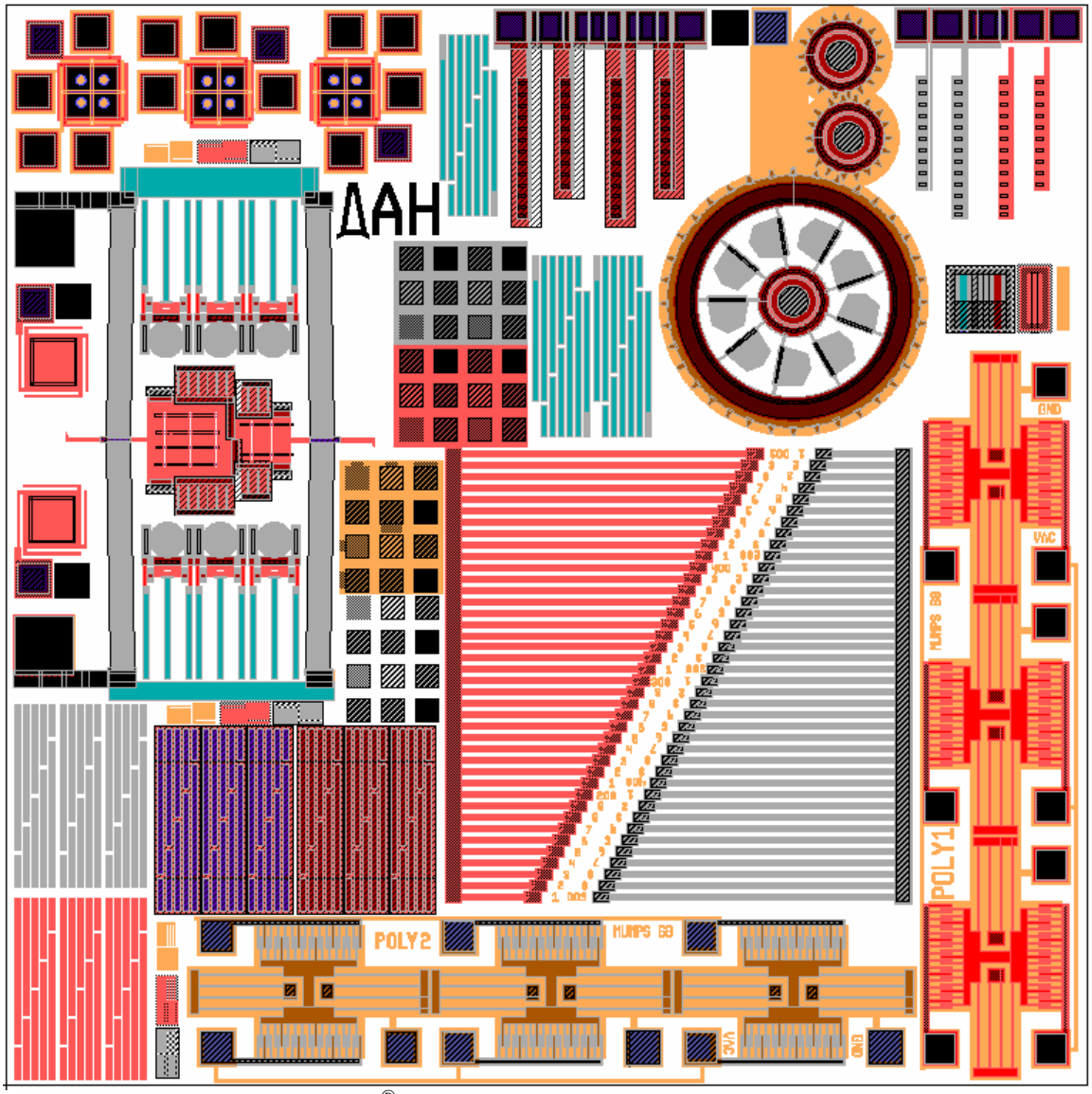


Figure A.16: MUMPs® 68 Denninghoff Chip9 Test Structures

MUMPs® run: 68 (all original excepts devices noted on previous chips)
Layout: Multi-directional micromirrors; line resolution bars; thermal actuators; cantilevers; gears and scratch drive; layer thickness bars; chevron actuator pulling apart safe-arm device; Fresnel lenses; vertical micromirror; etch depth squares; fixed beams; resonators;
Actuation: Electrostatic and electrothermal
Testing method: Standard testing for actuators, cantilevers, scratch drive, resonators, fixed beams; use profilometer or Zygo IFM for etch depth and layer thickness sections; visually observe resolution tests and separation on S/A device; flip up Fresnel lenses with probe
Comments: This chip is a comprehensive test chip that should be included on each design run to determine material and fabrication properties

A.4 MUMPs® Run 69 Masks

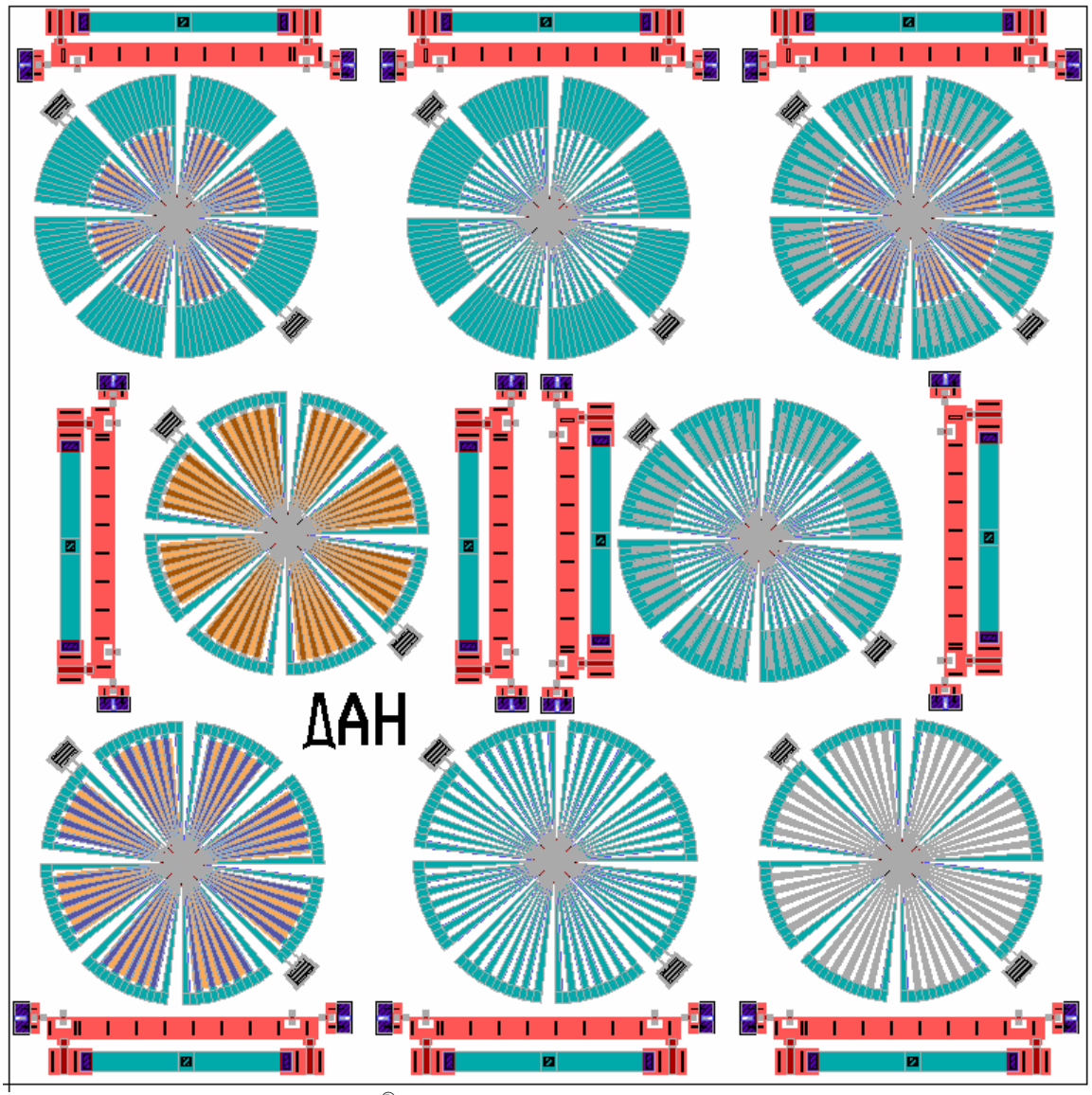


Figure A.17: MUMPs® 69 Denninghoff Chip1 Robots1

MUMPs® run:	69 (original designs)
Layout:	8 different 500-µm pinwheel designs anchored on *opposite sides*; residual-stress actuated flip-up hinged rulers with latches
Actuation:	Optothermal
Testing method:	Standard optothermal testing (660-nm laser diode)
Comments:	These robots are designed with a high wing-beat frequency, which is accomplished by making each wing flexure narrow and uniform in width; there is no space grading between each wing flexure; it abandons the rotating concept and adopts a simple flapping concept; half have Poly0 and half do not; the flip-up hinged rulers are used to measure deflection when powering the robots with the laser; anchoring on opposite sides facilitates measuring

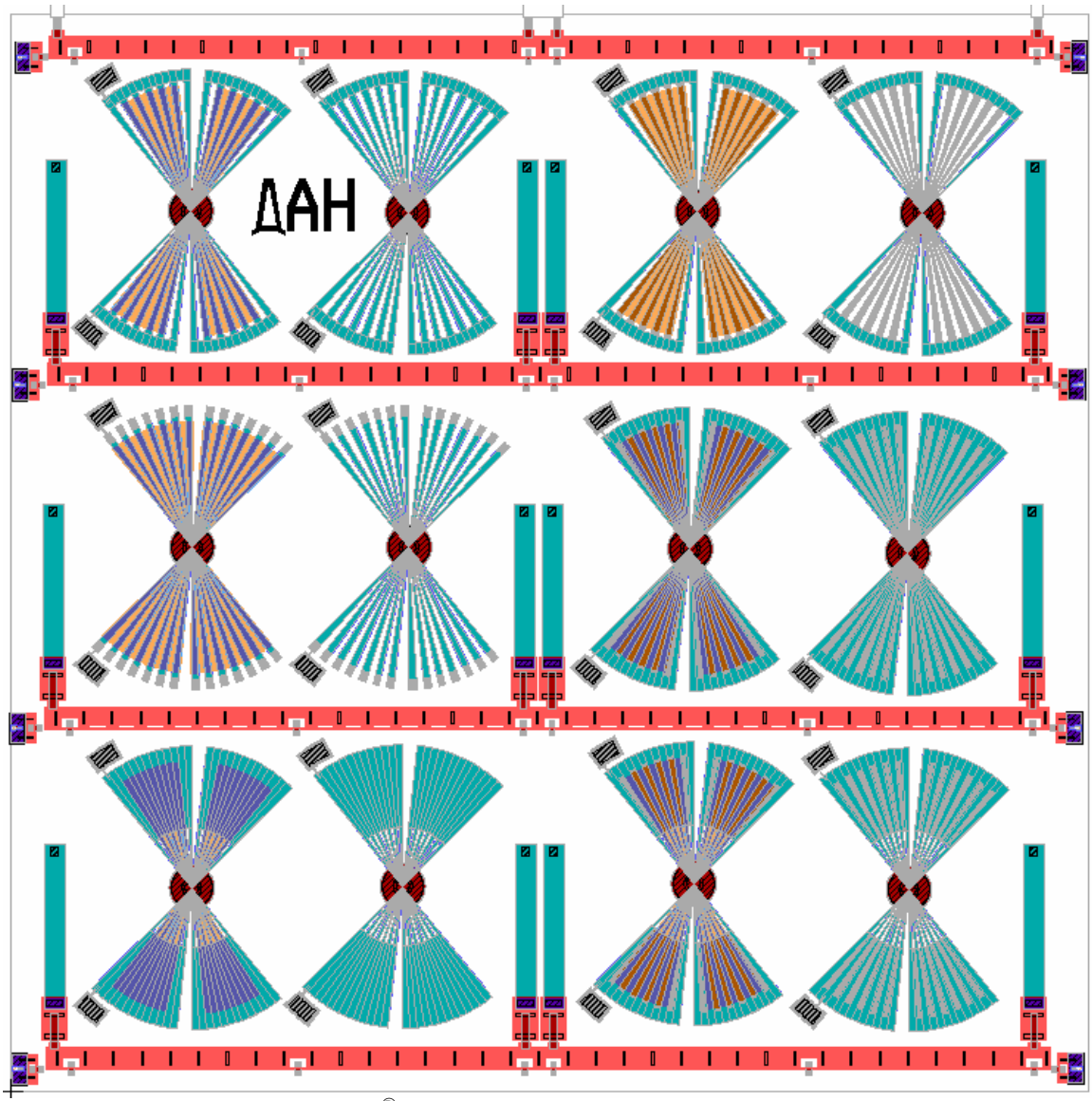


Figure A.18: MUMPs® 69 Denninghoff Chip2 InsectsT

MUMPs® run: 69 (original designs)
Layout: 12 different 500-μm insect-shaped designs anchored on *opposite sides*; residual-stress actuated flip-up hinged rulers with latches
Actuation: Optothermal
Testing method: Standard optothermal testing (660-nm laser diode)
Comments: These insect-like designs are variations of the full-size 8-winged pinwheel robots of the previous chip; again they are designed with a higher wing-beat frequency response as the main objective; this is accomplished by making each wing flexure as small as possible; half have Poly0 and half do not; long flip-up hinged rulers are included to measure downward deflection while the robots are actuated by the laser; anchoring on opposite sides facilitates measuring

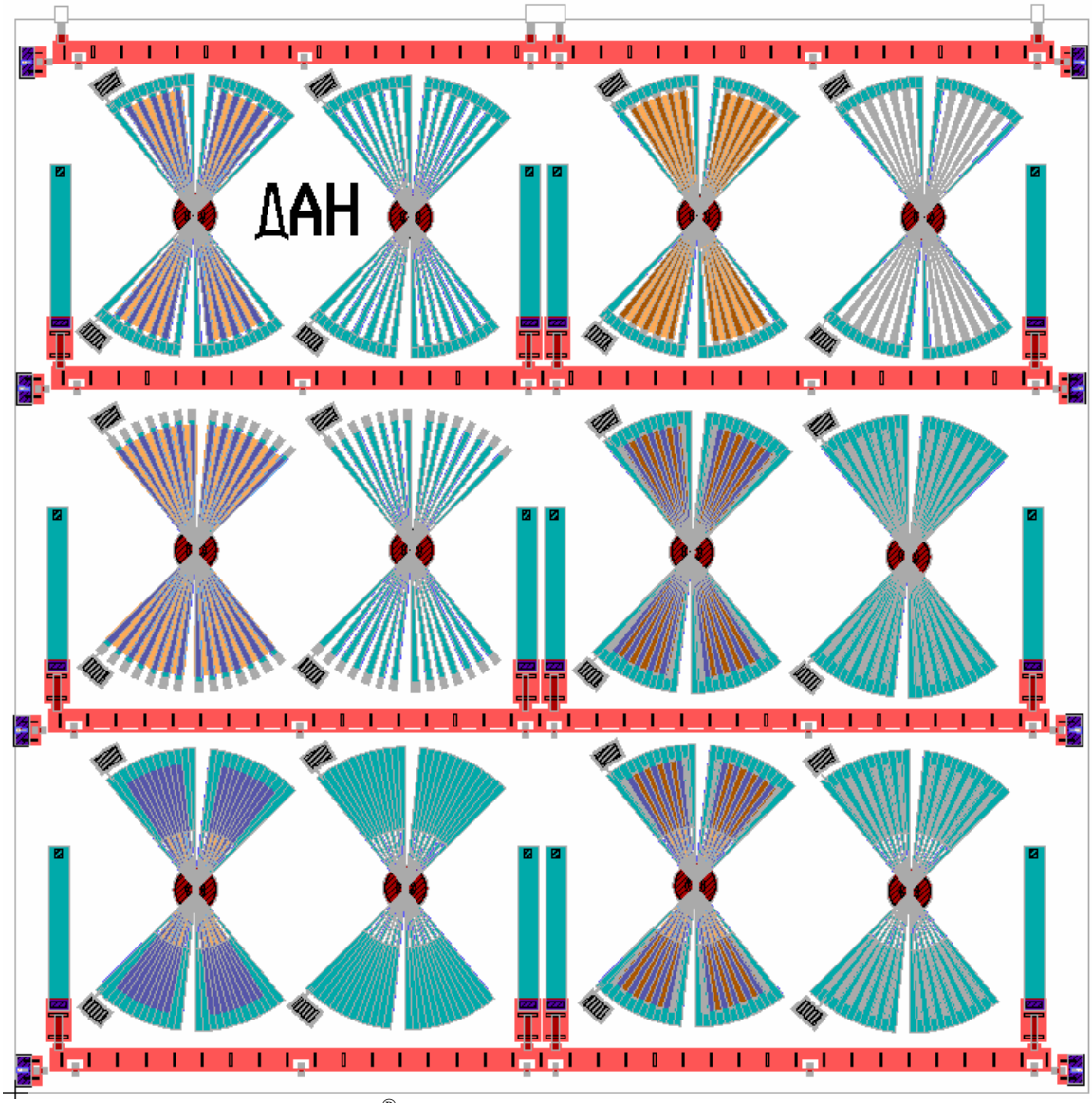


Figure A.19: MUMPs® 69 Denninghoff Chip3 InsectsR

MUMPs® run: 69 (original designs)
Layout: 12 different 500-µm insect-shaped designs with 11-µm center rotor spoke; residual-stress actuated flip-up hinged rulers with latches
Actuation: Optothermal
Testing method: Standard optothermal testing (660-nm laser diode)
Comments: These designs are identical to those on the previous chip except for the 11-µm center rotor spoke; these spokes are smaller than those of previous designs and are not capped in the center; thus they allow the robots to be removed from the substrate; the wings are not designed to spin, however, the smaller hole created by the rotor should allow more laser power absorption than the 50-µm versions in previous designs

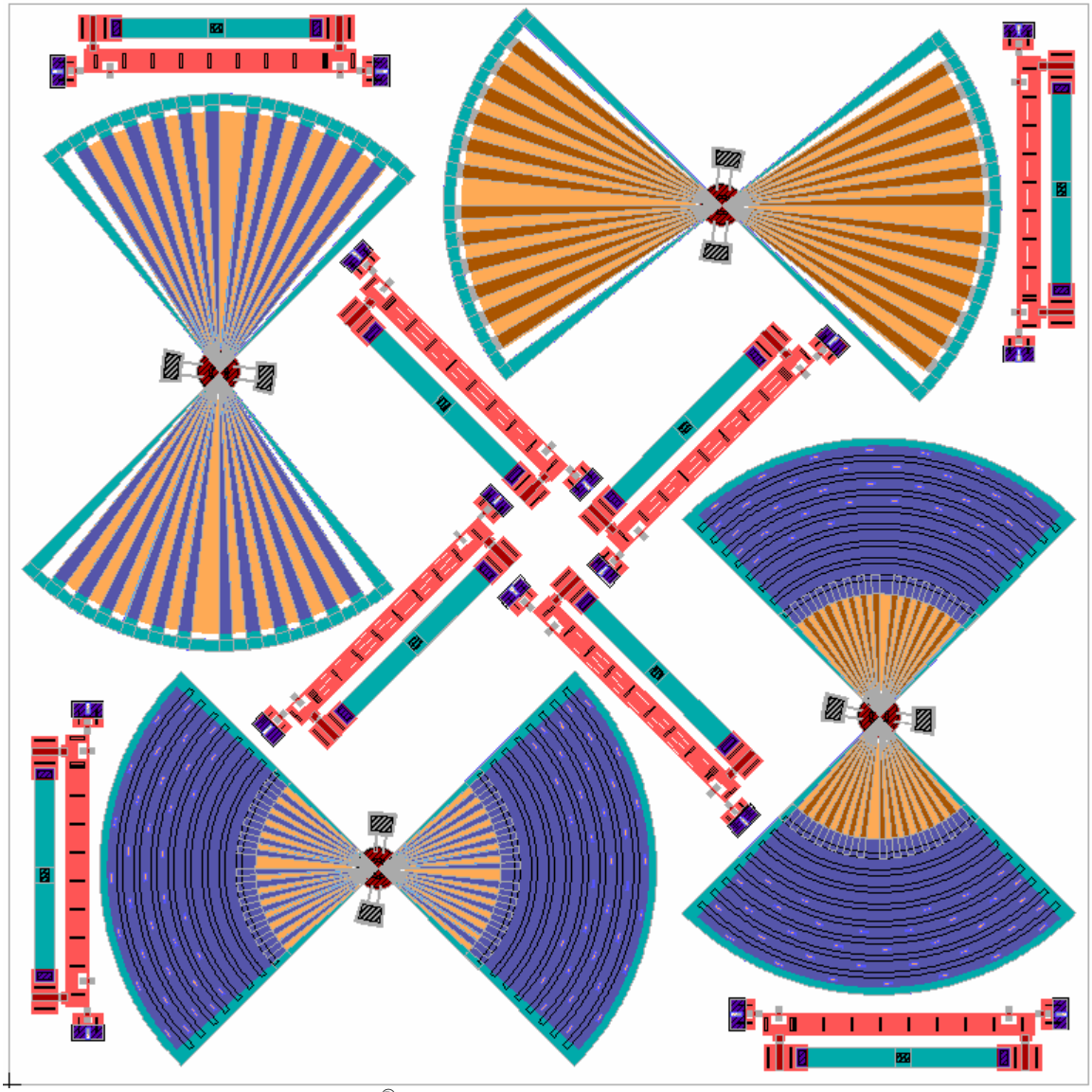


Figure A.20: MUMPs® 69 Denninghoff Chip4 Large Bugs

MUMPs® run: 69 (original designs)
Layout: 4 different two-wing 980-µm insect-shaped designs; residual-stress actuated flip-up hinged rulers with latches
Actuation: Optothermal
Testing method: Standard optothermal testing (660-nm laser diode)
Comments: These insect-like robots are designed with larger wing surface areas and higher wing-beat frequency as the main objectives; they have only two wings, which resembles most flying insects; the bottom two have the most surface area of any robot designed in this thesis; the flip up rulers are critical to measure deflection in these high-deflection designs; Zygo measurements are not capable for large deflection angles; the robots are anchored in the center to allow uninhibited wing deflection

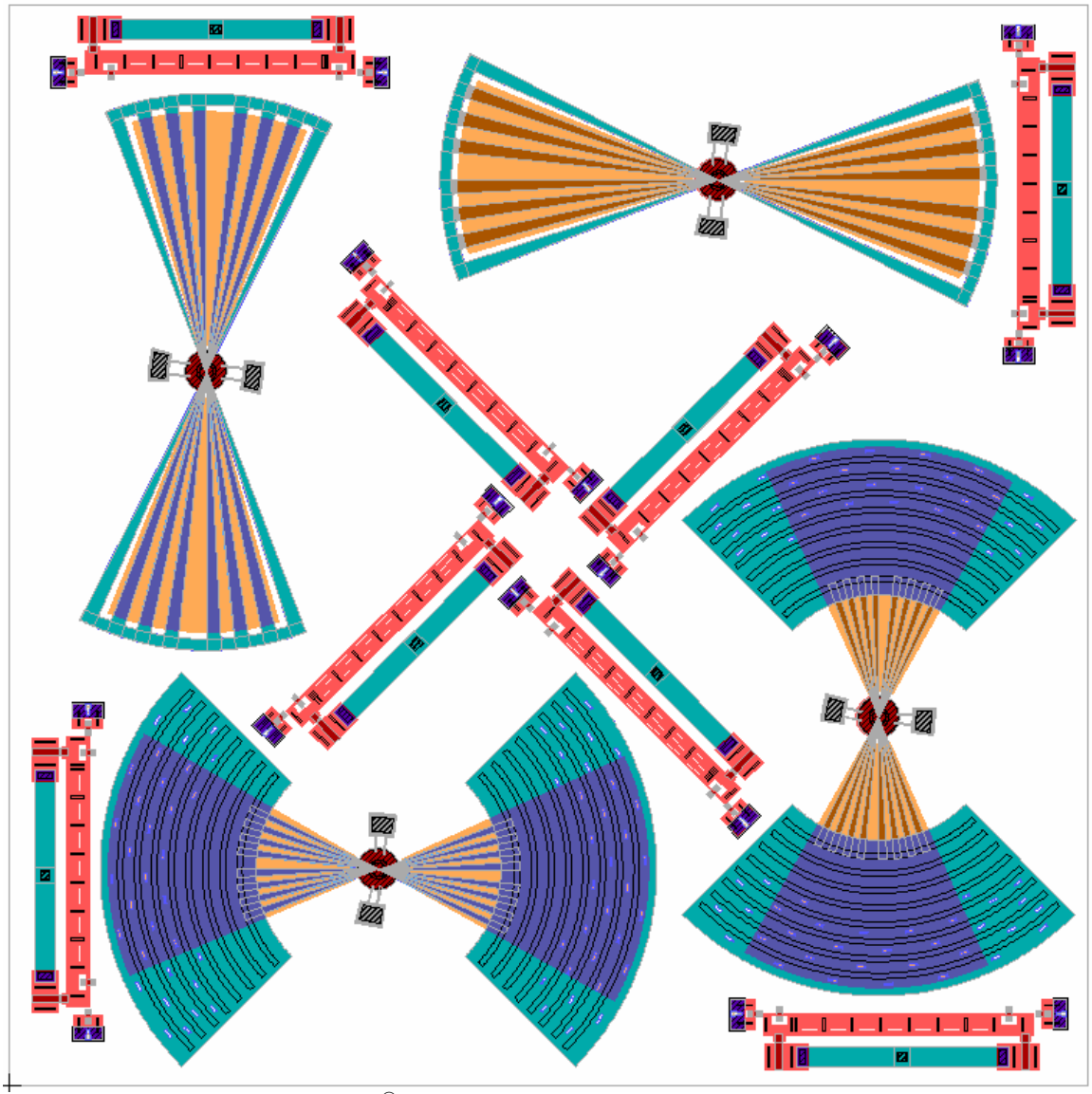


Figure A.21: MUMPs® 69 Denninghoff Chip5 Large Bugs2

MUMPs® run: 69 (original designs)
Layout: 4 different two-wing 980-µm insect-shaped designs; residual-stress actuated flip-up hinged rulers with latches
Actuation: Optothermal
Testing method: Standard optothermal testing (660-nm laser diode)
Comments: These insect-like robots resemble those of the previous chip except the number of wing flexures is reduced by half; the motivation for reducing the wing flexures is to increase flexibility and wing-beat frequency

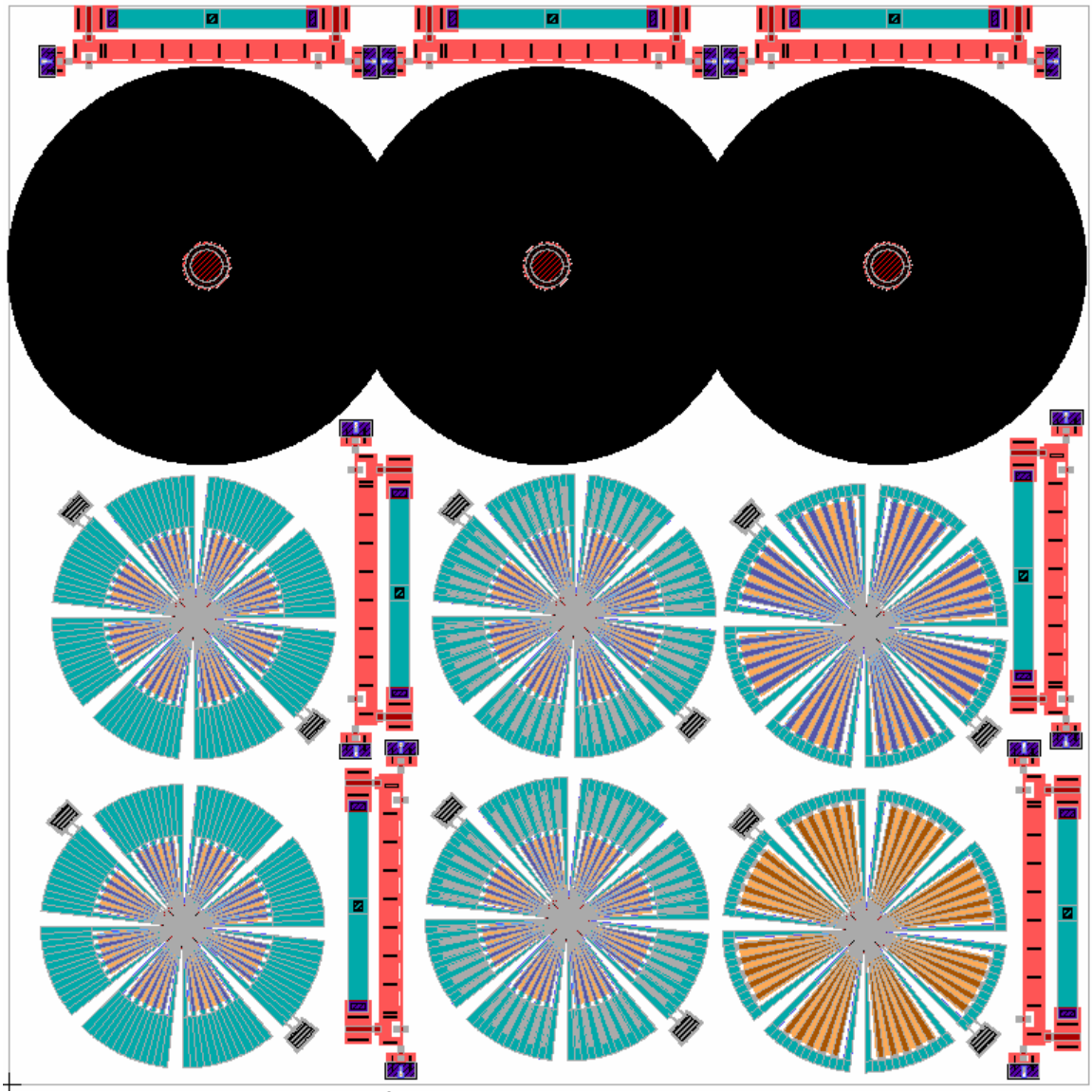


Figure A.22: MUMPs® 69 Denninghoff Chip6 Launch Pad1

MUMPs® run: 69 (original designs)
Layout: Selections from chip 1 pinwheel robots placed next to 3 'launch pads'; residual-stress actuated flip-up hinged rulers with latches
Actuation: Optothermal
Testing method: Standard optothermal testing (660-nm laser diode)
Comments: These pinwheel robots are the most promising 500-µm designs and are placed on the same chip as 6.75-µm-tall cylindrical posts with 600-µm diameter pits etched around them; the purpose is to give maximum separation between the robot and substrate for optothermal testing; the posts and pits allow the wings to flap freely without hitting the substrate; they also reduce the amount of heat loss to the substrate; these launch pads may be used to test robots from other chips as well

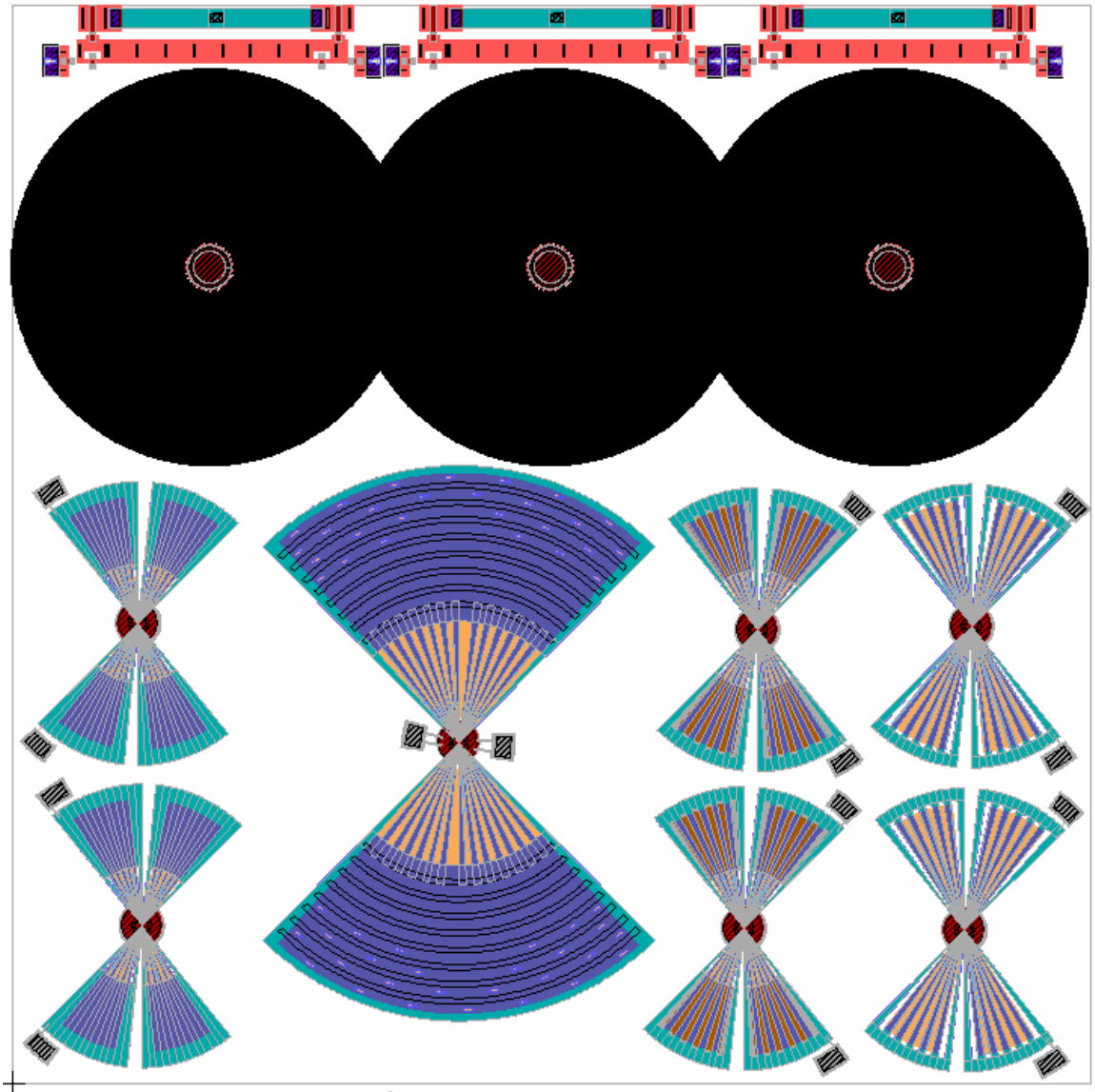


Figure A.23: MUMPs® 69 Denninghoff Chip7 Launch Pad2

MUMPs® run: 69 (original designs)
Layout: Selections from chips 2 and 4 placed next to 3 'launch pads'; residual-stress actuated flip-up hinged rulers with latches
Actuation: Optothermal
Testing method: Standard optothermal testing (660-nm laser diode)
Comments: These insect robots are the most promising insect-based designs and are placed on the same chip as 6.75-µm-tall cylindrical posts with 600-µm diameter pits etched around them; the purpose is to give maximum separation between the robot and substrate for optothermal testing; the posts and pits allow the wings to flap freely without hitting the substrate; they also reduce the amount of heat loss to the substrate; these launch pads may be used to test robots from other chips as well

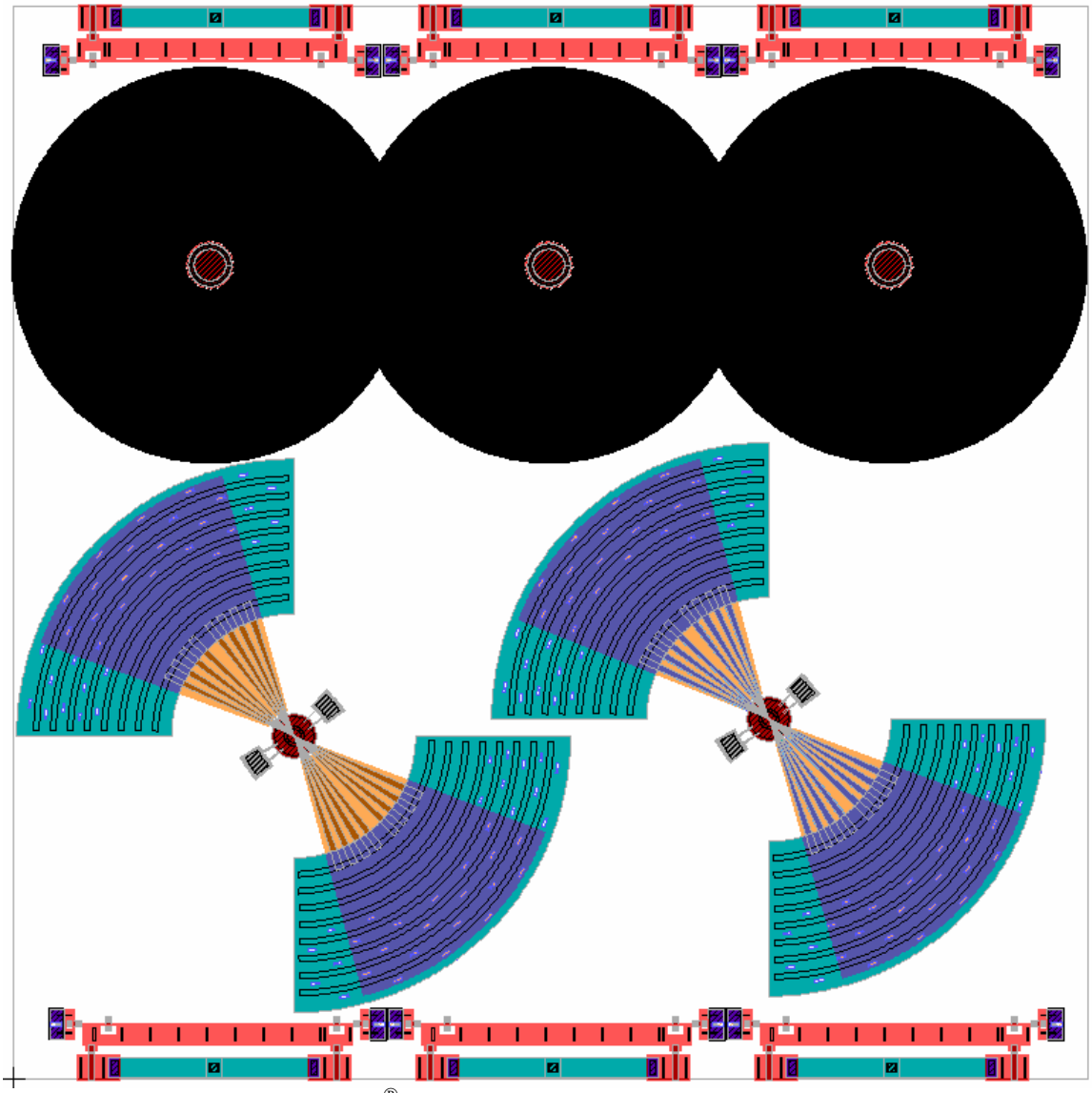


Figure A.24: MUMPs® 69 Denninghoff Chip8 Launch Pad3

MUMPs® run: 69 (original designs)
Layout: Selections from chip5 placed next to 3 ‘launch pads’; residual-stress actuated flip-up hinged rulers with latches
Actuation: Optothermal
Testing method: Standard optothermal testing (660-nm laser diode)
Comments: These insect robots are the most promising insect-based designs and are placed on the same chip as 6.75-µm-tall cylindrical posts with 600-µm diameter pits etched around them; the purpose is to give maximum separation between the robot and substrate for optothermal testing; the posts and pits allow the wings to flap freely without hitting the substrate; they also reduce the amount of heat loss to the substrate; these launch pads may be used to test robots from other chips as well

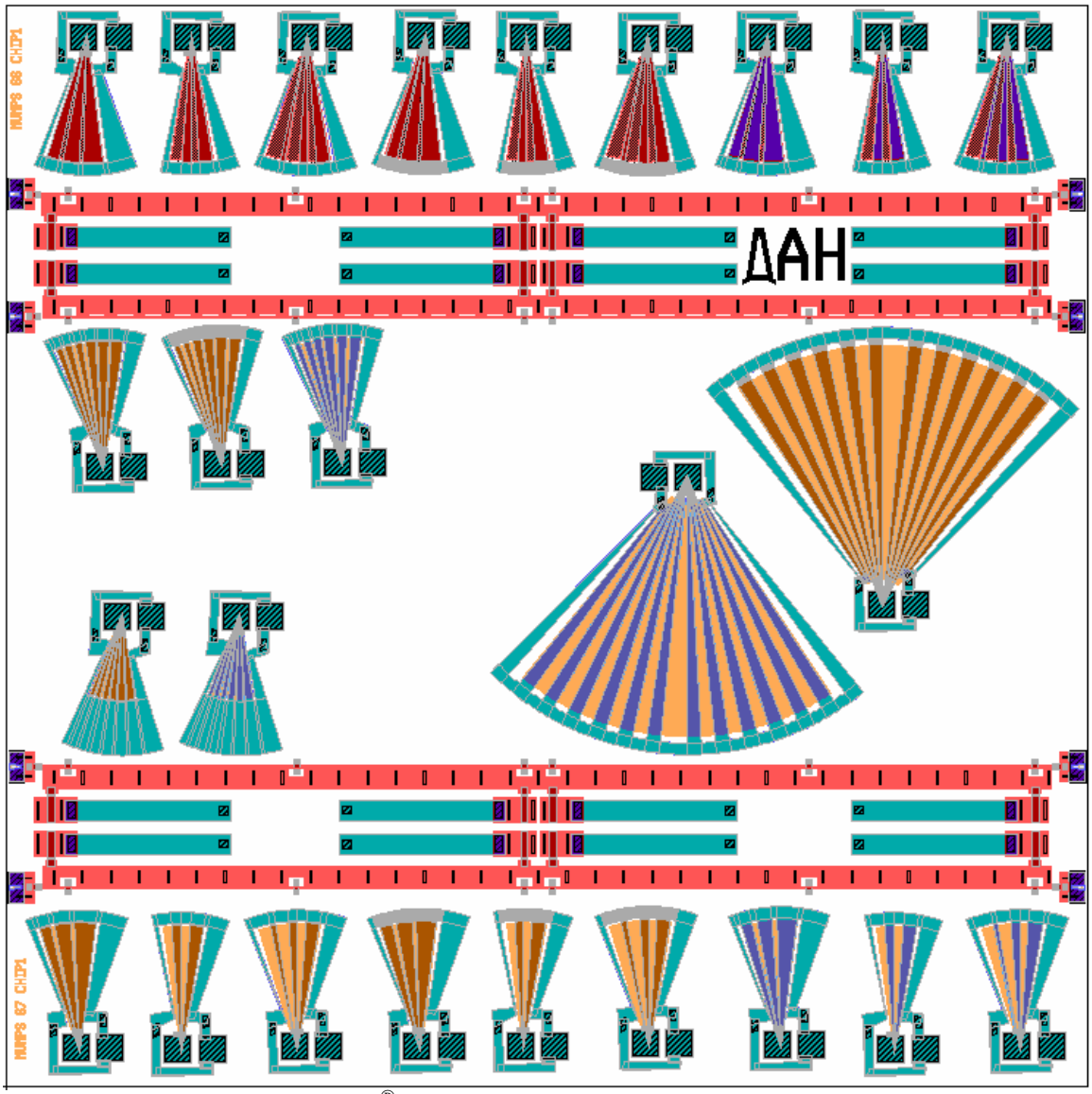


Figure A.25: MUMPs® 69 Denninghoff Chip9 66-67 Wings

MUMPs® run: 69 (original designs)
Layout: Electrothermal test wings from MUMPs® runs 66-67; larger wings from run 69; residual-stress flip-up hinged rulers with latches
Actuation: Electrothermal
Testing method: Standard electrothermal testing under Zygo IFM
Comments: These wings are electrical test structures from runs 66 and 67 that were never fabricated; their purpose is to quantify the differences in all the generations of robot designs; test deflection under Zygo and frequency response visually; some MUMPs® 69 wings are also included to fill in white space

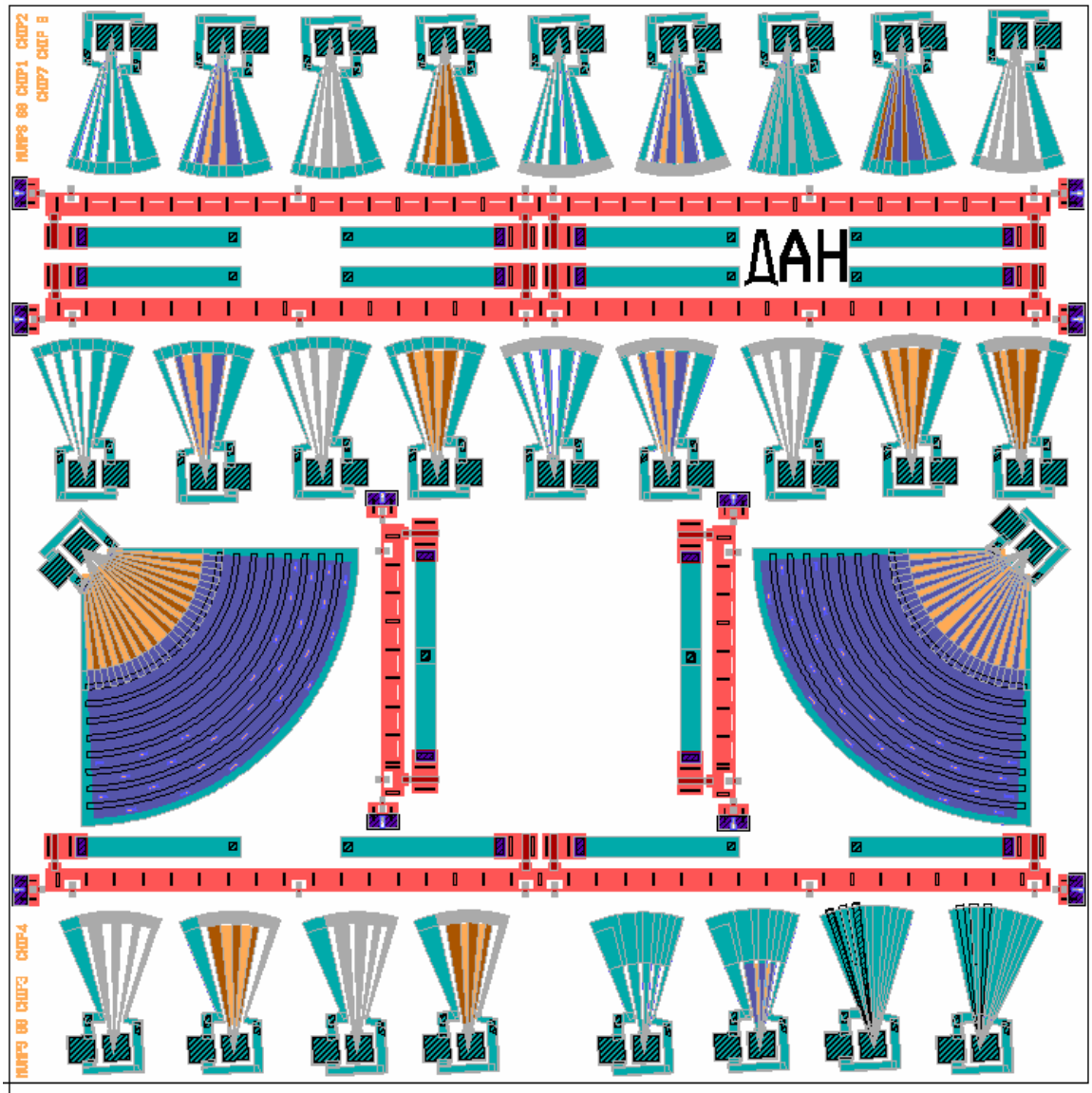


Figure A.26: MUMPs® 69 Denninghoff Chip10 68 Wings

MUMPs® run: 69 (original designs)
Layout: Electrothermal test wings from MUMPs® run 68; larger wings from run 69; residual-stress flip-up hinged rulers with latches
Actuation: Electrothermal
Testing method: Standard electrothermal testing under Zygo IFM
Comments: These wings are electrical test structures from run 68; they are repeats of those fabricated in run 68 but can be used as a standard between the two runs; again, their purpose is to quantify the differences in all the generations of robot designs; test deflection under Zygo and frequency response visually; some MUMPs® 69 wings are also included to fill in white space

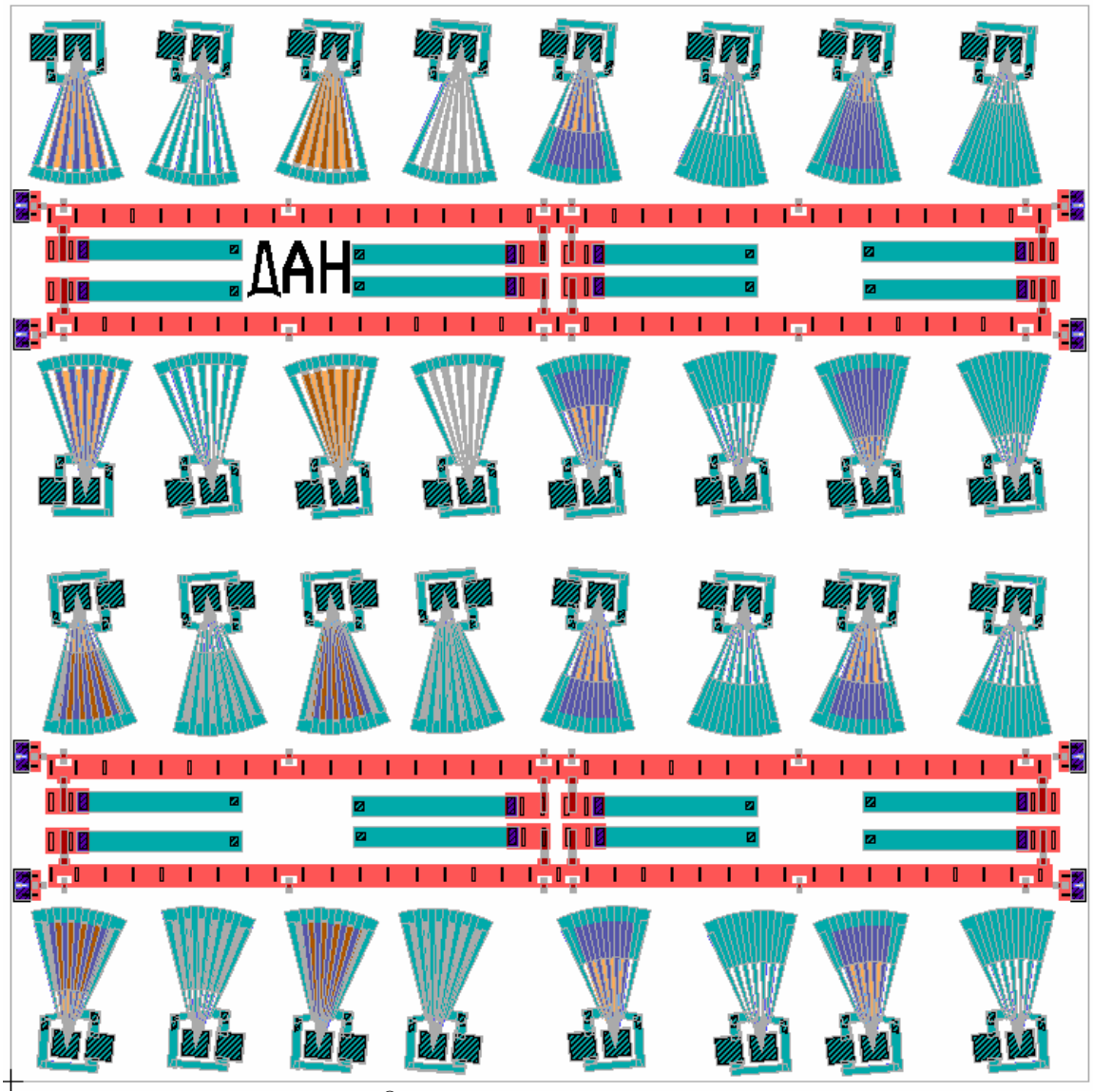


Figure A.27: MUMPs® 69 Denninghoff Chip11 69 Wings

MUMPs® run: 69 (original designs)
Layout: Electrothermal test wings from MUMPs® run 69; residual-stress flip-up hinged rulers with latches
Actuation: Electrothermal
Testing method: Standard electrothermal testing under Zygo IFM
Comments: These wings are electrical test structures from run 69; several are copies; they may be compared with those of earlier designs to determine which wing shape is optimum; test deflection under Zygo and frequency response visually

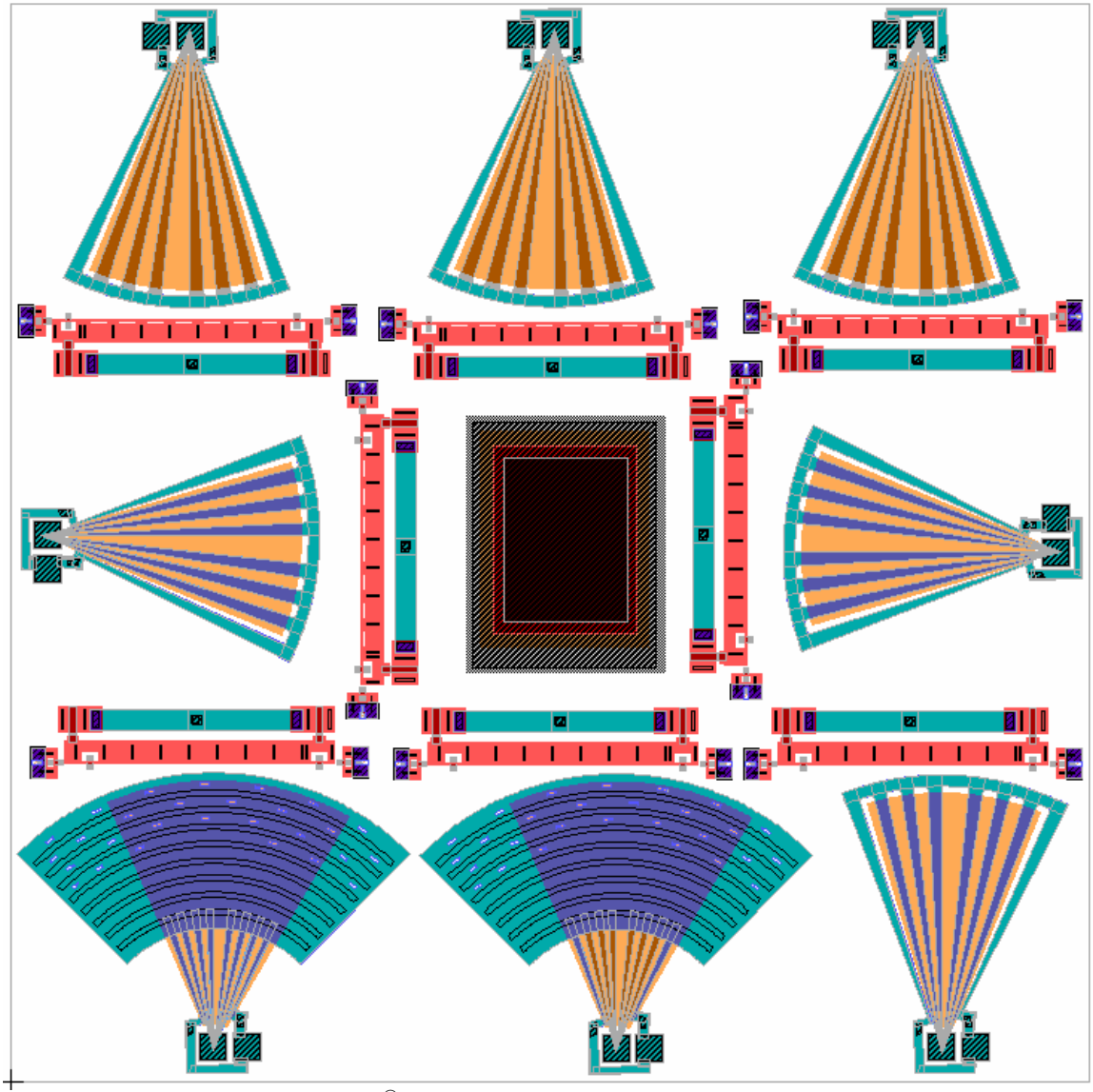


Figure A.28: MUMPs® 69 Denninghoff Chip12 Large Wings

MUMPs® run: 69 (original designs)
Layout: Large electrothermal test wings from MUMPs® run 69; residual-stress flip-up hinged rulers with latches
Actuation: Electrothermal
Testing method: Standard electrothermal testing under Zygo IFM
Comments: These wings are electrical test structures from run 69; several are copies; they may be compared with other designs; test deflection under Zygo and frequency response visually; the rulers are necessary in case the deflection is too great for the Zygo

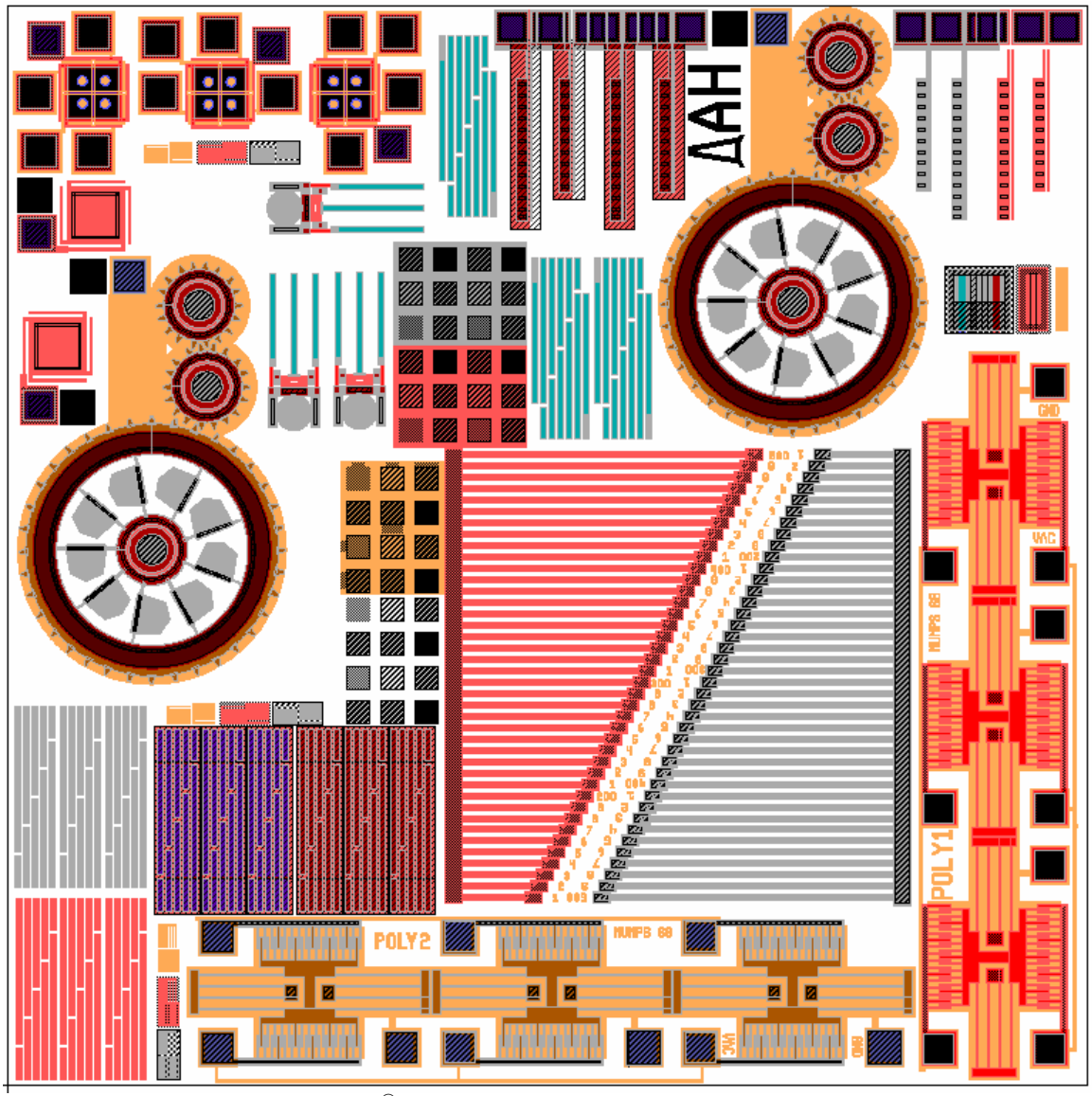


Figure A.29: MUMPs® 69 Denninghoff Chip13 Test Structures

MUMPs® run:	69 (all original designs except for comb drives)
Layout:	Multi-directional micromirrors; line resolution bars; thermal actuators; cantilevers; gears and scratch drive; layer thickness bars; Fresnel lenses; vertical micromirror; etch depth squares; fixed beams; resonators; *similar to that of MUMPs® 68*
Actuation:	Electrostatic and electrothermal
Testing method:	Standard testing for actuators, cantilevers, scratch drive, resonators, fixed beams; use profilometer or Zygo IFM for etch depth and layer thickness sections; visually observe resolution tests; flip up Fresnel lenses with probe
Comments:	This chip is a comprehensive test chip that should be included on each design run to determine material and fabrication properties

Appendix B: MatLab® Code

This appendix includes the MatLab® m-files used in this thesis.

B.1 Light Penetration Depth

```
% Program   Penetration Depth
% Author:   2nd Lt Dan Denninghoff
% Project:  Master's Thesis
% Date:     17 Nov 2005
%
% This program determines the amount of laser heat from an
% incident beam and the penetration depth.

clear;clc;clf

A = linspace(0.60,0.999,1000);   % Fraction of light absorbed
L  = linspace(0.2,1.2);          % Wavelength {um}
t  = linspace(0,10);             % Material thickness {um}
T  = 1-A;                        % Fraction of light transmitted
R  = 0.2;                        % Reflectivity of poly
a  = [8e3 2e5];                  % Absorption coefficient {cm^-1}
La = [0.66 0.4];                 % Wavelength {um}
i  = 2;                          % Choice of wavelength
d  = -log(T)/(a(i))*10^4;        % Penetration depth {microns}
Eg = 1.12;                       % Bandgap of silicon {eV}
hv = 1.24./L;                    % Energy {eV}
P_abs  = 1-exp(-t*1e-4*a(i));
P_heat = (hv-Eg)./hv;
P_ab   = 1-exp(-3.5*1e-4*a(i))
P_h    = (1.24/La(i)-Eg)/(1.24/La(i))
Tot    = (1-R)*P_ab*P_h

figure(1)
plot(A*100,d,'Linewidth',2,'Color','r'); hold on;
plot(A*100,1.5,'Linewidth',3,'Color','r')
plot(A*100,3.5,'Linewidth',3,'Color','b')
set(gca,'FontSize',12,'XColor',[0 0 0],...
    'XMinorTick','On','YMinorTick','On'); grid on;
title('Energy Absorption in Phosphorus-Doped
Polysilicon','Fontsize',14)
xlabel('Percentage of Non-Reflected Light Absorbed (%)','Fontsize',12)
ylabel('Layer Thickness (\mum)','Fontsize',12)
axis([60 100 0 5])

figure(2)
plot(L,P_heat*100,'Linewidth',2,'Color','r')
set(gca,'FontSize',12,'XColor',[0 0 0],...
    'XMinorTick','On','YMinorTick','On'); grid on
title('Absorbed Energy to Heat Efficiency in Silicon','Fontsize',14)
xlabel('Wavelength of Light (\mum)','Fontsize',12)
ylabel('Percentage of Absorbed Energy Converted to Heat','Fontsize',12)
axis([L(1) L(length(L)) 0 100])
```

B.2 Residual Stress Deflection in Cantilevers

```
% Program   Residual_Stress_Deflection
% Author:   2d Lt Dan Denninghoff
% Project:  Master's Thesis
% Date:     5 Aug 2005
%
% This program estimates the deflection due to residual stress in
% bilayer cantilever structures fabricated in PolyMUMPs.
%
% Assumptions:
% (1) The only applied force is the weight of the beam due to gravity,
%     and it will be assumed to be negligible throughout the
%     derivations and calculations.
% (2) The force due to residual stress is modeled as a single moment.
% (3) The polysilicon is undoped and there are no defects in the
%     material; thus, the internal stresses caused by doping and
%     defects are neglected
% (4) The dominant internal stress is gold-poly2 residual stress
% (5) The cantilever is in equilibrium

clear; clc;

L   = [49 99 149 199 249]; % Length of beams {um}
x   = linspace(1,1e3,1e3); % Data points for 1-mm beam
t   = [1.496 0.5421]*1e-6; % Thickness of [poly2 gold] {m}
E   = [161 74]*1e9;        % Young's modulus of poly2 {Pa}
n   = [0.23 0.44];         % Poisson's ratio of poly2 {unitless}
Ep  = E(1)/(1-n(1));       % Polysilicon biaxial modulus {Pa}
Eg  = E(2)/(1-n(2));       % Gold biaxial modulus {Pa}
a   = [2.33 14.3]*1e-6;    % Coefficient of thermal expansion {K-1}
T   = [300 333];           % [room temp  gold evaporation temp] {K}
sg  = [-7.3 0.00 25.7]*1e6;      % Residual stress of [poly2 gold] {Pa}
sgt = Eg*(a(1)-a(2))*(T(1)-T(2));% Stress due to CTE differences {Pa}

thr = 6*t(2)*(sg(1)+sgt)/(Ep*t(1)^2)*x*1e-6;    % Deflection {rad}
y   = 3*t(2)*(sg(1)+sgt)*x.^2/(Ep*t(1)^2)*1e-6; % Deflection {um}
thd = thr*360/(2*pi);                           % Deflection {deg}

Deflection_um(1:length(L))  = y(L)
Deflection_rad(1:length(L)) = thr(L)
Deflection_deg(1:length(L)) = thd(L)

ymeas = [0.3603383 1.51092 3.5762 6.266045 9.66784]
```

B.3 Temperature-Deflection Relationship in Cantilevers

```
% Program   Res_Temp_Deflection
% Author:   2d Lt Dan Denninghoff
% Project:  Master's Thesis
% Date:     6 Feb 2006
%
% This program estimates the deflection caused by heating
% bilayer cantilever structures fabricated in PolyMUMPs.

clear; clc;
L   = [49 99 149 199 249]; % Length of beams {um}
x   = linspace(1,1e3,1e3); % Data points for 1-mm beam
t   = [1.496 0.5421]*1e-6; % Thickness of [poly2 gold] {m}
E   = [161 74]*1e9;        % Young's modulus of poly2 {Pa}
n   = [0.23 0.44];         % Poisson's ratio of poly2 {unitless}
Ep  = E(1)/(1-n(1));       % Polysilicon biaxial modulus {Pa}
Eg  = E(2)/(1-n(2));       % Gold biaxial modulus {Pa}
a   = [2.33 14.3]*1e-6;    % Coefficient of thermal expansion {K-1}
T   = [300 333];           % [room temp  gold evaporation temp] {K}
Ta  = linspace(0,60);      % Applied temperature (additional to RT) {K}
y   = zeros(length(Ta),length(L));

for i = 1:length(Ta)
sg  = [-7.3 25.7]*1e6;     % Residual stress of [poly2 gold] {Pa}
% Stress due to CTE differences {Pa}
sgt = Eg*(a(1)-a(2))*(Ta(i)+T(1)-T(2));
% Deflection {um}
y(i,1:length(L)) = 3*t(2)*(sg(1)+sgt)*L.^2/(Ep*t(1)^2)*1e-6;
end
T_a = T(1)+Ta;

figure(1)
plot(T_a,y(1:i,1),'y','linewidth',2); hold on;
plot(T_a,y(1:i,2),'r','linewidth',2)
plot(T_a,y(1:i,3),'g','linewidth',2)
plot(T_a,y(1:i,4),'b','linewidth',2)
plot(T_a,y(1:i,5),'k','linewidth',2)
axis([T_a(1) T_a(i) -15 15]); grid on

% Define axis properties
set(gca,'FontWeight','Normal','FontSize',12,'XColor',[0 0 0],...
    'XGrid','On','YGrid','On','XMinorTick','On','YMinorTick','On')
% Define x and y labels
set(get(gca,'XLabel'),'string','Applied Temperature (K)',...
    'FontWeight','Normal','FontSize',12,'Color',[0 0 0])
set(get(gca,'YLabel'),'string','Deflection at Tip (\mum)',...
    'FontWeight','Normal','FontSize',12)
% Include title
header = sprintf('Temperature-Deflection Relationship in Gold-Poly2
      Cantilevers');
s = title(header); set(s,'FontSize',14);

legend('49-\mum Cantilever','99-\mum Cantilever','149-\mum Cantilever',
    '199-\mum Cantilever','249-\mum Cantilever')
```

B.4 Power-Deflection Relationship in Cantilevers

```
% Program   Res_Power_Deflection
% Author:   2d Lt Dan Denninghoff
% Project:  Master's Thesis
% Date:     9 Feb 2006
%
% This program estimates the deflection caused by heating
% bilayer cantilever structures fabricated in PolyMUMPs.

clear; clc;
L   = [49 99 149 199 249]; % Length of beams {um}
x   = linspace(1,1e3,1e3); % Data points for 1-mm beam
t   = [1.496 0.5421]*1e-6; % Thickness of [poly2 gold] {m}
w   = 10e-6;               % Width of beam {m}
D   = 2330;                % Density of poly {m}
E   = [161 74]*1e9;        % Young's modulus of poly2 {Pa}
n   = [0.23 0.44];         % Poisson's ratio of poly2 {unitless}
Ep  = E(1)/(1-n(1));       % Polysilicon biaxial modulus {Pa}
Eg  = E(2)/(1-n(2));       % Gold biaxial modulus {Pa}
c   = 678;                 % Specific heat capacity of poly {J/kgK}
a   = [2.33 14.3]*1e-6;    % Coefficient of thermal expansion {K-1}
T   = [300 333];           % [room temp  gold evaporation temp] {K}
Pa  = linspace(0,20);      % Absorbed power {mW}
tau = 0.35e-5;             % Pulse length {sec}
sg  = [-7.3 25.7]*1e6;     % Residual stress of [poly2 gold] {Pa}
y   = zeros(length(Pa),length(L));
for Li  = 1:length(L)
for i   = 1:length(Pa)
Ta(i)   = Pa(i)*1e-3*tau*Li/(c*D*t(1)*L(Li)*1e-6*w); % Incr temp {K}
Sgt(i)  = Eg*(a(1)-a(2))*(Ta(i)+T(1)-T(2));   % Stress from CTE
y(i,Li) = 3*t(2)*(sg(1)+sgt(i))*L(Li)^2/(Ep*t(1)^2)*1e-6;
end
end

figure(1)
plot(Pa,y(1:i,5),'k','linewidth',2); hold on;
plot(Pa,y(1:i,4),'b','linewidth',2)
plot(Pa,y(1:i,3),'g','linewidth',2)
plot(Pa,y(1:i,2),'r','linewidth',2)
plot(Pa,y(1:i,1),'y','linewidth',2)
axis([Pa(1) Pa(i) -15 15]); grid on
% Define axis properties
set(gca,'FontWeight','Normal','FontSize',12,'XColor',[0 0 0],...
    'XGrid','On','YGrid','On','XMinorTick','On','YMinorTick','On')
% Define x and y labels
set(get(gca,'XLabel'),'string','Absorbed Power (mW)',...
    'FontWeight','Normal','FontSize',12,'Color',[0 0 0])
set(get(gca,'YLabel'),'string','Deflection at Tip (\mum)',...
    'FontWeight','Normal','FontSize',12)
% Include title
header = sprintf('Power-Deflection Relationship in Gold-Poly2
      Cantilevers');
s = title(header); set(s,'FontSize',14);
legend('249-\mum Cantilever','199-\mum Cantilever','149-\mum
      Cantilever','99-\mum Cantilever','49-\mum Cantilever')
```

B.5 Temperature Distribution in a Conduction-Convection System

```
% Program Cond_Convec
% Author:   2nd Lt Dan Denninghoff
% Project:  Master's Thesis
% Date:     8 Feb 2006
%
% This program calculates the convection losses in a device
% with two different scenarios:  (1) a very long beam with an
% end-tip temperature matching the surrounding air; (2) a beam
% with a finite length.

clear; clc; clf

L   = [49 99 149 199 249]*1e-6;     % Length of beams {m}
w   = 10*1e-6;                      % Width of beams {m}
t   = (1.5+0.5)*1e-6;               % Thickness of beams {m}
x   = linspace(0,L(length(L)),1e3); % Position along beam {m}

h   = 3850;                      % heat-transfer {W/(m^2*K)}
k   = (149+318)/2;               % Ave therm cond poly,gold {W/(m*K)}
P   = 2*(w+t);                   % Perimeter {m}
A   = w*t;                       % Cross-sectional area {m^2}
m   = sqrt(h*P/(k*A));           % Substituting variable
T   = [400 300];                 % [T_end  T_ambient] {K}

i   = 5;
Ti  = (T(1)-T(2))*(exp(-m*x))+T(2); % Temp dist for inf beam {K}
Tf1 = cosh(m*(L(i)-x))+h/(m*k)*sinh(m*(L(i)-x)); % Num for fin beam
Tf2 = cosh(m*L(i))+h/(m*k)*sinh(m*L(i));         % Denom for fin beam
Tf  = (T(1)-T(2))*Tf1./Tf2+T(2);

figure(1)
plot(x,Tf,'r','linewidth',2); hold on
plot(x,Ti,'b','linewidth',2)

% Define axis properties
set(gca,'FontWeight','Normal','FontSize',12,'XColor',[0 0 0],...
    'XGrid','On','YGrid','On','XMinorTick','On','YMinorTick','On')
% Define x and y labels
set(get(gca,'XLabel'),'string','Position Along Beam (m)',...
    'FontWeight','Normal','FontSize',12,'Color',[0 0 0])
set(get(gca,'YLabel'),'string','Temperature Distribution (K)',...
    'FontWeight','Normal','FontSize',12)
% Include title
header = sprintf('Temperature Distribution in a Conduction-Convection
      System');
s = title(header); set(s,'FontSize',14);

legend('249-\mum-Long Beam','Infinitely Long Beam')
```

B.6 Normalized Gaussian Beam Intensity

```
% Program   Normalized_beam_intensity.m
% Author:   2nd Lt Dan Denninghoff
% Project:  Master's Thesis
% Date:     27 Oct 2005
%
% This program calculates and plots the theoretical Gaussian beam
% intensity as a function of distance from the laser output.

clear; clc;

sig     = [0.4 0.6 0.8];                % Variance
a       = 0;                            % Average
x       = linspace(-2,2,100);           % Data points
f       = 1/sqrt(2*pi*sig(n)^2)*exp(-(x-a).^2/(2*sig(n)^2));
[X1,Y1] = meshgrid(linspace(-2,2,1000)); % Mesh points
[X2,Y2] = meshgrid(x);                  % Data points
r1      = sqrt(X1.^2+Y1.^2);
r2      = sqrt(X2.^2+Y2.^2);

for n = 1:3;
F1      = 1/sqrt(2*pi*sig(n)^2)*exp(-(r1-a).^2/(2*sig(n)^2));
F2      = 1/sqrt(2*pi*sig(n)^2)*exp(-(r2-a).^2/(2*sig(n)^2));

% figure
% plot(x,f); grid on; axis([-2 2 0 1]);
% ylabel('Normalized Beam Intensity I/I_0');
% xlabel('Radial Distance \rho');

figure
imagesc(F1); axis xy; axis square; caxis([0 1])

figure
surf(X2,Y2,F2); shading interp; axis([-2 2 -2 2 0 1]); caxis([0 1])
end
```

B.7 Pixelscope Data Plotter

```
% Program   Pixelscope
% Author:   2nd Lt Dan Denninghoff
% Project:  Master's Thesis
% Date:     11 Nov 2005
%
% This program imports images from a file, changes the data type,
% and plots 3-D surface and 2-D intensity plots.

clear; clc;

I = 109; d = 16*2.54;    % Beam parameters
File = 'I:\MatlabFa05\Laser\109mA_16in_ND23.bmp'; % File name
A = importdata(File);                             % Grab data
B = double(A.cdata);                              % Convert data
C = zeros(480,640); B(480,1:640) = 0;             % Process data
```

```
C(1:480,631:640) = B(1:480,1:10); C(1:480,1:630) = B(1:480,11:640);

% Plot
figure(1)
imagesc(C); colormap jet; caxis([0 256])
title({['Laser Diode Beam Intensity at ',num2str(d),' cm'],...
    ['I = ',num2str(I),' mA with ND = 2.0 and 3.0 Filters']},...
    'fontsize',12); axis xy;
xlabel('Pixels (7 \mum per pixel)');
ylabel('Pixels (7 \mum per pixel)');

figure(2)
surfl((C),'light'); shading interp; colormap jet; caxis([0 256])
title({['Laser Diode Beam Intensity at ',num2str(d),' cm'],...
    ['I = ',num2str(I),' mA with ND = 2.0 and 3.0 Filters']},...
    'fontsize',12); axis([0 640 0 480 0 256]);
zlabel('Intensity (a.u.)');
xlabel('Pixels (7 \mum per pixel)');
ylabel('Pixels (7 \mum per pixel)');
```

B.8 Scaling in Insects

```
% Program   Scaling
% Author:   2nd Lt Dan Denninghoff
% Project:  Master's Thesis
% Date:     11 Nov 2005
%
% This program plots the scaling effects of wing area, wing beat, and
Reynolds number as a function of insect mass.

clear; clc; clf

mass     = linspace(1,100,1000);
wingarea = mass.^(2/3);
wingbeat = mass.^(-1/4);
Re       = mass.^(0.42);

figure(1)
title('Scaling Effects in Insects')
subplot(3,1,1)
plot(mass,wingarea)
xlabel('Mass (\mug)'); ylabel('Wing Area (\mum^2)');

subplot(3,1,2)
plot(mass,wingbeat)
xlabel('Mass (\mug)'); ylabel('Wing Beat Frequency (Hz)');

subplot(3,1,3)
plot(mass,Re)
xlabel('Mass (\mug)'); ylabel('Reynolds Number (unitless)');
```

Appendix C: Laser Safe Operating Procedures

This appendix contains the approved safe operating procedures of the laser used in this thesis. Extreme care must be taken while operating this high-power laser.

Class IIIb AlGaInP Laser Diode

Building 640 Room 224

1. Primary Operator: 2nd Lt Daniel Denninghoff Phone: 785-3636 x7502

Other Personnel with Authorized Access to Laser (as of 19 OCT 2005)
Capt Steve Mink Master's Student

2. Preventing Unauthorized Operation

- Ensure the lab door is locked at all times
- Place laser diode driver unit a locked compartment when not in use

Unauthorized personnel are not permitted to operate this laser system.
Authorized personnel should have completed laser safety training within the year
An eye examination is also required before access will be granted
An exit eye exam should be done upon the completion of work in the lab

3. Preventing Unauthorized Entry

- Ensure the lab door is locked at all times
- Illuminate "Laser In Use" warning sign during laser operation

4. Laser Hazard Control in Lab Room

- Ensure the door window is covered and sealed with opaque material

5-6. Beam Control/Termination

- Lab coats or long sleeve clothing should be worn for skin protection
- Ensure the laser is fixed and directed towards the target during operation
- Use an absorbing beam stop to separate laser setup from other equipment
- Place beam stop behind mirror during adjustments

7-8. Protective Eyewear

- Ensure protective safety glasses are worn during laser operation
- Three pairs of Thorlabs LG4 glasses (OD 3+ at 660 nm) are located in lab room
- Operation authorized for only one AlGaInP laser diode at 660 nm

9. Control Measures when Visitors Present

- Visitors must wear protective safety glasses during laser operation
- Visitors must be briefed on laser hazards and safety precautions

- Keep all visitors on opposite side of room from laser
- Do not allow visitors to touch anything

10. General Safety Precautions

- Remove all jewelry and reflective items from the person
- Put on a lab coat to cover metal belt buckles, uniform metals, and exposed skin
- Remove all clutter from the optics table to avoid reflection hazards
- Check all hoses and wiring for the laser to ensure they are not damaged
- Keep eyes above laser level

11. Safety Precautions with Magnifying Optics

- Do not look through microscope eyepieces
- Remove microscope eyepieces and cover with opaque tape
- Do not use magnifying optics for viewing the laser
- View laser target area in the TV monitor only

12. Approved Operation Location

- Operation of this laser is unauthorized anywhere except room 224, building 640
- Do not operate this laser in any other location

13. Laser Modification

- Laser approved for use $\leq$ 40 mW CW or 60 mW pulsed (with < 50% duty cycle)
- Laser modification requires approval from base laser safety officer (LSO)
- Laser modification may be performed only with proper training/license

14. Safety Precautions during Alignment

- Align laser only at lowest possible power (~ 1 mW)
- Do not remove protective eyewear except under very controlled conditions
- Use TV monitor for final alignment
- Ensure laser beam remains below eye level
- Do not sit down during laser alignment or any time during operation

15. Off-Table Beam Routing

- Ensure laser beam is confined within perimeter of optics bench

16. Electrical Shock Precautions

- Do not open laser mount while power is applied
- Keep all liquids away from optics bench and all electronic equipment
- Do not open any equipment chassis while power cord is connected
- Do not perform high-voltage maintenance without training/license or alone

17-18. Emergency Procedures

- In case of any emergency, ramp down power and turn off machines
- In case of fire, ramp down off power, evacuate, and pull fire alarm
- As good policy, always inform someone when working in the lab
- Call 9-911 for emergency assistance

• Immediately report all injuries/accidents to your advisor, the AFIT safety representative, the AFIT LSO, and the base LSO: (937) 255-6815

19. Unattended Operation

• The laser must never be unattended during operation

20-21. Laser Dyes and Class IV Precautions

• Not applicable

22. Emergency Shutdown Procedures

• Ramp down power
• Turn off all laser controlling equipment via master power switch
• Secure room

23. Operating and Alignment Instructions

Start Up

• Ensure door is secured and the laser DANGER sign is posted outside the lab
• Illuminate the "Laser In Use" warning sign
• Check all connections from temperature controller and driver to laser mount
• Turn on laser temperature controller, set desired settings, and push ENABLE
• Check the placement of the beam stop for the reflected beam (table marked)
• Make sure that a beam stop is in front of laser
• Don appropriate safety glasses
• Turn on laser diode driver, set desired settings, and push ENABLE
• Ramp up current to ~ 50 mA and check power reading (should be ~1 mW)
• Remove beam stop and check alignment

Shut Down

• Put beam stop in front of laser
• Ramp down current on laser diode driver
• Turn off laser diode driver and temperature controller
• Turn off "Laser In Use" warning sign
• Take off safety glasses

Beam Alignment

• Make sure all safety gear is on (glasses, lab coat, etc.)
• Start up laser and set to lowest wattage as possible (~1 mW)
• Use a piece of paper to follow the beam
• Place optics in appropriate place

24. Maintenance and Adjustments

• All Maintenance and adjustments should be done by a licensed professional
• Or under the supervision of a laboratory technician

Contact baser Laser Safety Officer, 74 AMDS/SGPB, at (937) 255-6815 for concerns or questions concerning this document.

Appendix D: Laser Equipment Operation Instructions

This appendix contains the simplified operation instructions for the laser equipment used in this thesis.

D.1 TEC 2000 Thermoelectric Temperature Controller Procedures

- Choose the desired temperature sensor on the switch marked "SENSOR" on the back of the temperature controller unit. The AD590 displays temperature in degrees Celsius; the 10-kΩ thermistor displays resistance in kΩ [use AD590].

- Connect the TEC2000-CAB shielded cable from the temperature controller to the DB9 male connection (labeled "TEC Driver") on the TCLDM9 mount.

- Turn on the TEC 2000 thermoelectric temperature controller unit.

- Set the current limit I_{LIM} to the desired value (< 2A) by adjusting the 20-turn potentiometer labeled "LIM I" [use 1.750 A].

- Set the desired control temperature by selecting T_{SET} on the display and adjusting the knob to the desired temperature [use 24.66 deg C].

- Enable the temperature controller by pressing the button labeled "ENABLE", and wait 10 minutes for the temperature sensor to stabilize.

D.2 LDC 500 Laser Diode Controller Procedures

- Review and comply with "Safe Operating Procedures."

- Review the specification sheet of the ML101J8 laser diode.

- Choose the cathode ground "CG" on the switch marked "LD" on the back of the driver controller unit. (The ML101J8 laser diode should have been inserted into the laser diode mount so that the cathode is grounded.)

- Connect the LDC500-CAB shielded cable from the diode controller to the DB9 female connection (labeled "LD Driver") on the TCLDM9 mount.

- Turn on the LDC 500 laser diode controller unit; wait 10 minutes for stabilization before enabling the unit.

- Set the current limit I_{LIM} to the desired value ($\leq$ 109 mA for the ML101J8) by adjusting the 20-turn potentiometer labeled “LIM I”.

- Ensure the LD driver current is zeroed by turning the LD driver current knob completely counter-clockwise.

- Set the LD controller unit to constant-current mode by pressing “I” in the section marked “MODE”.

- Select the driver current I_{LD} by pushing the down arrow.

- Ensure the door is secured, the “Laser In Use” warning sign is illuminated, safety glasses are donned, and a beam stop is in front of the laser.

- Enable the LD controller by pressing the button labeled “ENABLE”.

- Increase the driver current by slowly adjusting the driver current knob clockwise.

D.3 S20MM Silicon Power Meter Operation Procedures

- Establish the desired room conditions (brightness, temperature, etc.).

- Attach an appropriate neutral density filter to the power meter head. The ND=0.3 absorbs 50% of the transmitted light and is sufficient to reduce the 40 mW maximum power output from the ML101J8 laser diode to the 20 mW maximum power input of the S20MM power meter.

- Turn on the S20MM silicon power meter to the 20 mW setting.

- Turn on a digital multimeter and set to measure voltage (0-2 V range).

- Plug the banana connectors from the power meter to the voltage input of the DMM.

- Set the wavelength of the S20MM power meter by holding the λ button (wavelength) and pressing the up or down buttons. The DMM senses the wavelength setting and displays a corresponding voltage value. For the 660-nm ML101J8 laser diode, adjust the wavelength buttons until the DMM reads approximately “0.660 V DC,” which corresponds to 0.660 μm.

- Establish a baseline zero-point of the meter by turning the zero knob of the S20MM until the DMM reads approximately “0.0 mV DC.”

Appendix E: Microrobot Complete Initial Deflection Data

This appendix includes all the measured data from microrobot initial deflection. It also includes a description of each chip and compares every robot to the others. It complements the trends presented in Chapter 7. An L-edit® layout schematic and a photograph of each fabricated microrobot chip are included for clarity and comparative purposes. Each microrobot on the chip is numbered for reference. Also, the calculated mass and surface area values are included to compare each microrobot.

Figure E.1 illustrates a Zygo® IFM image of a microrobot, including the deflection profile. The 7.47179-µm initial deflection is measured along the white cursor. At least three samples of each microrobot were measured individually in this manner.

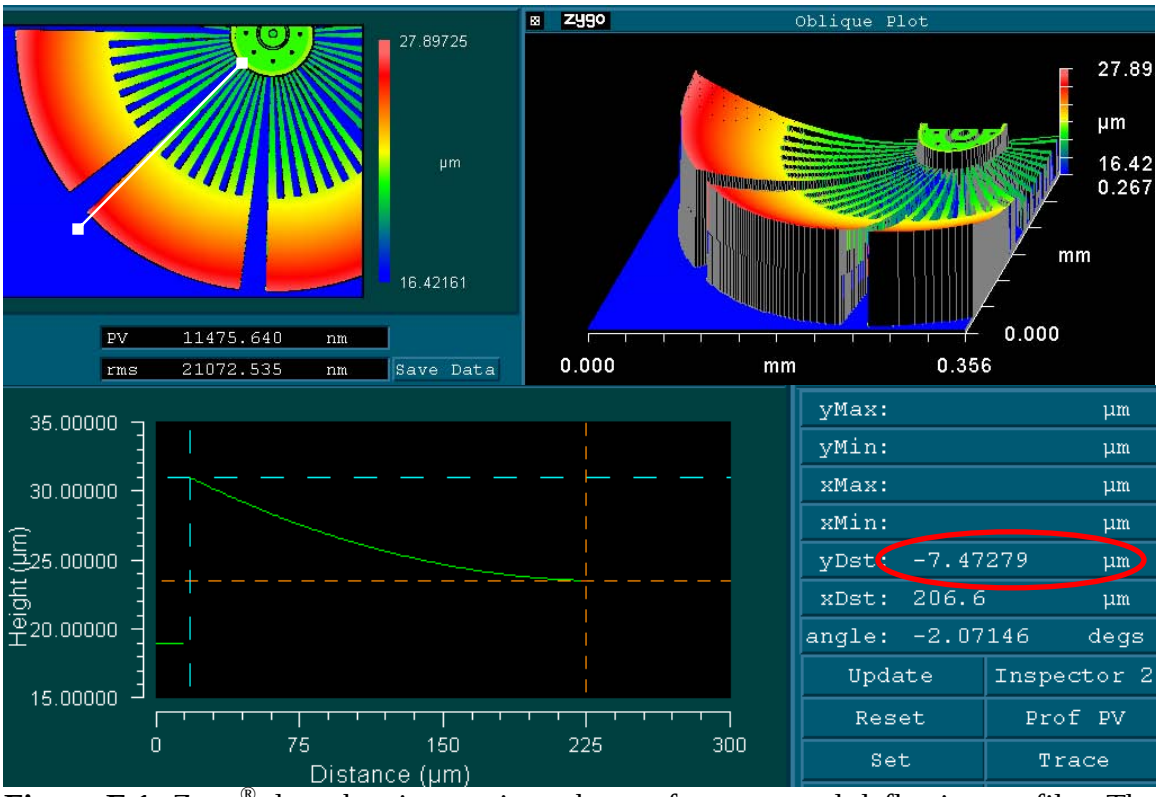


Figure E.1: Zygo® data showing a microrobot surface map and deflection profile. The initial deflection of this microrobot is 7.47279 µm at a 206.6-µm wing length.

E.1 Deflection in MUMPs® 66 Microrobots

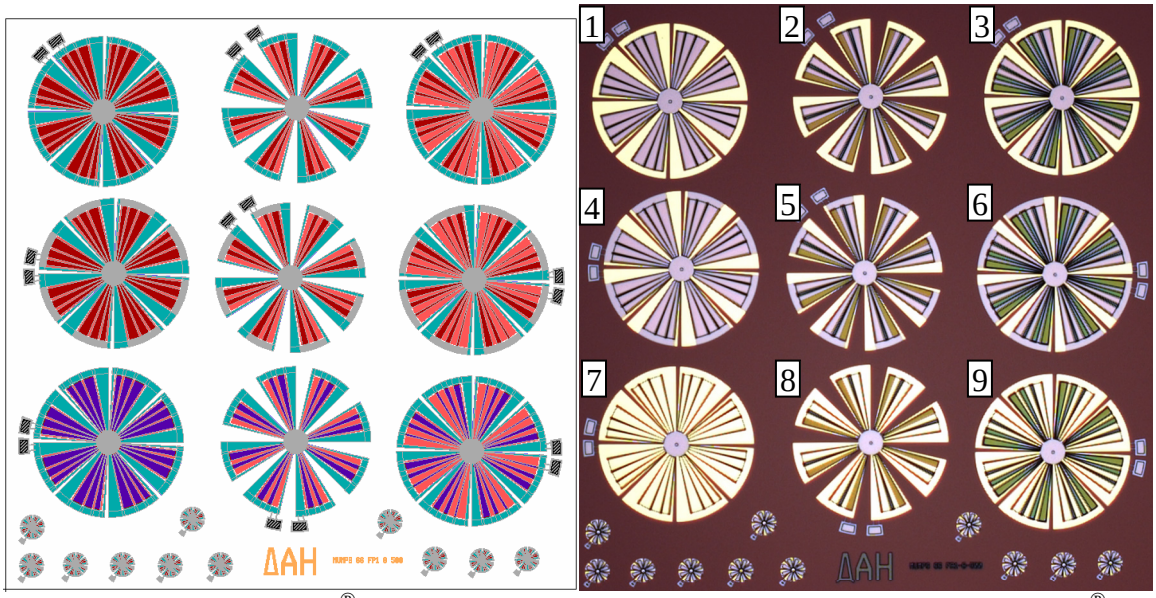


Figure E.2: (left) L-edit® design schematic and (right) photograph of MUMPs® 66 microrobots. The positions are numbered from 1–9 for reference.

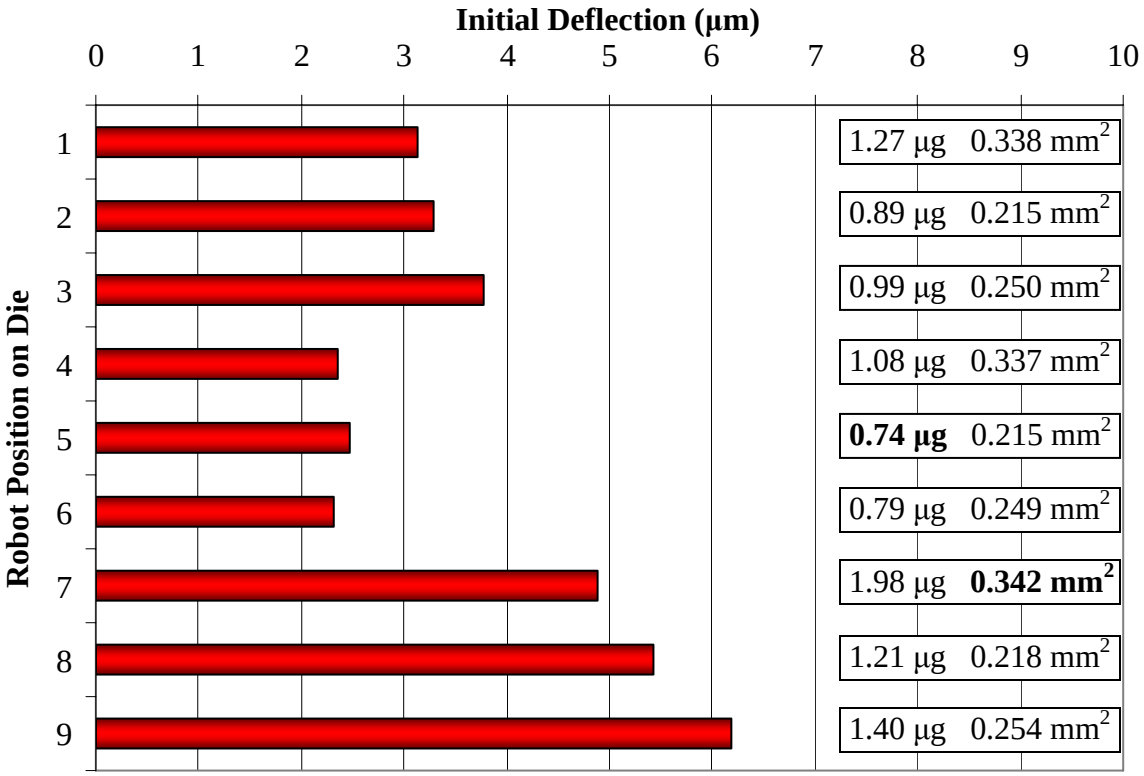


Figure E.3: Wing-tip deflection measurements of MUMPs® 66 microrobots. The positions correspond to the numbering scheme in Figure E.2. The calculated mass and surface area values of each microrobot are also listed. The minimum mass and the maximum surface area values are emboldened.

The three indicators of potential flight are initial deflection (or wing stroke distance), mass, and surface area (the surface area calculations include the top, bottom, and sides of each wing). The objective for successful flight is to maximize initial deflection and surface area while minimizing mass. A tradeoff between mass and surface area must be made since the two are directly proportional to each other: increasing surface area inevitably increases mass. The #9 microrobot shows the greatest initial deflection at 6.18 μm but the second most massive design. The #7 microrobot has the greatest surface area at 0.342 mm^2 but is the first most massive design. The #5 microrobot is the least massive at 0.74 μg but has the smallest surface area and third lowest deflection. Table E.1 shows the values and corresponding rankings for deflection (maximum), mass (minimum), and surface area (maximum).

Table E.1. Rankings of MUMPs® 66 microrobots in terms of deflection, mass, and area.

Position	Deflection (Rank)	Mass (Rank)	Surface Area (Rank)
1	3.12 μm (6^{th})	1.27 μg (7^{th})	0.338 mm^2 (2^{nd})
2	3.29 μm (5^{th})	0.89 μg (3^{rd})	0.215 mm^2 (8^{th})
3	3.78 μm (4^{th})	0.99 μg (4^{th})	0.250 mm^2 (5^{th})
4	2.36 μm (8^{th})	1.08 μg (5^{th})	0.337 mm^2 (3^{rd})
5	2.48 μm (7^{th})	**0.74 μg (1^{st})**	0.215 mm^2 (8^{th})
6	2.31 μm (9^{th})	0.79 μg (2^{nd})	0.249 mm^2 (6^{th})
7	4.88 μm (3^{rd})	1.98 μg (9^{th})	**0.342 mm^2 (1^{st})**
8	5.42 μm (2^{nd})	1.21 μg (6^{th})	0.218 mm^2 (7^{th})
9	**6.18 μm (1^{st})**	1.40 μg (8^{th})	0.254 mm^2 (4^{th})

An important trend is immediately evident in Figure E.3 and in Table E.1: the microrobots with the most gold show the greatest deflection. Thus, deflection is directly proportional to gold quantity:

$$\text{deflection} \propto \text{gold quantity}. \tag{7.1}$$

Microrobots 7, 8, and 9 have the most gold, followed by 1, 2, and 3, while 4, 5, and 6 have the least amount of gold. On the other hand, the highly deflecting gold microrobots are also the most massive. Thus, mass is directly proportional to gold quantity:

$$\text{mass} \propto \text{gold quantity}. \tag{7.2}$$

It is clear that a tradeoff must be made between deflection and mass. Both are proportional to gold quantity, and it is impossible to increase deflection without also increasing mass.

Something not clear from the measured deflection data is the relationship between microrobot gap spacing between each flexure and deflection. Also unclear is the relationship between flexure width and deflection. These parameters were varied in microrobot designs in later MUMPs® runs to determine which would yield the greatest deflection. Also, the poly1 spacer under each MUMPs® 66 microrobot was found to interfere with the robot movement. In all the subsequent runs, this spacer was made of poly0. Starting in run 68, the effect of the spacer on initial deflection was examined.

E.2 Deflection in MUMPs® 67 Microrobots

Two microrobot chips were fabricated in MUMPs® run 67: version 1 and version 2. The designs in version 1 are identical to those in run 66 except for two important differences: the poly0 layer is used as the spacer under each robot (see Figure E.4), and the center section has an additional poly1 layer to increase thickness for better laser energy absorption. In version 2, the spacing between each wing flexure was decreased in order to maximize surface area. Some four-wing butterfly-type designs are also included as well as electrically testable structures (see Figure E.5). The deflection results are given in the figures and tables below.

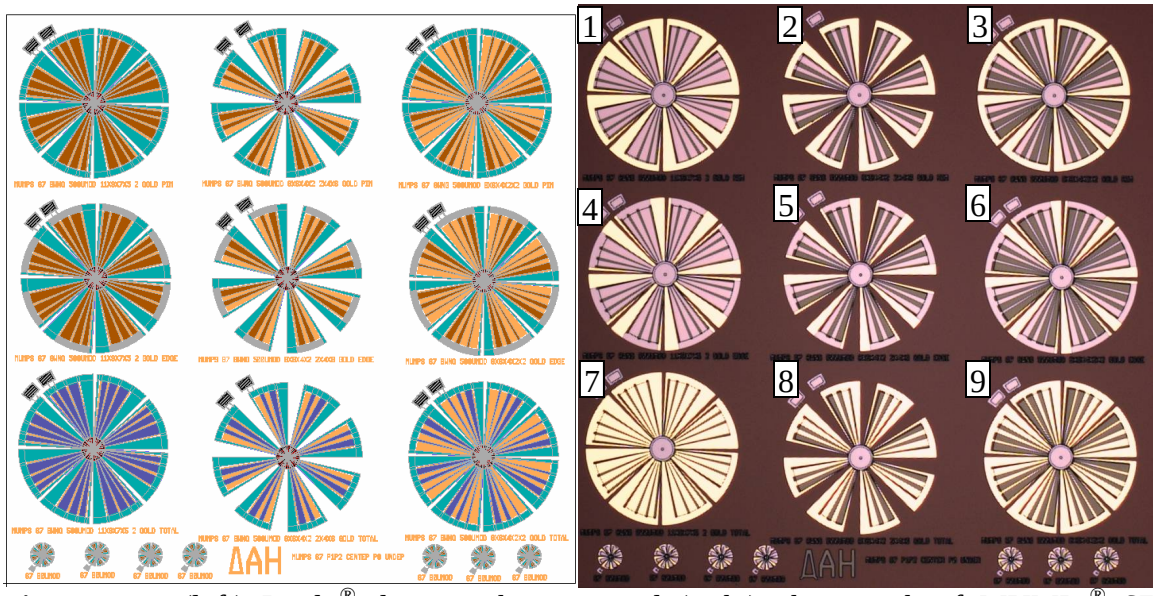


Figure E.4: (left) L-edit® design schematic and (right) photograph of MUMPs® 67 version 1 microrobots. The positions are numbered from 1–9 for reference. The designs are identical to those in Figure E.2 except that poly0 is used as the spacer material and poly1 is added to the center section for better laser energy absorption.

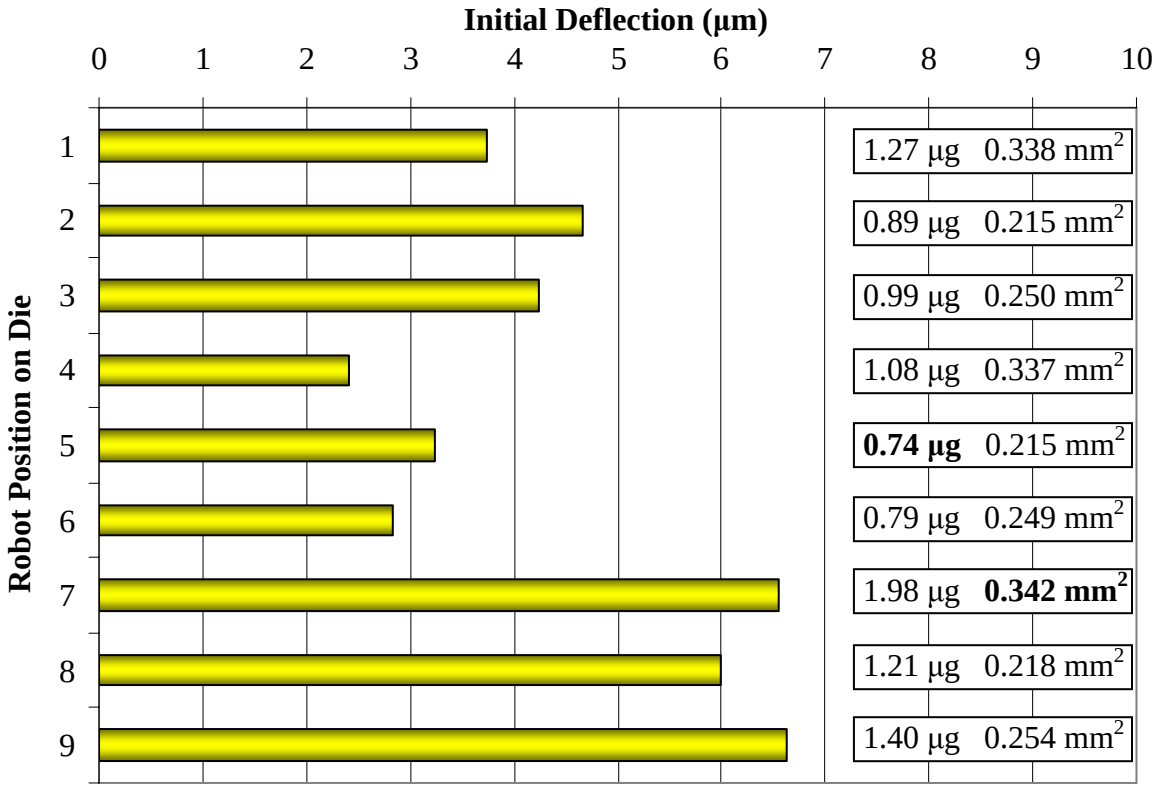


Figure E.5: Wing-tip deflection measurements of MUMPs® 67 version 1 microrobots. The calculated mass and surface area values of each microrobot are also listed. The minimum mass and the maximum surface area values are emboldened. The deflection is greater than that in MUMPs® 66 robots while the mass and surface area values are equal.

Table E.2. Rankings of MUMPs® 67 version 1 microrobots.

Position	Deflection (Rank)	Mass (Rank)	Surface Area (Rank)
1	3.73 μm (6^{th})	1.27 μg (7^{th})	0.338 mm^2 (2^{nd})
2	4.62 μm (4^{th})	0.89 μg (3^{rd})	0.215 mm^2 (8^{th})
3	4.25 μm (5^{th})	0.99 μg (4^{th})	0.250 mm^2 (5^{th})
4	2.40 μm (9^{th})	1.08 μg (5^{th})	0.337 mm^2 (3^{rd})
5	3.24 μm (7^{th})	**0.74 μg (1^{st})**	0.215 mm^2 (8^{th})
6	2.83 μm (8^{th})	0.79 μg (2^{nd})	0.249 mm^2 (6^{th})
7	6.55 μm (2^{nd})	1.98 μg (9^{th})	**0.342 mm^2 (1^{st})**
8	5.99 μm (3^{rd})	1.21 μg (6^{th})	0.218 mm^2 (7^{th})
9	**6.63 μm (1^{st})**	1.40 μg (8^{th})	0.254 mm^2 (4^{th})

Immediately evident in Figure E.5 and in Table E.2 is the deflection values for each microrobot in run 67 are greater than those for run 66. The only difference between the two designs is the spacer layer. It is clear that a thinner spacer increases deflection. The effect of removing the spacer entirely is examined in later runs. Though no cantilevers were fabricated in this run, it is important to compare the reported residual stress values in runs 66 and 67. The stress in run 67 is lower than that in run 66, which would result in lower deflection values. However, the deflection in 67 is greater than that in 66, despite the lower stress. It is clear that improved device design can increase initial deflection.

The deflection results from run 67 reinforce the gold-deflection trend: the microrobots with the most amount of gold exhibit the greatest deflection. Some deflection anomalies are evident in the version 1 chip: position #7 is higher than #8, which is opposite from run 66; #2 is greater than #3 and #5 is greater than # 6, which are also opposite from run 66. Due to these anomalies, the effects of flexure spacing and width remain unclear.

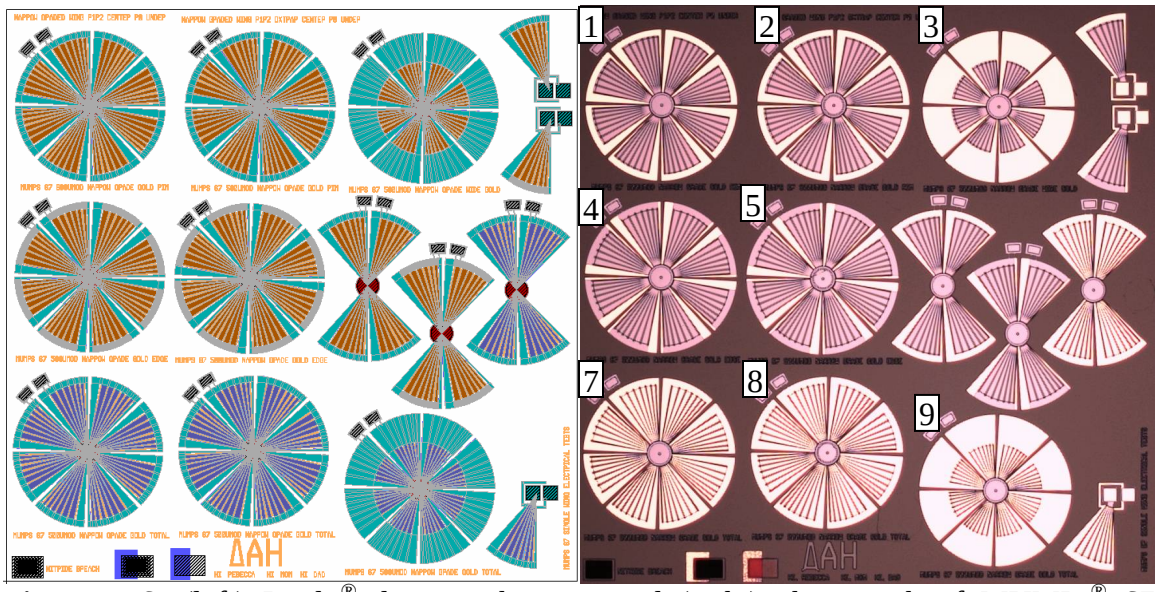


Figure E.6: (left) L-edit® design schematic and (right) photograph of MUMPs® 67 version 2 microrobots. The positions are numbered from 1–9, but the four-wing robots in position 6 are not included since their wing patterns are identical to those in positions 1, 4, and 7. The robots in the middle column (2, 5, and 8) have oxide trapped in the center section. The objective in this design run is to maximize surface area.

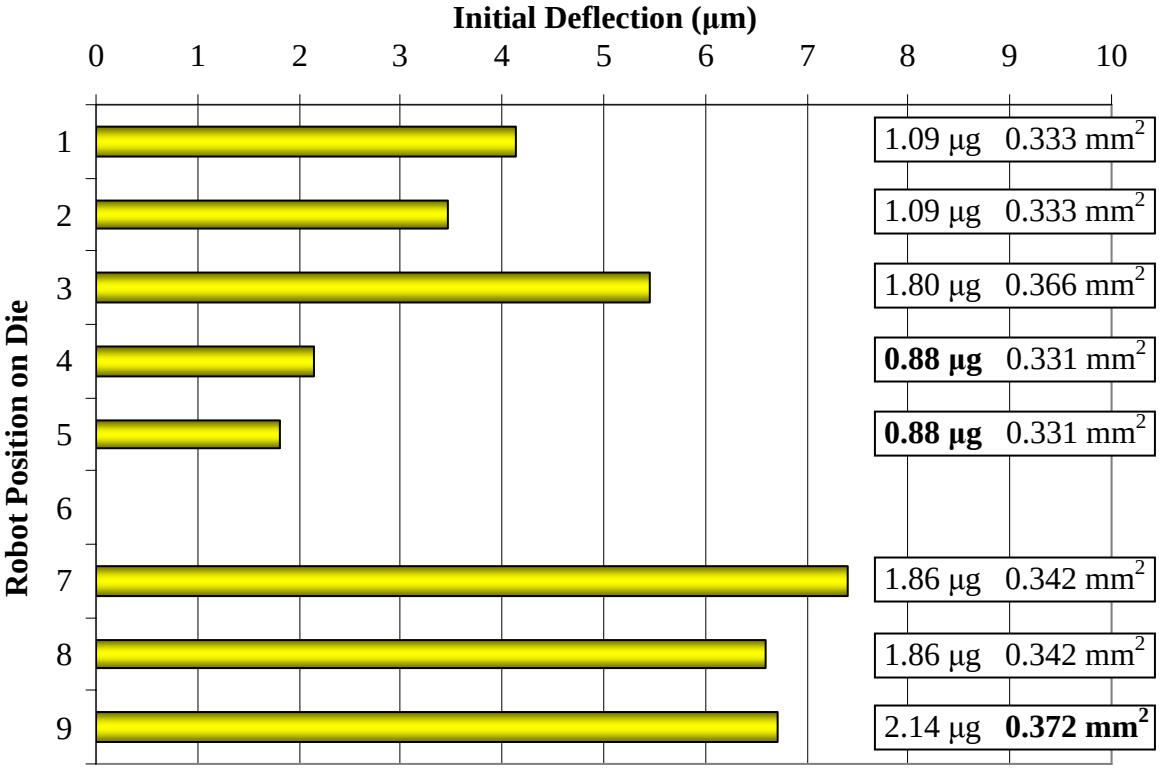


Figure E.7: Wing-tip deflection measurements of MUMPs® 67 version 2 microrobots. The calculated mass and surface area values of each microrobot are also listed. The minimum mass and the maximum surface area values are emboldened.

Table E.3. Rankings of MUMPs® 67 version 2 microrobots.

Position	Deflection (Rank)	Mass (Rank)	Surface Area (Rank)
1	4.14 μm (5^{th})	1.09 μg (3^{rd})	0.333 mm^2 (5^{th})
2	3.47 μm (6^{th})	1.09 μg (3^{rd})	0.333 mm^2 (5^{th})
3	5.46 μm (4^{th})	1.80 μg (5^{th})	0.366 mm^2 (2^{nd})
4	2.14 μm (7^{th})	**0.88 μg (1^{st})**	0.331 mm^2 (7^{th})
5	1.81 μm (8^{th})	**0.88 μg (1^{st})**	0.331 mm^2 (7^{th})
6	---	---	---
7	**7.39 μm (1^{st})**	1.86 μg (6^{th})	0.342 mm^2 (3^{rd})
8	5.59 μm (3^{rd})	1.86 μg (6^{th})	0.342 mm^2 (3^{rd})
9	6.72 μm (2^{nd})	2.14 μg (8^{th})	**0.372 mm^2 (1^{st})**

The deflection results shown, once again, that the microrobots with the most amount of gold exhibit the greatest deflection. Another trend evident in comparing the first column (positions 1, 4, and 7) with the second column (positions 2, 5, and 8) is the deflection in the second column is lower. The microrobots in the second column have oxide trapped in the center section; the purpose of this is to increase thickness for more laser energy absorption. However, the oxide proves to inhibit deflection, so this design is abandoned in future fabrication runs.

The microrobots in positions 3 and 9 have shorter flexures and gold longer rims than adjacent robots (1, 2 and 7, 8). With more gold, the deflection of these robots should be greater than those in 1, 2 and 7, 8. While this is true for the #3 robot, the #9 robot shows less deflection. This apparent inconsistency is evaluated in later fabrication runs. It is important to note that the #7 microrobot has the greatest deflection compared to the robots in this chip as well as in the two previous chips.

E.3 Deflection in MUMPs® 68 Microrobots

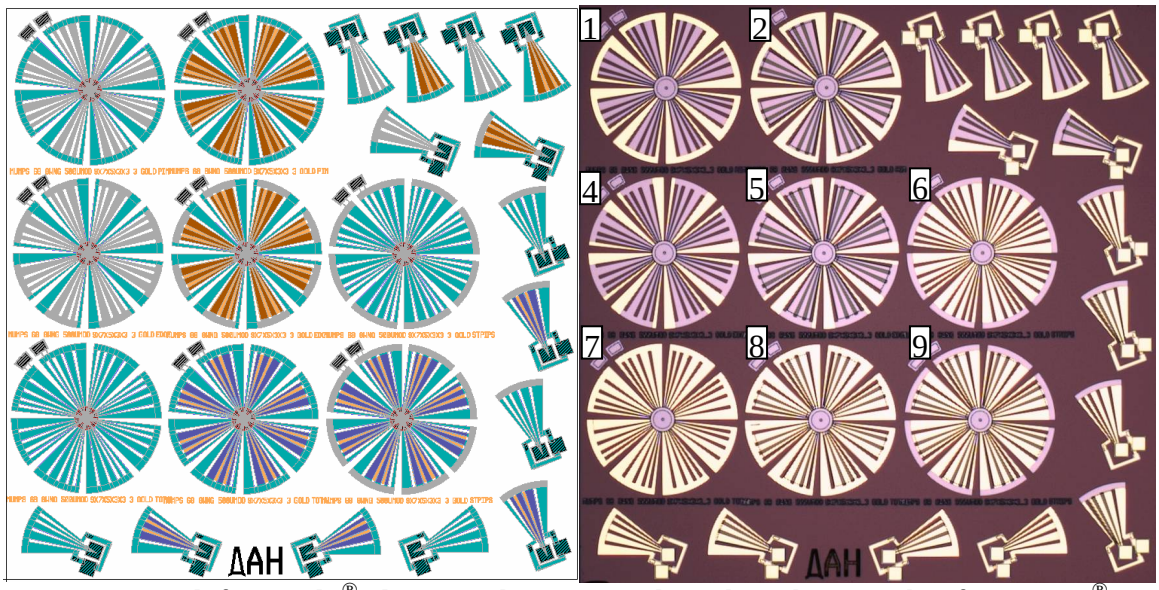


Figure E.8: (left) L-edit® design schematic and (right) photograph of MUMPs® 68 version 1 microrobots. The positions are numbered from 1–9 (position 3 not included). The poly2 wing patterns in each of the robots in this chip are the same, but the gold patterns vary. Also, half the robots have a poly0 spacer under them and half do not.

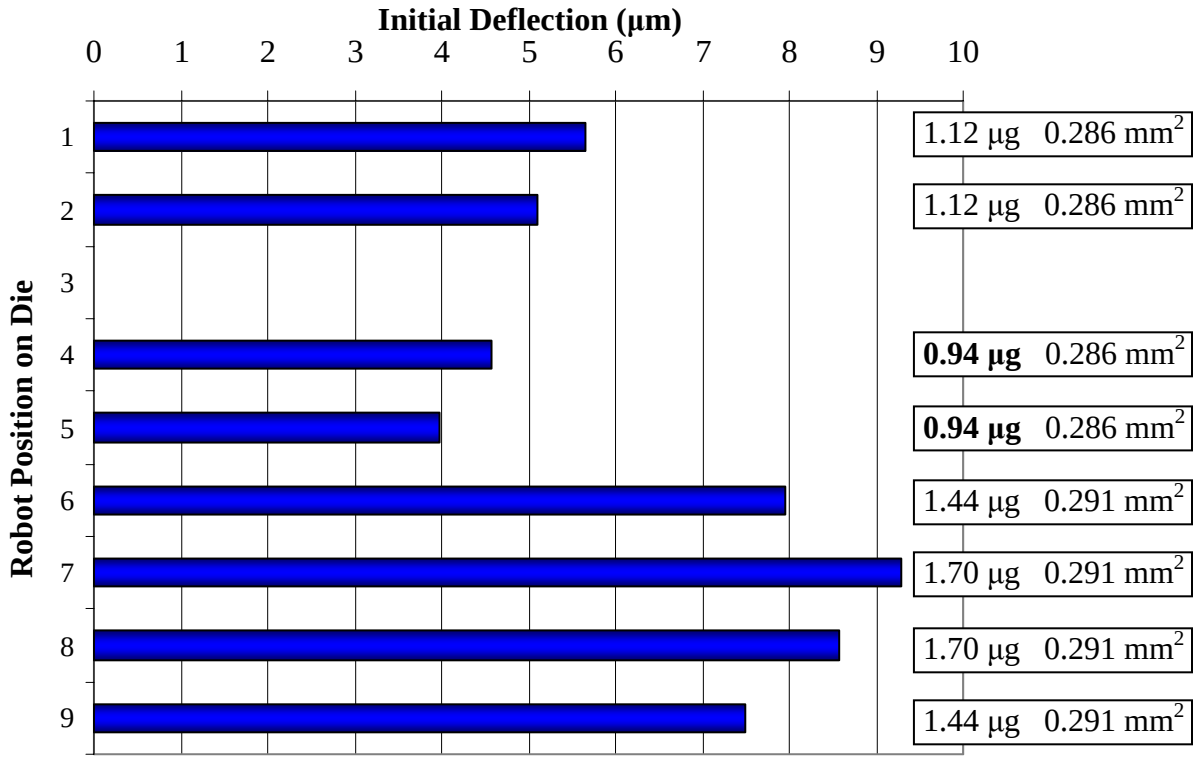


Figure E.9: Wing-tip deflection measurements of MUMPs® 68 version 1 microrobots. The calculated mass and surface area values of each microrobot are also listed. The minimum mass values are emboldened; all the surface area values are within the same range of 0.286–0.291 mm^2.

Table E.4. Rankings of MUMPs® 68 version 1 microrobots.

Position	Deflection (Rank)	Mass (Rank)	Surface Area (Rank)
1	5.66 μm (5^{th})	1.12 μg (3^{rd})	0.286 mm^2 (5^{th})
2	5.09 μm (6^{th})	1.12 μg (3^{rd})	0.286 mm^2 (5^{th})
3	---	---	---
4	4.57 μm (7^{th})	**0.94 μg (1^{st})**	0.286 mm^2 (5^{th})
5	3.97 μm (8^{th})	**0.94 μg (1^{st})**	0.286 mm^2 (5^{th})
6	7.97 μm (3^{rd})	1.44 μg (5^{th})	**0.291 mm^2 (1^{st})**
7	**9.29 μm (1^{st})**	1.70 μg (7^{th})	**0.291 mm^2 (1^{st})**
8	8.59 μm (2^{nd})	1.70 μg (7^{th})	**0.291 mm^2 (1^{st})**
9	7.50 μm (4^{th})	1.44 μg (5^{th})	**0.291 mm^2 (1^{st})**

The #7 microrobot in this run exhibits more deflection than any other microrobot for its size. The other microrobots on this version 1 chip exhibit relatively more deflection as well. Each robot wing pattern in this chip is the same: minimal spacing between each flexure, thus increasing flexure width. A constant wing pattern facilitates comparing the effects of other elements, such as gold patterns and the poly0 spacer.

The deflection data shows that the effect of the poly0 spacer is clear: the microrobots without the spacer have greater deflection than those with the spacer. This is consistently true for the 1-2, 4-5, 7-8, and 6-9 position pairs. The benefit of the poly0 spacer is the slight cupping shape under the center of the wings. It is supposed that this shape would improve the lift capability of the microrobots. The tradeoff, though, is less deflection.

The amount of surface area in these microrobots is about the median amount of the previous robots—some have more and some have less. The relationship between surface area and deflection is unclear. Comparing flexure width with deflection could yield a clearer relationship.

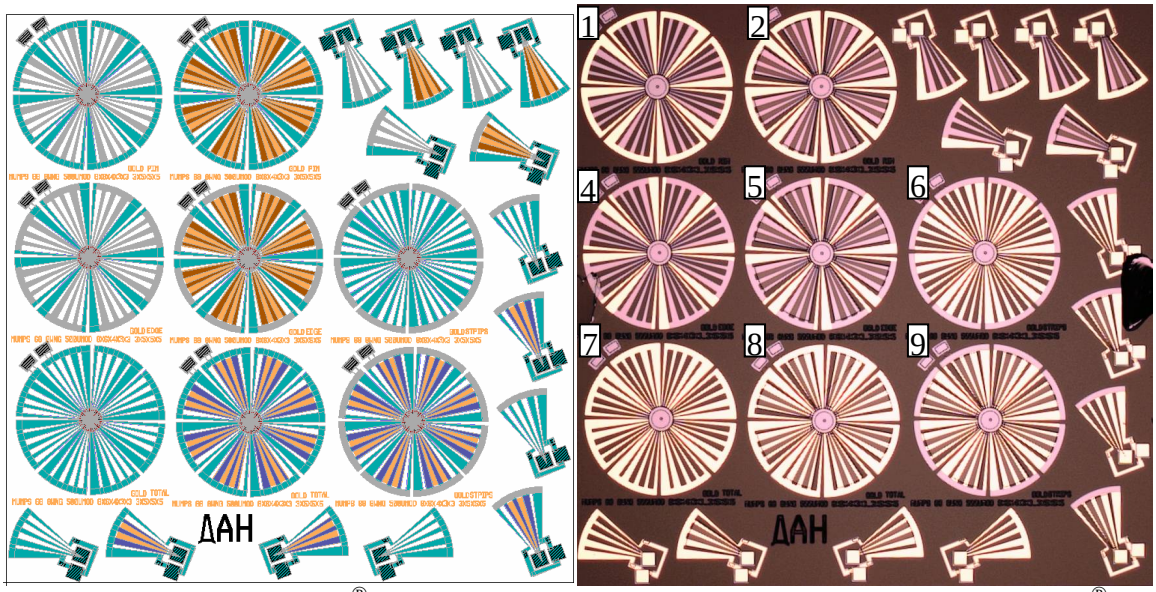


Figure E.10: (left) L-edit® design schematic and (right) photograph of MUMPs® 68 version 2 microrobots. The positions are numbered from 1–9 (position 3 not included). The poly2 wing patterns in each of the robots in this chip are the same, but the gold patterns vary. Half the robots have a poly0 spacer under them and half do not.

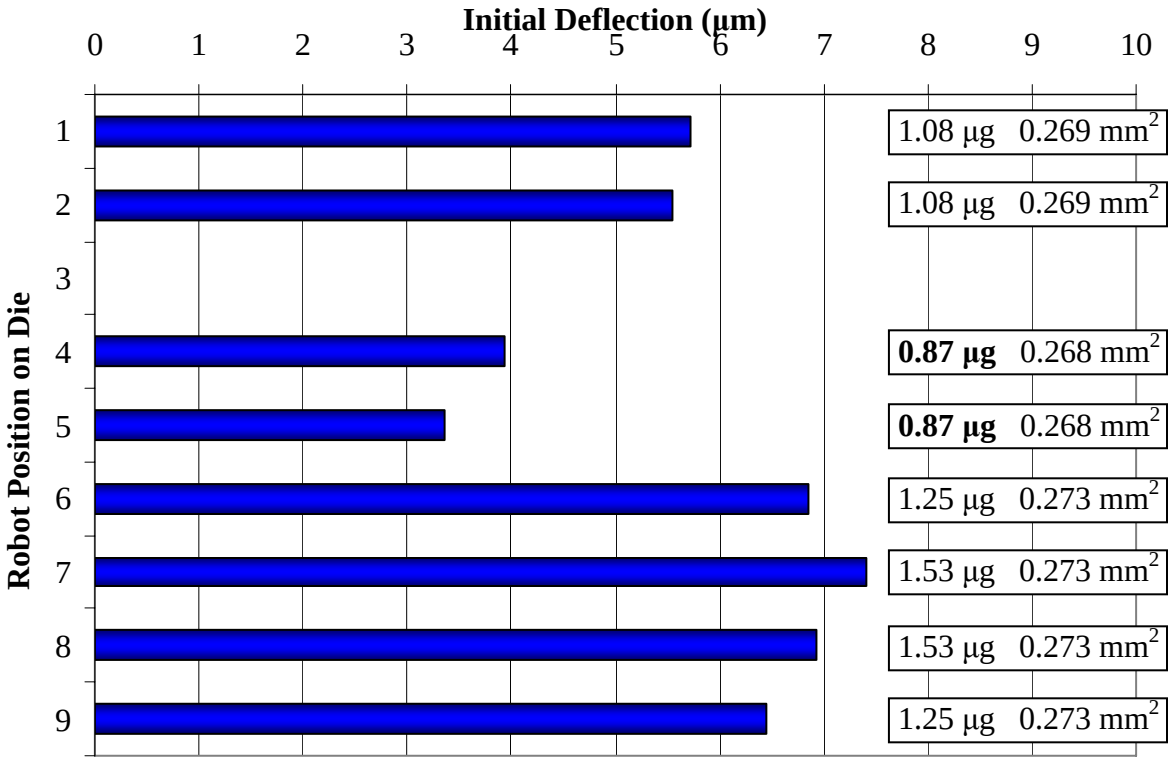


Figure E.11: Wing-tip deflection measurements of MUMPs® 68 version 2 microrobots. The calculated mass and surface area values of each microrobot are also listed. The minimum mass values are emboldened; all the surface area values are within the same range of 0.269–0.273 mm^2.

Table E.5. Rankings of MUMPs® 68 version 2 microrobots.

Position	Deflection (Rank)	Mass (Rank)	Surface Area (Rank)
1	5.72 μm (5^{th})	1.08 μg (3^{rd})	0.269 mm^2 (5^{th})
2	5.55 μm (6^{th})	1.08 μg (3^{rd})	0.269 mm^2 (5^{th})
3	---	---	---
4	3.93 μm (7^{th})	**0.87 μg (1^{st})**	0.268 mm^2 (7^{th})
5	3.37 μm (8^{th})	**0.87 μg (1^{st})**	0.268 mm^2 (7^{th})
6	6.85 μm (3^{rd})	1.25 μg (5^{th})	**0.273 mm^2 (1^{st})**
7	**7.41 μm (1^{st})**	1.53 μg (7^{th})	**0.273 mm^2 (1^{st})**
8	6.94 μm (2^{nd})	1.53 μg (7^{th})	**0.273 mm^2 (1^{st})**
9	6.44 μm (4^{th})	1.25 μg (5^{th})	**0.273 mm^2 (1^{st})**

Each robot wing pattern in this version 2 chip is the same: relatively wider spacing between each flexure and relatively narrow flexures. The wing pattern is the only difference between this version 2 chip and the version 1 chip; all the gold and poly0 variations are the same. The deflection rankings in version 2 microrobots are identical to those of version 1 microrobots, but the amount of deflection in the version 2 chip is noticeably less. In addition, the surface area and mass are less than in the version 1 chip.

The direct comparison between the two microrobot chips shows that relatively wider wing flexures (version 1) yield greater deflection than narrow flexures (version 2). Identical to the trend in the version 1 microrobots, the trend between the poly0 spacer and deflection in the version 2 robots is clear: the microrobots without the spacer have greater deflection than those with the spacer.

Another important point to emphasize is the residual stress values and the cantilever deflection results for MUMPs® 68 are lower than those for MUMPs® 66. However, the microrobot deflection is higher in MUMPs® 68, which is indicative of improved designs.

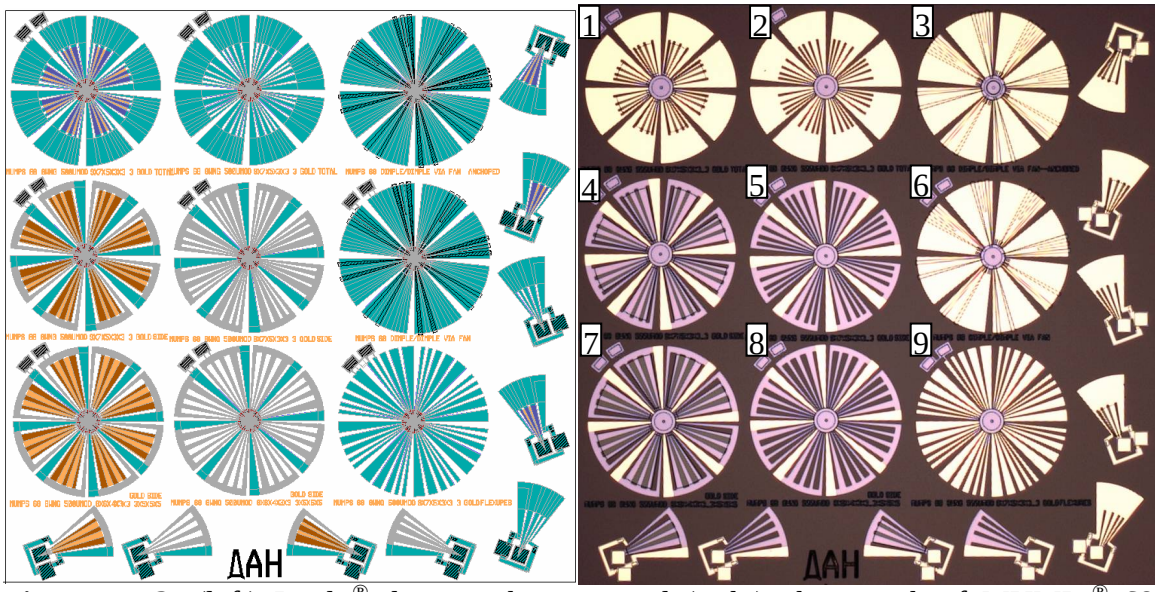


Figure E.12: (left) L-edit® design schematic and (right) photograph of MUMPs® 68 version 3 microrobots. The numbering follows from previous chips. The robots in the first column have the poly0 spacer and those in the second column do not. Robots 4 and 5 are based on the MUMPs® 68 version 1 chip; 7 and 8 are based on the version 2 chip.

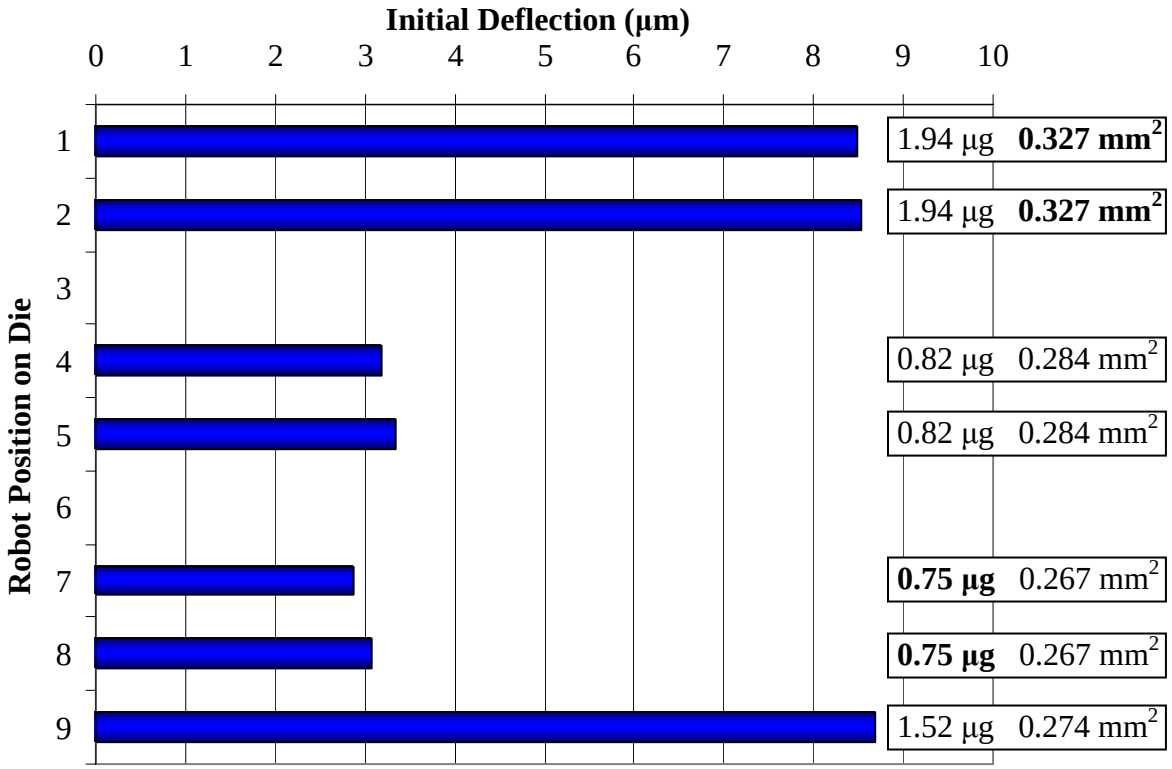


Figure E.13: Wing-tip deflection measurements of MUMPs® 68 version 3 microrobots. The calculated mass and surface area values of each microrobot are also listed. The minimum mass and maximum surface area values are emboldened. No deflection data is available for robots in positions 3 and 6.

Table E.6. Rankings of MUMPs® 68 version 3 microrobots.

Position	Deflection (Rank)	Mass (Rank)	Surface Area (Rank)
1	8.48 μm (3rd)	1.94 μg (6th)	**0.327 mm^2 (1st)**
2	8.54 μm (2nd)	1.94 μg (6th)	**0.327 mm^2 (1st)**
3	---	---	---
4	3.18 μm (5th)	0.82 μg (3rd)	0.284 mm^2 (3rd)
5	3.34 μm (4th)	0.82 μg (3rd)	0.284 mm^2 (3rd)
6	---	---	---
7	2.88 μm (7th)	**0.75 μg (1st)**	0.267 mm^2 (6th)
8	3.08 μm (6th)	**0.75 μg (1st)**	0.267 mm^2 (6th)
9	**8.69 μm (1st)**	1.52 μg (5th)	0.274 mm^2 (5th)

The microrobots in the first column (1, 4, and 7) have a poly0 spacer while those in the second column (2, 5, and 8) do not. It is demonstrated once again that the poly0 spacer inhibits initial deflection. Two microrobots of particular interest in this version 3 chip are those in positions 1 and 2, which are similar to the position 9 microrobot designed in MUMPs® 67, version 2 (see Figure E.6). The MUMPs® 67 robot had 6.72 μm of deflection while the 1 and 2 robots in this version 3 chip had 8.48 and 8.54 μm of deflection. The residual stress for run 68 is less than that for run 67, which suggests that the improved deflection is design-related.

The microrobots in positions 4 and 5 have the same wing pattern as the MUMPs® 68 version 1 chip; positions 7 and 8 have version 2 pattern. The results show that microrobots in 4 and 5 have greater deflection than those in 7 and 8, which is consistent with the results from the version 1 and version 2 chips: the wing pattern in version 1 yields greater deflection. It appears that wider flexures yield greater deflection; they also have more surface area. This trend is further investigated in MUMPs® 69.

E.4 Deflection in MUMPs® 69 Microrobots

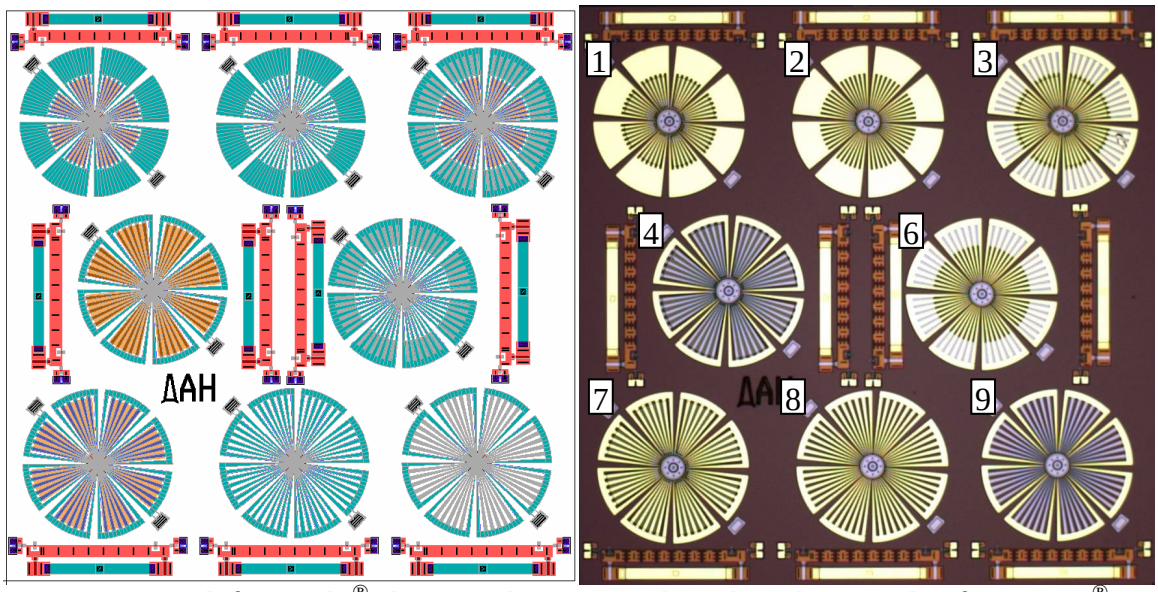


Figure E.14: (left) L-edit® design schematic and (right) photograph of MUMPs® 69 version 1 microrobots. The positions are numbered from 1–9 for reference (5 is not included). All the microrobot flexures in this chip are narrow. Half the microrobots have poly0 spacers and half do not. The flip-up rulers are also shown.

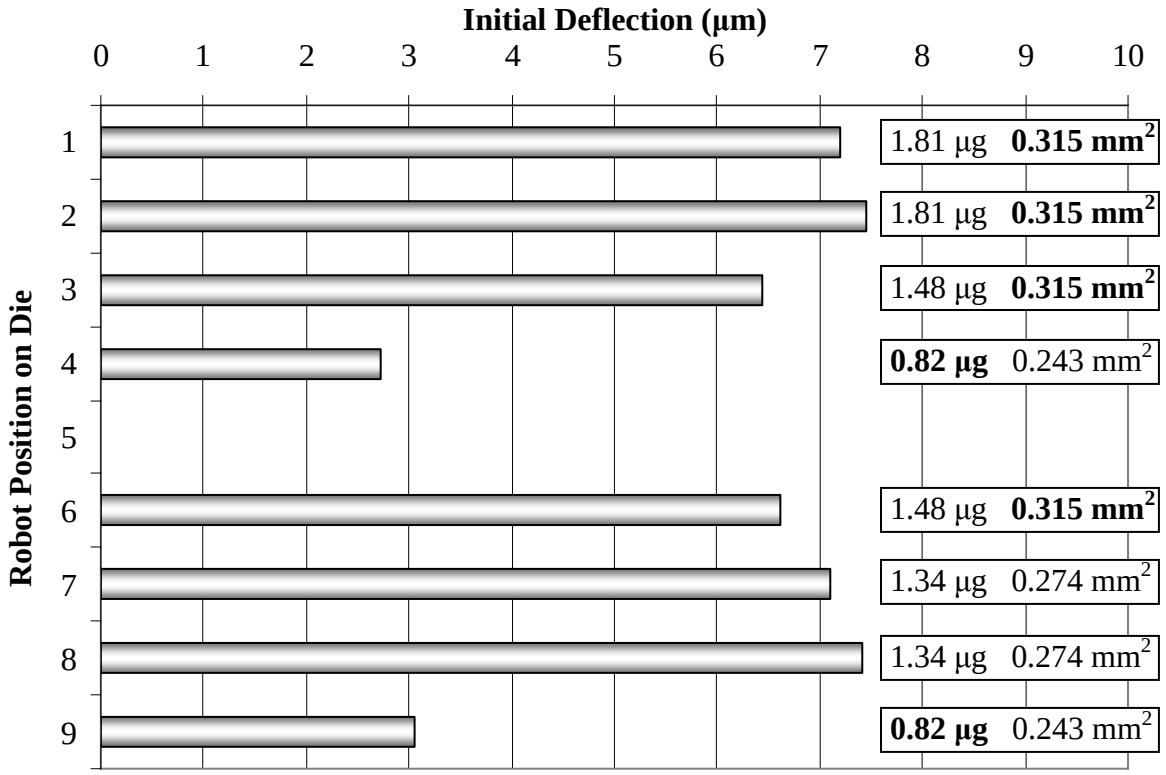


Figure E.15: Wing-tip deflection measurements of MUMPs® 69 version 1 microrobots. The calculated mass and surface area values of each microrobot are also listed. The minimum mass and maximum surface area values are emboldened.

Table E.7. Rankings of MUMPs® 69 version 1 microrobots.

Position	Deflection (Rank)	Mass (Rank)	Surface Area (Rank)
1	7.20 μm (4^{th})	1.81 μg (7^{th})	**0.315 mm^2 (1^{st})**
2	**7.45 μm (1^{st})**	1.81 μg (7^{th})	**0.315 mm^2 (1^{st})**
3	6.43 μm (6^{th})	1.48 μg (5^{th})	**0.315 mm^2 (1^{st})**
4	2.72 μm (8^{th})	**0.82 μg (1^{st})**	0.243 mm^2 (7^{th})
5	---	---	---
6	6.62 μm (5^{th})	1.48 μg (5^{th})	**0.315 mm^2 (1^{st})**
7	7.09 μm (3^{rd})	1.34 μg (3^{rd})	0.274 mm^2 (5^{th})
8	7.43 μm (2^{nd})	1.34 μg (3^{rd})	0.274 mm^2 (5^{th})
9	3.06 μm (7^{th})	**0.82 μg (1^{st})**	0.243 mm^2 (7^{th})

The 1-2, 3-6, 7-8, and 4-9 microrobot pairs show consistent results: those robots with the poly0 show less deflection. The microrobots in positions 1 and 2 have almost one micron less deflection than those in position 1 and 2 from MUMPs® 68 version 3. The main difference between the two runs is the width of the flexures: run 69 robots have more narrow flexures than the run 68 robots.

The robots in positions 7 and 8 have about the same amount of deflection as those in positions 8 and 7 from the narrow-flexured robots from run 68 version 2; but the wide-flexured robots from run 68 version 1 have more than a micron greater deflection than those in run 69. This indicates that the microrobots with wide flexures consistently exhibit the greatest deflection.

The residual stress in MUMPs® 69 is slightly less than the value for 68, which results in slightly less deflection. Even the 199-μm cantilevers show about 0.3 μm less deflection in run 69 compared to run 68. But the measured difference in the robots is more than a micron, which suggests that difference is design-dependent. It can be

concluded that the robots with narrow flexures have less deflection than those with wider flexures.

The size of every microrobot fabricated to this point has been 500-µm in diameter. For the first time in MUMPs® 69 were 990-µm-diameter microrobots fabricated, which are illustrated in Figure E.16. These two-wing designs mimic many small flying insects in that they, too, have only two wings.

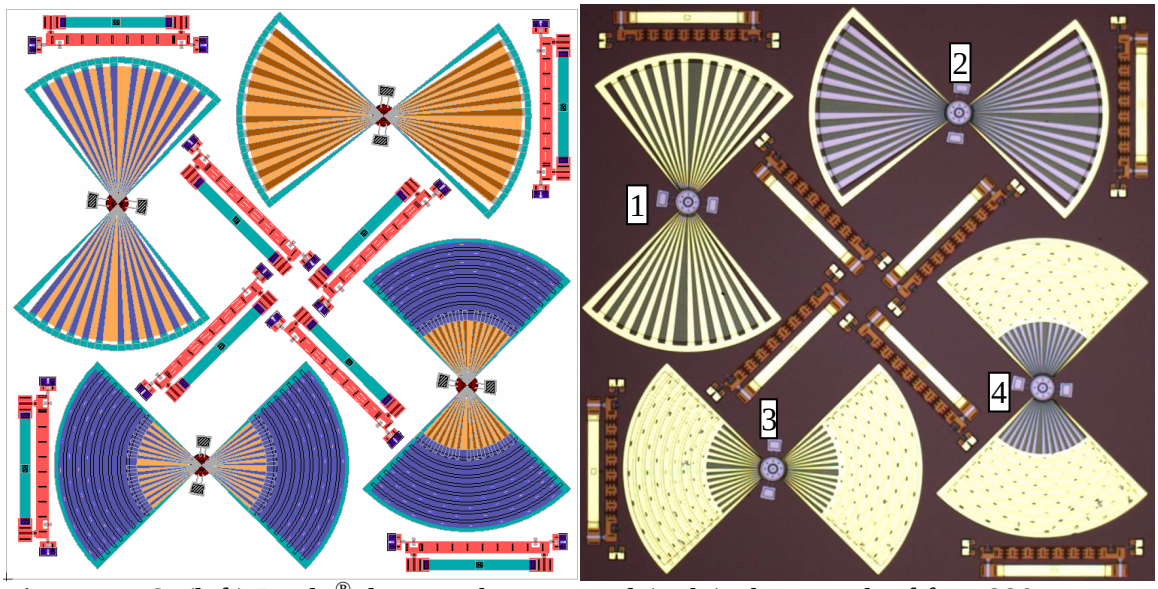


Figure E.16: (left) L-edit® design schematic and (right) photograph of four 990-µm two-wing microrobots from MUMPs® 69. The microrobot positions are numbered from 1–4 for reference. The flip-up rulers are also shown.

Table E.8. Deflection, mass, and surface area values for 990-µm microrobots from MUMPs® 69. A 500-µm microrobot similar to the design in position 3 is also included for comparison. The microrobot in position 3 has the greatest deflection and area.

Position	Initial Deflection {µm}	Mass {µg}	Surface Area {mm^2}
1	---	2.48	0.414
2	---	1.15	0.409
3	**30.9**	4.45	**0.709**
4	28.4	4.18	0.707
Run 69, 500-µm, pos. 1	**7.20**	1.81	**0.315**

Compared to the 500-µm robots, these 990-µm robots exhibit tremendous initial deflection. They follow the same trend as before: those with more gold have more deflection. Unfortunately, the largest-deflecting robots also have the most mass. In order

to make an even comparison with the MUMPs® 69 500-μm robot in position 1, the 990-μm position 3 robot has: 4 times the deflection (30.9 μm vs. 7.2 μm), only 2.5 times the mass (4.45 μg vs. 1.81 μg), and almost twice the surface area (0.709 mm^2 vs. 0.315 mm^2). To make an even comparison, the 500-μm robot must have half the number of wings; then the two designs would be more similar. This would reduce the mass and surface area by half, and the comparison would be: 4 times the deflection, 5 times the mass (4.45 μg vs. 0.905 μg), and 4.5 times the surface area (0.709 mm^2 vs. 0.1575 mm^2).

It is clear from these results that the 990-μm microrobots have advantages over the smaller microrobots in terms of deflection and surface area; however, the increased mass is a disadvantage.

Appendix F: Challenges in Measuring Power-Deflection in Microwings

As described in Chapter 6, the power from the laser diode is readily measurable with a standard optical power meter. The power lost at each optical interface is also readily obtainable with the same meter. However, the power that is absorbed—vice the power reflected or transmitted—by the silicon device can only be calculated. Measuring reflected and transmitted losses is very impractical in this setup. In addition, the fraction of that power which is converted to heat cannot be measured—only estimated. It is obvious, then, that there exists some degree of uncertainty in the amount of power that contributes to the device deflection.

To determine this degree of uncertainty, it is necessary to compare the optically induced deflection with an accurate power source (thermal or electrical). Electrically actuated test structures with the same configuration—shape and composition—as the optically testable robot wings were designed and fabricated to provide this desired benchmark. In theory, the expansion which occurs due to Joule heating is equivalent to the expansion which occurs due to optical heating. That is, the energy causing the same amount of expansion should be equal in both paradigms. Electrically actuated test structures would provide an accurate comparison.

It is impossible, however, to provide an accurate comparison between optically testable wings and electrically testable structures for two reasons. First, the structures are mounted to the substrate and a great deal of heat is conducted from the devices. The result of this is more power required for deflection. Second, the gold layer in the microrobot wings conducts the current away from the polysilicon layer—the layer in

which the necessary Joule heating occurs. Due to the higher electrical conductivity of gold, very little current will ever flow through the polysilicon layer, which means electrically testable wings made of gold will not deflect. It seems that the only way to cause deflection in electrically testable structures is to remove the gold, but this dramatically changes the device performance due to the dominant role of gold in deflection.

The electrically testable structures should not be completely discarded, however, since some of them were designed with very little gold, which correspond to identical robot wings. It is possible, then, to compare optically testable wings and electrically testable structures only in the robots without much gold. This is not the ideal scenario because the robots of greatest interests are the ones with the greatest deflection—the all-gold robots.

Another possible method to compare optically induced deflection with deflection from a known power source is thermally inducing deflection via a heated probe tip. In theory, a simple variable-temperature soldering iron could provide heat to the wings, which would induce deflection. There are many challenges to this testing paradigm.

First, the electrically testable structures cannot be used since most of the thermal energy will conduct through the anchored probe pads to the substrate instead of conducting through the wings. There would be a fraction of thermal energy that conducts through the wings, which would cause deflection, but this amount of energy is unknown. This uncertainty defeats the purpose of having this benchmark. Such a test would not be entirely useless because it would allow comparison among the various test structures. It

would determine which wings yield the greatest deflection given the same probe temperature. It would not, however, give a power-deflection relationship as desired.

Second, the releasable robots themselves cannot be heated easily with a probe because they are suspended in the air. In order to make contact, the probe would probably force the robot onto the substrate, causing the same problem with thermal conduction to the substrate. Some sort of anchored insulating layer could reduce this conduction if it could be applied to the underside of the robot or to a flat substrate. This is not ideal as there would still be some conduction losses through the insulating material. Third, assuming that the robot structures could be thermally isolated so that conduction losses are minimal, applying the soldering iron to a probe tip is a tricky job. The soldering iron would necessarily be securely mounted so as not to interfere with the probe movement and not to exceed the melting point of the plastic parts on the probe.

Vita

Daniel Denninghoff was born in Battle Creek, Michigan in 1979 and was raised with his seven siblings in Paris, Kentucky. After graduating from Bourbon County High in 1998, Daniel entered the United States Air Force Academy as a member of the Class of 2002. He earned a position on the Academy Wings of Blue Parachute Team as a cadet freefall instructor. He resigned from the Academy in 2000 in order to serve a two-year mission in Moscow, Russia for the Church of Jesus Christ of Latter-day Saints. In 2002, Daniel was re-accepted into the Academy as a member of the Class of 2004. He was commissioned on 2 June 2004 as a distinguished graduate, with a Bachelor of Science Degree in Electrical Engineering. He and his wife were married in Los Angeles shortly thereafter. Daniel entered the Air Force Institute of Technology in August 2004 through the direct accession program and completed the Microelectronics and MEMS sequences. Following graduation from AFIT he is assigned to work as a developmental engineer at the Air Force Research Laboratory Sensors Directorate.

REPORT DOCUMENTATION PAGE

Form Approved
OMB No. 074-0188

The public reporting burden for this collection of information is estimated to average 1 hour per response, including the time for reviewing instructions, searching existing data sources, gathering and maintaining the data needed, and completing and reviewing the collection of information. Send comments regarding this burden estimate or any other aspect of the collection of information, including suggestions for reducing this burden to Department of Defense, Washington Headquarters Services, Directorate for Information Operations and Reports (0704-0188), 1215 Jefferson Davis Highway, Suite 1204, Arlington, VA 22202-4302. Respondents should be aware that notwithstanding any other provision of law, no person shall be subject to an penalty for failing to comply with a collection of information if it does not display a currently valid OMB control number.
PLEASE DO NOT RETURN YOUR FORM TO THE ABOVE ADDRESS.

1. REPORT DATE *(DD-MM-YYYY)*	**2. REPORT TYPE**	**3. DATES COVERED** *(From – To)*
23-03-2006	**Master's Thesis**	Aug 2004 – Mar 2006

4. TITLE AND SUBTITLE

Power-Scavenging MEMS Robots

5a. CONTRACT NUMBER

5b. GRANT NUMBER

5c. PROGRAM ELEMENT NUMBER

6. AUTHOR(S)

Denninghoff, Daniel, J., Second Lieutenant, USAF

5d. PROJECT NUMBER
QFY76210422005

5e. TASK NUMBER

5f. WORK UNIT NUMBER

7. PERFORMING ORGANIZATION NAMES(S) AND ADDRESS(S)

Air Force Institute of Technology
Graduate School of Engineering and Management (AFIT/EN)
2950 Hobson Way
WPAFB OH 45433-7765

8. PERFORMING ORGANIZATION REPORT NUMBER

AFIT/GE/ENG/06-17

9. SPONSORING/MONITORING AGENCY NAME(S) AND ADDRESS(ES)

AFRL/MNAV AFMC
Attn: Mr. Chris E. Perry, Lead of Micromunitions Team
101 West Eglin Blvd, Suite 332
Eglin AFB FL 32536 DSN: 872-4651

10. SPONSOR/MONITOR'S ACRONYM(S)

11. SPONSOR/MONITOR'S REPORT NUMBER(S)

12. DISTRIBUTION/AVAILABILITY STATEMENT

APPROVED FOR PUBLIC RELEASE; DISTRIBUTION UNLIMITED.

13. SUPPLEMENTARY NOTES

14. ABSTRACT

This thesis includes the design, modeling, and testing of novel, power-scavenging, biologically inspired MEMS microrobots. Over one hundred 500-µm and 990-µm microrobots with two, four, and eight wings were designed, fabricated, characterized. These microrobots constitute the smallest documented attempt at powered flight. Each microrobot wing is comprised of downward-deflecting, laser-powered thermal actuators made of gold and polysilicon; the microrobots were fabricated in PolyMUMPs® (Polysilicon Multi-User MEMS Processes). Characterization results of the microrobots illustrate how wing-tip deflection can be maximized by optimizing the gold-to-polysilicon ratio as well as the dimensions of the actuator-wings. From these results, an optimum actuator-wing configuration was identified. It also was determined that the actuator-wing configuration with maximum deflection and surface area yet minimum mass had the greatest lift-to-weight ratio. Powered testing results showed that the microrobots successfully scavenged power from a remote 660-nm laser. These microrobots also demonstrated rapid downward flapping, but none achieved flight. The results show that the microrobots were too heavy and lacked sufficient wing surface area. It was determined that a successfully flying microrobot can be achieved by adding a robust, light-weight material to the optimum actuator-wing configuration—similar to insect wings. The ultimate objective of the flying microrobot project is an autonomous, fully maneuverable flying microrobot that is capable of sensing and acting upon a target. Such a microrobot would be capable of precise lethality, accurate battle-damage assessment, and successful penetration of otherwise inaccessible targets.

15. SUBJECT TERMS

Microelectromechanical systems, MEMS, microrobots, power-scavenging, autonomous, ornithopters, flying microrobots

16. SECURITY CLASSIFICATION OF:			**17. LIMITATION OF ABSTRACT**	**18. NUMBER OF PAGES**	**19a. NAME OF RESPONSIBLE PERSON**
REPORT	**ABSTRACT**	**c. THIS PAGE**			LaVern A. Starman, Maj, USAF (ENG)
U	**U**	**U**	**UU**	299	**19b. TELEPHONE NUMBER** *(Include area code)* (937) 255-6565, ext 4618; e-mail: LaVern.Starman@afit.edu

Standard Form 298 (Rev: 8-98)
Prescribed by ANSI Std. Z39-18